A spectroscopic study of detached binary systems using precise radial velocities

---

A thesis
submitted in partial fulfilment
of the requirements for the Degree
of
Doctor of Philosophy in Astronomy
in the
University of Canterbury
by
David J. Ramm

University of Canterbury
2004

Abstract

Spectroscopic orbital elements and/or related parameters have been determined for eight binary systems, using radial-velocity measurements that have a typical precision of about $15\,\mathrm{m\,s^{-1}}$. The orbital periods of these systems range from about 10 days to 26 years, with a median of about 6 years. Orbital solutions were determined for the seven systems with shorter periods. The measurement of the mass ratio of the longest-period system, HD 217166, demonstrates that this important astrophysical quantity can be estimated in a model-free manner with less than 10% of the orbital cycle observed spectroscopically.

Single-lined orbital solutions have been derived for five of the binaries. Two of these systems are astrometric binaries: β Ret and ν Oct. The other SB1 systems were 94 Aqr A, θ Ant, and the 10-day system, HD 159656. The preliminary spectroscopic solution for θ Ant ($P \sim 18$ years), is the first one derived for this system. The improvement to the precision achieved for the elements of the other four systems was typically between 1–2 orders of magnitude. The very high precision with which the spectroscopic solution for HD 159656 has been measured should allow an investigation into possible apsidal motion in the near future. In addition to the variable radial velocity owing to its orbital motion, the K-giant, ν Oct, has been found to have an additional long-term irregular periodicity, attributed, for the time being, to the rotation of a large surface feature.

Double-lined solutions were obtained for HD 206804 (K7V+K7V), which previously had two competing astrometric solutions but no spectroscopic solution, and a newly discovered seventh-magnitude system, HD 181958 (F6V+F7V). This latter system has the distinction of having components and orbital characteristics whose study should be possible with present ground-based interferometers. All eight of the binary systems have had their mass ratio and the masses of their components estimated.

The following comments summarize the motivation for getting these results, and the manner in which the research was carried out.

The majority of stars exist in binary systems rather than singly as does the Sun. These systems provide astronomers with the most reliable and proven means to determine many of the fundamental properties of stars. One of these properties is the stellar mass, which is regarded as being the most important of all, since most other stellar characteristics are very sensitive to the mass. Therefore, empirical masses, combined with measurements of other stellar properties, such as radii and luminosities, are an excellent test for competing models of stellar structure and evolution.

Binary stars also provide opportunities to observe and investigate many extraordinary astrophysical processes that do not occur in isolated stars. These processes often arise as a result of direct and indirect interactions between the components, when they are sufficiently close to each other. Some of the interactions are relatively passive, such as the circularization of the mutual

orbits, whilst others result from much more active processes, such as mass exchange leading to intense radiation emissions.

A complete understanding of a binary system's orbital characteristics, as well as the measurement of the all-important stellar masses, is almost always only achieved after the binary system has been studied using two or more complementary observing techniques. Two of the suitable techniques are astrometry and spectroscopy. In favourable circumstances, astrometry can deduce the angular dimensions of the orbit, the total mass of the system, and sometimes, its distance from us. Spectroscopy, on the other hand, can determine the linear scale of the orbit and the ratio of the stellar masses, based on the changing radial velocities of both stars. When a resolved astrometric orbital solution is also available, the velocities of both stars can allow the binary system's parallax to be determined, and the velocities of one star can provide a measure of the system mass ratio.

Unfortunately, relatively few binary systems are suited to these complementary studies. Underlying this difficulty are the facts that, typically, astrometrically-determined orbits favour those with periods of years or decades, whereas spectroscopic orbital solutions are more often measured for systems with periods of days to months. With the development of high-resolution astrometric and spectroscopic techniques in recent years, it is hoped that many more binary systems will be amenable to these complementary strategies.

Several months after this thesis began, a high-resolution spectrograph, HERCULES, commenced operations at the Mt John University Observatory, to be used in conjuction with the 1-metre McLellan telescope. For late-type stars, the anticipated velocity precision was $\lesssim 10\,\mathrm{m\,s^{-1}}$. The primary goals of this thesis were: 1. to assess the performance of HERCULES and the related reduction software that subsequently followed, 2. to carry out an observational programme of 20 or so binary systems, and 3. to determine the orbital and stellar parameters which characterize some of these systems. The particular focus was on those binaries that have resolved or unresolved astrometric orbital solutions, which therefore may be suited to complementary investigations.

HERCULES was used to acquire spectra of the programme stars, usually every few weeks, over a timespan of about three years. High-resolution spectra were acquired for the purpose of measuring precise radial velocities of the stars. When possible, orbital solutions were derived from these velocities, using the method of differential corrections.

Contents

Figures

Tables

Chapter 1

Introduction

Pairs of stars moving in gravitationally-bound periodic orbits about a common centre of mass are known as binary stars, and are said to constitute a binary system[1]. Two examples of these are illustrated in Fig. 1.1. These definitions distinguish such systems from other double stars that are not gravitationally bound (optical pairs) but simply appear 'near' to each other (i.e. having a small angular separation) as a result of fortuitously similar directions as viewed from the Earth[2].

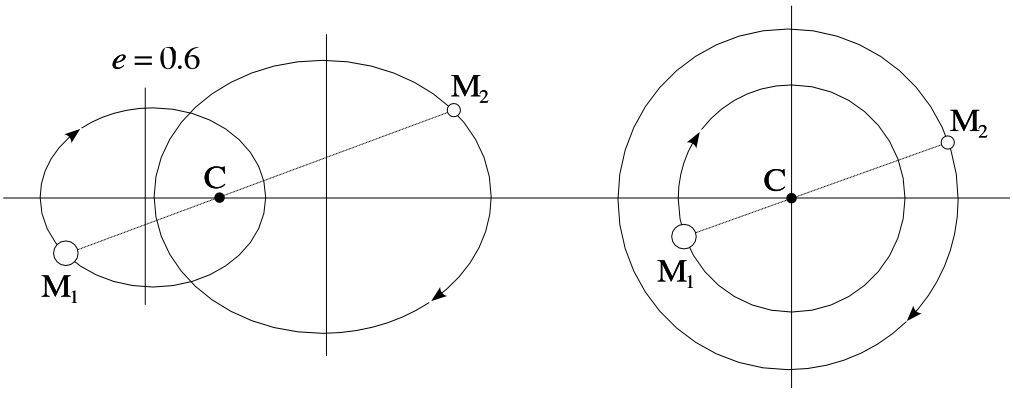

Figure 1.1: Binary systems with centre of mass, C, stars with masses M_1 and M_2, mass ratio $q = M_2/M_1 = 0.7$, and with eccentric and circular orbits.

1.1 The importance of binary systems

Since William Herschel established the existence of binary systems just over 200 years ago it has become increasingly evident that a large fraction of stars are members of such systems, rather than existing without stellar companions as does the Sun. As many as approximately 80% of all stars may be members of binary systems (Hogeveen 1990). Even so, the detected frequency of binaries is compromised by various selection effects. In the meantime, the proportion of

[1] A detailed description of bound orbital motion, including many definitions and derivations of related equations, is presented in Appendix A.

[2] Optical pairs may be further distinguished by establishing whether or not they share a common proper-motion — the common-proper-motion pairs.

stars recognized as inhabiting binary systems continues to increase (e.g. Nidever et al. 2002; Wichmann et al. 2003; Ramm et al. 2004), principally owing to improvements in the available instruments and analytical methods such as are available for high-resolution spectroscopy, the principal line of study for this thesis. Therefore the study of binary stars is important, as these systems provide a window on the majority of stars.

A second reason to study binary stars is that they provide the primary source of information relating to the fundamental properties of stars. The model-free determination of stellar masses has, to date, been achieved in all cases using binary systems[3]. The mass of a star is probably its most important property. Together with the initial chemical composition, the initial mass of an isolated star almost uniquely defines its structure and subsequent evolution. This is stated in the Vogt-Russell theorem, which asserts that for a star in hydrostatic and thermal equilibrium, with a given mass and composition, there is a unique solution to the equations of stellar structure.

Eclipsing binary systems that have both photometric and double-lined spectroscopic orbital solutions are able to provide high-precision estimates of a star's radius, which is the most direct diagnostic of a its evolution (Andersen et al. 1993). Knowing the radius and the effective temperature allows the Stefan-Boltzmann law to be used to ascertain each star's luminosity, and, based on the spectro-photometric data, a measure of the distance, even for those binaries that are extragalactic (see e.g. Harries et al. 2003). Extragalactic parallaxes measured using binary stars provide important support for the distance scale of the universe. Unfortunately, distances that are determined this way are dependent on various models and calibration relations. These assumptions can be avoided and the parallax measured in a hypothesis-free manner if the binary system has both resolved astrometric and a double-lined spectroscopic orbital solutions (see e.g. Pourbaix 2000, and Eq. (3.6) and Eq. (3.7) on page 24). Such systems, though, must be relatively nearby (as is discussed in § 4.1.2 on page 37).

Binary systems provide opportunities for astronomers to probe the atmospheres of stars at different heights (e.g. via atmospheric eclipses, limb darkening and surface irradiation effects) that are not possible from the study of single stars.

Many astrophysical processes and objects arise only in the environment of a binary system. Many of these objects are broadly classified as close or interacting binaries[4]. As their name suggests, the components of these systems are sufficiently close that some portion of their single-star evolution is significantly modified due to mass exchange between the components[5]. Whilst

[3]In principle, microlensing observations combined with high-precision astrometry, the latter to deduce the direction of the lens-source relative proper motion, can be used to measure the mass of a single star (Ghosh et al. 2004). It could be argued that two stars and the gravitational force are still involved, but now the stars are unbound.

[4]Two useful summaries of many aspects of binary star interactions may be found in Sahade et al. (1993) and Charles & Seward (1995).

[5]§ 2.2 (beginning on page 14) describes in more detail the underlying principles and classification of interacting and non-interacting binary systems in terms of the Roche model.

such interactions complicate the evolution of the individual stars, their benefit to us lies in the creation of an extraordinary menagerie of astrophysical objects that otherwise would not exist. For instance, when close binaries enter the phases of their evolution when mass-exchange arises, they may display evidence of accretion discs, streams and hot-spots, become systems exhibiting the Algol paradox, or become one of the cataclysmic variables (including the novae and dwarf novae). Interacting binaries also lead to the symbiotic, type I-a supernovae and various sources of high energy radiation e.g. as from X-ray binaries when one star is a compact object. Other astrophysical objects seem to exist in binary systems in a higher proportion than they do for single stars. Examples of these objects include stars with abundance peculiarities such as barium and S stars (Jorissen et al. 1998), as well as blue stragglers (Livio 1993) and Wolf-Rayet stars (Batten 1973; van der Hucht & Hidayat 2001).

As a larger archive of higher precision measures of stellar properties is acquired (in particular masses, radii, luminosities, and metallicities), it becomes increasingly possible to test and constrain stellar structure and evolutionary models (Andersen 1991; Andersen 1993). In turn, improvements in our understanding of the relationships that calibrate these fundamental parameters against each other can also be expected to improve, in particular the relationships of mass–luminosity and mass–radius. As better agreement is achieved it becomes possible more confidently to expand our investigations to stars less well studied (e.g. those massive stars that are rare or absent in the solar neighbourhood). Extending these comparative model studies to other regions of the Galaxy or other members of the Local Group will ultimately provide opportunities to assess how robust our models are for stars forming and evolving in perhaps significantly different environments (e.g. in terms of the density of stars, or regions of space that are relatively metal-deficient).

Finally, since binary systems are so common they deserve careful investigation so that we might better understand why this form of existence is favoured. After selection effects have been assessed, statistical compilations of stellar and orbital data on pre- and main-sequence binaries provide important guidelines for assessing competing theories of origin. Not only would such knowledge help in our understanding of the binary stars themselves, but it would presumably assist in our understanding of the circumstances that lead to the alternative formation of single stars such as the Sun. Indeed, binary systems are now considered as one of the best constraints on stellar formation models.

1.2 Motivation and goals of this study

Any satisfactory assessment of our understanding of stellar structure and evolution requires accurate and precise measures of the stellar properties (such as masses and radii) for which the behaviour of competing models is particularly sensitive. Unfortunately, there continues to be an extraordinary shortage of such empirical data, even with the considerable advances in our observational and analytical techniques (e.g. high-resolution spectroscopy and methods of digital

cross-correlation). For instance, Andersen (1991) identified only 45 eclipsing binary systems that met the criterion of having fundamentally determined masses and radii to ± 2% or better. In a more recent survey by Hilditch (2001), it was reported that only 114 stars had well-determined measures (accuracies better than ± 2%) of mass, radius, luminosity and temperature. Similarly, the mode or modes of the formation of binary systems that predominate are also still a matter of serious debate[6]. Our understanding of orbit evolution (e.g. the processes of orbit circularization and synchronization and their timescales for different systems) is also imperfect (e.g. Zahn 1977; Zahn & Boucet 1989; Goldman & Mazeh 1991; Tassoul 1995; Claret & Cunha 1997).

Motivated by these circumstances, there are two principal areas of study that are the goals of this research:

1. To assist with the establishment of the HERCULES spectrograph operating at the Mt John University Observatory. This is one of the first of the new breed of high-resolution vacuum spectrographs.

2. To contribute to the solution of some of the aforementioned important issues in binary star research by the measurement of certain fundamental binary system parameters. These parameters include the spectroscopic orbital elements, the mass ratios, and if possible, the masses of the stars of several binary systems.

1.2.1 Overview of strategy

The most commonly used observational techniques in binary star research are astrometry, spectroscopy and photometry. Binary systems that allow model-free measurements of the component masses and the orbital elements using data from a single one of these techniques are rare. Such systems are limited to the few visual binaries that have the parallax and absolute orbits of both stars measured astrometrically. For the vast majority of binary systems, the masses and a complete set of orbital elements will only result if at least two techniques can be applied to the system (e.g. van den Bos 1962; Griffin 1992). Owing to the selection effects inherent in the various observational techniques (the subject of Chapter 4), there are in fact a disappointingly small number of amenable binary systems even to a complementary strategy (Popper 1980; McAlister 1985; Griffin 1992).

One approach is to combine data acquired photometrically from an eclipsing binary with data derived spectroscopically from radial-velocity measurements (e.g. Popper 1967; Andersen 1991). This approach is not entirely model-free as the photometric analysis relies upon modelling of the measured light-curve. An alternative is to combine spectroscopically measured radial-velocity data with the orbital solution obtained astrometrically. This can be achieved in several ways and will be the basis of the observational part of this thesis. The spectroscopic-astrometric methods are described in some detail in Chapter 3, but will be summarized now.

[6]There are at least six competing theories for the origin of binary stars: cluster disintegration, conucleation, capture, fission, fragmentation, and disk instability. For a review, see De Buizer & van der Bliek (2003)

The spectroscopic measurement of the radial velocities of stars in suitable binary systems allows deduction of most orbital parameters to a precision dependent on the velocity variation, the precision of the velocity measures, the completeness of phase sampling and the number of orbital periods observed. The inclination of the system's orbit to the observer's line of sight is a crucial element that is never provided by a spectroscopic orbital solution in a model-free manner. As a consequence of this limitation, neither the component masses nor the total mass of the system can be deduced with this technique alone. However, if changes to the radial velocities of both stars can be measured, the ratio of the component masses can be derived without reference to any spectroscopic orbital solution and solely from these velocities. When the velocities of only one star can be measured, the mass ratio cannot be derived (unless the relative orbit has been determined; the mass ratio so determined is, though, very sensitive to systematic errors in the astrometric orbital elements). Instead, with the velocities of only one star, it is only possible to measure a quantity related to the masses, known as the mass function. The mass function can only be measured if the corresponding spectroscopic orbital solution is also known.

The resolved and unresolved astrometric orbital solutions provided by visual and astrometric binaries respectively complement the radial-velocity measurements by providing the orbital inclination. Of these two binary types, the orbital solution of a visual system provides the more complete parameter set, as the true angular size of the orbit can be determined. A binary's total mass can be deduced using Kepler's third law, if the relative orbit and the system's parallax are known. The parallax can be measured astrometrically, or by combining the radial velocities of both stars with the relative orbit data. In any case, armed with estimates of the binary's total mass and the component mass ratio, it becomes possible to measure the masses of the individual stars. Challenges of a more general nature imposed by the use of visual binaries is that these systems rarely provide adequate orbit sampling or radial-velocity changes over three years (the approximate duration of the observational portion of this thesis), since their orbital periods are typically decades or centuries. A further limitation of visual binaries is that the radial-velocity difference of the components is frequently insufficient to separate the spectral lines of each component, so that the spectral lines are blended, thus making the measurement of the velocity of each star difficult or impossible.

The study of unresolved astrometric binaries permit the increased likelihood of adequate radial-velocity changes over two to three years as many of these systems have a period of this order of magnitude. Unfortunately, these binaries do not give a measure of the size of the relative orbit. Since a typical astrometric binary has only one star's spectrum sufficiently bright to allow radial velocities to be measured, the problem of line blending is unlikely to be present. However, without the angular size of the true orbit and faced with a single radial-velocity curve, once again the masses cannot be measured directly. However, if the orbital inclination and an estimate of the primary star's mass from photometry and theoretical evolutionary tracks are combined with the mass function, then the secondary mass may be measured.

1.3 Thesis structure

Following this introduction, the thesis is divided into several chapters and appendices:

Chapter 2 This chapter provides an overview of schemes used to classify binary systems.

Chapter 3 The importance of knowing stellar masses with high precision is discussed. This is followed by a detailed description of the possible combinations of spectroscopic and astrometric data that allow measurement of the component masses using the orbital elements and other parameters associated with a binary system. Finally various calibration relations that allow the masses of single stars to be deduced are presented.

Chapter 4 One of the challenges of this type of work is the selection effects that overshadow the observations and which differ from method to method. A statistical analysis of certain portions of three recent catalogues is conducted to put some of these biases in as current a perspective as possible. This chapter concludes with the list of binary systems selected for observation.

Chapter 5 The instruments employed, observations undertaken and reduction methods utilised are described.

Chapter 6 The measurement of the radial velocities, the corresponding orbital solutions, and error estimation methods are described. The HERCULES template library is also presented and its use discussed.

Chapter 7 A detailed analysis of six binary systems observed during this thesis is delivered. Many of the strategies described in the previous section, combining astrometric and spectroscopic data, will be utilized.

The main body of the thesis ends with some concluding remarks and is followed by five appendices:

Appendix A Definitions and theoretical background relating to orbital motion and radial velocities obtained from binary stars, as well as a method for deducing the convective blueshifts (and other spectroscopic properties) of these stars.

Appendix B Preliminary spectroscopic orbital solutions for two additional systems, as well as the cross-correlation functions for the observations of two triple-lined systems.

Appendix C Tables of the velocities measured for the eight binary systems analysed.

Appendix D Some comments on the well-documented distribution of orbital eccentricities in relation to periods.

Appendix E The introductory pages and a sample of tables and spectral maps from the HERCULES Thorium-Argon Atlas produced during this project.

Chapter 2

Classification of binary systems

There are a great many combinations of stellar types and orbital parameters in which binary systems present themselves to observers. Dividing such a heterogenous collection of related objects into more nearly homogeneous sub-classes helps to identify their similarities, differences and opportunities for study. Accordingly, various classification schemes have been devised. They include classification by the methods of observation (e.g. see Batten 1973), the morphologies of the systems (Kopal 1955, 1959), and the evolutionary stages of the components, i.e. their relative positions on the H-R diagram (e.g. Sahade 1962). Binary systems are commonly distinguished using one of the first two schemes as follows:

a. The **observational method** employed: this classification is due primarily to the relationship of the stars and orbit relative to the observer e.g. how bright the stars are, whether the orbit has a large or small angular dimension or has an orbital plane that is edge-on or otherwise. Since certain binaries can be observed using more than one method, this scheme has the weakness that it does not place each binary system in a unique class. However, the binary cannot be categorized using one of the other schemes until some basic understanding of the system is acquired as a result of observation.

b. The **morphology** of the system: this approach is based on the absolute or intrinsic parameters of the binary e.g. the size and masses of the stars and their true separation, and, if the stars are close enough to one another that they may interact, how the interaction influences the binary's evolution. A binary's characteristics are described in terms of the Roche model. This scheme has no regard for the system in relation to any observer.

2.1 Classification by observational method

Since this thesis is based on observational data, it is this classification that is most relevant and therefore it will receive the most attention. The recognition that a pair of stars form a binary system is based in the first place by specific observations whose variation over time can only be interpreted as evidence of closed-orbital or Keplerian motion. The three principal methods used for observing binary stars are astrometry, spectroscopy, and photometry. At least four types of binaries can be identified based on the method of observation:

	method		binary type	label		orbital solution
i.	astrometry	–	visual	VB	⇒	astrometric
ii.	astrometry	–	astrometric	AB	⇒	photocentric
iii.	spectroscopy	–	spectroscopic	SB	⇒	spectroscopic
iv.	photometry	–	eclipsing	EB	⇒	photometric

The astrometric binaries may also be distinguished by indicating whether they are resolved systems (having 'astrometric' solutions), or are unresolved (those with a 'photocentric' orbital solution).

The ease with which a given binary system is recognized and observed with a particular technique is influenced by many factors. In addition to those already mentioned (i.e. the brightnesses of the stars, their angular separation, and the orbital inclination), the relative velocities and accelerations of the stars as they move around their common centre of mass are especially significant for spectroscopic binary studies. Over time, the orbital motion of the stars in any binary system will inevitably lead to changes to some of the observer-dependent parameters so that the opportunity for observation can also be expected to vary. The eventual success of the observing programme is also a result of such issues as the availability of telescope time, the suitability of the telescope and detector, the quality of the observing site, and the sophistication of the reduction and analytical methods applied to the observational data.

Until a reliable orbital solution has been derived, the possibility exists that the measurements obtained are inconsistent with a single pair of orbiting objects. In these cases the analysis may lead to the suspicion of additional components in the system, or other processes mimicing the measurements undertaken (e.g. when spectroscopic radial velocities target the centre-of-mass motion but also include contributions to wavelength shifts by rotational motion or activity of the stellar surface. The final sections of Appendix A, beginning on page 230, describe these various effects.).

2.1.1 Visual binaries

If a binary system allows direct measurement of the polar coordinates of one star relative to the other it can be classified as a visual binary. The polar coordinates, in the plane of the sky, are the *angular separation* ρ and the *position angle* θ (see § A.11.1 and Fig. A.3). The determination of the relative orbit of a binary system is likely to be complicated by additional motions arising from the motion of the system's barycentre against the celestial sphere of background 'fixed' stars i.e. the proper motion, as well as effects arising from the Earth's own motion e.g. the parallactic orbit (whose size is proportional to the binary's parallax) and the larger shifts due to nutation and aberration (see e.g. van de Kamp 1967).

There are several techniques that are used to measure the polar coordinates. Initially, they were only obtained by visual means at the eyepiece, hence the name. Success relies upon

observing objects whose separation exceeds the diffraction limit δ of the instrument used. For a circular primary mirror used for observations in visible light,

$$\delta'' = 251\,643.3\,\frac{\lambda}{D}\,, \tag{2.1}$$

where D is the telescope aperture, and λ is the observing wavelength in the same units. Many other selection effects influence the observability of visual binaries (§ 4.1) including the relative brightness of the stars and the local seeing conditions.

The minimum angular separations achievable visually occur during brief moments of exceptional clarity and seeing and are typically no better than about $0.2''$. Photographic and standard CCD image resolution is typically an order of magnitude or so poorer. This is a result of the difficulty of recording separate but proximal faint diffraction patterns, exacerbated by the accumulated smearing effect of atmospheric turbulence and guiding errors during the exposure. The resolution of close stellar images has been improved dramatically using adaptive optics[1].

The development of interferometric techniques has provided the means to resolve much smaller stellar separations. To date, speckle interferometry has been the most productive of the various interferometric methods for investigating visual binaries (e.g. Mason et al. 1998b) and is successful for angular separations in the range $0.035'' < \rho < 1.5''$ (McAlister 1985). When moderate aperture (4-m) single telescopes are used, speckle interferometers require the components to be brighter than about magnitude 8 and to have a magnitude difference $\Delta m_{\rm v} < 3$ mag. The largest telescopes can extend these limits to a resolution closer to $0.02''$ and be suitable for a magnitude difference of up to 5–6 magnitudes. The most recent addition to the available techniques for the study of visual binaries has been the develoment during the past 15 years or so of long-baseline optical interferometry. These developments have allowed the resolution of binary orbits as small as 0.01–$0.02''$.

Measurement of the smallest binary separations using Earth-based instruments are realised when the Moon is used as an occulting disc. Whilst limited to binaries located within a band $\sim 10^\circ$ wide centered on the ecliptic, and made difficult by the infrequent passage of the Moon across a given system, analysis of the resulting diffraction pattern intensities can measure stellar separations as small as $0.001'' = 1$ mas (Kallrath & Milone 1999).

Telescopes and interferometers placed in space beyond the restrictions of the Earth's atmosphere, for example the proposed future instruments SIM (Space Interferometer Mission) and TPF (Terrestrial Planet Finder), offer many advantages including the ability to observe binary and planetary systems with unprecedented precision and accuracy. For example, SIM, an optical Michelsen interferometer, promises astrometry with microarcsecond accuracy (Danner & Unwin 1999).

[1]For a review of adaptive optics see Beckers 1993.

The angular measures of a visual binary provide an astrometric orbital solution where the semimajor axis is naturally also an angular measure, namely a''. For the rare systems that allow the absolute orbits to be measured, a_1'' and a_2'' can also be determined. Only if the parallax p'' is known can $\mathcal{A} \in \{a,\ a_1,\ a_2\} = \mathcal{A}''/p''$ be deduced from these orbital solutions. The other orbital elements[2] that may be measured are e, i, ω, Ω, P and T.

2.1.2 Astrometric binaries

When a binary presents only one light source at the time of an astrometric observation, two causes are possible. First, the separation of the two stars may be less than the resolution available for that observation, so that only the combined light of both stars is visible. Alternatively, the stars may be resolvable but the brightness difference may be sufficient that the fainter star is lost in the glare of its brighter companion (e.g. historically, the classic case of Sirius A & B). The binary nature of such an object may be ascertained if it is sufficiently nearby that its proper motion against the background stars can be found to be variable. When this is achieved, the system can be classified as an astrometric binary.

The possibility of recording only a single image for a binary system is particularly prevalent when they are studied photographically (see e.g. van de Kamp 1962; van de Kamp 1967). The weighted centre of the light intensity of the single image resulting from the combined light is known as the photocentre. The photocentre, P, centre of mass, C, and the two stars, A and B, in an astrometric binary lie on the same line (Fig. 2.1). The position of the photocentre relative to these other three positions on the apparent orbit depends upon the mass ratio q, the luminosities L_1 and L_2 and spectra of the stars, and the processes involved in the spreading of light on the detector (Couteau 1981).

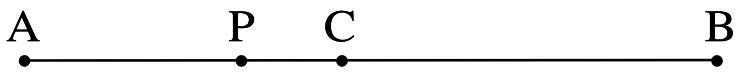

Figure 2.1: The principal points corresponding to an astrometric binary. The respective labels are for the photocentre, P, centre of mass, C, and the two unresolved stars, A and B.

When only the luminosity difference and mass ratio are considered, a complete photocentric orbital solution has the general properties of the relative orbit (e, i, ω, Ω, P and T), but with a scaled orbital size $a_{\rm p}''$ defined by

$$a_{\rm p}'' = a''(B - \beta)\,, \tag{2.2}$$

[2]See § A.2 for the definition of these symbols.

$$\text{where} \qquad \frac{a''_{\rm p}}{a} = \frac{\rm PC}{\rm AB}\,, \qquad B = \frac{\rm AC}{\rm AB} = \frac{q}{1+q} = \frac{M_B}{M_A + M_B}$$

$$\text{and} \quad \beta = \frac{\rm AP}{\rm AB} = \frac{L_2}{L_1 + L_2} = \frac{1}{1 + 10^{0.4\Delta m_{\rm v}}}\,,$$

with $\Delta m_{\rm v} = m_{{\rm v},\,2} - m_{{\rm v},\,1}$ being the magnitude difference of the stars. When the complicating effects of the light diffusion properties and spectral sensitivity of the detector are considered, the value of β may be modified empirically (Couteau 1981). One of the challenges presented by astrometric systems is to estimate B and β so as to be able to deduce a'' accurately and precisely.

2.1.3 Spectroscopic binaries

The radial-velocity observations that identify most spectroscopic binaries originate in the Doppler shifting of the star's spectral lines. For the non-relativistic case, as is appropriate for binary systems of normal stars (and indeed the majority of others as well), the relationship that expresses this physical process is

$$\frac{\lambda - \lambda_0}{\lambda_0} = \frac{\Delta\lambda}{\lambda_0} = \frac{V}{c}\,, \tag{2.3}$$

where V is the radial velocity, c is the speed of light, λ is the observed wavelength of a spectral line and λ_0 is its rest wavelength. By definition, the radial velocity is positive when the spectrum is redshifted since this is when $\Delta\lambda > 0$. When the radial velocity is negative, the spectrum is blueshifted. The binary nature of the object becomes apparent either with evidence of two spectra (assuming the object is not an optical pair, which would be unlikely) or as is more typical, with radial velocity changes that are consistent with Keplerian motion.

Spectroscopic binaries are not subject to the spatial resolution limitations of visual binaries. Their observation is in the first place only limited by the ability of the detection system adequately to resolve the spectral lines of one or both stars. If the spectral lines of both stars can be resolved, the binary can be recognized, in principle, with a single observation. Until the relative positions of the lines of the two components are observed to change, the system can only be classified as a spectrum binary. A line-width spectroscopic binary is a system whose spectra are never individually separated (LWSB; Duquennoy & Mayor 1991). LWSB systems reveal themselves by unresolved but variable line widths. Once the lines become separated and are seen to vary with opposite phase, the system can be classified as a double-lined spectroscopic binary or SB2. When the lines of only one star are evident throughout all orbital phases, the object's binary nature can only be recognized if a series of radial-velocity measurements reveals Keplerian motion. In this case, if the invisible companion has an estmated mass consistent with it being a star, the system is classified as a single-lined spectroscopic binary or SB1. Substantially less massive companions herald the discovery of extrasolar planets. With the observation of

more favourable orbital phases and improvements to detection and reduction methods, a spectroscopic binary's classification may change e.g. from LWSB or SB1 to SB2, or if three sets of lines become evident, to a triple-lined spectroscopic system[3].

Lucy and Ricco (1979) derived an expression for the visibility f of the lines of the secondary with respect to the primary star in a binary's spectrum. Based upon a main-sequence mass-luminosity relation and taking into account Wien's displacement law, they found:

$$f = \frac{2}{1 + q^{-6}}\,, \tag{2.4}$$

where f is the factor by which a line's depth is reduced relative to that seen in a binary with $q = 1$. This formula indicates that the visibility of the secondary lines decreases rapidly as q becomes smaller. This is consistent with the observed distribution of mass ratios of SB2s, which is dominated by systems with $0.8 \lesssim q \leq 1$ (Lucy & Ricco 1979; Staniucha 1979; Halbwachs et al. 2003).

Determining whether or not a shift in a spectral line position has occurred is based, first, by identifying the line in the spectrum[4], and if successful, then upon delicate measurements of the line position relative to a calibration scale of a laboratory determined reference spectrum. Modern high-precision radial-velocity measurements most commonly use a calibration source provided by a cell of iodine gas, or as in this study, a thorium-argon lamp. Stellar radial velocities have been measured with extraordinary precision using both of these reference spectra. Iodine cells have allowed $\sim 3\,\mathrm{m\,s^{-1}}$ precision (e.g. Marcy et al. 1996) whilst the latest state-of-the-art spectrograph using a thorium lamp (HARPS - Queloz & Mayor 2001) has allowed claims of $1\,\mathrm{m\,s^{-1}}$ precision.

The general equation for a spectroscopic orbital solution (derived in § A.13 beginning on page 226) is

$$V_n = \gamma + K_n\big[e\cos\omega_n + \cos(\upsilon + \omega_n)\big]\,,$$

where $n = 1$ or 2 for the primary and secondary star respectively[5]. The orbital position at a given time t is defined by Kepler's equation (Eq. (A.55) on page 222) using e, P and T so that a spectroscopic orbital solution includes γ, e, P, T, ω_n, and K_n. The latter two elements are dependent upon which component's radial-velocity curve is computed. The influence of the

[3]During this project's observing programme, the star HD 10800 was discovered to be a triple-lined spectroscopic binary. The series of cross-correlation functions corresponding to the 51 observations obtained are presented in Appendix B.

[4]The availability of lines in HERCULES spectra over time, as a result of shifts in the relative position of the spectrum on the detector, is described in § 5.10 beginning on page 100.

[5]§ A.1 on page 207 discusses the conventions of labelling the components of binary systems depending upon the method of study.

semimajor axis a_n and inclination i is restricted to scaling K_n. Consequently, the most that can be deduced from each radial-velocity curve is a value for $a_n \sin i$. If the binary system also allows an astrometric, photocentric or photometric orbital solution, the problem of the unknown inclination can be resolved. There are hundreds of binary systems with spectroscopic orbital solutions (Pourbaix et al. 2004) whose components are predicted to have angular separations of the order of one milli-arcsecond or more. The progressive development and utilization of high-resolution instruments both on the ground and in space promise the determination of the corresponding astrometric orbits of many of these systems. Model-free measurement of the masses will then be possible.

2.1.4 Eclipsing binaries

This thesis does not base any of its results on an analysis of any eclipsing binary system. Most of the comments relating to these systems in this thesis will be included here.

If, by chance alignment with the observer, the stars of a binary system eclipse each other, the system can be classified as an eclipsing binary. Due to the typical separation of stars in binary systems, such systems must have their orbital plane close to being edge-on to the observer, and therefore these systems are rare. To a first approximation, for two stars of radii R_1 and R_2 and separation r, the minimum requirement for an eclipse to occur is that the inclination i of the orbital plane be in the range

$$90^\circ - \sin^{-1}\left(\frac{R_1+R_2}{r}\right) < i < \ 90^\circ + \ \sin^{-1}\left(\frac{R_1+R_2}{r}\right) \ \sim 90^\circ \,. \tag{2.5}$$

The detection and investigation of eclipsing binaries is biased towards components which not only have nearly edge-on orbits, but also have stars that are relatively large and luminous, moving in relatively small orbits (Batten 1973). This is so that the eclipses will be deeper and last a larger fraction of the total period, so that they are more easily observed. Such systems typically comprise main-sequence stars of spectral types F and earlier (Popper 1967). Improvements to techniques in recent years, such as in light-curve analysis for the photometric solution, and the choice of a larger number of available fitting functions for the velocity measurement for the spectroscopic solution, have provided opportunities to investigate later-type stars with shallow eclipses (e.g. Hill et al. 1990). Stars that are poorly represented are the rare hot and massive O-type dwarfs and the faint and relatively small K- and M-type dwarfs. Stars moving in close, highly-inclined orbits are also likely to provide relatively large radial velocities so that when the spectra of both stars are observable, line blending is less likely.

To date, non-interacting SB2 eclipsing binaries have provided the largest number of precise mass determinations of the more common medium to higher mass stars (e.g., see the reviews by Popper 1980, and Andersen 1991). Double-lined spectroscopic eclipsing binaries also allow measurement of the radii of the components. The light-curve information can provide the size

of each orbit relative to the stellar radii ($a/R_{1,2}$). The unscaled value for a can be determined using the orbital inclination, also derived from the light-curve, in conjuction with the SB2 value for $a \sin i$. When combined with the effective temperature of each star, the stellar radius also allows direct measurement of the luminosities.

In recent years, new eclipsing SB2 M-dwarf systems have been discovered (e.g. Delfosse et al. 1999; Maceroni & Montalbán 2004), providing rare opportunities to derive accurate masses for such low luminosity stars, and to be able to compare their observed properties to M-dwarf models. Acquiring accurate metallicities for these low-mass stars is another challenging but worthy goal as the metallicity makes a significant contribution to the luminosity of them. These very low mass stars have the benefit that they evolve so slowly that one can be confident that they have not yet left the zero-age main sequence, making studies of their unevolved properties possible.

2.2 Classification by morphology: Roche models

The close or interacting binaries described in the introduction (§ 1.1 on page 2) are just one of a group of binary system classifications based upon the relationship of the components to the closed equipotential surfaces surrounding each star. For circular orbits with synchronous rotation[6] these surfaces are where the potential energy (sum of rotational and gravitational energy per unit mass) is constant. Near the stellar centres these surfaces are almost spherical, but closer to the companion star, the profiles of them, have a figure-of-eight profile.

The surfaces are generally referred to as Roche surfaces, after the French mathematician É. Roche who described them in 1873. His analysis was based on the approximation that the gravitational potential was the same as if the total mass of the body was concentrated at its centre.

On a particular Roche surface, the motion of a third body, of negligible mass compared to the other two, has zero velocity relative to a coordinate system that rotates uniformly with the two principal masses. The value of a description of these surfaces for binary stars is that they provide a means of quantifying the shapes of the stellar surfaces and their possible interaction by the exchange or loss of particle masses. A summary of some of the principal aspects of the Roche geometry follows.

A convenient place to start is the geometric point that exists between the two masses where the independent Roche surfaces for each body meet (see Fig. 2.2). This is the inner Lagrangian point, L_1 (named after another French mathematician, J. L. Lagrange), which is an unstable equilibrium point. The Roche surfaces that meet at L_1 are called the Roche limits, or inner

[6]Synchronous rotation exists when a star in a circular orbit has a rotation period equal to its orbital period. This is the case for many close binaries. Binaries having eccentric orbits tend to to have their rotational angular velocity synchronized with the orbital angular velocity at periastron (Hut, 1981).

Lagrangian surfaces, and encompass the two respective three-dimensional limiting volumes typically known as Roche lobes[7].

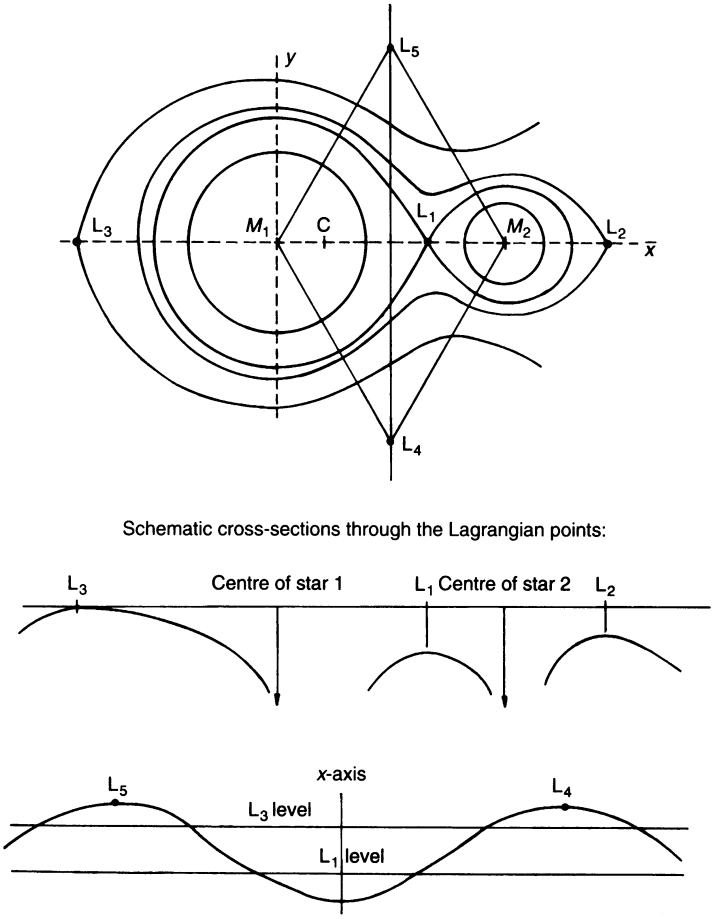

Figure 2.2: Roche surfaces, Lagrangian points and the corresponding relative potentials. The upper diagram illustrates the potential contours in the orbital plane, the x-axis being an axis of symmetry that includes the two masses, the centre of mass, C, and the Lagrangian points L_1, L_2 and L_3. The lower diagrams represent schematic cross-sections through the five Lagrangian points (diagram from Smith 1995).

In stellar systems, the closer a star's surface approaches its Roche lobe, the more distorted will that surface become. Each Roche surface within a lobe represents the approximate shape a star would have if it was large enough to reach the given surface. The actual size of each Roche lobe is determined primarily by the separation of the components, and to a lesser extent, by the mass ratio, q. The lobes are of equal size when $q = 1$, whilst for $q < 1$, the lobe is larger about the more massive star. Of key importance with regard to our understanding of interacting binary stars is the fact that each Roche lobe identifies the surface from which the star can lose

[7]In more general models including those with eccentric orbits and asynchronous rotation, the Roche limits and lobes may be referred to as critical limits and critical lobes (Kallrath & Milone 1999).

matter to its companion.

Beyond the Roche limiting surfaces are additional equipotential surfaces that surround the entire binary system in various ways. One of these surfaces, the outer Lagrangian surface, meets at the outer Lagrangian point, L_2. For systems where $q \neq 1$, this point is on the opposite side of the less massive star, on the same straight line that includes the gravitational centres of the stars and L_1. The importance of L_2 is that it is the theoretical point at which matter can escape the gravitational grasp of the binary system. A third Lagrangian point, L_3, exists at a somewhat higher potential than L_2. L_3 is positioned on the opposite side of the more massive star. There are two more Lagrangian points that correspond to the potential maxima. These are labelled L_4 and L_5. Their positions form equilateral triangles with the two masses.

2.2.1 Estimating the size of a Roche lobe

When considering the possibility that a close binary might have one or both components filling its Roche lobe, and therefore the stars interacting in one way or another, it is necessary to be able to measure the sizes of the Roche lobes relative to the stellar radii. A convenient measure of the size of the Roche volume is its effective or volume radius $r_{\rm L}$, which is the radius of a sphere of the same volume as the Roche lobe, relative to the component separation a. Thus the actual effective radius is $R_{\rm L} = r_{\rm L} a$. A useful formula (Eggleton 1983) for estimating $r_{\rm L}$ to an accuracy of $\sim 99\%$ for all sensible values of q is

$$r_{\rm L} = \frac{R_{\rm L}}{a} = \frac{0.49 q_{\rm L}^{2/3}}{0.6 q_{\rm L}^{2/3} + \ln\left(1 + q_{\rm L}^{1/3}\right)}\,, \tag{2.6}$$

where $q_{\rm L} = M_{\rm L}/M_{\rm c}$ and $M_{\rm L}$ is the mass of the component whose effective radius is calculated and $M_{\rm c}$ is that of its companion.

2.2.2 Classifying binaries using the Roche geometry

The concept of the Roche geometry allows us to classify binaries into several morphological classes. In his study of the apparent irregular period changes of eclipsing binaries, Wood (1950) suggested dividing close binary stars into two categories — one in which neither component fills its Roche lobe, and the other in which at least one component fills its Roche lobe. This idea was extended by Kopal (1955), who recommended that close binaries be categorized as follows:

1. Detached systems: neither component exceeds its Roche limit. Kopal identified these systems as having both stars on the main sequence or not too far evolved from it.

2. Semi-detached systems: only one component fills *exactly* its Roche lobe. Kopal suggested that this class would represent Algol-type binaries, with the more massive primary star on the main sequence whilst the secondary star was evolved from it. These systems are synonymous with close or interacting binaries and mass-transfer is via the inner Lagrangian point.

3. Contact systems: both components fill their Roche lobes, so that the stellar surfaces are in 'contact' with the corresponing critical surfaces.

Kallrath and Milone (1999) argue that contact systems should be specifically only those systems that have both critical surfaces *just* in contact. This would be rare, as such systems should rapidly evolve to other types because of instability to even small perturbations or mass transfer. They also define two additional morphological classes:

4. Double-contact systems: each component fills a critical lobe. However, one component rotates supersynchronously owing to it being spun-up by accreting material. Its critical surface is not bounded by the inner Lagrangian surface, but instead is bounded by the equipotential that has equatorial material rotating at close to the centrifugal limit.

5. Over-contact systems: These are also known as common envelope binaries. Both components exceed the size of their critical lobes so that material from both components share the same equipotential region whose outer bound is the outer critical surface.

Significant mass transfer and mass loss will have important consequences. The modification to the original component masses and possibly composition (as a result of prior significant mixing) will alter the subsequent evolution accordingly. As a result of the demands of conservation of energy and angular momentum, changes to the orbital separation and eccentricity can also be anticipated. Subsequently, any of the related properties can be expected to change as well (Andersen 1997). Therefore, only data relating to non-interacting binaries are likely to be typical of comparable normal single stars, and so be of use for comparing stellar models and establishing comprehensive calibration relations.

The binary systems that are at the centre of this thesis are all detached systems which are assumed to have never experienced mass exchange. Detached binaries provide the basis for the empirical calibration of the mass-luminosity and mass-radius relationships. These systems serve as guides for single-star structure. The opportunity to expand these investigations to tests of evolutionary theory is made possible by the observation of detached binaries comprising evolved components, i.e. of stars that have not yet experienced mass-transfer or mass-loss. Unfortunately examples of these latter systems are rare (Hilditch 2001).

Chapter 3

Stellar masses

From theoretical considerations, stellar masses are believed to lie between $\sim 0.08\,\mathcal{M}_\odot$ and 60–$100\,\mathcal{M}_\odot$ (Batten 1973; Heintz 1992). The lower mass limit is set by the expectation that at least $0.08\,\mathcal{M}_\odot$ must be present to create sufficiently high central temperatures ($T_\mathrm{c} \sim 2{\times}10^6\,\mathrm{K}$) to move beyond the deuterium-burning brown dwarfs and enter the realm of core hydrogen-burning true stars. The upper mass limit is less certain but is expected for a number of reasons. For instance, the rapidly increasing radiation pressure produced by the formation of such massive stars is expected to counteract their condensation. Other limitations include vibrational instabilities in their interiors and the very high angular momentum associated with such masses, which should lead to fission of the protostar so that a binary or multiple system results instead[1].

3.1 The importance of mass for a star

The fundamental characteristics of a star that are in principle measureable by direct observation include its mass, radius, surface temperature and chemical composition, magnetic field strength and rate of rotation. Of these, the mass is the most important. The mass of a star determines much of its underlying structure, its observed features and ultimately its evolution.

This is especially true of main-sequence stars which comprise 80-90% of all observed stars. For instance, in general, main-sequence stars of increasing mass $\mathcal{M}$ will:

- have a higher central temperature, T_c , and so can initiate higher atomic number nuclear fusion reactions;
- have a higher effective temperature, T_eff, and so radiate especially at bluer wavelengths;
- have a greater intrinsic luminousity, L;
- have a greater radius R but lower density ρ;
- have a greater equatorial velocity, v_equ, i.e. axial rotation rate (for spectral types $\sim$ B5 and later);
- have a shorter main-sequence lifetime;

[1] Until recently, observational evidence seemed to challenge this upper limit with the apparent existence of supermassive objects such as 30 Doradus in the Large Magellanic Cloud whose mass was estimated to be $\sim 1000 - 3000\,\mathcal{M}_\odot$. Eventually, photographic speckle interferometry and other techniques resolved 30 Doradus into multiple separate components with masses closer to the much lower theoretical upper limit (Humphreys 1992).

- reside closer to the Galactic plane (Allan 1964);
- have lower spatial number densities (Bahcall & Soniera 1980);
- experience mass loss fluxes that are greater, (de Jager et al. 1988), and more violent;
- have evolutionary paths that carry them higher across the Hertzsprung-Russell (H-R) diagram; and
- evolve to stellar remnants of increasing density i.e. white dwarfs, neutron stars, or black holes.

Values for several of these stellar properties are listed in relation to main-sequence mass in Table 3.1. Even in advanced evolutionary phases, theoretical investigations suggest that the mass maintains its key role in determining structure, appearance and subsequent evolution — other properties are secondary in comparison.

The influence of these secondary but non-the-less important parameters is demonstrated in a number of ways. For instance, studies of accurate and precise stellar masses show that there is a range of mass for each spectral type along the main-sequence. This scatter is not due to measurement error since the average mean error of the mass and colour values are considerably less than the scatter (Andersen 1991). The scatter is due to real differences in these secondary parameters, which include the chemical composition and age of the stars. Mass differences due to evolution within the main-sequence for a given spectral type or colour can easily amount to $\sim 30\%$ (Andersen 1997). The combined influence of the mass, initial composition and age of a star is embodied in the Russell-Vogt theorem.

Even this view is somewhat simplified, as there are other properties that differ between stars of the same mass, composition and age, and that modify their position on an H-R diagram. For instance, the main-sequence position of a star depends upon its equatorial rotation speed[2], the rotation law relevant to the star, and the inclination of the rotation axis to the line of sight (Maeder & Meynet 2000)[3]. As well as the main-sequence position, the prediction of consistent and accurate main-sequence lifetimes over a wide range of mass has been shown to require consideration of several additional effects. Again, rotation, including its effect on luminosity and mixing, seems to have a significant role to play, as does core convection and the rate of mass loss, particularly in more massive stars (Scalo 1986).

[2]The H-R diagram position of a star rotating at $\sim 200\,\mathrm{km\,s^{-1}}$ is estimated to shift by 0.1–0.3 mag in M_V and 200–250 in T_eff (Maeder & Peytremann 1970).

[3]This seems to be particularly true of more massive stars, where extensive mixing may take place (as a result of fast rotation), modifying the nuclear fuel reservoir and the surface abundances, so altering all the associated stellar properties and subsequent evolution (Meyner & Maeder 2000). Indeed, it has been argued that for massive O- and B-type stars at least, the initial rotation rate is as fundamental a parameter as the initial mass and composition (Langer, Heger & Fliegner 1997).

Mass ($\mathcal{M}_\odot$)	spectral type	$M_{\rm bol}$	$B-V$	$T_{\rm c}$ $\times 10^6$ (K)	$T_{\rm eff}$ (K)	radius ($R_\odot$)	density ($\rho_\odot$)	v_{equ} (km s^{-1})
60	O5	-10.0	-0.33	–	42 000	12	0.03	–
17.5	B0	-7.2	-0.30	–	30 500	7.4	0.04	170
6.0	B5	-2.7	-0.17	28.7	15 000	3.9	0.1	240
3.0	A0	+0.35	-0.02	24.2	9 800	2.4	0.2	180
2.0	A5	+1.8	+0.15	21.5	8 200	1.7	0.4	170
1.6	F0	+2.6	+0.30	19.6	7 300	1.5	0.5	100
1.4	F5	+3.4	+0.44	17.8	6 600	1.3	0.6	30
1.05	G0	+4.2	+0.58	–	5 900	1.1	0.8	10
1.00	**G2**	**+4.74**	**+0.65**	**15.7**	**5 800**	**1.0**	**1.0**	**2**
0.8	K0	+5.6	+0.81	–	5 600	0.85	1.25	< 10
0.7	K5	+6.6	+1.15	11.5	5 100	0.7	1.8	< 10
0.5	M0	+7.4	+1.40	–	3 850	0.6	2.2	–
0.2	M5	+9.6	+1.64	–	–	0.27	10.0	–

Table 3.1: The *mean* values of some theoretical and observed features of main-sequence stars as a function of mass. The values in bold type are for the Sun. (Adapted from Drilling & Landolt 2000; entries '–' were not provided.)

The strong relationships that the star's mass have with other stellar parameters place equally strong demands upon the precision with which stellar masses need to be measured, if they are to be useful for the purposes of comparing competing stellar models of structure and evolution. For instance, to compare satisfactorily opacity tables or theories of convective overshooting, mass errors of no more than about 2% are now required. Similar precision is required for values of stellar radii and temperature (Andersen 1993; Kippenhahn & Wiegert 1994). For unevolved systems, the masses and luminosities are the basis for evaluating a particular mass-luminosity relation (see § 3.3 on page 30 for further comment on this important relationship). If a model is valid, it must reproduce the H-R diagram position (i.e. the star's luminosity and effective temperature) of both components of a binary system for a single age and a single initial chemical composition[4]. Binary systems with increasingly unequal masses will provide the most demanding tests. Demands upon stellar theories made by stars in binary systems have additional significance in that, to date, binary systems have provided the only means for determining stellar masses in a model-independent manner. If mass errors are large enough that competing models can be made to fit the data by adjusting any free parameters, little insight can be expected. At the same time, improving mass precision below 1% seems unwarranted as other parameters such as metal abundances often then become the dominant source of error (Andersen 1991; Delfosse et al. 1999).

The importance of knowing the precise masses of individual stars extends beyond understanding the close relationship of mass to other stellar properties. In many investigations the integrated appearance and interactions of a large number of stars are the focus of attention. Knowledge of individual stellar masses therefore forms the basis for estimating the global properties and evolution of larger groups of stars such as clusters and galaxies. The frequency distribution of stellar masses at birth, the so-called initial mass function, is especially important in this regard, and provides a significant link between stellar and galactic evolution and, when combined with accurate mass-luminosity relations, allows estimates of galactic dark-matter to be made (e.g. see Scalo, 1986).

3.2 Stellar masses

The opportunity to measure the masses of objects as distant as stars in a fundamental manner is the result of the gravitational force acting on the orbiting bodies. No other means has yet been identified that can measure stellar masses as reliably.

Measuring the mass of each star in a binary system in an hypothesis-free manner requires two independent mass equations. Two such equations are the sum of the primary mass $\mathcal{M}_1$ and the secondary mass $\mathcal{M}_2$:

$$\mathcal{M}_{\rm S} = \mathcal{M}_1 + \mathcal{M}_2 \,, \tag{3.1}$$

[4]For this general statement to be fair, it is assumed that the binary is a non-interacting system.

which we call the system mass or total mass, and the ratio of the masses, which in this thesis is defined as

$$q = \frac{\mathcal{M}_2}{\mathcal{M}_1} \leqq 1\,. \tag{3.2}$$

The component masses are therefore derived according to

$$\mathcal{M}_1 = \frac{1}{1+q}\mathcal{M}_\mathrm{S} \qquad \text{and} \qquad \mathcal{M}_2 = \frac{q}{1+q}\mathcal{M}_\mathrm{S}\,. \tag{3.3}$$

The system mass is given by Kepler's third law[5] in terms of the linear semimajor axis of the relative orbit a and the orbital period P:

$$\mathcal{M}_\mathrm{S} = \mathcal{M}_1 + \mathcal{M}_2 = \frac{a^3}{P^2}\,, \tag{3.4}$$

where the masses are in solar mass units ($\mathcal{M}_\odot$), a is given in astronomical units (AU), and P is in years. It is this expression that presents the greatest difficulty for determining the component masses due to the fact that the (unscaled) value for a is rarely obtainable from one observational method. The mass ratio of the binary can be determined in a variety of ways, typically in relation to the ratio of the component values for another system parameter, for example $a_{1,2}$ or $K_{1,2}$ (the semi-amplitudes of each radial-velocity curve)[6].

The following sections present a series of equations that underlie the computation of stellar masses using different parameter sets of observational data. All but the first, which is provided to show how masses can be measured using a single observational technique, are relevant to this study.

3.2.1 Astrometric orbital solution only

The rare binaries whose component masses can be measured using a single observational technique are those visual binaries whose absolute orbital solutions for both stars (providing a_1'', a_2'' and P) and the system parallax p'' (in arcseconds) can be determined as a simultaneous solution to the observations. The system mass and mass ratio are defined by

$$\mathcal{M}_\mathrm{S} = \left(\frac{a_1'' + a_2''}{p''}\right)^3 \frac{1}{P^2} \qquad \text{and} \qquad q = \frac{a_1''}{a_2''}\,,$$

so that the component masses are

[5] This fundamental equation is derived in § A.9 beginning on page 219.

[6] See Eq. (A.39) on page 218 and Eq. (A.72) on page 228 respectively. Other expressions for q are found in the following pages as well as in Appendix A.

$$\left.\begin{aligned} \mathcal{M}_1 &= \frac{a_2''}{(p'')^3}\left(\frac{a_1''+a_2''}{P}\right)^2 \mathcal{M}_\odot \\ \mathcal{M}_2 &= \frac{a_1''}{(p'')^3}\left(\frac{a_1''+a_2''}{P}\right)^2 \mathcal{M}_\odot\,. \end{aligned}\right\} \tag{3.5}$$

Such binaries must have relatively bright components with similar luminosities, adequate angular separation, and be close enough that the system parallax can be measured. Typically they have been restricted to the solar neighbourhood. Other significant demands are that the period be short enough that the orbit can be adequately sampled within an acceptable interval of time, and that the binary has a suitable background of 'fixed' stars to act as a reference system against which the absolute orbits can be measured.

3.2.2 Combining astrometry with spectroscopic radial velocities

When, as is more often the case, only a visual binary's relative orbit can be measured (so that only a'' is known), the mass ratio used in Eq. (3.5) is no longer available. The system parallax may also be highly uncertain or unknown owing to the parallactic orbit being unmeasureable, as a result of the distance to the system. However, the combination of an SB2-spectroscopic solution with a resolved-astrometric solution has one important property: the parallax is not needed, and, indeed, it can be calculated from the complementary solutions using

$$p'' = \frac{a''\sin i}{a\sin i}\,, \tag{3.6}$$

where the numerator is provided by the astrometric solution and the denominator is provided by the SB2 one. Such strategies can sometimes allow the system's parallax to be measured with greater accuracy and precision than is possible by trigonometric or other techniques (e.g. see Ségransan et al. 2000, for the case of Gl 866). The parallax can also be measured using a relative orbit and a series of radial velocities (V_1, V_2) without an SB2 orbital solution, since

$$V_2 - V_1 = \frac{1}{p''}\frac{2\pi}{P}\frac{a''\sin i}{\sqrt{1-e^2}}\Big[e\cos\omega + \cos(\upsilon+\omega)\Big] \tag{3.7}$$

represents a straight line with slope $1/p''$.

For SB1 systems, as will be shown shortly, the parallax is an important parameter that must be known in advance, if the component masses are to be determined. A significant contribution to this aspect of the problem was provided by the success of the *Hipparcos* mission (ESA 1997), which provided the parallax measurements of about 118 000 stars, almost 18% of which had $\sigma_{p''}/p'' < 0.1$ (e.g. see Söderhjelm 1999). Alternative indirect methods for determining the parallax of difficult systems include using moving-groups (Popper 1967), and calibration relations such as the Wilson-Bappu effect for H and K Ca II lines, which relates the absolute magnitude

to line widths (Wilson & Bappu 1957).

Visual binaries with a relative orbital solution and whose parallax is known can have the component masses measured if the mass ratio can be determined by some other means. The typical way to achieve this is with the aid of radial velocities, obtained with adequate orbital-phase sampling of either SB2 or SB1 spectra. First consider the strategy when a spectroscopic orbital solution has also been determined — an uncommon occurrence given the typical orbital periods of visual binaries (e.g. Pourbaix 2000).

SB2 orbital solution available

If both K_1 and K_2 are known, the mass ratio can be measured using $q = K_1/K_2$. The component masses are

$$\left.\begin{aligned} \mathcal{M}_1 &= \frac{1}{1+q}\mathcal{M}_{\rm S} = \frac{K_2}{K_1+K_2}\left(\frac{a''}{p''}\right)^3 \frac{1}{P^2}\ \mathcal{M}_\odot \\ \mathcal{M}_2 &= \frac{q}{1+q}\mathcal{M}_{\rm S} = \frac{K_1}{K_1+K_2}\left(\frac{a''}{p''}\right)^3 \frac{1}{P^2}\ \mathcal{M}_\odot\,. \end{aligned}\right\} \tag{3.8}$$

The challenge that remains, is in identifying the uncommon binary systems that permit this complementary approach to be applied to them. The various observational selection effects that obstruct this desirable outcome are described in some detail in Chapter 4, with a summary in § 4.5, beginning on page 61.

SB1 orbital solution available

It is possible to measure stellar masses using only the velocities of one star, *if the relative astrometric orbital solution and the parallax are also known*. We assume that the spectra observed belong to the primary star (in terms of the definition of the mass ratio). Then, since $q = K_1/(K - K_1)$, the relevant equations, in terms of K_1, are as follows:

$$\left.\begin{aligned} \mathcal{M}_1 &= 0.211 \times \left(1 - \frac{K_1 P\, p''\sqrt{1-e^2}}{2\pi a'' \sin i}\right)\left(\frac{a''}{p''}\right)^3 \frac{1}{P^2}\ \mathcal{M}_\odot \\ \mathcal{M}_2 &= 0.211 \times \frac{K_1\sqrt{1-e^2}}{2\pi P \sin i}\left(\frac{a''}{p''}\right)^2\ \mathcal{M}_\odot\,, \end{aligned}\right\} \tag{3.9}$$

where K_1 is in kilometres per second and the period P continues to be given in years, the conventional time units of visual binaries. If in fact the secondary star had been observed, the confusion will reveal itself when the component masses are compared. This approach has the decidedly unfortunate weakness that, like the mass sum, the mass ratio is also sensitive to systematic errors in the orbital elements (which determine the calculated value of K).

No spectroscopic orbital solution

When a spectroscopic orbital solution is not possible (hence K_1 , K_2 will not be known) as is more likely for a visual binary, the component masses can still be measured with, in principle, as few as two observations taken at different epochs that also have different radial velocities for each star observed. When SB2 spectra are available, the mass ratio can be determined by calculating the linear regression of the primary star's velocities, V_1, with respect to those of the secondary star, V_2 (see e.g. Paddock 1915; Wilson 1941; Jones 1969; Irwin 1973):

$$V_1 = -qV_2 + (1+q)\gamma\,. \tag{3.10}$$

This expression represents a straight line with slope $s = -q$ and y-intercept $(1+q)\gamma$. Eq. (3.10) is theoretically correct, but is an approximation when it is applied to real data, which includes contributions to the measured velocities that are not a result of the orbital motion of the binary stars (see § A.14 beginning on on page 230 for a discussion of the various effects that contribute to the observed radial velocity and their influence on the measured values for γ and q). So long as the total contribution to the measured velocities for each star are constant for that star, the slope of the line should still be an accurate measure of the mass ratio, q. However, the common velocity zero-point that is measured, $V_{\rm Z}$ (defined in Eq. A.84 on page 233), is unlikely to be the same as the true systemic velocity, γ.

Another issue that deserves consideration when applying Eq. (3.10), is the fact that V_1 and V_2 are related to each other by the mass ratio, q, and their common centre-of-mass velocity, γ. Therefore, as pointed out, for instance, by Jones (1969) and Popper (1974), the errors in V_1 and V_2 are not independent. However, Popper (1974) notes that if the observations are adequate to reliably determine q, the matters of somewhat greater significance relate to the challenges of measuring the velocities accurately and precisely in the first place, made difficult, for example, as a result of variable line blending.

For a given number of velocities measured with a given precision, the mass ratio precision will improve if the range of velocities sampled is greater i.e. ideally if both quadratures are observed[7]. The component masses are:

$$\left.\begin{aligned} \mathcal{M}_1 &= \left(\frac{a''}{p}\right)^3 \frac{1}{(1+q)P^2}\ \mathcal{M}_\odot \\ \mathcal{M}_2 &= \left(\frac{a''}{p}\right)^3 \frac{q}{(1+q)P^2}\ \mathcal{M}_\odot\,. \end{aligned}\right\} \tag{3.11}$$

[7]Orbits with high eccentricity and $\omega \sim \pi/2$ or $3\pi/2$ will have the quadratures separated by a small fraction of the total orbital phase. Therefore this method does not strictly rely upon observing a large fraction of the orbit to measure a precise mass ratio.

When only SB1 spectra are available, the equations relevant to deriving a solution are Eq. (A.75a) and Eq. (A.75b) on page 229:

$$V_1 = \gamma - \frac{q}{1+q} V_{\rm rel}$$

and (3.12)

$$V_2 = \gamma + \frac{1}{1+q} V_{\rm rel}\,.$$

Each of these equations is also that of a straight line defined by the independent variable $V_{\rm rel}$, which can be determined from the system parameters for each time of observation, and the respective component velocities V_1 or V_2 (van den Bos 1962; Popper 1974). The line slope, s, is determined theoretically by q, but in practise it is also influenced by the systematic errors in the orbital elements used to calculate the values of $V_{\rm rel}$ corresponding to the observation times. The measure of the systemic velocity is effected in a similar manner, and comes from the y-intercept.

Assuming the orbital elements and parallax have been determined without recourse to any empirical calibration relation or theoretical model, this method can also be considered to be based on fundamental principles. If it is uncertain which star has been observed (in terms of the definition of the mass ratio), the sign of the slope of the line identifies its owner — the slope is negative if it is the primary star and positive if it is the secondary star. As was the case for mass estimates made using Eq. (3.9), even though only one star has had its radial velocities measured, the masses of both stars can be estimated according to Eq. (3.11), except that now there is also an absence of any spectroscopic orbital solution. Again, though, the accuracy of the mass ratio will be rather sensitive to the accuracy of the relative orbit.

When velocities are available for both stars, Eq. (3.12) can be applied to both sets to obtain separate values for q and γ. As Eq. (A.79) on page 232 shows, the ratio of these two slopes can still equate to the mass ratio obtained using Eq. (3.10). Popper (1974) identifies difficulties of a statistical nature with both methods, but concludes his discussion by noting that with 'good observations', as we have presumably acquired with HERCULES, the results obtained are not significantly inflenced by the choice of either of these methods.

3.2.3 Spectroscopic orbital solution and the orbital inclination

Spectroscopic orbital solutions of SB2 systems come closest to solving the problem of mass determination using a single observational technique. Such an approach does not require the parallax of the system since the semimajor axis a is obtained as a linear measure. Unfortunately, a is scaled by the unknown orbital inclination i. The inclination can be obtained if the orbital solution can also be determined astrometrically or photometrically. Until interferometric techniques became available to measure SB2 orbits (which are selectively biased to having components with small separations), photometric observations were the most likely to provide

the inclination, if fortuitously the system was observed to undergo eclipses[8]. The component masses can be measured according to

$$\left.\begin{aligned}\mathcal{M}_1 &= (1.0361\times10^{-7})\times P\,K_2(K_1+K_2)^2\left(\frac{\sqrt{1-e^2}}{\sin i}\right)^3\ \mathcal{M}_\odot \\ \mathcal{M}_2 &= (1.0361\times10^{-7})\times P\,K_1(K_1+K_2)^2\left(\frac{\sqrt{1-e^2}}{\sin i}\right)^3\ \mathcal{M}_\odot\,.\end{aligned}\right\} \tag{3.13}$$

The period P is now given in days, which are the conventional units of time for spectroscopic binaries. K_1 and K_2 are again given in kilometres per second.

3.2.4 Combining photocentric and spectroscopic orbital solutions

The difficulty presented by using the inclination from a photocentric orbital solution is that astrometric binaries are not likely to provide an SB2 orbital solution, but only that of the component contributing most light to the photocentre. If this is the case, now all that can be obtained is a mass measurement related in a complex way to the component masses known as the mass function $f_{\mathcal{M}}$. Assuming once again that the component observed is the brighter or primary star, then the mass function is expressed in terms of K_1 (in $\mathrm{km\,s^{-1}}$, with P in days) as follows

$$f_{\mathcal{M}} = \frac{(\mathcal{M}_2\sin i)^3}{(\mathcal{M}_1+\mathcal{M}_2)^2} = (1.0361\times10^{-7})\times PK_1^3\,(1-e^2)^{3/2}\ \mathcal{M}_\odot\,. \tag{3.14}$$

In these situations, direct measurement of the component masses becomes impossible. Instead, an estimate of the mass $\mathcal{M}_1$ from the star's photometry and spectrum is required. With the further assumption that the secondary is not a massive degenerate object, the secondary star's mass has an upper bound constrained by its inherent faintness (e.g. see Skuljan et al. 2004). Two possibilities arise, depending upon this estimate of the system mass $(\mathcal{M}_1+\mathcal{M}_2)$. The first is that the inferred *minimum mass* $\mathcal{M}_2\sin i$ suggests that $\mathcal{M}_2 \lll \mathcal{M}_1$ e.g. the companion may be an extrasolar planet. In this case, the denominator in the second expression for $f_{\mathcal{M}}$ is simplified to $\mathcal{M}_1^2$ and the minimum companion mass is

$$\mathcal{M}_2\sin i \ \cong\ (5.0737\times10^{-3})\times P^{1/3}\,\mathcal{M}_1^{2/3}\,K_1\sqrt{1-e^2}\ \mathcal{M}_\odot\,. \tag{3.15}$$

If instead the minimum mass is significant so that $\mathcal{M}_2 \sim \mathcal{M}_1$ is likely, Eq. (3.14) can be re-written as:

$$f_{\mathrm{q}} = \frac{f_{\mathcal{M}}}{\mathcal{M}_1\sin^3 i} = \frac{q^3}{(1+q)^2} = (1.0361\times10^{-7})\times\frac{P}{\mathcal{M}_1}\left(\frac{K_1\sqrt{1-e^2}}{\sin i}\right)^3. \tag{3.16}$$

[8]Actually, the reverse approach was the norm — first find an eclipsing system with nearly equal components and then observe both stars spectroscopically.

This expression is a cubic polynomial in q and can be solved using standard methods applicable to such functions. The shape of this function is illustrated in Fig. 3.1. For a given precision in the measurement of $f_{\rm q}$, as $f_{\rm q}$ approaches zero, the corresponding value for q becomes less precisely defined.

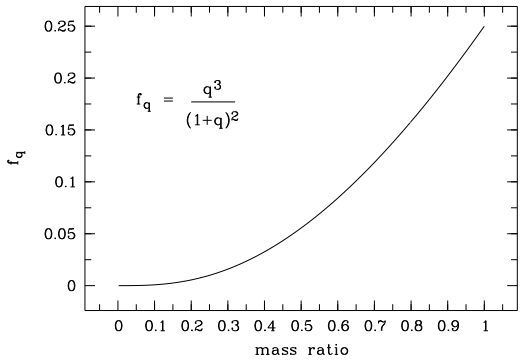

Figure 3.1: The curve representing Eq. (3.16)

One potential complication of the upper bound of one for the mass ratio, as defined in Eq. (3.2) on page 23, arises for typical SB1 systems for which the derived mass function will always allow the possibility of the unobserved companion being a stellar remnant, such as a white dwarf, which may have the greater mass of the two components. However, as the secondary mass increases, the inclination corresponding to $f_{\mathcal{M}}$ approaches zero, and this is less likely to be observed for statistical reasons.

3.2.5 Error propogation

The precision $\sigma_{\mathcal{M}}$ of the measured mass $\mathcal{M}$ will result from the propagation of the errors of the involved variables (e.g. see Bevington 1969). The largest contribution will come from the variable x whose error σ_x is greatest and/or those which have terms of highest power. The greatest power that occurs in the preceding equations to measure stellar masses is cubic. These terms deserve the closest attention since, in general, $\mathcal{M} \propto x^{\pm n} \Rightarrow \sigma_{\mathcal{M}} \sim n\sigma_x$. When many orbital parameters have been determined so that a choice exists as to how to finally measure the component mass, obviously the expression that yields the smallest propogated error is the appropriate choice. Similarly, the variable quality of the available orbital solutions obtained by one method e.g. astrometrically, can be expected to influence the choice of systems for complementary study e.g. by spectroscopic means. The important issue of error estimation, for the binary systems analysed in detail for this thesis, is given its due consideration in § 6.7 on page 122, and when the results are presented in Chapter 7.

3.3 Stellar masses using calibration relations

Astronomers would like to know the mass of any star, regardless of its membership in a binary system, star cluster or larger association or moving group, or its isolation in space as a single star. The gravitational mass of a single star, in complete isolation, cannot be measured in a model-free manner, since the gravitational force is not usually evident in an observable way. As mentioned on the first page of this thesis, it is possible, in principle, to measure the mass of a star *not* in a binary system, using microlensing techniques and high-precision astrometry (Ghosh et al. 2004). As more and more microlensing events are observed, and the required astrometric precision is routinely achieved, many precise masses of single stars may result from this approach. An indirect method of mass determination, suitable for degenerate stars, relies upon measuring the gravitational redshift, which can provide a direct measure of $\mathcal{M}/R$, and hence $\mathcal{M}$, if the object's radius is also known. Similarly, if the surface gravity, g, of a star has been measured spectroscopically, and again R is known, the mass can be deduced since $g = G\mathcal{M}/R^2$.

As summarised in § 3.1, many other properties of stars are strongly mass-sensitive. Therefore attempts have been made to determine reliable relationships between a star's mass and other more easily observable properties, e.g. brightness and spectral type. An approach such as this would be applicable to all stars. If our theories of stellar structure and evolution are correct (and therefore consistent), it should be possible to reproduce these empirically determined relationships theoretically (just as Newton's laws of motion and gravitation can reproduce Kepler's orbital laws).

Mass-luminosity relations

Since the brightness is the most visible property of a star, it is a calibration parameter with much appeal. Furthermore, as most stars cannot have their mass measured using any of the methods described above (at least with currently available techniques), the present-day and initial-mass functions, which describe the respective stellar mass populations as a whole, are impossible to determine correctly from the luminosity function alone, without an accurate mass-luminosity relation (see Scalo 1986 for a comprehensive discussion of these issues).

The apparent brightness or magnitude $m_{\rm v}$ of a star depends upon both its distance and intrinsic brightness or luminosity L. The luminosity of a star can be estimated using the Stefan-Boltzmann law, $L = 4\pi R^2 \sigma T_{\rm eff}^4$. The stellar radii can be measured occasionally using high-angular resolution techniques, or, if in an eclipsing binary system, if both the photometric and SB2 orbital solutions are available. Alternatively, L can be estimated using the star's absolute bolometric magnitude $M_{\rm bol}$, calculated from its absolute magnitude $M_{\rm V}$ and bolometric correction BC: $\log(L/\,L_\odot) = 0.4(4.74 - M_{\rm bol})$, where $M_{\rm bol} = M_{\rm V} + BC$. For single stars, both of these latter methods often require knowledge of the star's parallax. However, other observed properties such as Ca II emission, may yield a star's luminosity (e.g. based on the Wilson-Bappu effect; Wilson & Bappu 1957), which consequently can provide a measure of the parallax. Stellar radii and parallaxes continue to be challenging parameters to measure, with relatively few being

known with high precision[9].

Eddington's understanding of stellar structure led him to be the first to surmise a mass-luminosity relation for main-sequence stars of the form

$$L/L_{\odot} = (\mathcal{M}/\,\mathcal{M}_{\odot})^{\alpha}\,. \tag{3.17}$$

His first theoretical models suggested that $\alpha \approx 3$. Eddington (1926) produced the first empirical mass-luminosity ($M_{\rm bol}$) curve.

At first glance, a mass-luminosity diagram for main-sequence stars shows a tight, well defined relation (e.g. Smith 1983; Schönberner & Harmenec 1995; Hilditch 2001; see Fig. 3.2). Closer inspection, taking into account the individual uncertainties, reveals that the departures from any mean relation are real, being due to various effects. These departures are primarily due to composition differences and evolutionary effects (e.g. radius and temperature differences) within the main-sequence band for a given spectral type (Nordström 1989; Andersen 1991, 1997; Henry & McCarthy 1993). Rotation also introduces scatter into the mass-luminosity relation (Meynet & Maeder 2000). Thus a single mass-luminosity relation does not imply it is the only relation for stars of a given mass, but that it gives an average luminosity for all stars in that mass interval.

The exponent α in Eq. (3.17) represents the slope of the associated log-log curve and varies for different segments. The changes in α are due to differences of internal structure, sources of opacity and so on for stars of differing mass. Estimates of the value of α for the lowest stellar masses may be best obtained at infrared wavelengths (Delfosse et al. 2000). This is an important goal to strive for, as red-dwarf stars, whilst having the lowest stellar masses, are believed to constitute about 50% of the Galaxy's total stellar mass (Henry 2004). Studies of M dwarf binaries have contributed some accurate masses for the less well-defined low end of the mass-luminosity relation (e.g. see Delfosse et al. 1999; Forveille et al. 1999, Ségransan et al. 2000). Other workers, for instance Mazeh et al. (2002), have employed infrared detectors to measure the radial velocities of faint secondaries in known SB1 systems.

For the lowest stellar masses, these results have also served to highlight an increasing scatter in the V band mass-luminosity relations, as compared to those derived for the J,H, and K bands (Delfosse et al. 2000). These authors also emphasized that the quality of their data warranted the need for higher-order (fourth degree) polynomial fits. In the mass range $0.08\,\mathcal{M}_{\odot} \lesssim \mathcal{M} \lesssim 0.18\,\mathcal{M}_{\odot}$ the value of α is estimated to be ~ 1.7 whilst for $0.18\,\mathcal{M}_{\odot} \lesssim \mathcal{M} \lesssim 0.5\,\mathcal{M}_{\odot}$ it is closer to ~ 2.4 (Henry & McCarthy 1993). Above this mass to about 10–15 $\mathcal{M}_{\odot}$, $\alpha \approx 3.9$ (Lampens et al. 1997). At still higher masses, once electron-scattering opacity becomes dominant, theory predicts $\alpha \approx 3$, and once radiation pressure becomes dominant $\alpha \approx 1$ (Smith 1983). At the opposite end of the mass scale, there is a precipitous drop in luminosity for a small change in

[9]For example, in the *Hipparcos* Catalogue (ESA 1997), only 168 parallax measures have a relative error less than 1%, all but one of which belonging to stars closer than 20 pc.

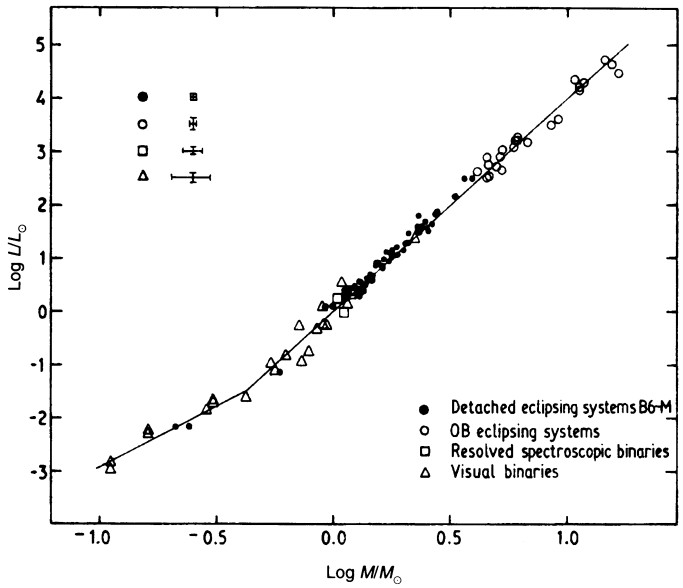

Figure 3.2: Empirical mass-luminosity diagram. Data for four groups of binary systems, identified in the key, are plotted for 126 stars (Source of data, Popper 1980; plot from Smith 1983)

mass at the stellar/substellar transition region ($\mathcal{M} \sim 0.08\,\mathcal{M}_\odot$), no doubt contributing to the difficulty of detecting these elusive bodies (Henry & McCarthy 1993).

All of the usual caveats apply to the use of these mean values for α, such as consideration of possible differences of the ages and metallicities of the stars under investigation, as well as the wavelength bandpasses used to determine the luminosity, L. For instance, in a survey of high-proper motion stars, Goldberg et al. (2002) derived $\alpha = 7.4 \pm 0.6$. They attributed this large value to the mismatch of the sample's mean peak luminosity with the bandpass used for the observations, and found that their value for α was consistent with certain models for low-metallicity stars.

By using the most up-to-date interior physics and non-grey atmosphere models, Baraffe et al. (1998) were able to get excellent agreement between their theoretical mean mass-luminosity relationships and the observational data of Henry & McCarthy (1993), for low-mass stars $0.075\,\mathcal{M}_\odot \leq \mathcal{M} \leq 1.0\,\mathcal{M}_\odot$. Satisfying results such as these suggest that the evolutionary models, based upon our understanding of stellar interiors, are becoming increasingly reliable.

Mass-spectral type relations

Spectral type would be an ideal calibration parameter, as determining the spectral type is the result of a single observation — the recording of the spectrum — which is then classified. In particular, it is independent of the parallax. This approach has the added advantage that a large number of spectra can be obtained with a single observation. Classification can then be accomplished quite rapidly, as was demonstrated at the turn of the 20$^{\rm th}$ century when the Henry

Draper Catalogue was prepared.

Unfortunately, it has been shown that the effects of evolution on main-sequence stars will result in an inherent inaccuracy of ± 15% in the estimated mass, if a single *mean* spectrum-mass relation is used. Thus, although a mean spectral-type-mass relation for the entire main-sequence can always be derived (the same can probably said of any parameter-mass relation), it cannot tell much about the accurate mass of a given star, no matter how well classified, unless an accurate indicator of evolution e.g. surface gravity, is also available (Nordström 1989). Giant stars seem to have even wider ranges of mass for given spectral types (Andersen 1991). In addition, the discrete nature of spectral types further limits their usefulness as a single calibration parameter.

Other mass-parameter relations

Other parameters for calibrating stellar mass estimations have also been explored. Balona (1984) was the first to combine temperature and luminosity indicators, respectively the Strömgren-Crawford c_o and β indices, to derive mass estimates of early-type main-sequence stars. Unfortunately, this study included interacting binary stars as well as the combined-light luminosities for some primary component comparisons, thereby limiting the accuracy of the mass estimations to about 15%. This made no significant improvement to previous single-parameter calibrations. Using samples of better quality and different evolutionary models, the precision of this approach has been improved by a factor of two or so (Balona 1994; Ribas et al. 1997). Using isochrones derived from the evolutionary calculations of Bertelli et al. (1994), Allende Prieto & Lambert (1999) applied transformations from the theoretical ($\log g$, $T_{\rm eff}$)-plane to the observational ($M_{\rm V}$, $B-V$)-plane precisely enough to derive masses with an uncertainty of about 8% for unevolved solar-metallicity stars over the considerable mass range $0.8\,\mathcal{M}_{\odot} \lesssim \mathcal{M} \lesssim 22\,\mathcal{M}_{\odot}$.

3.3.1 Other indirect mass-measurement methods

Finally, comment will be made on a specific group of stars whose pulsational properties have led to several strategies for estimating their mass. These are the astrophysically important Cepheid variables. Each method is based on some form of theoretical model or relation involving the pulsational period and luminosity (see e.g. Cox 1980; Böhme-Vitense 1992). These are: 1. the pulsational or Q-mass, 2. the Wesselink-radius mass, 3. the evolutionary mass, 4. the beat or period-ratio mass, 5. the theoretical mass, and 6. the bump or Φ-mass. Having several methods available to estimate Cepheid masses allows consistency checks of the underlying evolutionary and pulsation theories. If in a binary system, and if the theory underlying a method is correct, the mass estimates determined by the various techniques, including the model-free approach provided by an orbital solution, should be in agreement. Many difficulties arise trying to achieve this goal. Agreement is not common, and this is known as the Cepheid mass discrepancy problem.

Chapter 4

Observed properties and selection effects

The statistics of measured stellar and orbital parameters are inherently biased by selection effects. The manner and extent to which these effects influence our ability to measure each parameter is likely to depend on the particular observational method employed. An examination of the observational biases that compromise the study of a sample of the various binary types is a justifiable and revealing exercise. In the first place, it provides insight into the general characteristics of each classification. For specific purposes, such as measuring stellar masses, the similarities and differences identified can expose the advantages and challenges that an observer can expect when attempting to measure and combine orbital parameters of a binary system using more than one observational method.

Many of the selection effects that bias the discovery and measurement of different categories of binary stars have been recognized for decades (e.g. apparent magnitudes and their difference, angular separation and spectral types of the components, inclination of the orbits). Other effects, no doubt, are yet to be discovered or at least properly defined. These include the selection effects that influence our understanding of the actual mass-ratio distribution of binaries (see e.g. Trimble 1990; Mazeh & Goldberg 1992; Halbwachs et al. 2003).

The following discussion places some of these biases in a particularly modern setting as the source material has been acquired from catalogues that are substantially up-to-date and comprise samples that are as large as are currently available from single sources.

Unbiased samples

The following analysis is not aimed at deducing anything in particular about the *actual* distributions of the various parameters that exist for binary stars. Studies that focus upon estimating the actual distributions are challenging for a number of reasons; in addition to the ubiquitous selection effects are the obstacles presented to our understanding by small-number statistics. These investigations are, though, of fundamental importance, and many have been undertaken (e.g. in the past two decades, Popova et al. 1982; Halbwachs 1983; Trimble 1984; Hogeveen 1990; Trimble 1990; Mazeh & Goldberg 1992; Duquennoy & Mayor 1991; Hogeveen 1992; Boffin et al. 1993; Halbwachs et al. 2003). For instance, the completeness of our understanding of binary-star formation will be determined to a large part upon the ability of any star-formation model being able to reproduce binaries with the statistical properties which we observe, once careful attention has been paid to the various selection effects that bias our samples. The distributions of the properties we wish to explain include those of the periods, linear separations, eccentrici-

ties, and mass ratios, as well as how they relate to each other, for example, the eccentricities in terms of the periods (see Fig. 4.18 on page 62, and Appendix D for the $e-P$ distribution), and so on.

Catalogue sources

The source material for the following discussion has been provided primarily by three comprehensive catalogues. These are the Sixth Catalog of Orbits of Visual Binary Stars (6VB, Hartkopf & Mason 2004) which includes both astrometric and photocentric orbital solutions, the Ninth Catalogue of Spectroscopic Binary Orbits (9SB, Pourbaix et al. 2004), and the Hipparcos Catalogue (ESA 1997)[1].

The 6VB is a database included in the Washington Double Star Catalog (WDS)[2]. To April 2004, the 6VB included 1811 orbital solutions for a total of 1715 systems. There were 299 photocentric orbital solutions of 288 systems[3].

The 9SB continues the series of compilations of spectroscopic orbital solutions provided over the past 35 years by Batten and his collaborators. As of April 2004, it included 2684 orbital solutions of 2381 spectroscopic systems. As well as the solutions of systems harbouring 'normal' stars, the 9SB includes 10 X-ray sources. Several systems have as many as four orbital solutions[4].

The spectral type, $(B-V)$ colour index and parallax information have been obtained from the Hipparcos Catalogue, which has a considerable overlap with both 6VB and 9SB. This overlap is owing to the fact that all three catalogues are strongly biased by the usually dominant selection effect — brightness. There are 1301 systems in the 6VB and 1809 systems in the 9SB (both being 76% of their totals) that are listed in the Hipparcos Catalogue[5].

---

[1]The 6VB and the 9SB are updated regularly as new or improved orbital solutions become available. This analysis relates to the electronic versions obtained on 23 April 2004.

[2]Maintained by the United States Naval Observatory, WDS is the world's principal database of double and multiple star information.

[3] This compilation replaced the Fifth Catalog (5VB, Hartkopf et al. 2001) in late 2001. The 5VB was originally the principal source of visual and astrometric binary data for this project. It included 1471 orbital solutions of 1411 systems. The 5VB had 231 photocentric orbital solutions. The 6VB therefore has 340 additional orbital solutions. Once allowance has been made for corrected typographical errors, minor adjustments in the elements due to additional significant figures and so on, it was found that about 1240 orbital solutions in the 5VB were esentially unaltered in the version of the 6VB examined here. The 6VB includes 318 entirely new solutions as well as about 230 solutions that have been modified in some way. It was decided that these improvements justified using 6VB for the following discussions as they are especially concerned with statistical matters.

[4]The predecessor to the 9SB, the Eighth Catalogue of the Orbital Elements of Spectroscopic Binary Systems (8SB, Batten et al. 1989) included 1469 orbital solutions of as many systems (see Pourbaix et al. 2004 for a comparison of 8SB and 9SB).

[5]The completeness of the Hipparcos Catalogue depends upon such parameters as the Galactic latitude and spectral type: completeness varies from $Hp = 7\overset{\mathrm{m}}{.}3$ near the Galactic plane to $Hp = 9^{\mathrm{m}}$ in the polar regions. The stars catalogued are also strongly influenced by the initial selection of stars based on their astrophysical interest (Dommanget & Lampens 1993; Mignard 1997).

4.1 Visual binaries

Visual binaries suffer from many selection biases. These have been described in numerous papers, including those by Halbwachs (1983); Gianuzzi (1987); Hogeveen (1990); and Ruymaekers et al. (2000). Halbwachs (1983; 1986) identified three dominant effects that determine the detectability of a visual binary: the apparent magnitude of the primary star, the difference magnitude of the components, $\Delta m_{\rm v}$, and finally, their angular separation. A series of twelve histograms and related diagrams presented in Fig. 4.1–Fig. 4.6 illustrate these and several other characteristics of this class of binary.

4.1.1 Solution grades

In the 6VB, visual binary orbital solutions are classified according to the anticipated quality of the orbital elements. Orbits of grade 1 are definitive and of the highest quality whilst those of grade 5 are the least certain [Fig. 4.1(a)][6]. Only 3.5% of the 1506 6VB visual binary solutions are classified as grade 1. Included in this first histogram is the grade distribution of the 1237 visual binary solutions in the last version of the 5VB[7]. Whilst there have been additions to all grades in the 6VB, the grades that have benefited most by an increase in the number of solutions are those of poorer quality. This fact demonstrates the considerable challenge that exists for determining new definitive orbital solutions of VB systems after the passage of an interval of time as long as three years, which is insignificant in terms of typical VB orbital periods, even when the considerable contributions of the ever-maturing fields of interferometry and adaptive optics are taken into account (see e.g. Mason et al. 1998b; Beuzit et al. 2004).

The parameter that is most closely related to the solution grade is the orbital period P, as illustrated in Fig. 4.1(b)[8].

4.1.2 Distances, declinations and apparent magnitudes

Two observational biases that arise are associated with position. The first, and perhaps the dominant of all observational biases for visual binaries, arises from the fact that a VB is more easily recognized and its orbit measured if it is relatively nearby (Batten 1973). When nearby, for a given linear separation, the binary will have a greater angular separation between the stars. The Galaxy extends over approximately 30 000 parsecs of space, yet of the 1284 systems listed in the 6VB with a *Hipparcos* parallax, 1027 (80%) are within 150 pc [Fig. 4.2(a)][9].

[6] The photocentric orbital solutions are classified as grade 9.

[7] The only solution new to the 6VB that has a grade 1 classification was measured interferometrically for HD 83808 (see reference in the 6VB).

[8] For clarity, six solutions whose period exceed 10 000 years are not included (two of grade 4 and four of grade 5; the longest period listed in the 6VB is that of HD 38 whose period is estimated to be 32 000 years). An exponential relationship between the mean period $\langle P \rangle$ and orbital grade g can be deduced: $\langle P \rangle \cong 9\, e^{0.83g}$. The angular semimajor axis has a weaker correlation with the grade due to it being directly related to the binary's parallax. Other system paramters such as the eccentricity, inclination, and parallax have no significant correlation with the orbital solution grade of the 6VB sample of visual binaries.

[9] There are 1274 systems with standard errors less than $3\,\sigma$, with the median precision of *Hipparcos* parallaxes for $Hp < 9$ being $\sigma = 0.97$ mas (ESA 1997).

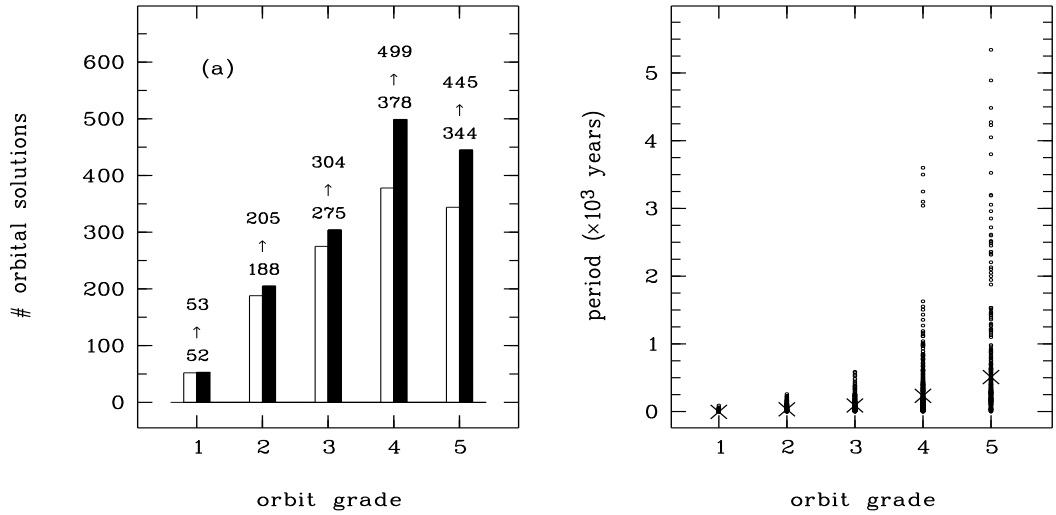

Figure 4.1: (a) Distribution of orbital solution grade for the visual binaries compiled in the Fifth (2001) and Sixth (2004) Catalog of Orbits of Visual Binary Stars. The statistics for the Fifth Catalog (1237 solutions) are illustrated with open columns and those of the Sixth Catalog (1506 solutions) with solid columns. (b) Orbital period of the 6VB as a function of grade. The mean period for each grade is identified with a '×'.

The second bias associated with position is that of the geographical location of the observers. The history of visual binary observing extends much further into the past in the northern hemisphere, than it does in the southern hemisphere. Therefore, in recent decades, even though the discovery rate in the south may at times exceed that in the north (Heintz 1969), the likelihood of adequate observations existing for these typically long-period systems is not great. Consequently, two-thirds of the VB solutions are for objects in the northern sky [Fig. 4.2(b)]. This imbalance is even greater for grade 1 orbital solutions, which has three-quarters of its members with a northern declination. Since the majority of visible stars (which are found in the plane of the Galaxy) are actually more favourably placed for southern observers, the southern skies can confidently be expected to harbour a greater proportion of unsolved VB orbits.

One characteristic that suffers from a selection bias which is common to all observing methods is brightness. For visual and SB2 spectroscopic binaries, the effect acts in favour of systems with relatively bright secondary components, i.e., with larger mass ratios (Halbwachs et al. 2003). The contribution of light from companions, possibly not yet detected, to the total magnitude further biases sample statistics too brighter objects (e.g. Kuiper 1935; Branch 1976).

Of the 1427 visual binary systems in the 6VB, there are 1154 (81%) that have the primary

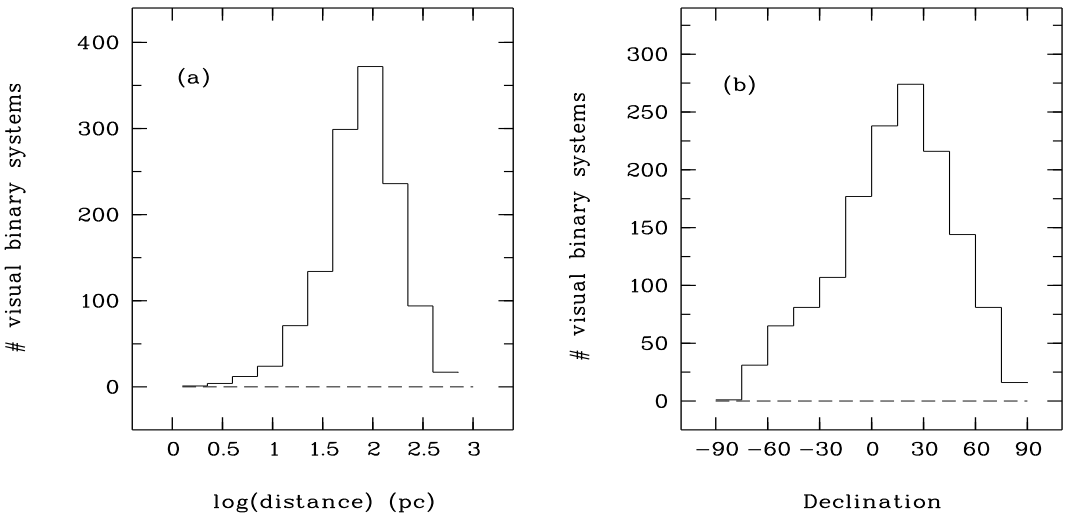

Figure 4.2: Histograms illustrating the observed distribution of (a) distance (1284 systems with a *Hipparcos* parallax), and (b) declination, of 1431 visual binaries in the 6VB.

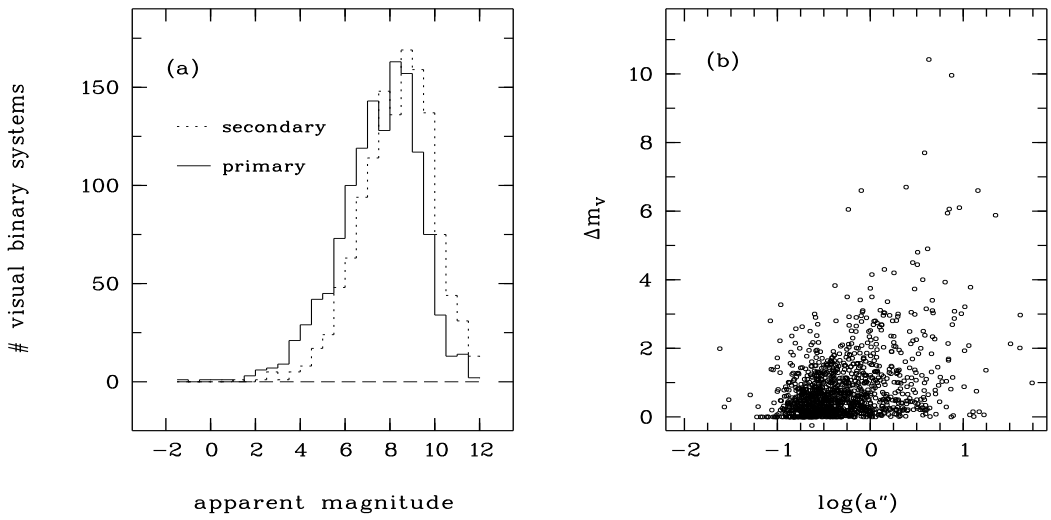

Figure 4.3: Histograms illustrating the observed distribution of (a) apparent V magnitude (1431 systems), and (b) magnitude differences (1309 systems) as a function of the angular semimajor axis a'', for a sample of visual binaries in the 6VB.

star brighter than magnitude $9^{\rm m}$ [Fig. 4.3(a)]. The luminosities of the two stars lead to other selection effects as well. For instance, an intrinsically luminous star is more likely to have a much fainter companion than is a fainter star (Batten 1973; Scalo et al. 1978). Visual binaries are more difficult to detect if the magnitude difference, $\Delta m_{\rm v}$, between the components is large, particularly when the angular separation is small. These biases are clearly illustrated in Fig. 4.3(b) where it is seen that, of 1309 systems with magnitudes listed for both components, 1188 (90%) have $\Delta m_{\rm v} < 2$. Fig. 4.3(b) also illustrates the relationship between the magnitude difference and the angular separation of the components — not only are systems with similar component magnitudes more likely to have their orbits solved, but as the angular size of the orbit diminishes, then $\Delta m_{\rm v}$ decreases as well (which is discussed in some detail in e.g., Kuiper 1935; Hogeveen 1990).

Whilst earlier studies suggested that there was a spectral-type dependance on Δm for binaries amongst main-sequence stars (e.g. Kuiper 1935), more recently, Abt (1979), and Halbwachs (1983), have deduced that there is no significant difference between the Δm values for binaries amongst these stellar sub-samples. This is supported by the 6VB sample, for which the mean $\Delta m_{\rm v}$ is close to $1^{\rm m}$ for all spectral types from B–M. Certainly, though, the spectral types of visual binaries that are observed are strongly biased in other ways.

4.1.3 Luminosity and spectral classes

The following two histograms (Fig. 4.4) limit their representation to the 1292 visual binaries included in the Hipparcos Catalogue with spectral types, of which 731 systems also have a luminosity class. Stars spend the majority of their lives on the main-sequence and comparatively little time as higher luminosity giants. The luminosity function shows that, in general, the most luminous stars are rare and the prevalence of stars increases considerably with decreasing intrinsic luminosity (Scalo 1986). Furthermore, since we know that the observation of VBs is biased toward stellar pairs of similar luminosity [Fig. 4.3(b)] it is also less likely that a VB will comprise an evolved star and a main-sequence star. Therefore, the dominance of dwarf primary stars (with dwarf companions) in the 6VB sample is to be expected, as is overwhelmingly illustrated in Fig. 4.4(a).

Since a less massive star will have a considerably longer main-sequence lifetime than a more massive star[10] we might expect that visual binaries (i.e. those with orbiatl solutions) hosting massive and high luminosity early type stars should be rare, whilst less luminous, less massive late-type stars should be more prevalent. The distribution of spectral types as shown in Fig. 4.4(b) is therefore only partially consistent with our preliminary expectations. Certainly early-type stars are uncommon in VB systems. The prevalence of later spectral types increases quickly, but only as far as type F, then gradually decreases for the cooler stars. Either the cooler stars do not tend to form binary systems or they are simply more difficult to recognize because of their intrinsic faintness. The latter reason has the greater merit: at a typical VB distance

[10] A main-sequence star has $L \sim M^{3.9}$ (§ 3.3 on page 30) so that its main-sequence lifetime $t_{\rm MS} \sim \frac{M/\mathcal{M}_\odot}{L/L_\odot} \sim M^{-2.9}$.

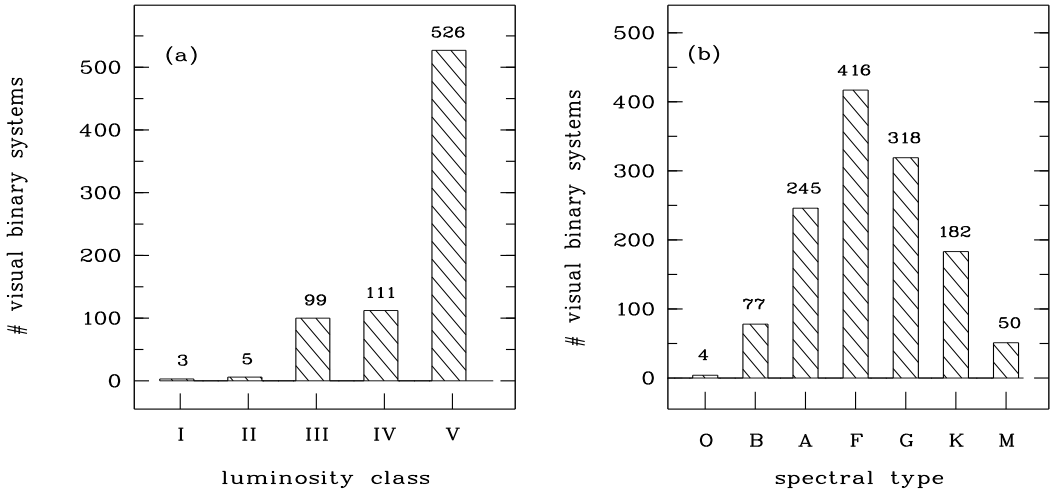

Figure 4.4: Distribution of (a) luminosity class (731 systems), and (b) spectral type (1292 systems), for a sample of visual binaries in the 6VB.

of 100 pc, a dwarf star of apparent magnitude 9 or brighter must have an absolute magnitude $M_{\rm V} \sim 4$ and therefore a spectral type of about F8 or earlier. Stars of later spectral type will be fainter and as Fig. 4.3(a) illustrates, less likely to be recognized and have their orbit solved. A colour-magnitude diagram (Fig. 4.9) illustrates the distribution of visual binary systems relative to the astrometric binary systems in the 6VB for $\sigma_{\rm p''}/p'' < 0.2$.

4.1.4 Periods and angular semimajor axes

Fig. 4.5 illustrates the distributions of orbital period and angular semimajor axis and their differences when 5VB solutions are compared to those of the 6VB. In both catalogues, the vast majority of solutions have relatively long orbital periods: only 7% of the solutions in the 5VB and the 6VB have a period less than 10 years. For the 5VB, the median period was 113 years, whilst for the 6VB it is 123 years. The observational biases toward visual binaries with regard to their periods and orbital sizes result from two opposing selection effects for any binary of given mass and parallax. These two biases are governed by Kepler's third law which relates the period, linear semimajor axis and component masses (see § A.9).

The significance of the orbital period has already been mentioned with regard to its association with orbital solution grades. For systems at a given distance, widely separated components are more easily recognized, but have longer periods. This necessitates their observation over longer time-spans so that a sufficient portion of the orbit can be observed to allow a solution to be estimated. If less of the orbit is measured for a given precision of ρ and θ, the solution must be less certain, so that orbits with longer periods are expected to have poorer grades, as

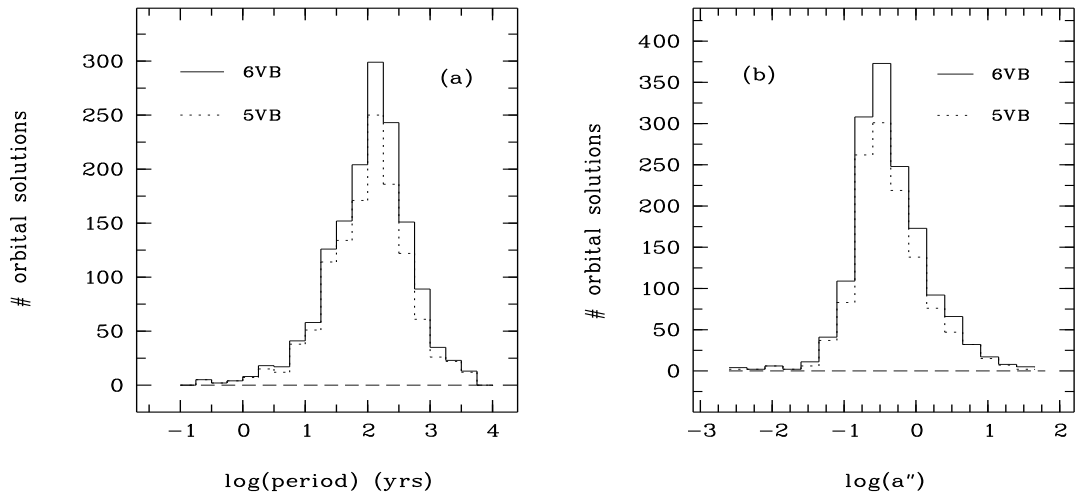

Figure 4.5: Distribution of (a) orbital period, and (b) the angular semimajor axis a'', for a sample of visual binaries in the 6VB.

Fig. 4.1 (b) has already illustrated. Since the majority of visual binaries have not been observed for much longer than one hundred years, we expect that measured periods will typically be no longer than several times that interval of time. However, short period orbits can have all orbital phases sampled over less time, but only if the components can be separated. Until the advent of modern techniques such as adaptive optics and interferometry, the very short period systems were rarely resolved. It will be interesting to see how rapidly interferometry, adaptive optics and techniques yet to be discovered can influence these distributions over the coming years.

The distribution of angular separations is strongly skewed toward values greater than $a'' = 0.2''$ [Fig. 4.5(b)], which is the peak value and is close to the observational limit for binaries measured visually at the eyepiece (non-interferometrically). There are 315 solutions (21%) which have orbital solutions with angular sizes less than $a'' = 0.2''$.

4.1.5 Linear semimajor axes and inclinations

Histograms of the linear semimajor axes for the visual binary solutions with a *Hipparcos* parallax are presented in Fig. 4.6(a). Included are two sub-samples: those with $\sigma''_p/p'' \leq 0.2$ (1075 solutions) and those with $\sigma''_p/p'' \leq 0.1$ (647 solutions). The complete sample (solid line), peaks at solutions corresponding to VBs with $\log a$ (AU) $\sim 1.8 \equiv 60$ AU. This is rather similar to the position of the frequency peak reported 35 years ago by Heintz (1969), who found the peak frequency for a for his sample of about 300 systems was at about 45 AU. Since Heintz included some spectroscopic binaries in his sample it is impossible to make a valid comparison between his and our samples. Selection effects that would have a bearing on any change in this regard

would include the longer timespan available for observations to be acquired, the improvements to observational techniques, and the possibility that the distribution of a has simply changed owing to changes in the measured parallaxes, as a result of *Hipparcos* and other studies.

When the solutions included in the histogram are restricted to those with more precise parallaxes, the distributions become increasingly skewed to smaller orbits. For the solutions with $\sigma''_p/p'' \leq 0.1$, the median of the semimajor axis for the 6VB sample of visual binaries is about 22 AU. The possibility of deriving an orbital solution for these systems is biased toward those being closer, brighter and with shorter periods. Since there is also a strong correlation between a and a'' in the 6VB sample, the bias toward smaller orbits is also a reflection of the bias toward systems with a relatively small a'', so long as these systems can be adequately resolved, as discussed in the previous section.

Fig. 4.6(b) illustrates the distribution of orbital inclinations of visual binaries. The distribution is strongly bi-modal owing to the fact that it represents two distinct VB populations, namely, those systems with prograde orbits ($i < 90°$), and those with retrograde orbits. If the orbital planes are randomly distributed in $\sin i$, as we would expect for an unbiased sample, statistical arguments predict that the mean value of $\sin^3 i$ is ~ 0.59 (Aitken 1935) $\Rightarrow i \approx 57°$ for a prograde orbit and $i \approx 123°$ for a retrograde orbit. These values are *mean* ones, not the modal peaks that appear in Fig. 4.6(b), which must be coincidental. Face-on orbits, ($i \sim 0°$), would allow the greatest component separation possible for all orbital phases, but very few visual binaries have such orbits as they can only be recognized if by considerable chance the orbital axis is pointing toward the observer.

Instead, we expect that the most common inclinations observed should be for those systems that are edge-on, ($i = 90°$), or at least nearly so. A random sample of systems inclined at any particular angle will project themselves onto the sky, with the direction of the orbital axes covering the full 360° of space. The observability of a particular inclination is proportional to $\sin i$. Therefore, the axis direction that corresponds to the orbit with the greatest coverage of the sky, with all other orbital elements equal, occurs for $i = 90°$. The relative absence of these systems from the 6VB sample must be due to one or more selection effects. This is owing, in part, to the difficulty of discovery and of observing pairs of stars which cross each other's apparent path, or at least, closely approach each other, during each orbital cycle. In fact, consideration of such selection effects leads us to conclude that for $\|\sin i\| > 0.5$, the number (per interval of $\sin i$) gradually drops to about one third of the normal value if $\sin i \sim 90°$ (Heintz 1969).

Another challenge for determining the orbital solutions of edge-on visual binaries is the misidentification of the primary star that sometimes occurs due to the similar appearance of typical VB components[11]. Both of these possible selection efffects are much reduced for *unresolved*

[11]Two of the binary systems analysed in detail in Chapter 7, HD 206804 and HD 217166, are this type of binary system. Comments therein relate to the problems arising from the confusion, and subsequently complicating the analysis of the astrometric observations.

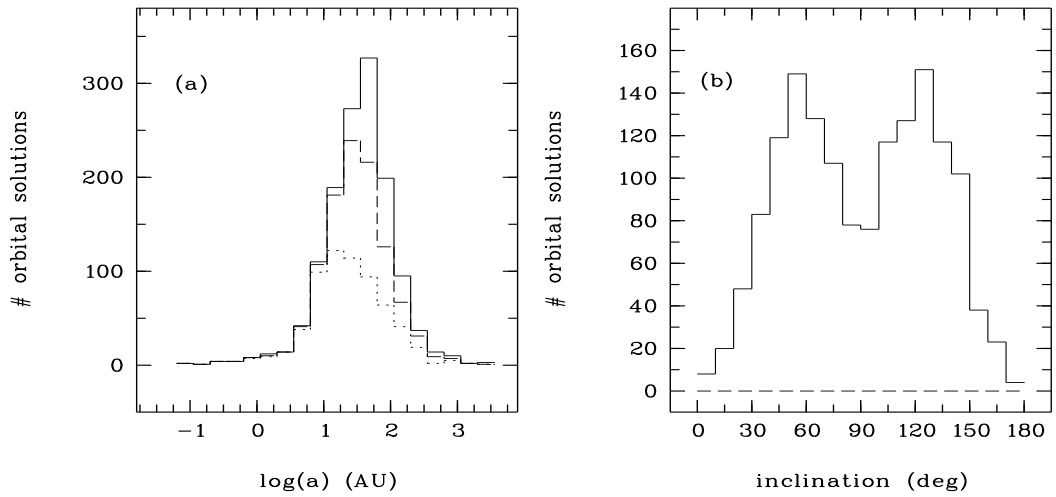

Figure 4.6: (a) Histograms of the linear semimajor axes of orbital solutions having a *Hipparcos* parallax; solid line, 1346 solutions), those with $\sigma''_p/p'' \leq 0.2$ (dashed line; 1075 solutions) and those with $\sigma''_p/p'' \leq 0.1$ (dotted line; 647 solutions). (b) The distribution of inclinations of 1505 orbital solutions. All samples are from the 6VB.

astrometric binaries. Indeed, as will shortly be shown, the sample of such systems included in the 6VB presents a unimodal inclination distribution whose peak value is at $i \sim 90^\circ$, just as we might predict.

4.2 Astrometric binaries

Once again, the compilation of the 6VB described above is the source of the following analysis. Of the 299 photocentric solutions (i.e. grade 9), 11 are of Sagittarius A which have been discounted from the following, which leaves 288 solutions of 267 systems. The *Hipparcos* Catalogue (DMSA/O; ESA 1997) provided 235 solutions of as many systems.

There are various selection effects that govern the detection and allow determination of a photocentric orbital solution for an unresolved astrometric binary. The 3.3-year duration of the *Hipparcos* mission had a strong influence upon the solutions it could achieve. This is reflected in the period histogram. Furthermore, very few *Hipparcos* solutions (only 46 of them) were derived with all elements as free parameters, without the aid of other independent solutions, such as had previously been determined spectroscopically (Martin & Mignard 1997). Consequently, the selection effects in many of these orbital solutions are not limited to those specifically for photocentric orbits, so that additional caution is appropriate when considering the relative merit of each distribution.

There are 88 photocentric solutions in the 6VB obtained from non-*Hipparcos* sources. These have been acquired from a variety of observational programs, so that the distribution measured for a particular parameter are generally less specifically defined, in comparison to the *Hipparcos* results. This is evident in some of the following diagrams.

4.2.1 Distances, apparent magnitudes and declinations

Astrometric binaries have their orbits measured based on the same fundamental method as visual binaries i.e. astrometry. Therefore, it should not be surprising that the former orbital solutions are also dominated by binaries that are relatively nearby so that the motion of the photocentre against the background stars can be measured. Of the 260 6VB astrometric systems with a *Hipparcos* parallax, 226 (87%) are within a distance of 150 pc [Fig. 4.7(a)], which is a proportion that is similar to that described for visual binaries. Similarly, unresolved astrometric binaries also present themselves as relatively bright objects: 238 or 86% of the 6VB sample have an apparent magnitude brighter than $9^{\rm m}$ [Fig. 4.7(b)]. This proportion is somewhat higher than that of the VB sample, and is expected, since two stars are contributing to the total light. This is an important selection effect for unresolved binary systems (Kuiper 1935; Branch 1976). The photocentric solutions acquired from other sources occupy similar regions of the same parameter space as do the *Hipparcos* systems. This is also not surprising, as the observability of unresolved astrometric systems is not especially sensitive to the *duration* of the observing programme in relation to either of these properties. The declinations corresponding to the photocentric orbits, which are not illustrated, are more nearly uniformly distributed between the northern and southern skies. This is owing to the large fraction of them coming from the *Hipparcos* space mission.

4.2.2 Luminosity and spectral classes

Whilst some of the observational biases are not unlike those of visual binaries, there are others that differ in significant ways. The differences result principally from the fact that an unresolved astrometric binary has only one apparent light source, the photocentre, which is the combined light of both stars. One distinguishing influence can readily be identified. The angular size of the photocentric orbit depends both on the angular size of the true relative orbit and on the mass and luminosity ratios [$q = \mathcal{M}_2/\mathcal{M}_1$ and $l = L_2/L_1$ respectively; Eq. (2.2)]:

$$a''_{\rm p} = a'' \left(\frac{q}{1+q} - \frac{l}{1+l} \right) .$$

Therefore, unlike visual binaries, the detection of astrometric binaries is increasingly unfavourable for components that have $q \approx l \sim 1$. Instead, high-luminosity primary stars which may harbour fainter more common lower-luminosity companions should be more prevalent (Binnendijk 1960). This is evident in the histograms presented in Fig. 4.8, where the relative proportion of giant to dwarf components is 4.5× that presented earlier for visual binaries. In fact, the first unresolved astrometric binaries were identified by Bessel for systems that included faint but massive compact companions to bright main-sequence stars, namely Sirius and Procyon.

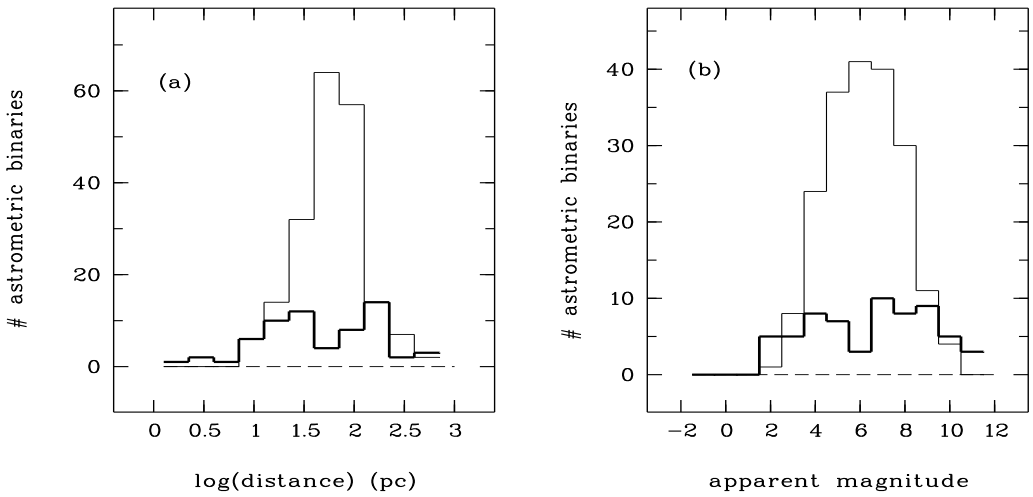

Figure 4.7: Histograms illustrating the observed distribution of (a) distance (260 systems), and (b) apparent V magnitude of the photocentre (267 systems), for the unresolved astrometric binaries included in the 6VB. (*Hipparcos* solutions: thin line, others: bolder line.)

Similarly, unresolved astrometric binaries with intrinsically faint M-dwarf primaries are rare, as these stars are faint at the typical distance of these systems. Moreover, without the contribution of a more luminous companion, any Keplerian motion is less likely to be detected, regardless of the size of $a''_{\rm p}$ and the non-uniformity of the motion of the photocentre. When the mass ratio and especially the luminosity ratio are particularly small, e.g. when the unseen companion is an extrasolar planet, $a''_{\rm p} \sim a''_1$ is tiny so that only high-precision astrometric observations will reveal the photocentric orbit[12].

A sub-sample of the 6VB data has also been used to create a colour-magnitude diagram (Fig. 4.9), but only the solutions with $\sigma_{\rm p''}/p'' < 0.2$ are included (1020 VB systems and 238 AB systems). The distribution of the two groups of orbital solutions is similar, though, as expected, there is a tendency for late-type systems with an unresolved astrometric solution to be evolved significantly from the main sequence. It is also notable that the vast majority of these systems have an absolute magnitude brighter than about $M_{\rm V} \sim +6^{\rm m}$. Unevolved stars of this intrinsic brightness have spectral types of about K0V. At the typical distance of binary systems with these types of orbital solutions, stars later than about K0V will be fainter than $11^{\rm m}$. This is consistent with the respective histograms of apparent magnitudes [Fig. 4.3(a) and Fig. 4.7(b)].

[12]This is the promise of future space missions such as the Terrestrial Planet Finder TFP (Danner & Unwin 1999). The challenge can be abbreviated as follows: a Jovian planet ($\mathcal{M}_{\rm p} \sim 10^{-3}\,\mathcal{M}_\odot$ and $M_{\rm V} \sim +26^{\rm m}$), in an orbit around a solar-type star ($\Rightarrow l = L_2/L_1 \sim 10^{-9}$) with a semimajor axis $a = 1\,$AU, and 10 pc distant, has $a''_{\rm p} \sim 0.1\,$mas.

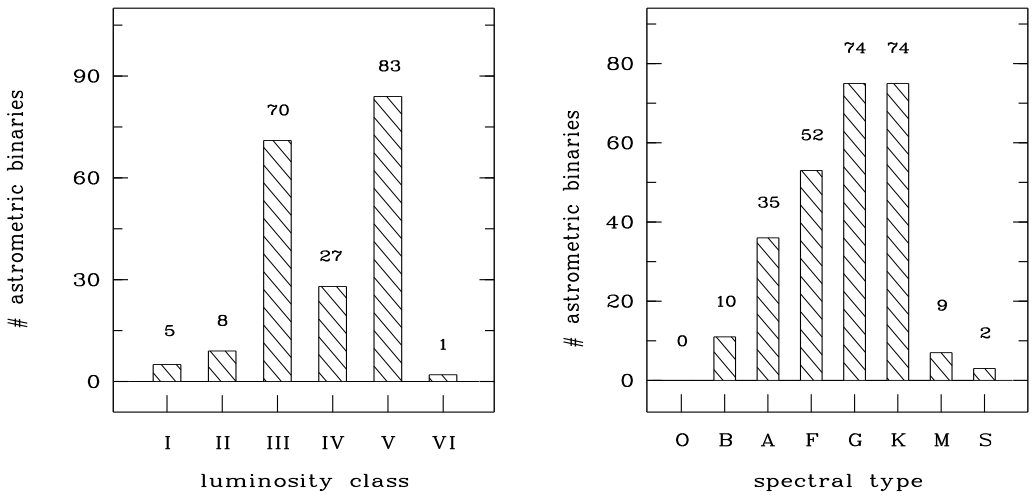

Figure 4.8: The observed distribution of (a) luminosity class (199 systems), and (b) spectral type (263 systems), for a sample of unresolved astrometric binaries included in the 6VB.

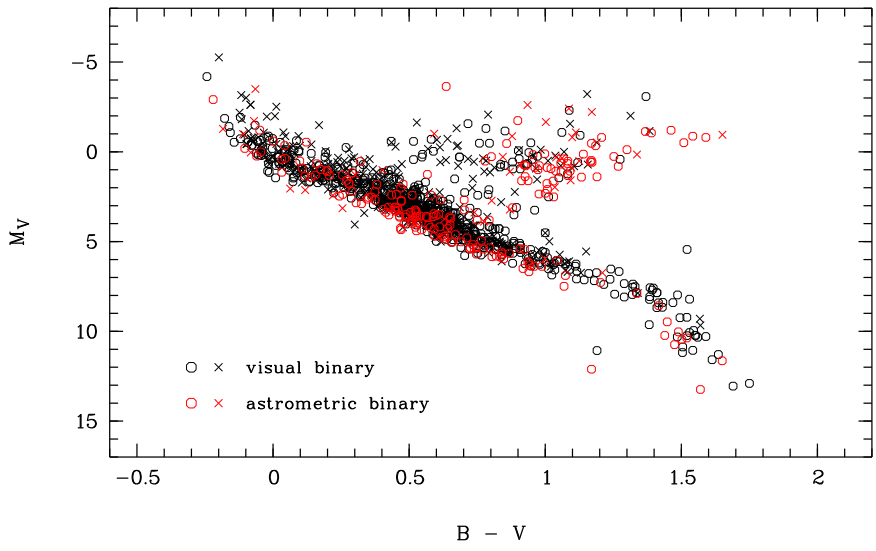

Figure 4.9: Colour-magnitude diagram of the 619 VB and 194 AB systems with $\sigma_{p''}/p'' < 0.1$ (open symbols) and the 401 VB and 44 AB systems with $0.1 \leqq \sigma_{p''}/p'' < 0.2$ (crosses).

4.2.3 Periods and the size of the photocentric orbits

Next, mention is made of the distributions of the period and the angular size of the photocentric orbits [Fig. 4.10]. The period histogram illustrates the bias of the *Hipparcos* measurement interval of 3.3-years. Unresolved astrometric binaries with periods significantly greater than the *Hipparcos* mission time cannot be adequately measured, as the motion of the photocentre did not differ appreciably from uniformity (Martin & Mignard 1997). Thus we find that the median period is only 2 years, whereas the median period of the non-*Hipparcos* photocentric solutions is ∼12 years. Only three solutions are listed with a period of 100 years or greater, none of which was derived by the *Hipparcos* consortium.

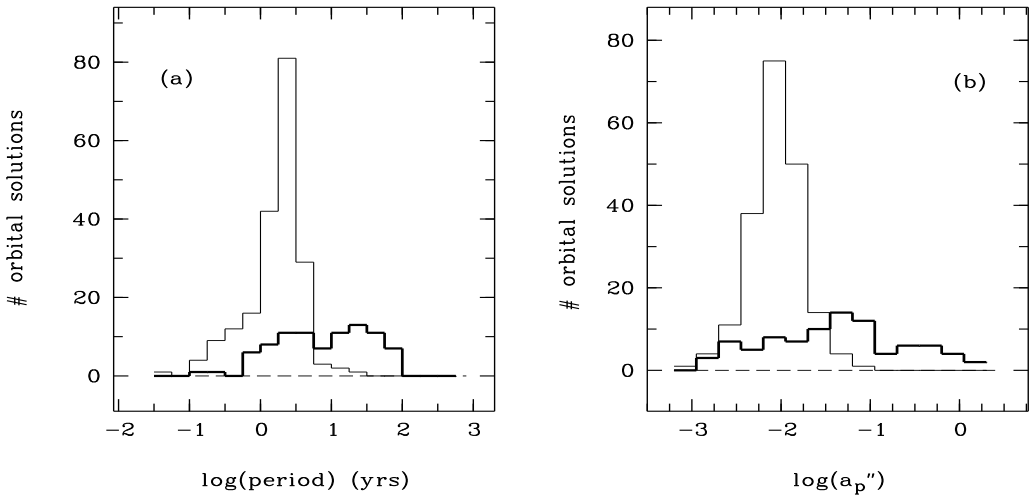

Figure 4.10: Distribution of (a) orbital period, and (b) the angular photocentric semimajor axis $a''_{\rm p}$, for a sample of unresolved astrometric binaries in the 6VB. (*Hipparcos* solutions: thin line, others: bolder line.)

The angular semimajor axes of the photocentric orbits are typically an order of magnitude smaller than the relative orbits of visual binaries. The median value for $a''_{\rm p} \sim 0.01''$, a consequence of the smallness of a'' for short period binaries and the value of the bracketed term in the expression for $a''_{\rm p}$ on page 45.

4.2.4 Inclinations and eccentricities

Finally, the histograms for the orbital inclination and the eccentricity are presented (Fig. 4.11), the former with the claim that selection effects may be minimized (relative to those present for visual binaries), and the latter to demonstrate a strong bias created by the demands placed by the desire to determine a preliminary solution.

As was the case for visual binaries, orbital solutions that are face-on or nearly so are rare [Fig. 4.11(a)]. However, unlike the VB histogram, rather than a bimodal distribution, the inclination distribution for astrometric systems is approximately unimodal and centred in the vicinity of $i \sim 90°$. This is particularly evident when the photocentric solutions from the *Hipparcos* and other sources are combined (the dashed-line histogram), but it is also demonstrated for each sample independently. This distribution, and its difference from that illustrated for the VB sample in Fig. 4.6(b), is supportive of the *absence* of the selection effects making the solution of high-inclination visual binary orbits difficult. For a photocentric orbital solution, the observations do not depend upon resolving components of similar appearance moving across similar apparent paths in space.

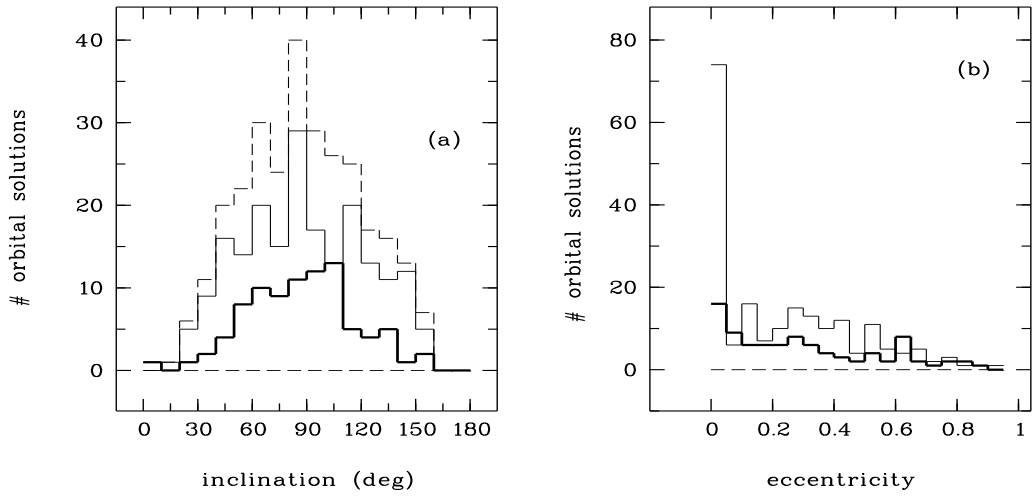

Figure 4.11: Distribution of (a) orbital inclination, and (b) eccentricity, of unresolved astrometric binaries in the 6VB. (*Hipparcos* solutions: thin line, others: bolder line. The dashed histogram included in (a) corresponds to the combined samples of *Hipparcos* and the other sources of photocentric solutions.)

The large proportion of circular *Hipparcos* orbital solutions [Fig. 4.11(b)] is due to the orbits having their eccentricity fixed so that a preliminary orbital solution could be determined with the available data. The artificiality of this computational bias is further emphasised by the fact that of the *Hipparcos* solutions where the eccentricity was included as a free parameter (46 systems), all have non-circular orbits with only seven of them having $e < 0.1$. Furthermore, the non-*Hipparcos* solutions also display a substantially smaller rise in prevalence for circular orbital solutions.

4.3 Spectroscopic binaries

Binary systems that lend themselves to spectroscopic orbital solutions (from the 9SB; Pourbaix et al. 2004), present a somewhat different proportion of selection effects to an observer. SB1 solutions (1757 of them for 1583 systems) and SB2 solutions (927 of them for 798 systems) have different probabilities of measurement. Whilst the discovery and orbital solutions of both rely upon velocity variations, the nature of these variations differ for the two types of systems. SB1 systems are often recognized by absolute velocity variations whereas SB2 systems are typically detected by relative velocity variations, i.e. line doubling (Batten 1973)[13]. However, the complexity of the detection law for an SB is unlikely to be so simply defined. It also depends upon the distribution of the epochs of the observations (Duquennoy & Mayor 1991).

4.3.1 Solution grades

The grading scheme for the solution quality for the 9SB is the *reverse* of that used for the 6VB i.e. orbits of grade 5 are definitive and of the highest quality whilst those of grade 1 are the least certain. At the time the catalogue was acquired, there were 711 solutions that were as yet unclassified [which for this thesis have been labelled grade 0; see Fig. 4.12(a)].

Of the many solutions that have been graded, a greater proportion have definitive orbits (grade 5) than do VB systems (nearly 400 or about 20% of the 1973 graded solutions). This improved proportion of definitive solutions is in part due to the considerably shorter periods of SB systems so that complete and repeated orbital phase sampling can more easily be achieved (see Fig. 4.17 for SB period statistics). Satisfyingly, the proportion of the definitive orbits in the 9SB is 4–5 times greater than was the case for the three previous SB catalogues (Batten & Fletcher 1990). This improvement can be attributed to better instrumentation, including faster and more efficient telescopes and detectors, as well as modern analytical methods. All grades have more SB1 than SB2 solutions, presumably a result of the greater ease of measurement of the former, but also perhaps because binaries with small luminosity ratios, $l = L_2/L_1$, are more prevalent.

Fig. 4.12(b) illustrates the tendency for SB systems to have a better quality solution if the primary star has a smaller radial-velocity amplitude, K_1. A similar pattern emerges for K_2 and $K = K_1 + K_2$ (SB2s only of course). This trend, commented upon for the 'Eighth Catalogue' by Hogeveen (1992), is in part the result of the relationships between spectral type, typical velocity precision, and the velocity amplitude K. From Kepler's third law, we have $a/P = \sqrt[3]{M_{\rm S}/P}$, so that the radial-velocity amplitudes K and K_1 are

$$K = \frac{2\pi \sin i}{\sqrt{1-e^2}} \sqrt[3]{\frac{M_{\rm S}}{P}} \qquad \text{and} \qquad K_1 = \frac{q}{1+q}\, K \ . \tag{4.1}$$

Therefore, for a given orbital period, eccentricity, inclination, and mass ratio, less massive later

[13]SB1 and SB2 status was determined by the availability of K_1 and/or K_2 in the 9SB — SB1: only K_1 or occasionally only K_2 , SB2: both K_1 and K_2 are listed.

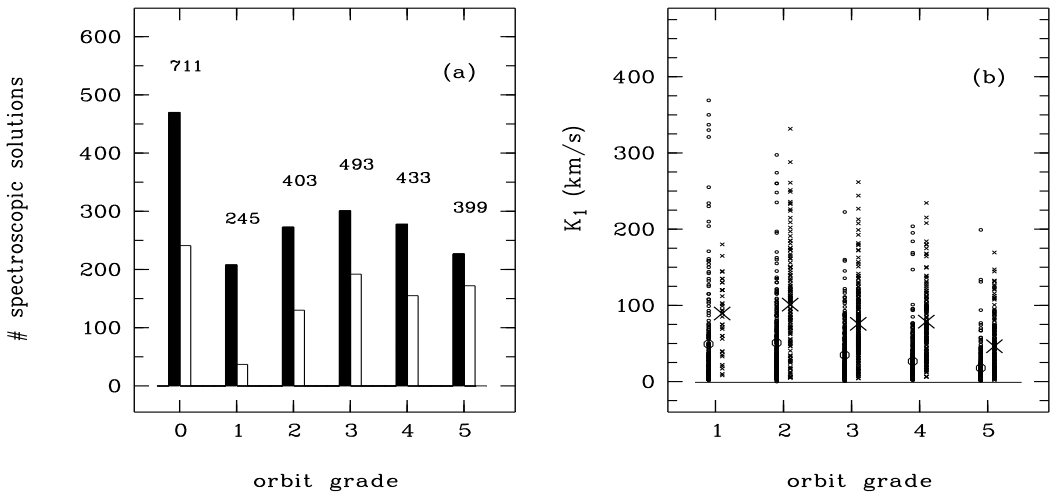

Figure 4.12: (a) Distribution of orbital solution grade found in the Ninth Catalogue of Spectroscopic Binary Orbits (9SB). Solutions that were ungraded at the time of this analysis were given a grade 0. SB1 (1757 solutions): solid columns, SB2 (927 solutions): open columns. The numbers above each grade are the total number of orbital solutions (SB1+SB2). (b) Semi-amplitude of the radial-velocity curve K_1 as a function of grade. SB1: left column of circles, SB2: right column of crosses. The mean value of each column is identified with an enlarged like-symbol. The minimum K_1 for each SB2 grade is greater than that for each respective SB1 grade owing to the need for sufficient velocity amplitude to allow measureable spectral line separation.

spectral-type systems will have a smaller velocity amplitude[14]. These smaller velocity amplitudes are also more likely for solutions of late-type systems, since these SBs also tend to have longer periods, as will be illustrated shortly, in Fig. 4.17(c)[15]. On the face of it, this trend appears to be inconsistent with the long-recognized bias toward easier detection of SBs with higher velocity amplitudes. However, these somewhat lower velocity amplitudes are still quite large enough to be measured, and because of the large numbers of sharp spectral lines compared to early-type stars, the late-type systems can have their velocities measured more precisely, hence the better orbital solution quality[16].

[14]We have defined the primary component for a SB system to be that which has the smaller velocity amplitude $\Rightarrow \mathcal{M}_1 \geqq \mathcal{M}_2$ so that the system mass must also be smaller for systems that have later spectral type primaries. Late-type giants are also usually less massive than early main-sequence stars. Furthermore, the mass ratio can be expected to be relatively small when the primary is a giant star, and SBs with giant components are predominantly SB1 systems. Therefore, K_1 is even lower than if $q \sim 1$.

[15]This trend is especially noticeable for SB1 systems which have a period range almost two orders of magnitude greater than that for SB2s.

[16]For a theoretical treatment of the precision attainable for radial velocities from stellar spectra, see Murdoch

4.3.2 Distances, declinations and apparent magnitudes

As was the case for visual and astrometric binaries, spectroscopic orbital solutions continue to be predominantly of systems that are relatively nearby and with northern declinations (Fig. 4.13). Two-thirds of solved SB orbits have northern declinations, a proportion mirrored by the VB solutions. Fig. 4.13 shows that, in addition, there is no obvious difference for how SB1 and SB2 systems present themselves with regard to these particular characteristics.

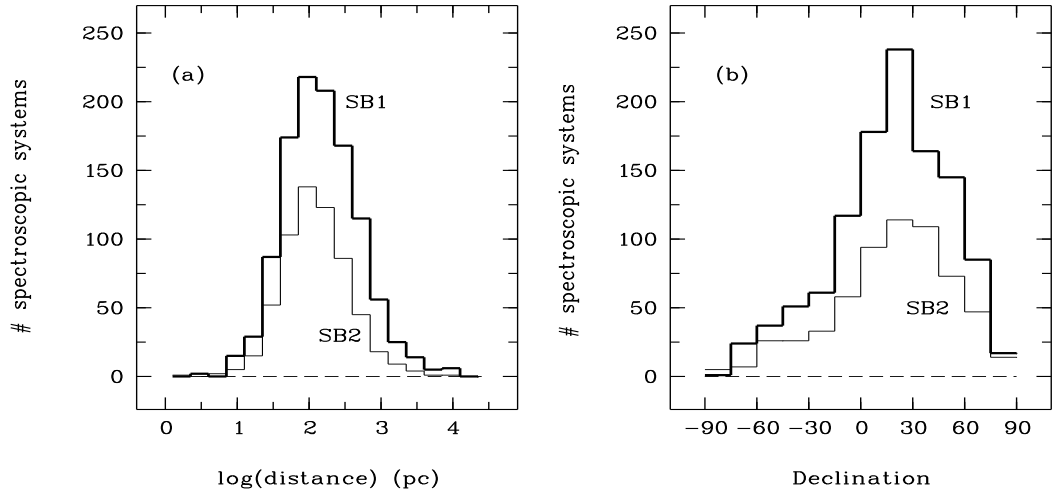

Figure 4.13: Histograms illustrating the observed distribution of (a) distance (1729 systems), and (b) declination, of a sample of spectroscopic binaries in the 9SB.

Spectroscopic binaries with orbital solutions also tend to be relatively bright objects and so are often nearby (whereas visual binaries need to be nearby to achieve spatial resolution, as well as be bright). Many systems with SB orbital solutions are fainter than $m_v = 10$. Indeed, whereas there are only 52 (3.6%) VB systems whose distances exceed 300 pc, there are 424 (18%) spectroscopic systems that do so (some of which are in neighbouring galaxies such as the Large Magellanic Cloud).

There are considerably fewer secondary magnitudes listed in the 9SB as compared to the 6VB. When only one magnitude is given, it is reasonable to anticipate that the magnitude estimate is for the combined light of both stars[17]. This is unfortunate, but not too surprising,

& Hearnshaw (1991).

[17]This includes SB2 systems of which only about one-quarter of the systems include the magnitude of both stars. Since there are about 2000 systems with only one magnitude given, and presumably the combined light in most cases, it was considered unrealistic to undertake the thorough analysis necessary to better estimate the individual magnitudes. It is hoped that the general trends described are little affected by this decision.

as each star's magnitude would ideally be determined by individual photometric examination, which is impossible for an astrometrically-unresolved spectroscopic binary.

In the worst-case scenario, if the secondary star is as bright as the primary star, the combined magnitude will be $0^{\mathrm{m}}.75$ too bright. However, magnitude differences are related to the system's mass ratio, particularly for main-sequence pairs (which Fig. 4.16(a) demonstrates are common for SB2 systems), and so the magnitudes can be estimated from the mass ratio and the spectral types for the SB2 systems. This, in turn, may explain the greater number of secondary magnitudes in the 9SB for SB2 systems (about twice as many as are found for SB1 systems).

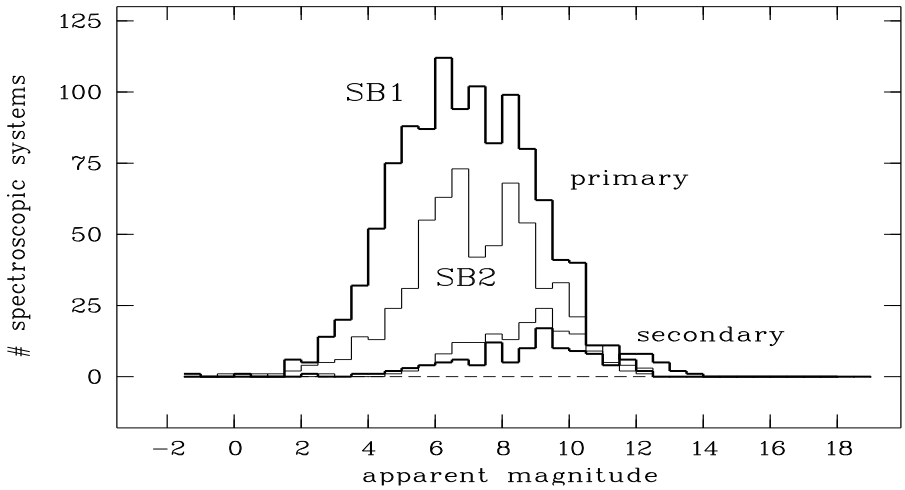

Figure 4.14: Distribution of apparent V magnitude of primary (2365 systems) and secondary stars (412 systems) with spectroscopic orbital solutions in the 9SB. The magnitudes recorded in the 9SB for the primary stars will, in many cases ($\sim$ 2000 of them), be the combined light of both stars, so that the individual values for the primary stars included here may be as much as $0^{\mathrm{m}}.75$ too bright.

It is also interesting to note the relative absence of SB2 systems with apparent magnitudes of about 7–8 mag. Since there is no comparable dip in the luminosity function this is surely another selection effect. The same local minimum in the observed V magnitude distribution is also evident in the SB2 (and a lesser one for the SB1) distribution reported by Popova et al. 1982. The elapse of two decades with its many changes to observing techniques and analytical methods, increases ones curiousity as to why this feature exists and is so long lived. It suggests that a greater proportion of binaries with primary components of this brightness await discovery and/or an orbital solution. At the typical distance of an SB2 system[18], seventh-magnitude dwarf stars would have late-A to early-F spectral types[19].

[18]For the SB2 binaries with a *Hipparcos* parallax, the median distance is ~ 120 pc.

[19]The only SB2 system discovered and whose orbit was solved during this project was the seventh magnitude

4.3.3 The colour-magnitude diagram for SBs

A sub-sample of the 9SB data was used to create a colour-magnitude diagram (Fig. 4.15), and as for the 6VB sample, only the solutions with $\sigma_{p''}/p'' < 0.2$ are included (1079 systems). Approximately 60% of the 9SB dwarf systems are represented but only 40% of the evolved binaries, because of the larger parallax errors that remain common for these typically more distant objects. A slight under-representation of SB2 solutions with components with $(B-V) \sim 0^{\rm m}.3$ (spectral class about F0V) can be seen, in particular, in relation to the later F-type stars (the latter of which usually have larger numbers of sharper spectral lines for radial-velocity measurements).

The vast majority of datapoints on this diagram correspond to systems that have an absolute magnitude brighter than about $M_{\rm V} \sim +6^{\rm m}$, just as did the visual and astrometric systems. More evident is the relative absence of SB1 or SB2 solutions for late-type systems on the main sequence. The selection effects operating here are, in part, related to the relative faintness and lower masses of the unevolved late-type stars, so that the corresponding velocity variations are smaller and so harder to detect and measure.

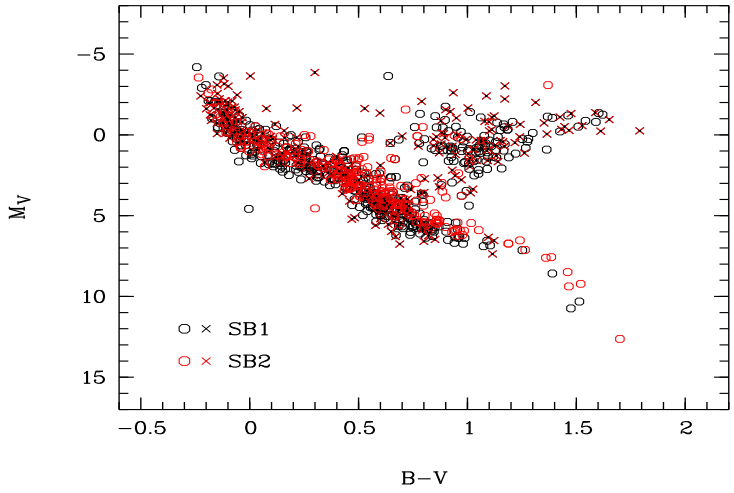

Figure 4.15: Colour-magnitude diagram of the 453 SB1 and 259 SB2 systems with $\sigma_{p''}/p'' < 0.1$ (open symbols) and the 238 SB1 and 129 SB2 systems with $0.1 \leqq \sigma_{p''}/p'' < 0.2$ (crosses).

4.3.4 Luminosity and spectral classes

The distributions of luminosity class and spectral type are presented in Fig. 4.16. Many comparisons and generalisations can be made from these diagrams, so I shall comment on just a few

HD 181958 which comprised a pair of nearly equal F-type dwarfs. The spectroscopic orbit and related analysis is presented in § 7.6 beginning on page 192, and reported in Ramm et al. (2004).

of them. First, Fig. 4.16(a) once again illustrates the bias toward orbital solutions for the more common dwarf stars in the solar neighbourhood. Second, the proportion of SB1 to SB2 systems in each luminosity class is also consistent with previous discussions. A typical binary system is more likely to have a dwarf companion than an evolved one, and similarly, higher luminousity stars (classes I–III) can be expected to have significantly fainter companions. Thus, amongst dwarf primaries, SB2 systems are almost as common as SB1 systems (the latter binaries presumably being dominated by those having spectroscopically undetected M-type companions), whereas SB systems with a subgiant primary are about twice as likely to be SB1 than SB2. For systems that have a giant primary, SB1 systems outnumber SB2 systems by about 5:1. For systems with more luminous components (classes I and II, this trend continues, i.e. SB1s dominate over SB2s. The smaller numbers of systems recognized in these luminosity classes make it unreasonable to try to comment any further with regard to any possible trends.

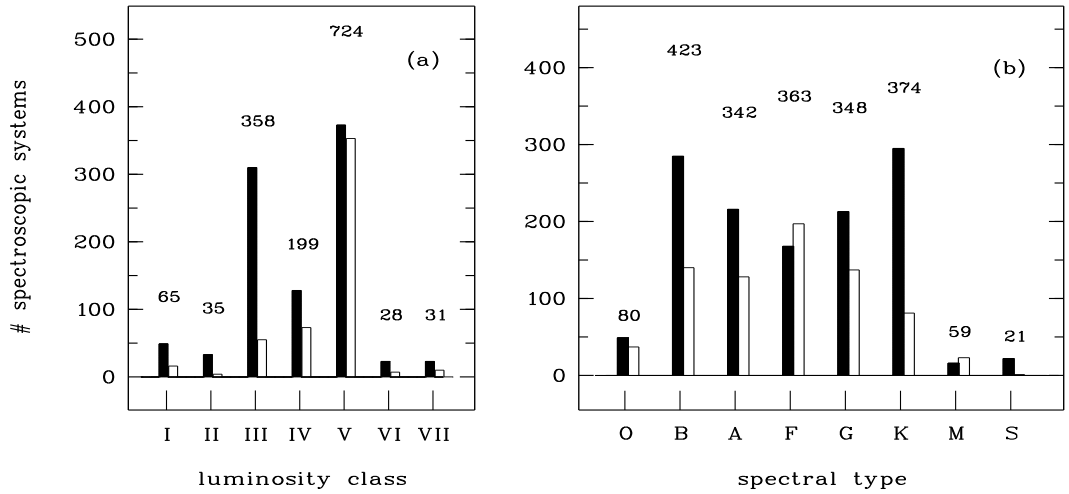

Figure 4.16: Distribution of (a) luminosity class (1440 systems), and (b) spectral type (1995 systems), for a sample of primary stars in the 9SB (orbital grades 0–5). SB1: solid columns, SB2: open columns. The numbers above each class are the total number of orbital solutions (SB1+SB2).

The SB1 solutions that include dwarf components are dominated by early-type stars (O, B, and A), whereas the dwarf SB2 systems are dominated by stars later than about mid-F, although this is not evident from the figure. Only F and M-type stars have more SB2 than SB1 systems. It is also noteworthy that the spectral types B–K are now reasonably equally represented in the 9SB. This is a significant change from the predecessor to the 9SB, the 8SB (Batten et al. 1989), which was dominated by early-type stars (peaking at about late-B to early-A type stars) and declining gradually for later spectral types. The same general prevalence of B–A type stars was

reported in the survey of about 1000 SBs conducted by Popova et al. (1982). Their sample had dwarfs outnumbering giants by about 3:1, another imbalance that has been significantly addressed by subsequent investigations.

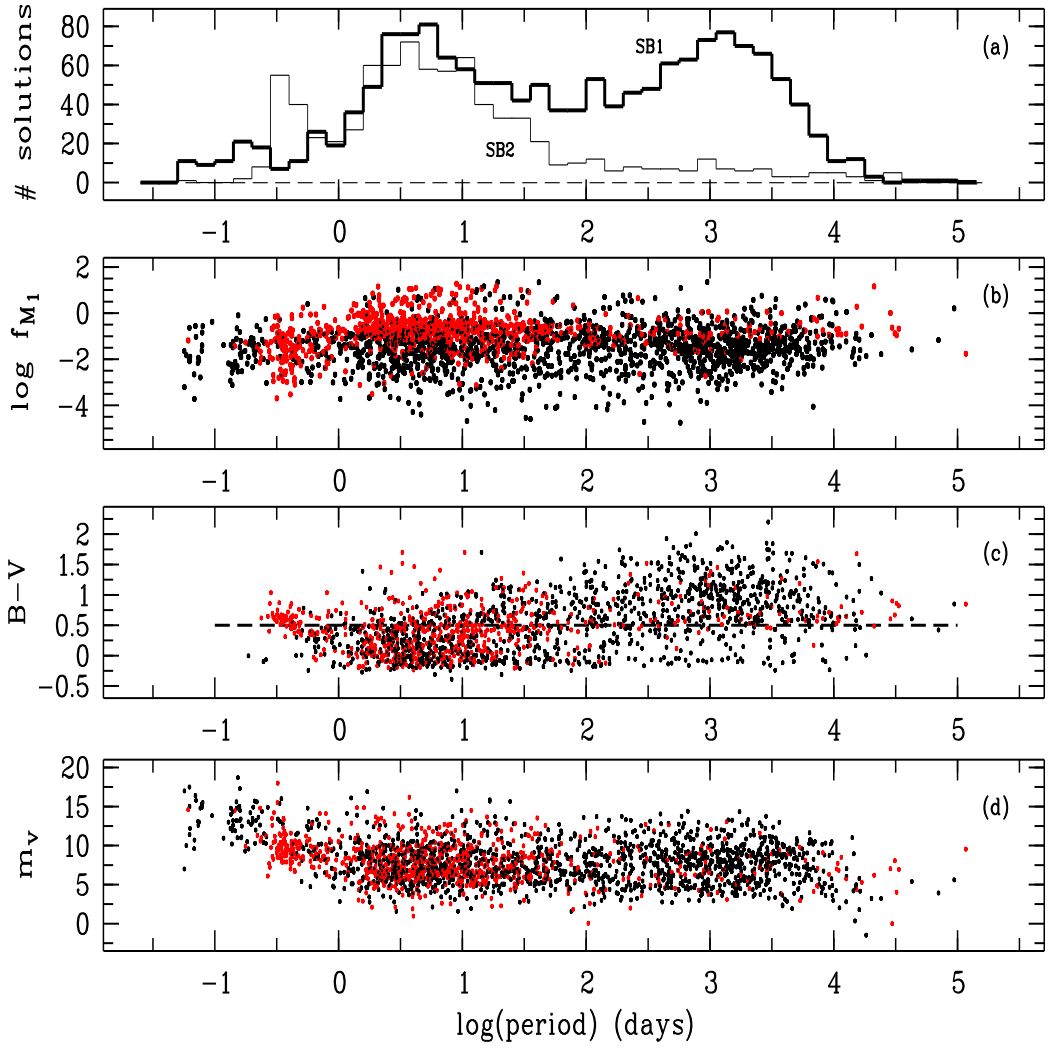

Figure 4.17: (a) Distribution of the orbital period of SB1 and SB2 solutions in the 9SB. (b) The mass function of the primary star ($f_{\mathcal{M}_1}$), (c) the $(B-V)$ colour index, and (d) the apparent magnitude, m_v, as a function of the period. SB1: black, and SB2: red symbols. The dashed line in (c) at $(B-V) = 0\overset{m}{.}5$, represents an approximate division between early- and late-type stars.

4.3.5 The period distribution and its relation to other parameters

Fig. 4.17 presents some interesting issues in relation to the periods of SBs with orbital solutions. The top diagram in this figure illustrates the histograms of $\log P$ for the SB1 and SB2 solutions in the 9SB. In the first place, SBs have much shorter orbital periods as compared to typical visual and astrometric binaries. This is primarily because the discovery of SBs, and the solving of their orbits, is biased toward, for instance, stars having larger velocity variations, and, for a given system mass, (as shown by Eq. 4.1 on page 50), $K \sim P^{-1/3}$. More specifically, the distributions are bimodal, which is in contrast to the period histogram for VB solutions which is distinctly unimodal[20]. In the SB histograms, only the peak in the vicinity of $\log P \sim 0.6$ ($P \sim$ 3–5) days is common to both SB1s and SB2s.

For the SB2 solutions, the shorter-period peak at $\log P \sim -0.4$ ($P \sim 0.4$) days, owes its presence to a large degree to the sample of contact binaries included. Contact binaries, of which the W-UMa-type are a good example, present spectroscopic observers with a curious anomaly: the components are about equally bright (which explains their absence in the SB1 statistics), yet the mass ratios measured are typically $0.3 \lesssim q \lesssim 0.6$. These observed features are believed to be the result of a common convective envelope, at nearly constant temperature, surrounding two otherwise dissimilar stars (Hilditch 2001). The corresponding clusters of datapoints in Fig. 4.17(c), and with regard also to the colour-magnitude diagram in Fig. 4.15, identifies the typical spectral types of these shorter-period SB2 systems in the 9SB sample, i.e. $\sim$ F–K, IV–V.

The second broader period-peak for SB2s is populated by systems with somewhat greater mass functions, $f_{\mathcal{M}_1}$, than the contact systems have [see Fig. 4.17(b)]. For a given primary-star mass and orbital inclination, larger values of $f_{\mathcal{M}_1}$ correspond to larger values of q. In fact, these longer-period SB2s are binaries with $0.8 \lesssim q \leq 1$. Therefore, one property that biases inclusion of a binary system in one or the other of the SB2 dominant modes of the period distribution is their mass ratio.

The distribution of mass functions for the SB1 sample shows no trend whatsoever in relation to the orbital period. This is also true for any sub-sample based on luminosity classes, e.g. the 305 SB1s with a giant component, or the 351 main-sequence systems. With regard to this study's giant SB1 sample, this result contradicts the work of Eggleton & Tout (1989), who claimed an unambiguous correlation with mass function and period. The lack of any significant correlation here, is though, consistent with other studies, e.g. Boffin et al. (1993).

The mass functions of the SB1 solutions are typically comparable to the mass functions of the contact systems, which implies the mass ratios extend over a similar range, i.e. $0.3 \lesssim q \lesssim 0.6$. Although this estimate is hardly rigorous, it is consistent with the range of inferred mass ratios for typical SB1 systems that has been documented many times before (see e.g. Staniucha 1979;

[20] Since two distinct samples are included in the AB period histogram, it is not so surprising that a weak bimodal distribution would appear here if the two samples were combined.

Hogeveen 1992; Halbwachs et al. 2003)[21]. Regardless of the method employed to estimate the mass ratios of the SB1 systems, the overall distribution of mass ratios, for SB1 and SB2 systems combined, is well-documented as being bimodal, with a broad peak from $q \sim 0.2$ to $q \sim 0.6$, and a sharper peak between $q \sim 0.8$ to $q = 1.0$ (Staniucha 1979; Popova et al. 1982; Halbwachs 2003). Rather than this implying that binaries can be formed by more than one physical process (Trimble 1974), the different distributions of q for SB1s and SB2s may instead be the result of a selection effect. On this occasion, the greater minimum value, $K_{\rm min}$, required for the detection of an SB2, in comparison to an SB1, may lead to this bias (and could be as much as ten times the $K_{\rm min}$ required for an SB1 of the same mass; Popova et al. 1982).

The second longer-period peak for SB1 solutions occurs at $\log P \sim 3.1$ ($P \sim 1200$) days. This feature appears to be becoming more evident as the SB sample increases. It was hardly noticeable for the 'Seventh Catalogue' sample, but is quite evident for that of the 'Eighth Catalogue' (see Hogeveen 1992, for a comparison). The orbital solutions to the longer-period systems were substantially due to the development of the new breed of correlation radial-velocity instruments, such as used by R. Griffin. These instruments were particularly suited to later-type stars, so their application to the study of SBs was also one of the principal reasons for the increased numbers of late-type SB orbital solutions described earlier.

The rather striking selection effect that appears to place SB1 solutions in the longer-period region of the distribution is related to the spectral type of the primary star. The SB1 short-period peak is dominated by stars with $(B-V) \lesssim 0.5$, whilst the long-period peak is dominated by stars with $(B-V) \gtrsim 0.5$. This value for $(B-V)$ corresponds to a spectral type of about F7. At the typical distance for an SB system, a dwarf star having this spectral type would have an apparent magnitude of about $9^{\rm m}$. Approximately 80% of SB1s with a period less than 10 days have a $(B-V)$ index less than $0\overset{\rm m}{.}5$, whilst the same proportion of these systems with a period greater than 100 days have a $(B-V)$ greater than $0\overset{\rm m}{.}5$. This is illustrated in Fig. 4.17(c), and is emphasised by the dashed line that divides the plot into two portions[22].

This tendency has been recognized for many years (e.g. Batten 1973), but it is noteworthy that it has not disappeared with a larger sample of SB1 solutions as is provided by the 9SB. The colour-magnitude diagram demonstrates that these late-type systems are also predominantly evolved stars, as has been illustrated in SB studies that have specifically examined late-type giants (Boffin et al. 1993). Therefore, these longer-period SB1 systems tend to comprise evolved later-type stars, whilst the shorter period systems typically comprise earlier substantially un-

[21] Various methods have been applied to the challenge of estimating the mass-ratio distribution from the mass-function distribution. Some authors do this by estimating the mass of each primary star, for instance using a mass-spectral-type relation, and then solving the cubic expression Eq. (3.16) on page 28 in terms of $f_{\mathcal{M}_1}$ and a mean value for $\sin^3 i$ (e.g. Hogeveen 1992). This approach is discouraged on statistical grounds by others (e.g. Boffin et al. 1993; Halbwachs et al. 2003), who use alternate strategies, such as various forms of model-fitting algorithms (see also Trimble 1990; Mazeh & Goldberg 1992).

[22] The visual and unresolved astrometric binaries with orbital solutions do not show any significant bias with regard to their spectral types and orbital periods.

evolved stars. The question that naturally presents itself is, are these differences solely due to observational selection effects, or do they reflect a real difference in the types of binary stars in the Sun's neighbourhood with mass ratios probably substantially less than 1 (since they are SB1s)?

One possible explanation for this trend is, as mentioned earlier, that the longer-period systems will be harder to detect and study owing to smaller velocity variations. This selection effect, that disfavours the measurement of the orbits of these systems, can be offset if, instead, the primary stars are more massive, namely, ones that have evolved from the main sequence, as indeed we find. However, since late-type giants are not that much more massive than dwarf stars of the same spectral type (perhaps only 2–4×, and $K \sim \mathcal{M}_{\rm S}^{1/3}$), this is unlikely to be the main reason for this bias. Instead, the relative faintness of the late-type main-sequence stars, as discussed earlier, can be expected to have a strong influence upon the types of SB1s that can be observed. Furthermore, since the companion of an SB1 primary will be considerably fainter, the total light cannot be expected to be that much more than that of the primary alone.

The absence of late-type systems, both SB1s and SB2s, with shorter periods, requires a somewhat different explanation, since these would be expected to have ample velocity variability to be detected with ease. First of all, we know not to expect too many late-type dwarfs in the short-period sample of SB1s, owing to there inherent faintness. This may change in time as a result of, for instance, the many extrasolar planet searches being undertaken, since these surveys measure velocities with very high precision, and target short-period variations of late-type stars. The relative absence of evolved late-type stars in short-period systems can be explained, with good agreement, by an analysis of the sizes such stars would have if they filled their Roche lobes. This has been demonstrated recently by Pourbaix et al. (2004).

Since the mass function appears to have a more or less constant distribution with regard to period, we might expect the same would be true for mass ratios, although this should not be done without caution. However, the absence of the longer-period SB1 peak in the SB2 histogram deserves some comment as well. This finding may be explained, in part, by the predicted small amplitudes of radial-velocity separation that must occur for longer-period SB2 systems. The later-type main-sequence stars will be fainter at a given distance, and, having lower masses, they will have smaller velocity separations for measurement than if the stars had earlier spectral types. Conversely, when the stars have early-type spectra, the velocity separations will be that much harder to detect and measure owing to the fewer and broader spectral features of these hotter stars. Finally, when stars are old enough to evolve from the main sequence, small differences of mass lead to significantly different rates of evolution. Consequently, SB2s including a pair of evolved stars are unfortunately rare (as Hilditch 2001 emphasizes). Whether or not longer-period SB2s do exist in relatively large undetected numbers remains to be seen. It is interesting to note in this regard that a recent study by Halbwachs et al. (2003) reached the conclusion that the short-period peak for SB2s may be the result of a physical process that preferentially creates approximately equal mass binary pairs with $P \lesssim 50$ days. Eggenberger et

al. (2004) repeat this claim, and suggest that the incidence of binary twins decreases gradually toward longer-period systems.

As an example of the characteristics of possible SB2 systems with long orbital periods, the following simple analysis can be described. The mean velocity separation for the two quadrature phases is $Ke\cos\omega$. Based upon other reasonable assumptions (e.g. $\langle\sin i\rangle \sim 0.88$ (Trimble 1983), $\langle e\rangle \sim 0.3$, $\langle\mathcal{M}_{\rm S}\rangle \sim 1.4\,\mathcal{M}_{\odot}$) for K-type unevolved binaries with $P \sim 1000$ days, we can estimate $K \sim 20\,{\rm km\,s^{-1}}$, although favourable values of ω would increase this estimate for particular quadrature phases. Whilst such a velocity separation for an SB2 would have been difficult to measure successfully in the past, it is quite sufficient for modern high-resolution spectrographs, such as HERCULES, to measure. Of course, though, for much of the ~ 1000 day orbital cycle, the velocity difference will be much less, and unlikely to be detected by chance. The prediction provided by an astrometric solution is therefore of considerable assistance for studying these lower-mass systems. Indeed, one of the binaries observed during this thesis, HD 206804 (K7V+K7V, $P \sim 6\,$years), was shown to be an SB2 system. A spectroscopic orbital solution was determined for the first time, thus making a contribution to this otherwise relatively empty portion of the observed range of periods for SB2 systems[23].

The lowest plot in Fig. 4.17 shows that the difference between the two period populations is not related to their apparent magnitudes, since both shorter- and longer-period systems have a similar range for $m_{\rm v}$. The only systems that display a significant preference for particular values of $m_{\rm v}$ are those with ultra-short periods, namely with $\log P \lesssim -0.5$, where it is seen that $m_{\rm v}$ tends to be greater than about $10^{\rm m}$. This would seem to be a result of a real absence of such systems in the Sun's local neighbourhood, since it goes against the common trend for all observing biases, namely that brighter objects are more likely to be detected and studied. In fact, many of these systems have intrinsiclly faint white-dwarf primary stars. The absence of these systems in the $(B-V)$ plot is owing to the lack of these values in the *Hipparcos* Catalogue for these systems.

It is unclear why there is a relative lack of spectroscopic systems with solutions with moderate periods, i.e. $P \sim 100$ days. Fig. 4.17(c) again shows a tendency for these systems to have later spectral types. Either such systems are uncommon in the Sun's local neighbourhood, which seems unlikely, or this may reflect the scarcity of observing programmes that would lead to their discovery and the determination of an orbital solution. For instance, typical observing programmes may be biased to the discovery and follow-up of binaries with orbits that have periods of days or years, but not months. However, this also seems hard to believe.

The relationship between the eccentricity and the period, illustrated in Fig. 4.18 on page 62, has attracted considerable attention for over one century, and this has continued in recent years (e.g. see the IAU conference proceedings devoted to this topic; Duquennoy & Mayor 1992). Spectroscopic binaries are particularly suited to these investigations as they provide relatively

[23]With regard to this binary system, preliminary comments are to be found in § 4.5.1 beginning on page 64, and the detailed analysis of the HERCULES observations and the system are presented in § 7.4 beginning on page 167.

large samples that are also dominated by short-period systems with a wide range of mass ratios (both measured for SB2s and inferred for SB1s). The distribution that relates these two orbital parameters is described in some detail in Appendix D, where numerous references to the literature are also to be found.

4.4 Summary of selection effects

One of the primary goals of this thesis is the determination of the spectroscopic orbital solutions of several binary systems that already have resolved or unresolved astrometric solutions. The previous sections described some of the varied and numerous selection effects that influence the observation of VB, AB and SB systems. In particular, these comments have exposed several characteristics of VB and SB systems that makes measuring a spectroscopic orbital solution of a typical VB challenging. Astrometric, photocentric and spectroscopic orbital solutions are dominated by relatively bright stars, as was illustrated in Fig. 4.3(a), Fig. 4.7(b) and Fig. 4.14. However, this is one of the few shared characteristics of these systems. Northern hemisphere observers would have a slight advantage with regard to choosing suitable binaries with regard to the above mentioned goal as the majority of VB [Fig. 4.2(b)] and SB [Fig. 4.13(b)] systems have a northern declination.

Resolved astrometric orbital solutions are biased toward nearby dwarf systems with components of similar luminosity [Fig. 4.3(b) and Fig. 4.4(a)]. These tendencies are reflected in the corresponding properties also found for SB2 systems (e.g. Fig. 4.16). In contrast, unresolved astrometric systems are more similar to SB1 systems in terms of their respective biases toward unequally bright components, with the primary star more likely to be evolved [Fig. 4.8(a) and Fig. 4.16(a)].

The orbital parameter that most distinguishes typical representatives of these binary types is the period, as is illustrated in Fig. 4.18. This figure combines the period distributions of VB, AB and SB1 and SB2 systems [Fig. 4.5(a), Fig. 4.10(a) and Fig. 4.17(a)]. Whilst the distribution of the AB and SB1 systems occupy common ground, the VB and SB systems overlap very little on the $e - \log P$ plane. The promise of modern astrometric instruments such as interferometers and modern high-resolution spectrographs is to provide the opportunity for greater overlap of observable VB and SB systems.

4.5 Selection of binary systems for this study

The selection of suitable binary systems for this project must make due consideration of the selection biases outlined above, as well as other factors, some of which will be discussed below. In particular, having a longer orbital period naturally leads to the prediction of a lower total radial-velocity amplitude K for a typical VB system. Fig. 4.19 illustrates just how low K often is, relative to the SB2 sample of 9SB. Furthermore, the selection effects skew the histograms in

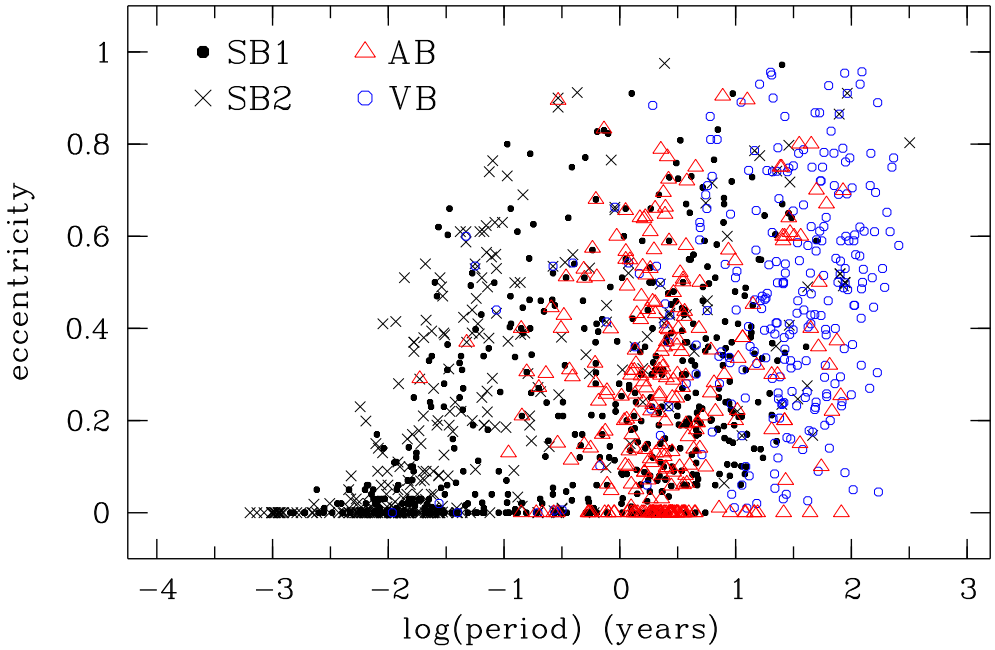

Figure 4.18: Distribution of orbital eccentricity as a function of period (in years) for the VB and AB sample in the 6VB, and the SB1 and SB2 sample in the 9SB. Only VB and SB orbital solutions that are assigned grades indicating average or better solution quality are included.

opposite directions. The VB solutions are skewed toward lower values of K whilst the SB solutions are skewed toward higher values. Even though there is some overlap of the two histograms, the VB and SB systems occupying this shared territory on Fig. 4.19 are quite different orbital systems in terms of other properties e.g. the eccentricity and period. For instance, in Fig. 4.19, for $1.3 < \log K < 1.7$, the median values for e and P are — VB: $e \sim 0.7$ and $P \sim 20\,\mathrm{years}$, SB2: $e \sim 0.4$ and $P \sim 1\,\mathrm{year}$. Based on these orbital parameters, for equal values for K, $(a \sin i)_{\mathrm{VB}}/(a \sin i)_{\mathrm{SB2}} \sim 16$. We have seen in previous histograms that the distributions and typical distances to VBs and SB2s are similar. Therefore, the binaries in these two sub-samples also differ in the likely angular size of their projected orbits — the systems with astrometric solutions are several times or more larger than those with SB2 solutions.

To somewhat quantify the challenge of identifying VBs that may be successfully observed as SB2 systems, assume the minimum radial-velocity separation the slowly-rotating late-type stars can have for relatively easy measurement is $K \sim 15\,\mathrm{km\,s^{-1}}$. We also assume that $\Delta m_{\mathrm{v}} < 2^{\mathrm{m}}$. There are 228 VB solutions in the 6VB that meet these criteria, but only 95 of them have a southern declination. Of these, only 24 solutions have a high quality grade of 1 or 2 and $\sigma_{\mathrm{p}''}/p'' \lesssim 0.2$. Of course, the necessary velocity separation must occur during the observing pro-

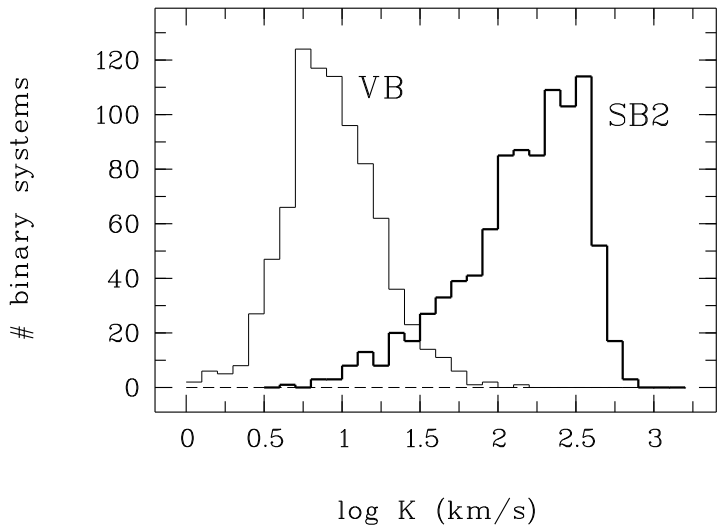

Figure 4.19: Comparison of the observed total radial-velocity amplitude K for the SB2 sample in the 9SB with the predicted K for a sample of the VB systems in the 6VB which have $\Delta m_{\rm v} < 2^{\rm m}$ and $\sigma_{\rm p''}/p'' < 0.2$.

gramme. This is another selection effect — a given measurement may or may not be successful based entirely on it actually occurring during an observation. This effect can be compensated for with observations being taken more frequently (for instance, when the object's future behaviour is entirely unknown), or by waiting for later opportunities based on prediction. The bias toward recording *observable events*, rather than simply candidate systems, limits the choice of objects suitable for a given telescope schedule even further.

At any one time, only a small fraction of known visual binary systems have radial velocities that permit the methods of mass determination of § 3.2 to be applied. To identify such systems for a particular time, the theoretical radial-velocity curves (primary, secondary and their difference) are required. To achieve this, the following orbital parameters are necessary: $a = a''/p''$, e, i, ω, P and T.

The velocity-difference curve, $\Delta V(t)$, defined by Eq. A.75c on page 229, and velocity amplitude K of a VB system can be predicted without any knowledge of the orbiting masses. The mass of each star, or at least their ratio, is needed if the radial-velocity curve of either component is to be predicted. In rare cases, the masses will have been measured previously by other workers. More typically, each mass was estimated from $M_{\rm V}$, the colour indices, and/or the spectral type.

Ideally, only definitive VB orbital solutions would be considered so that an accurate and precise total mass for the binary would also be available. Since these systems are rare, and

many of them already have good quality measures of the component masses, all grades were considered for selection with the hope that eventually the precision of the orbital solution would improve[24].

For the cases of AB systems, it was decided that the crucial element was the inclination, since that is one parameter that a spectroscopic study cannot determine. With sufficient phase coverage the other orbital elements of an AB could be measured with high precision also, leaving only an estimate of the primary mass to be determined so that the companion's mass could also be measured. The radial-velocity curve of the primary star of each AB was estimated assuming $L_2/L_1 \sim 0$ so that $a'' \sim a''_{\rm p}(1+q)/q$, with q estimated to be typically about 0.3.

The orbital elements were sourced from the 5VB (Hartkopf et al. 2001; see footnote (3) on page 36 for brief comments about this catalogue). Additional criteria that guided the binary system selection process for this project were dictated by the observing location, available instrumentation and the need for precise radial velocities (described in detail in Chapter 5). The latter criterion implied the need for late-type stars which typically provide many sharp spectral lines for the digital cross-correlation of spectra. Therefore the systems selected had to brighter than $m_{\rm v} \sim 9\overset{\rm m}{.}5$, have a declination south of about $+20^\circ$ and a spectral class no earlier than F5. Using these criteria for the initial assessment, approximately 400 orbital solutions in 5VB were analysed and their radial-velocity curves produced utilising the theoretical ideas and equations described in Appendix A (in particular those of § A.10 and § A.13).

The longest period for which a potentially suitable VB system was identified, $P = 990\,\text{yrs}$ (!), was for HD 3125. The published orbital solution (see the first entry in Table 4.1) has a high eccentricity, $e \sim 0.95$, and a time of periastron passage in mid-2002. The stars are about seventh magnitude with $\Delta m \sim 0\overset{\rm m}{.}5$. The predicted radial-velocity separation of the components during 2000 and 2004 was 15–20 $\text{km}\,\text{s}^{-1}$. Of course, since the orbital solution is, understandably, assigned a low-quality grading, it was somewhat optimistic to include this system in the target list. However, HD 3125 was felt to be deserving of at least some attention, as the successful measurement of the mass ratio for such a long-period binary would have been very rewarding[25].

4.5.1 HD 206804: an example of the selection process

As an example of the selection process for the observational part of this thesis, a potentially worthwhile SB2 candidate, HD 206804, and its predicted radial-velocity curves will be described briefly. The primary star has a spectral type of K7V and both stars are nearly the same magnitude, so it is reasonable to assume that the secondary star has a similar spectral type with a similar mass i.e. $q \sim 1$. Such late-type dwarfs provide many sharp lines, allowing the measurement of precise radial velocities. The system has two orbital solutions, originally derived

[24] However, this should be considered unlikely to occur before this thesis is complete. Of the one hundred or so improved orbital solutions in the 6VB (compared to the 5VB), only three improved to grade 1 with a further 14 improving to grade 2, but only four of these 17 were in the southern skies and none were on the thesis target list.

[25] As it turned out, the spectra obtained of this system during this project were always unresolved.

by Finsen (Rossiter 1977), and subsequently modified slightly by Söderhjelm (1999); the more recent solutions are included in the following discussion. The two sets of orbital parameters provide quite different radial-velocity curves, as Fig. 4.20 illustrates. Interestingly, Söderhjelm (1999) also suggested that the mass ratio is either $q = 1.61 \pm 0.30$ or $q = 1.88 \pm 0.34$, with the possibility therefore of the secondary star in fact harbouring a yet to be recognized third companion.

Ignoring the complication of a possible third companion, solution (2) — represented by the top figure in Fig. 4.20 — predicted that the velocity separation would not exceed $10\,\mathrm{km\,s^{-1}}$ during the observing time-span of this thesis. Therefore the system would always be a line-width spectroscopic binary, i.e. one having only variably blended spectra, using the available instrumentation. However, solution (1) promised a profitable though short-lived SB2 target for several months during 2001 whilst the velocity separation attained close to $30\,\mathrm{km\,s^{-1}}$. This second solution presents another selection effect for the complementary spectroscopic observing of visual binaries (Batten & Fletcher 1990): ω is close to 0°, so that the quadrature-velocity difference, $\Delta V = K(1 + e\|\cos\omega\|)$, for the two stars is close to the maximum possible given the other orbital elements.

A single spectrum might determine the more valid solution if an observation was made in mid-2001. If a double-lined spectrum was obtained, implying that the solution (1) scenario was likely to unfold, HD 206804 would remain on the observing list as long as useful spectra could be obtained. Evidence for or against the possible third star might also make itself felt sooner or later. If the initial observations suggested solution (2) was closer to the truth, the system would be discarded. As it turned out, the favourable solution was vindicated and a series of precise radial velocities were obtained leading to the measurement of a precise mass ratio and spectroscopic orbital solution (see § 7.4 beginning on page 167).

The list of visual and astrometric binary systems targeted for spectroscopic observation for this thesis are presented in Table 4.1.

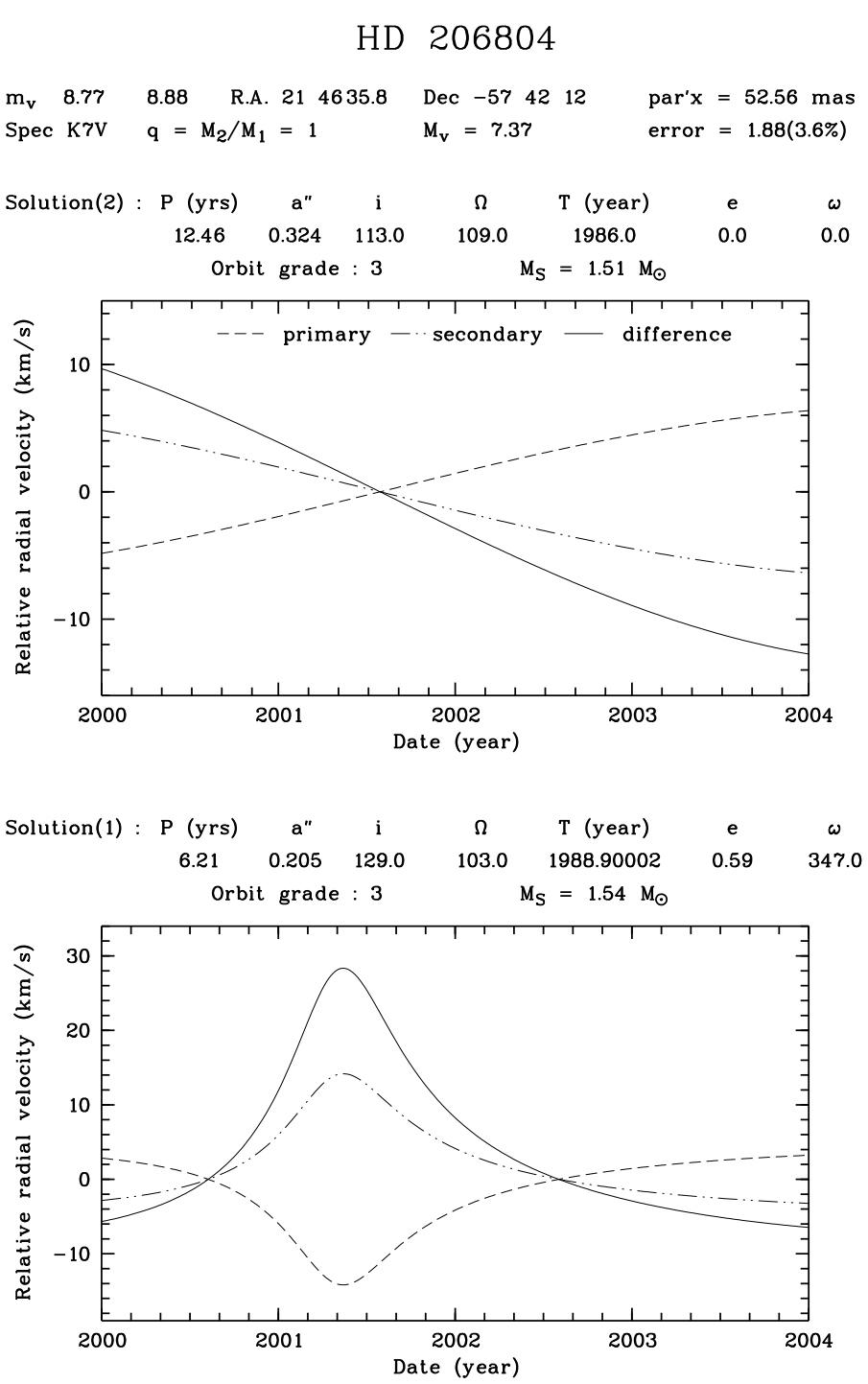

Figure 4.20: The predicted radial-velocity curves for the two resolved astrometric orbital solutions for HD 206804 (Söderhjelm 1999) assuming $q = 1$. Also included with the respective sets of orbital elements are the *Hipparcos* parallax and error, the component magnitudes from the 5VB, the estimated $M_{\rm V}$, and the system mass $M_{\rm S}$ derived using Kepler's third law.

HD	HIP	$m_{v\,1}$	Sp	$m_{v\,2}$	P (yrs)	a''	i (°)	Ω (°)	T (year)	e	ω (°)	grade
3125	2713	7.6	G0(IV)	8.1	990.	1.88	79.2	92.7	2002.5	0.948	271.9	4
16234	12153	5.7	K0V	.	1.924	0.119	101.0	171.3	1986.83	0.884	256.9	2
16620	12390	4.8	KOIV	6.1	2.654	0.107	24.	86.	1991.12	0.23	46.	1
21175	15799	6.8	KOV	11.0	111.	1.8	32.	49.	1982.	0.20	348.	5
23817	17440	3.9	KOIV	.	5.23351	0.0271*	82.85	22.39	1992.6837	0.2100	13.80	9
28307	20885	3.8	G7III	.	16.26	0.2178	92.35	355.54	1998.51	0.570	250.1	3
38089	26926	6.0	F3/F6V	6.7	20.15	0.206	71.7	98.2	1959.04	0.399	273.4	2
79555	45383	8.0	KO(V)	11.0	29.	0.252	117.	172.	1973.5	0.50	74.	5
83610	47328	6.9	F6V	8.9	110.4	2.042	96.1	5.4	1999.3	0.913	77.4	4
84367	47758	4.8	A8m+G7III?	5.7	18.29	0.123	123.0	174.5	1965.74	0.466	316.0	2
118261	66438	5.6	F6V	6.0	35.0	0.45	117.	71.	1967.5	0.78	94.	2
128620/1	71683/1	0.0	G2IV-V	1.4	79.9	17.59	79.23	204.82	1955.56	0.519	231.8	2
176891	93625	8.9	G5V	9.1	46.4	0.20	42.0	133.5	1954.2	0.42	175.0	4
179930	94739	9.4	K9V	9.4	7.70	0.26	117.	20.	1995.3	0.32	69.	3
187858	97851	7.9	F8V	8.1	44.5	0.193	81.35	157.09	1959.25	0.727	22.25	4
202275	104858	4.5	F5/F8V	4.8	5.6998	0.2313	99.57	203.68	1987.166	0.4386	7.02	1
202447	104987	4.0	G0III	.	0.27051	0.0112	151.5	33.9	1989.1786	0.0056	270.	1
205478	107089	3.8	K0III	.	2.84	0.052*	65.	118.	1906.471	0.25	37.	9
(1)206804	107522	8.8	K7V	8.9	6.21	0.205	129.	103.	1988.9	0.59	347.	3
(2)206804	107522	8.8	K7V	8.9	12.46	0.324	113.	109.	1986.0	0.00	0.	3
213429	111170	6.1	F7V	.	1.7253	0.0716	67.	262.4	1979.330	0.38	352.	4
217166	113445	7.0	G2V	7.3	26.0	0.35	89.	166.	1978.1	0.50	262.	2
219834	115126	5.2	G6IV	.	6.29	0.189	46.0	156.9	1980.87	0.175	223.1	2

Table 4.1: The binary systems surveyed for this thesis. The component magnitudes and orbital elements were sourced from the 'Fifth Catalog of Orbits of Visual Binary Stars' (5VB, Hartkopf et al. 2001). The spectral classes were sourced from Hipparcos (1997) and SIMBAD. The '*' symbols identify measures of the semimajor axis of the *photocentric* orbit of these unresolved astrometric binaries, i.e. $a''_{\rm p}$. The two solutions for HD 206804, described in § 4.5.1, are included.

Chapter 5

Instrumentation, observations and reductions

The observational part of this thesis was conducted at the Mt John University Observatory (MJUO), Lake Tekapo, New Zealand (170° 27.9′ E, 43° 59.2′ S) for approximately three years between June 2001 and August 2004. All observations were acquired using the 1-m McLellan telescope. Light was fed from the f/13.5 cassegrain focus to the High Efficiency and Resolution Canterbury University Large Échelle Spectrograph (HERCULES, Hearnshaw et al. 2002).

5.1 The HERCULES spectrograph

HERCULES is a fibre-fed échelle spectrograph designed for the purpose of high resolution stellar spectroscopy and precise stellar radial-velocity measurements. The design and construction of HERCULES were centred at the Department of Physics and Astronomy, University of Canterbury. HERCULES began operations at MJUO on 2001 April 3. The anticipated radial-velocity precision was $\lesssim 10\,\mathrm{m\,s^{-1}}$, for late-type stars.

Principal optical elements and vacuum tank

The major elements of HERCULES (see Fig. 5.1 on the following page) are fixed to an optical bench enclosed within a cylindrical steel vacuum tank (4.3 × 1.2 m) maintained at 1–5 torr[1]. Light enters the tank via one of three optical fibres, which will be described in more detail shortly. A 21-cm diameter parabolic collimator mirror ($f_{\mathrm{coll}} = 783$ mm) directs the fibre output toward the échelle grating. Between the collimator and the grating is a large single BK7 prism used in double-pass for cross-dispersion. HERCULES uses an R2 échelle grating with 31.6 grooves per millimetre for the main dispersion ($\tan\theta_{\mathrm{B}} = 2.08$) with a ruled area of 204 × 408 mm. A folded Schmidt camera focusses the dispersed light onto the detector. The camera comprises a 52.5-cm BK7 Schmidt corrector plate, a 55-cm diameter fold flat, a 50-cm diameter spherical primary mirror ($f_{\mathrm{cam}} = 973$ mm) and a field-flattening lens. The fold flat has a 100-mm central perforation through which the spectrum finally travels toward the detector. Just before the Schmidt corrector, light that would be lost due to the perforation is instead redirected by a small diagonal mirror and relay lenses to a photomultiplier tube (PMT). The final relay lens and field flattening lenses act as windows for the tank. The tank is housed in a thermally isolated

[1]The vacuum was first established on 2001 June 26.

and insulated room, approximately 12 metres from the telescope.

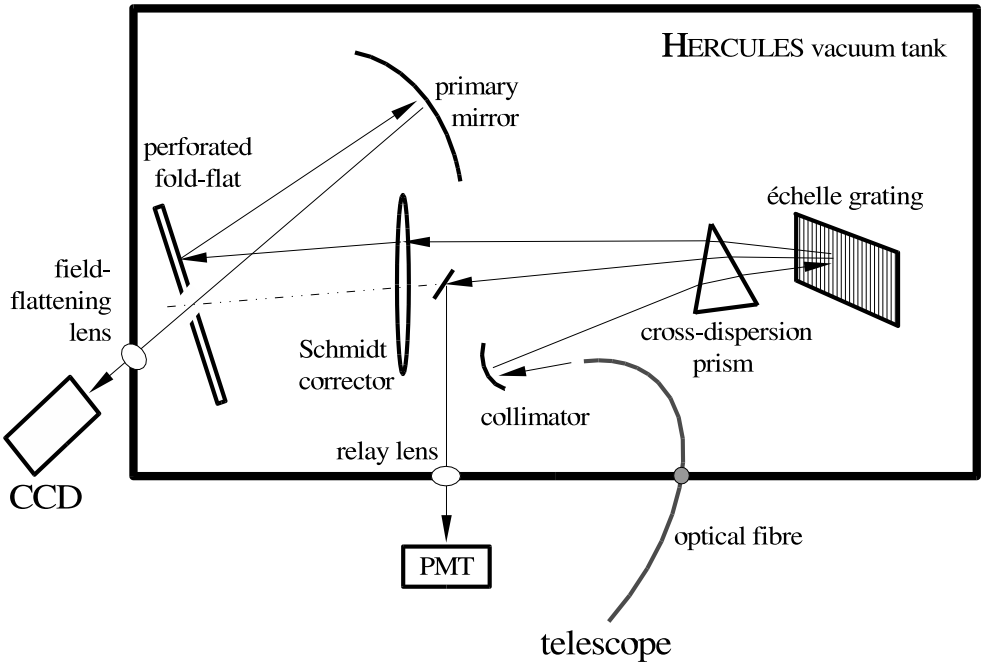

Figure 5.1: Schematic diagram of the optical design of HERCULES.

CCD detector and positioning

The nominal wavelength range (380–880 nm) should be imaged onto a single 50-mm square 2k × 2k-pixel CCD detector. However, since HERCULES operations began, the detector has been a SITe 1k × 1k-pixel CCD with 24-μm pixels. To achieve complete spectral coverage, four separate CCD positions are presently required. One of these, assigned position 2 ($\lambda\lambda \sim 4500$–7200 Å) was determined specifically to address the compromise required in terms of trying to maximize the spectral-line density, continuum flux and CCD's efficiency. This detector position is centred close to the MgI b triplet ($\lambda = 5170$ Å in order 110), and allows a large proportion of the radial-velocity important spectral range to be imaged. This was the only CCD position used throughout this observing programme[2]. Approximately 48 orders are imaged, between order numbers $n_1 = 79$ and $n_2 = 126$. The wavelength window for each order corresponds to $567\,000 \lesssim n \times \lambda[\text{Å}] \lesssim 571\,000$.

The detector is cooled to $\sim -95^\circ$ C using liquid nitrogen to provide a low dark current. Coolant is pumped automatically from a supply dewar external to the HERCULES room typically twice-daily, approximately every 12 hours. Each afternoon refill is scheduled so that it

[2]Further comments on the stability of the detector position relative to the HERCULES image plane are presented in § 5.10.

occurs at least one, but preferably two, hours before an observing session begins. The morning refill is scheduled after all spectra relevant to an observing session have been acquired. The consequences for not taking these precautions are described in § 5.8 and § 5.9. This refill frequency is generally adequate, but it relies upon the CCD system having a good vacuum ($\sim 10^{-6}$ torr). Each refill takes 10 – 15 minutes.

Fibre choice and resolving powers

A choice of three resolving powers is possible by the selection of the appropriate optical fibre (Table 5.1).

fibre	core diam (μm)	microslit (μm)	R	$\theta''_{\rm F}$
1	100	–	41 000	4.5
2	50	–	82 000	2.25
3	100	50	70 000	4.5

Table 5.1: HERCULES fibres, resolving powers and angular sizes of the fibre input.

A microslit is on the exit face of fibre 3. Each fibre is fed at f/4.5 as a result of a microlens cemented onto its input face so that the angular size of the fibre core projected onto the sky, $\theta''_{\rm F}$, is increased. This allows HERCULES to perform better than would otherwise be the case with inferior seeing. Whilst fibres 2 and 3 have similar resolving power, fibre 3 will provide superior throughput in poorer seeing ($\theta_* \gtrsim 2.0''$), but because of its exit-face microslit, it will be out-performed by fibre 2 in better seeing. The three fibres are in a common protective and light-proof sheath 22 metres long that connects the telescope with HERCULES. The fibre for an observation is selected by rotating a dial on the side of the fibre-feed module attached at the cassegrain focus. As soon as a larger (at least) 50-mm square CCD is acquired, so that the entire available spectrum can be imaged simultaneously, the only routine mechanical operation for HERCULES will be for the fibre selection.

Fibre-feed module: selection of light-path

The fibre-feed module includes several optical components which direct or receive light from various sources. The specific light-path is determined by a computer signal driving a turntable of selection mirrors. These various mirrors direct either starlight, light from a thorium-argon (Th–Ar) hollow cathode lamp or a white lamp into the chosen fibre, ensuring the light-path is essentially identical for each. The Th-Ar lamp is for wavelength calibration and the white lamp allows échelle order tracing and flat-fielding to be accomplished in the process of spectrum reduction.

A Philips intensified CCD guide camera receives starlight for acquisition (FOV $= 5.3 \times 3.7'$) as well as guiding (FOV $= 2.1 \times 1.4'$). Guiding is maintained either manually or in an automated mode. The original design directed all incoming starlight either to the fibre or the intensifier, so that intermittent guiding on the fibre, was necessary. In the automated mode, an integer number of minutes, chosen by the observer, elapsed before a guiding correction was made. The strategy behind this approach, rather than one utilising a beamsplitter to allow constant monitoring of the image relative to the fibre, was to avoid the continuous loss of a small percentage of the starlight to the intensifier. An increasing number of problems were identified with intermittent guiding. These were treated and substantially resolved with the introduction of a beamsplitter. Further details of the reasons for this change will be described at the end of this chapter (see § 5.11 beginning on page 103).

The PMT and exposure meter

The PMT signal has its readout provided by an exposure meter. The exposure meter has several useful purposes:

1. its readout assists with acquisition of the star;
2. it allows fine-tuning of the position of the star on the fibre entrance during an observation (this was particularly relevant pre-beamsplitter when guiding corrections to the image position on the fibre could only be carried out intermittently);
3. metering the spectrograph's throughput more accurately defines the flux-weighted time of mid-exposure, required for calculating the barycentric radial-velocity correction, the barycentric Julian Day correction, and interpolated dispersion solution of an observation; and
4. it provides the total readout estimated to be necessary for an exposure to obtain a given signal-to-noise ratio (S/N).

The total count required to obtain a given S/N was mildly dependent upon the star's spectral type, the rate of data acquisition (e.g. as a result of seeing, airmass and fibre-centering), and varied over time owing presumably, in part, to temperature and humidity changes. Spectra with low S/N can be expected to produce unwanted variations in the profiles of the cross-correlation functions analysed to estimate the corresponding velocity[3]. The nominal signal for this project's observations was $S/N \sim 100$, a value generally considered adequate for good radial-velocity results (Hill 1993; Hilditch 2001).

5.2 Observations

All observations were conducted from the MJUO dataroom, primarily using a computer to control the observation sequence and the CCD detector, a computer to control the Hercules

[3]Cross-correlation functions and their analysis are described in some detail in § 5.6 beginning on page 86.

fibre-feed module and guiding mode, and aided by the PMT readout meter.

5.2.1 Fibre choice: rate of data acquisition and velocity resolution

Before observations could be undertaken routinely, a decision was required as to which of the three HERCULES fibre should be used for a given programme star assuming median seeing conditions[4]. This decision depended upon the anticipated exposure time required to yield the desired $S/N \sim 100$ and the velocity resolution provided by each fibre. The length of the programme list (which would increase as a result of the need for a concurrent radial-velocity standard-star programme and a substantial list of $S/N \sim 150 - 200$ template spectra), meant that longer exposures to acquire higher resolution spectra with little significant advantage had to be avoided[5].

It immediately became obvious that the use of fibre 2, with its smaller core diameter, could not be justified for several reasons:

1. its resolving power was only marginally better than that of fibre 3;
2. its throughput was only superior to fibre 3 if the seeing was better than $\theta''_{\rm F} \sim 2''$, which at MJUO was expected to be uncommon;
3. not only does this narrow fibre provide less throughput in poorer seeing, even when the seeing is exceptional, the anticipated increased throughput would only be achieved if the guiding accuracy and precision were also optimal; and
4. the chosen fibre for any star should be maintained throughout the observing programme to minimise possible systematic errors in the measured radial velocities.

Table 5.2 lists the typical exposure times required to achieve $S/N \sim 100$ for stars of given magnitude for an observation conducted with seeing $\theta_* \sim 3''$ using fibres 1 and 3. A particular exposure time will depend upon factors such as seeing, the portion of the detector selected to measure the S/N, the spectral type and the observation's airmass.

Estimating the velocity resolution of the HERCULES fibres is especially relevant for those binaries that have been included on the programme list as potential SB2 systems. Such systems

[4]The median seeing at MJUO has been reported to be about $3.5''$ (Hearnshaw et al. 2002). At the completion of this observing programme the median (and mean) seeing of the 95 nights whose seeing quality was measured was found to be slightly worse, $\theta_* \sim 4''$. It is believed that the poorer seeing was partly due to the increased prevalence of El Niño weather patterns. This results in strong north-westerly winds at MJUO that are quite frequent and often persist for two or more days. The seeing was estimated using a one-dimensional gaussian fit to an unsaturated stellar image acquired at a low airmass and integrated over several seconds. This measurement was sometimes conducted more than once during a given night, particularly if the required exposure time for a star was not consistent with that expected from earlier observations.

[5]The template spectra part of this observational programme is described in detail from § 6.2 to § 6.5 beginning on page 108. These template spectra would be used for cross-correlating single- and double-lined spectra, determining the relative weights of the échelle orders used for a radial-velocity measurement, and for estimating the barycentric velocities.

	exposure time (mins)	
$m_{\rm v}$	fibre 1	fibre 3
1	0.1	0.25
3	0.5	1
5	3	5
7	15	25
9	90	140

Table 5.2: Approximate exposure times for HERCULES to achieve a S/N of 100 as a function of apparent V magnitude using fibre 1 or fibre 3. Times are estimates based upon HERCULES observations. The signal measurement was made at $\lambda \sim 5173$Å (near the centre of the detector for CCD position 2), and for spectra acquired at a low airmass.

include HD 206804, whose radial-velocity curves based upon published orbital parameters were presented in Fig. 4.20 on page 66. Measurable separation of the two spectra demands that the velocity difference of the components is no less than a fibre's possible velocity resolution for a given $v_{\rm equ} \sin i$. Inspection of Th-Ar spectra revealed that typical sharp emission lines had a *full-width at half-maximum* FWHM ~ 3.1 pixels for fibre 1 and FWHM ~ 1.8 pixels for fibre 3. Each pixel corresponds to $\sim 2.1\,{\rm km\,s^{-1}}$ in velocity space. If the stellar lines are assumed to be Doppler broadened by only $v_{\rm equ} \sin i = 2\,{\rm km\,s^{-1}}$ (a reasonable estimate for late-type stars; see Table 3.1 on page 21), these widths indicate that a velocity separation of about $13\,{\rm km\,s^{-1}}$ is required, in order clearly to resolve two lines whose FWHM is $\sim 7\,{\rm km\,s^{-1}}$. This figure is for just unblended spectra using fibre 1, and becomes about $8\,{\rm km\,s^{-1}}$ using fibre 3. Consequently, in general, programme stars with $m_{\rm v} = 6$ or fainter were observed using fibre 1 and stars brighter than $m_{\rm v} = 6$ were observed using fibre 3.

5.2.2 Observing statistics and schedule

The statistics of the three-year observing period are presented in Fig. 5.2 and include the 38 observing runs undertaken during 33 months. Of 1987 scheduled observing hours, 904 hours were unusable due to cloud, fog and/or strong winds, 248 hours were interrupted due to weather, and 835 hours or 42% were clear. It is notable, though, that nearly 150 of the clear hours occurred during only two observing months (the second and the second last), so that the typical fraction of clear hours in an observing run was somewhat less that 40%, as inspection of Fig. 5.2 will demonstrate. Instrumentation problems occasionally introduced further delays to the observing schedule.

A night's observing schedule was governed by the prevailing atmospheric conditions and the airmass path of each star on the programme list. Marginal atmospheric conditions necessitated a preference for brighter stars and those which utilised fibre 1 which allowed faster exposures than were possible with fibre 3. To assist with deciding the order of observations, an airmass plot

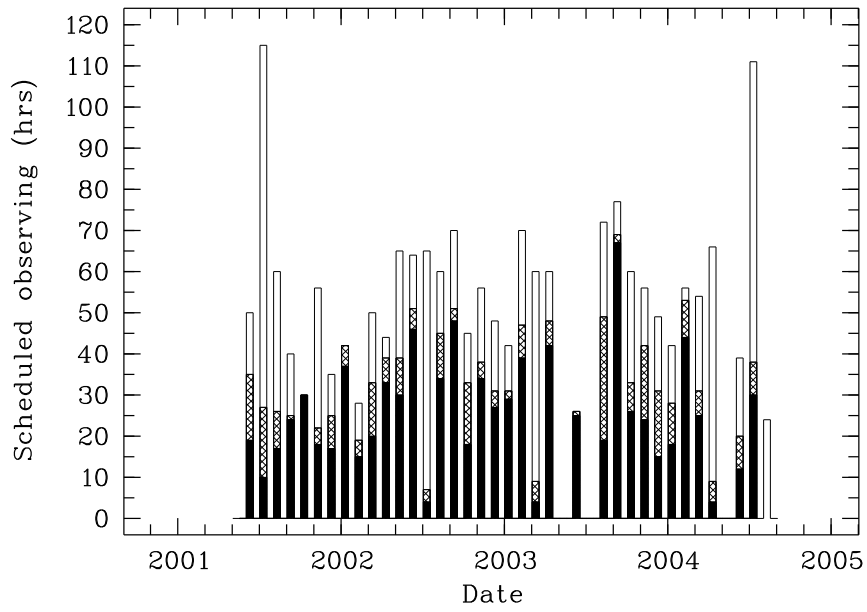

Figure 5.2: Distribution of the observing hours per month with the relative proportions of clear (open), partially interrupted (hatched) and unusable hours (solid) illustrated.

was prepared for each programme star throughout the year, as well as a table of star altitudes for each successive hour for each observing run.

Each observation entailed archiving spectra for the sequence 1. Th-Ar calibration lamp, (a thorium exposure), 2. the programme star, and 3. a second thorium. All three exposures were conducted after the star had been acquired and centred on the fibre for a maximum count rate, as soon after one another as practical and with no telescope movement other than that required for smooth guiding. Later in the observing programme, after it became obvious that accurate and precise fibre positioning was paramount to both short- and long-term precise radial-velocity measurements, careful adjustment to the telescope's sidereal rate for each observation was also conducted. Regardless of the acquired signal, the duration of any star's observation was generally limited to one hour. White-light exposures for each fibre used were also taken for the purposes of échelle order definition and flat-fielding.

5.3 Thorium - argon spectra: wavelength calibration

Stellar spectral features will be Doppler-shifted as a result of the motion of the source. With known rest wavelengths for spectral features, the Doppler effect [Eq. (2.3)] can be used to measure the radial velocities of stars and other astronomical objects. However, a stellar spectrum that is recorded on a CCD detector is dispersed across the pixels without a useful wavelength

scale, just the scale of the pixel position.

The wavelength calibration, known as a dispersion solution, expresses the correspondence of any pixel position x with its associated rest wavelength λ such that $x = f(\lambda)$. The rest wavelength is determined by recording a calibration spectrum across the pixel plane. However, a single dispersion solution cannot be associated with a given detector because of variations of factors that influence the light path at a given time. Some of these factors include temperature, atmospheric pressure, and the possibility of changes to the positions of the optical elements relative to each other. Variations of any of these will produce different optical paths taken by the light from the source to the detector over the course of an observing programme. Therefore, a given wavelength can, at different times, correspond to different pixel positions, necessitating different dispersion solutions which in turn mimic radial-velocity shifts (e.g. see Murdoch 1992).

Measuring precise radial velocities requires similarly precise dispersion solutions. Greater precision can be attained by using a large number of calibration lines, preferably spaced uniformly across the échelle orders. Any significant drift of the spectrum across the detector during an observation will mean that the dispersion solution derived at the time of the calibration spectrum will not match that of the star. This is the reason why two thorium spectra are recorded, the first thorium just before and the second just after any stellar observation. The flux-weighted time of the star's mid-exposure is chosen to make it more likely that the mean dispersion solution linearly interpolated to this time is consistent with the stellar spectrum[6].

So that the dispersion solution is more likely to be reproducible from observation to observation, exactly the same set of calibration lines should always be used[7]. Also, the method chosen to measure each calibration line's position must be as accurate and precise as possible.

The Hercules calibration lines are measured using a gaussian profile, as is recommended by Gulliver & Hill (1990). Another advantage of using this function, is that it matches the profile fitting methods of other parts of the reduction process, such as for the final velocity measurement (see § 5.7). Gulliver & Hill (1990) conducted an investigation to assess the relative and absolute accuracies of seven of the available techniques for fitting calibration lines. Various forms of gaussian, parabolic and centroid fits were studied. The relative accuracies, which are especially important for precise radial-velocity measurements, were tested by comparing the r.m.s. scatter in the observed and the calculated wavelengths of about 30 iron and argon lines in very high S/N spectra ($S/N \sim 1000$). Amongst their conclusions was that the best fits were obtained using an all-parameter-free gaussian, particularly if the instrument profile was asymmetric or

[6] A spectrograph designed to allow the simultaneous imaging of both the stellar spectrum and the calibration spectrum will remove the complication of the time difference, e.g. the HARPS spectrograph which uses a Th-Ar source (Queloz & Mayor et al. 2001). If the calibration source is an iodine cell, an added advantage is that the light paths of the starlight and the source are identical as well e.g. HIRES (Vogt et al. 1994).

[7] During the course of this observing programme, a long term drift of the spectrum across the CCD was found. These gradual changes made it necessary to modify the table of calibration lines used so that the same lines were available for all spectra acquired for a given star. See § 5.10 for further comments.

unknown. The poorest fits were found for a least-squares parabolic function. We have come to an analogous conclusion, using a different strategy, for the fitting function employed to measure the peak of the cross-correlation function (see § 5.7.2).

As noted earlier, the calibration source for this study was a Th-Ar lamp. Th-Ar lamps are an excellent choice for a number of reasons. They produce thousands of sharp emission lines across the visible spectrum, whose wavelengths have been measured with high accuracy and precision (e.g. Norlén 1973; Minnhagen 1973; Palmer & Englemann 1983; DeCuyper & Hensberge 1998). The lamps are also relatively inexpensive and generally reliable. The principal emission lines are of neutral and singly ionized thorium and argon (Th I, Th II, Ar I and Ar II), each of which has a relative intensity that varies depending upon the lamp current/temperature and the respective excitation and ionization energies involved. The appearance of the spectrum also depends on the lamp design (i.e. the manufacturer), the spectral resolution, and the lamp's age.

Given the large number of lines produced by a Th-Ar lamp, it may seem a straightforward matter to identify a very large number of lines so that an accurate and precise dispersion solution could be easily obtained. However, a large fraction of the lines are blended with one another. Furthermore, the degree of contribution made to a blended line is likely to vary depending on the lamp circumstances at the time the spectrum is recorded, which can result in changes to the relative intensities of the lines present. Therefore, any set of stable and reliable calibration lines must avoid those which arise from such blends. Another difficulty that presents itself is the wide range of line intensities that occur for a given lamp current and exposure time. The best an observer can do, constrained by the recommended operating current of the Th-Ar lamp, is to choose an exposure duration that minimises the number of unusable lines that result from saturation or underexposure.

5.3.1 Constructing a Th-Ar calibration table

The Hercules Reduction Software Package[8] (HRSP, Skuljan 2004) included a preliminary table of 284 Th-Ar lines corresponding to this study's detector position. These were not intended to be the final set of calibration lines but were provided to allow HRSP to be available to observers as soon as possible. The possibility of determining a more complete table of suitable calibration lines (ones that are unblended, stable and have accurately known rest wavelengths; Gulliver & Hill 1990) was therefore investigated.

The line selection process was guided in two ways. First, by acquiring the published rest wavelengths of as many thorium and argon lines as possible so that the relative intensities and possible blends could be identified. To make this aspect of the task easier and more certain, this information, acquired from several sources, was combined into a Th-Ar atlas specific to the

[8]Many of the details of HRSP will be described shortly as it was assessed and used for the reduction of all spectra obtained during this study (see § 5.5 beginning on page 84).

HERCULES instrument[9].

The second part of the line selection process was to assess as many lines as possible based on their isolation from other relatively bright lines. The important aspects of this part of the investigation were to ascertain if any relationships existed between the line intensity or species and the stability of the line position, line width, and residual to the dispersion solution.

HRSP and MIDAS[10] were used to select a preliminary extended list of nearly 600 thorium and argon lines using a single HERCULES Th-Ar spectrum. Each candidate line had its position and width estimated by the gaussian fitting algorithm of MIDAS. The line position was then incorporated into HRSP, which could identify and measure each line in subsequent spectra. Several series of 30 or so Th-Ar spectra was analysed so that a statistical assessment of the properties of each line could be determined. Each series of spectra was obtained during a single observing session. Suitable calibration lines were considered to be those that had the following desirable properties:

1. The line should be isolated from any other line that might corrupt its position. In particular, a suitable line should not be blended with any other line of a different species or ionization level, particularly if the blending line is relatively bright. The likelihood of significant blending was relatively easily assessed using the HERCULES Thorium - Argon Atlas.

2. The line's centre should have a low scatter about its mean pixel position throughout the observing session.

3. The line's FWHM should have a low scatter about its mean value.

4. The line's dispersion solution residual should also have a low scatter.

Examples of the results of this analysis are provided in the following three pairs of figures.

First, Fig. 5.3 illustrates a well-defined relationship between the line intensity and the scatter of the line's central position and its FWHM. Th-Ar lines produced by HERCULES that have a central intensity less than about 10^4 ADU have a position and FWHM that are much more variable, a finding in part presumably a result of the relative increase in photon noise for the faintest lines. The identification of the four species in Fig. 5.3(a) demonstrates that they behave similarly with regards position and width stability. The abrupt high intensity tail-upturn in Fig. 5.3(b) is a reminder that the maximum peak central intensity of an unsaturated line is close to 3×10^5 ADU. It is somewhat surprising that saturated lines do not show any significant loss of position stability and appear to have a limiting FWHM scatter of about 0.01 pixel, at least

[9]The atlas is divided into four volumes, one for each of the current detector positions. The introductory pages and a sample of atlas tables and spectral maps are included in Appendix E.

[10]MIDAS is the acronym for Munich Image Data Analysis System of the European Southern Observatory.

for this particular sample.

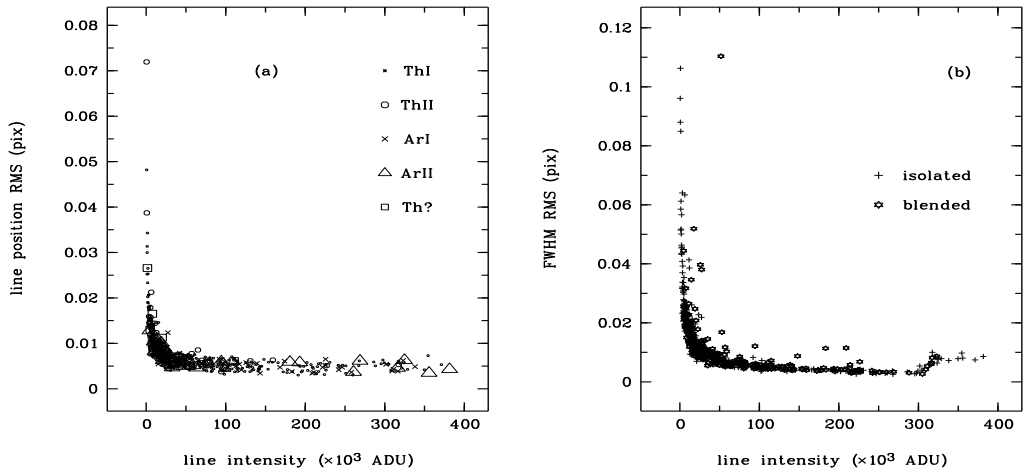

Figure 5.3: Statistics for 586 potential calibration lines based upon 30 Th-Ar spectra obtained on 2002 May 31. (a) The scatter of the measured line position, and (b) the scatter of the FWHM, as a function of the intensity of the line centre. The species of each line is identified. Lines labelled 'Th?' are thorium lines whose level of ionization is uncertain (Palmer & Englemann 1983).

It might be considered possible that the instability of a line's position and width may increase as the FWHM increases, since broader lines of a given intensity might be less precisely measured. Fig. 5.4 illustrates that this is not the case. So long as the line is brighter than about 10^4 ADU, the FWHM can vary between 2.8 and 3.8 pixels and not display any correlation with the stability of the line position or its width measurement. Instead, as Fig. 5.3(b) in particular illustrates, lines of a given intensity that are blends are apparently only more likely to have a variable width. This is an anticipated consequence of line-blending — such lines are more likely to have a larger FWHM scatter because of the variable influence of the lines involved, although this effect only arises occasionally, presumably when the blended lines have similar intensities.

Before some of the statistical properties of Th-Ar lines with respect to the dispersion solution are described, it is worthwhile making the following comment. As noted by Skuljan (1999), since there is a correlation between the positions of spectral lines in the different échelle orders, rather than treat each order separately, it makes better sense to derive a dispersion solution after combining all the orders together. This is made possible by the physical properties of the dispersion process, since the grating equation $n\lambda = d\,(\sin\alpha + \sin\beta)$ states that for any given groove spacing, d, incidence angle, α, and diffraction angle β, $n\lambda$ is a constant. Therefore, the

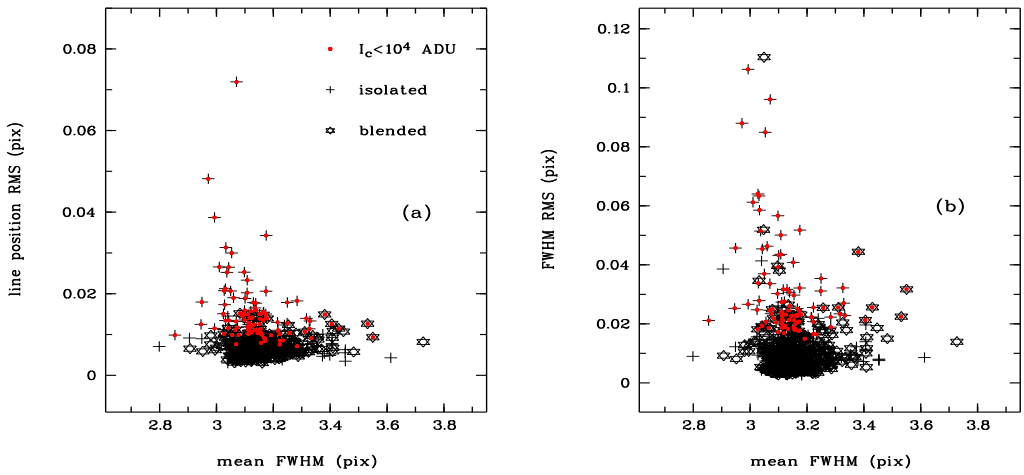

Figure 5.4: Statistics for 586 lines based upon 30 Th-Ar spectra obtained on 2002 May 31. (a) The scatter of the measured line position, and (b) the scatter of the FWHM, as a function of the line's mean FWHM.

HRSP dispersion solutions are derived with the form $x = f(n, \lambda)$. The dispersion solutions are computed by a two-dimensional polynomial regression, of degree three along the orders and degree four across the orders.

Fig. 5.5 continues to emphasise the importance of the line intensity with regards identifying suitable calibration lines. Fig. 5.5(a) illustrates that lines that have a central intensity less than about 10^4 ADU also have significantly more scatter in their dispersion solution residual. This is not surprising, as a faint line that has a highly variable position relative to its mean position (with some contribution to this instability owing to photon noise), can be expected to be similarly variable in its distance from the dispersion solution. Finally, the typical dispersion solution residual for a line, as illustrated in Fig. 5.5(b), sometimes is greater than would be expected from the random error of the measurement of the line position, in particular for some rather strong lines whose positions are very stable [as demonstrated in Fig. 5.3(a)]. The cause of these discrepant line positions did not have an obvious cause, but may have been a result of minor line blends or unrecognizable inaccuracies in the rest wavelengths. Since the cause was not determined, and only relatively few lines were affected in this way, it was decided to remove them from the line table.

Guided by these results, the original list of nearly six hundred candidate lines was reduced to a final calibration table that included 322 thorium and argon lines, only 38 more lines than the original preliminary HRSP calibration table. Lines that had a tendency to have large residuals (relative to the anticipated measurement error of a line's position), or were blended with

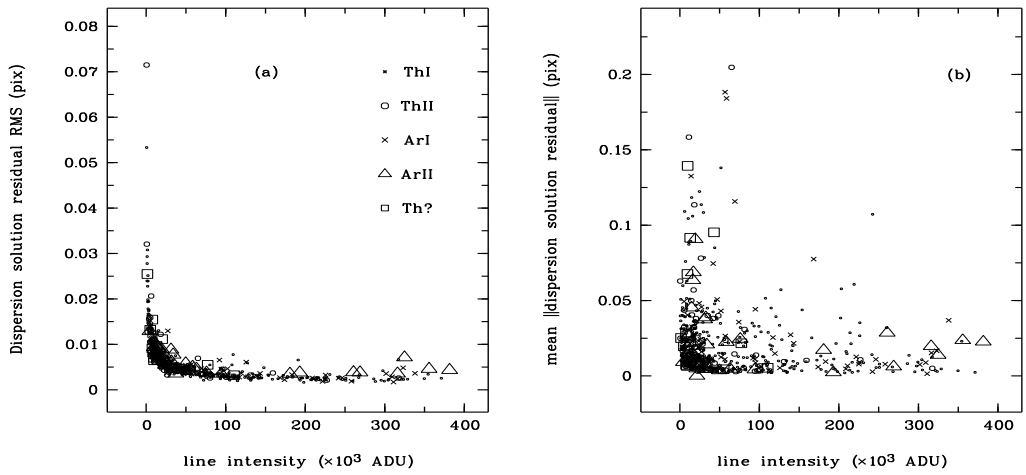

Figure 5.5: Statistics for 586 lines based upon 30 Th-Ar spectra obtained on 2002 May 31. (a) The scatter of the dispersion-solution residual, and (b) the mean of the absolute value of the dispersion solution residual as a function of the intensity of the line centre.

other lines of a different species or ionization level were discarded. Exclusion based upon a line's intensity was somewhat more flexible, since the mean intensity of any Th-Ar exposure was influenced by the lamp current and the duration of the thorium exposure. It was therefore worthwhile to try to select an optimum combination that would expose the largest number of lines suitably, raising the brightness of fainter lines above the $\sim 10^4$ ADU threshold for stability, without saturating a similar number of bright lines.

A reference spectrum was selected that reflected these demands and subsequent thorium exposures were compared to it from night to night. After selecting ten or so lines of each species (Th I, Th II, Ar I and Ar II), a comparison was made of each line's central intensity (as measured by a MIDAS gaussian profile) with the respective line's intensity in the reference spectrum. It was hoped that by monitoring the line strengths throughout the study, adjustments could be made as necessary to the exposure duration so that the line strengths could be kept much the same. As the majority ($\sim$ 85%) of the dispersion-solution calibration lines were produced by thorium species, the exposure duration was always adjusted so that the thorium line intensities were closest to those of the reference spectrum.

Unfortunately, as Fig. 5.6 demonstrates, occasionally the Th-Ar lamp produced spectra that would not allow this goal to be achieved. Whilst the relative intensity of the neutral and ionized lines produced by each element (Th or Ar) tended to remain much the same, episodes arose when the thorium lines became considerably fainter relative to the argon lines. Presumably this occurred when the thorium metal was depleted, for instance when the lamp's useful life was

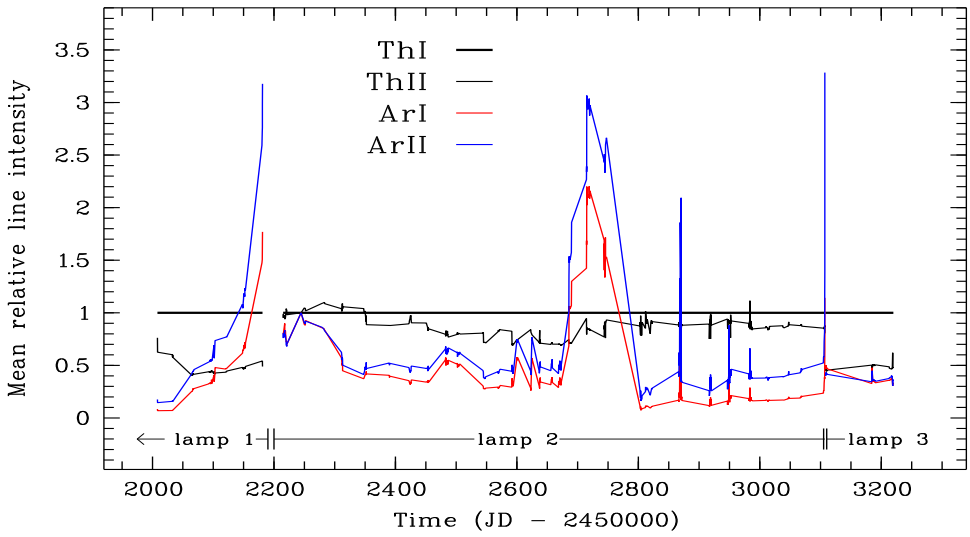

Figure 5.6: The mean intensity of the four Th–Ar species of lines relative to the mean Th I intensity (based on a small set of lines of each species), as a function of time. The intervals of time when the three Th–Ar lamps were used during this study are indicated.

coming to an end or as a result of uneven thorium metal deposition on the lamp cathode[11]. This was an unfortunate situation as maintaining the brightness of the much more prevalent thorium lines led to saturation of many of the bright and therefore positionally-stable argon lines.

5.4 Identifying Th-Ar species using emission line statistics

An interesting result has been found when the standard deviation of each *unblended* and *unsaturated* emission line's intensity, $\sigma_{\rm I}$, is compared to its mean intensity I. Once again, a series of Th-Ar spectra acquired during a single observing session have been used. Two typical examples are illustrated in Fig. 5.7. Each species is confined to a narrow locus of the graph plane which can be described with an equation of the form

$$\frac{\sigma_{\rm I}}{I^s} = \text{constant} = 10^{\,h}\,,$$

where s is the slope and h is the y-intercept of each log-log locus.

The relative positions of the loci of the four species depend upon the particular series of Th-Ar spectra analysed. The theoretical basis for this outcome has not been identified. However, it appears that variations of lamp temperature has some influence. As the Th-Ar lamp is

[11] At about Time = 2700 (Fig. 5.6) the Th-Ar lamp produced emission lines that had relatively faint thorium lines. Just as it was becoming more likely that the lamp would be replaced, it recovered and the relative intensity of the lines returned to close to their previous levels. A similar short-lived episode occurred at Time = 2870.

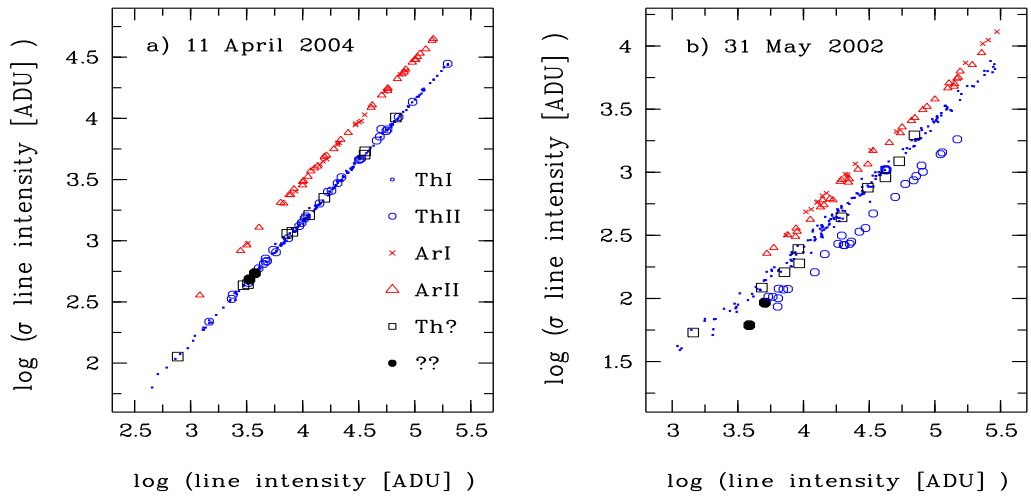

Figure 5.7: The standard deviation of an emission line's intensity, σ_I, as a function of its mean intensity I, based upon a series of 25-30 Th-Ar spectra acquired during a single observing session. The results for two observing sessions are illustrated. The apparently mis-identified Th II line has a bolder symbol in the figure on the right.

operating in a non-LTE environment, the explanation is expected to be complex.

Some of the statistical outcomes can lead to some or all of the loci being concurrent or nearly so. Fig. 5.7(a) illustrates particularly tight loci for all of the lines analysed. Both ionization species of argon have concurrent loci, as do the separately placed thorium loci, the latter being slightly less variable for a given mean intensity — for the night analysed. Other series of spectra, obtained from another observing session, might show the opposite, i.e. the argon lines having less variability for a given intensity. The night of 2004 April 11 was unusual in that this was the night that lamp 2 became highly unstable and replaced later that day (see Fig. 5.6, Time = 3107). Using spectra from this series, it appears that any line whose species is unknown (but expected to be either an argon or a thorium species) can have its parent atom identified using this approach[12]. In fact, there are two such lines, given the label '??'. Both fall squarely on the combined thorium locus and can be confidently claimed not to be emitted by argon atoms and quite reasonably identified as thorium lines.

The separation of the loci for Th I and Th II lines in Fig. 5.7(b) allows the species identification process to be taken to the next level. Emission lines can, with some confidence, have

[12] At least, it is possible to be confident which species i.e. Th or Ar, is *not* the likely emitter. Species other than Th and Ar are possible, though rare, in a Th-Ar lamp's emission as a result of trace quantities of contaminants; for example, thorium oxide and atomic hydrogen and oxygen, which if present, are possibly due to water entering the lamp before it is finally sealed (Palmer & Englemann 1983).

their ionization level confirmed or brought into question, as one Th II line demonstrates. The line having $\lambda_{\rm vac} = 4948.0443$ has previously been identified as being produced by singly-ionized thorium atoms (Th II - Palmer & Englemann 1983), yet in Fig. 5.7(b), its position is unequivocally on the Th I locus. This is repeated on all other suitable plots created using these methods. If the ionization level of a thorium line was previously unknown (those labelled Th?), it can be surmised (see Table 5.3 on the current page).

				Species	
$\log I$	Échelle order	$\lambda_{\rm vac}$ (Å)	$\lambda_{\rm air}$ (Å)	Old label	New label
4.63	115	4948.0443	4946.6637	Th II	Th I
3.59	99	5758.6992	5757.1025	??	Th II
3.71	95	5985.0391	5983.3817	??	Th II
3.16	87	6537.9498	6536.1441	Th?	Th I
3.68	94	6072.0219	6070.3412	Th?	Th I
3.85	114	4988.9497	4987.5582	Th?	Th I
3.96	121	4699.5396	4698.2248	Th?	Th I
3.97	109	5205.2970	5203.8479	Th?	Th I
4.29	93	6099.8086	6098.1205	Th?	Th I
4.49	117	4854.2242	4852.8685	Th?	Th I
4.62	93	6123.1019	6121.4075	Th?	Th I
4.73	93	6109.2243	6107.5337	Th?	Th I
4.84	125	4547.1901	4545.9156	Th?	Th I

Table 5.3: The surmised species-type and ionization level of 13 Th-Ar lamp emission lines, using their plotted positions on Fig. 5.7(b). When a thorium line's ionization level was uncertain, Palmer & Englemann (1983) left the ion identification blank (≡ Th? here).

5.5 Reduction of HERCULES spectra

The HERCULES Reduction Software Package (HRSP) was developed by J. Skuljan (2004) with the first near-complete version available during the early part of 2001. The algorithms are written in C and the entire reduction process can be applied to standard FITS image files. All parameters that control the reduction are specified in various additional configuration files. These are written in ASCII format and can be edited by the user. As well as using keywords provided with each FITS image, HRSP creates additional keywords or descriptors that are necessary for the reduction process. The keywords and descriptors can also be edited so that HRSP proceeds with the correct understanding of each spectrum's history, e.g. star observed, fibre used, detector position and so on.

The reduction of each observation set (stellar, thorium and white lamp spectra) includes the following steps so that a final image file is created which is suitable for a radial-velocity measurement by digital cross-correlation:

1. Each original two-dimensional spectrum is first prepared for reduction by rotating and flipping the coordinate axes of each image so that the échelle orders appear horizontal and the wavelengths increase from left to right. The median bias (derived from $\sim 10^5$ pixels making-up the bias strip accompanying each spectrum) is subtracted.

2. All bad pixels are identified based on information in one of the HRSP configuration files and a new value for each is estimated by interpolating between the neighbouring pixels. HRSP treats these pixel values with caution in subsequent reduction steps.

3. One of the thorium images is used to locate its position relative to the HERCULES image plane by using the Th–Ar calibration line table. A set of polynomial-regression coefficients is computed to allow HRSP to be able to transform each image between the pixel positions and the absolute coordinate frame used by HRSP.

4. A gaussian is fitted to each order cross-profile of the white lamp spectrum to determine the position and width of each order. Combined with the table of calibration line data, which includes the order number of each line, and the set of coordinate-transformation regression coefficients, the information obtained from the white lamp allows each échelle order, and therefore the inter-order space, to be defined on each two-dimensional image.

5. The background light in the inter-order space of the stellar image is estimated from a filtered spectrum using a two-dimensional, high-order (typically seventh or eighth) polynomial regression. The filtering box is constructed around each pixel in the inter-order space. This is governed by specified filter parameters, such as the box size and a threshold argument. If the central pixel value differs from the median for the box by more than the threshold allows, the central pixel value is replaced with the median. The background light is subtracted so that the order profiles have a zero base level.

6. Cosmic rays in the stellar image are removed using a modified median filter. This filter uses a normalized extraction slit profile extending above and below the central order position, and a low-degree polynomial to establish which pixels are contaminated with cosmic rays.

7. Using the échelle order definition information obtained from the white lamp image, individual one-dimensional spectra are extracted from the two-dimensional stellar, thorium and white lamp spectra.

8. A flat-field spectrum is created from the extracted white lamp spectrum. This defines the global curvature of the continuum level which is principally a result of the blaze function of the spectrograph.

9. The flat-field spectrum is used to 'straighten' the extracted stellar and thorium spectra so as to minimize possible variations of response from pixel-to-pixel. This step is also important for a stellar spectrum as the subsequent velocity measurement by cross-correlation will lead to a systematic error if substantial curvature in the continuum is retained (Hilditch 2001).

10. A dispersion solution is determined for each thorium spectrum associated with a stellar spectrum (usually there will be two thoriums), using the table of calibration lines described in § 5.3. The r.m.s. of the fit is typically ~ 0.03 pixel. A mean dispersion solution for the flux-weighted mid-time of the stellar spectrum is calculated using linear interpolation between the mid-times of the thorium exposures.

11. The stellar spectrum is normalized so that the maximum pixel value in any order is equal to 1. This maximum corresponds to the continuum. Normalization balances the flux distribution so that the relative weights of different spectral regions are independent of factors such as the spectrograph's wavelength response.

12. The barycentric radial-velocity correction and Julian Day correction are computed for each stellar image, using the flux-weighted mid-exposure time. Solar spectra are treated differently to other stars as the former are acquired from the day-time sky, and certainly not in the direction of the Sun. HRSP uses its own tables of the positions and velocities of the Earth, precomputed using the DE200/LE200 ephemerides provided by the Jet Propulsion Laboratory.

13. Finally, the normalized one-dimensional extracted stellar spectrum is rebinned, order by order, from pixel space to wavelength space using the dispersion solution. This is achieved using an interpolating spline function. Two images are produced, one having a linear wavelength scale (in angströms), and the second image having a natural logarithmic scale. The latter image provides the means to measure the radial velocity of the star relative to a template spectrum using cross-correlation.

5.6 Cross-correlation of stellar spectra

The radial velocity of a star might be measured by estimating the Doppler-shift of a single spectral line. This approach could not be expected to be very accurate as it is well known from studies conducted in this way e.g. of pulsating variables, that different lines display different velocities — line level effects — in terms of both magnitude and rate of change. This is understood to be due to the fact that different lines are created at different depths in the stellar photosphere and therefore are subject to different temperatures, velocity gradients and so on (see e.g. Butler 1993).

A preferable alternative is to consider a large number of lines and measure the average velocity. Measuring individual lines in this way is complicated by the general lack of isolated lines

in many spectra, in particular of SB2 systems. A powerful variation of this approach is provided by the mathematical principles of convolution and the related methods of cross-correlation.

The cross-correlation function (CCF) is at the heart of the radial velocity measurements of this thesis. Such functions may be continuous or discrete. The continuous CCF can be defined as

$$c_{\rm c}(\Delta x) = t(\Delta x) \otimes p(\Delta x) = \int_{-\infty}^{\infty} t(x)p(x - \Delta x)\,{\rm d}x\,. \tag{5.1}$$

The discrete CCF is defined to give a function which is as close as possible to a continuous CCF of the data, if it existed:

$$c_{\rm d}(\Delta x) = \sum_{x=1}^{N} t(x)p(x - \Delta x)\,. \tag{5.2}$$

Δx is called the lag of $c_{\rm c}(\Delta x)$ and $c_{\rm d}(\Delta x)$.

The discrete CCF is more appropriate for spectra recorded with a CCD because of the pixel format. The functions t and p can be thought of as representing a template spectrum and a programme star's spectrum respectively. New values for $c_{\rm d}(\Delta x)$ are generated for each shift Δx that increases or decreases the correlation between t and p. $c_{\rm d}(\Delta x)$ is most sensitive to Δx when the spectra t and p are identical but also have a complex character that is not regular or periodic (Tonry & Davis 1979). Spectra of single stars are therefore often ideal for cross-correlation. The template spectrum should therefore be of the same star, or of a star whose spectrum is as similar as possible to the component being measured, so as to avoid any unnecessary spectral mismatch, which is known to affect the shape of the CCF (Hill 1993) and the accuracy of the velocities measured (Griffin et al. 2000). When these principles are followed, $c_{\rm d}(\Delta x)$ will be an extreme (a trough or as for this thesis a peak, depending upon the orientation of the lines) when the programme star's spectrum is shifted by Δx, since then the intrinsic shift of p relative to t will be cancelled. Thus, the velocity determined using the cross-correlation function will always be on a relative velocity scale whose zero-point is that of the template spectrum t, since it is assumed that no scale errors or zero-point shifts are introduced by the cross-correlation technique (Popper 1993).

5.7 The velocity measurement

Of course, it is only sensible to calculate $c_{\rm d}(\Delta x)$ if t and p have the same uniform scale. However, inspection of the classical Doppler-shift expression (Eq. 2.3 on page 11) reveals that the wavelength shift $\Delta\lambda$ is a function of both the radial velocity V *and* the rest wavelength λ_0 of a given spectral line. This is not a satisfactory situation for examining the correlation of two spectra since a given Doppler shift due to a radial velocity V will shift different parts of the spectrum

by differing amounts. This complication is removed by transforming the linear wavelength scale into a logarithmic one (Tonry & Davis 1979), since Eq. (2.3) then becomes

$$\Delta \ln \lambda = \ln \lambda - \ln \lambda_0 = \ln \left(1 + \frac{V}{\mathrm{c}} \right) . \tag{5.3}$$

Using this uniform logarithmic wavelength scale, the lag of the CCF is $\Delta x = \Delta \ln \lambda = \ln(1 + V/\mathrm{c}) =$ constant, for a given velocity V.

A fast-Fourier-transform algorithm (Press et al. 1994) is typically used to evaluate $c_\mathrm{d}(\Delta x) = c_\mathrm{d}(\Delta \ln \lambda)$. These algorithms require the spectra to be as free as possible of sharp discontinuities, as always exist at both ends of each échelle order. Therefore, the following steps are taken next. Each stellar spectrum is first trimmed using the $n \times \lambda$ limits found in one of the HRSP configuration files. These limits define a particular wavelength window for an order. The arithmetic mean of the signal in all pixels is then subtracted from each datapoint, so that the resulting spectrum has a zero mean. The order ends are smoothed with a flat-topped cosine function. When applied to each order, the cosine window causes the ends to taper gradually to zero. These modifications to the échelle orders are in accordance with standard procedures (Brault & White 1971; Simkin 1974). Using the default argument for the cosine window in HRSP (64 bins), only 6.25% of the bins at each end of the HERCULES spectra are affected.

The cross-correlation can now be executed and a measure made of the extreme value of the CCF peak. This must be performed at least twice for the proper determination of each velocity. The reason for this is that, whilst the barycentric velocity of the template is a constant, the velocities of all of the other spectra relative to the template are unlikely to be so in a strict sense. The spectral features available in the template's wavelength window (as determined by the $n \times \lambda$ limits of HRSP) is the spectral map for that series of spectra. The first cross-correlation estimates the velocity of each spectrum relative to the template, assuming the velocity is zero. Doppler-shifting of the programme star's spectrum relative to the template will cause the spectral features within the programme star's wavelength window to differ from the required spectral map of the template. Using the initial relative velocity estimate, the reduction software adjusts the programme star's $n \times \lambda$ limits so that the same spectral features are included for both images in the cross-correlation. A warning is given if this is not possible and revised $n \times \lambda$ limits at either order end are prompted. The final velocity measurement makes allowance for any velocity shift corresponding to an $n \times \lambda$-adjustment. For spectra such as those belonging to SB2 systems, the situation is considerably more complex since these will ideally require two templates with two different Doppler-shifts for each cross-correlation.

5.7.1 Matching the spectral maps of the cross-correlated spectra

The consequences of not making allowance for the relative velocity of the programme spectrum to the template is illustrated in Fig. 5.8, which is a result typical of any other star. A total of 130 spectra of the SB1 HD 205478 acquired during this study have been used. The full amplitude

of the radial-velocity curve is about $14\,\mathrm{km\,s^{-1}}$ (see Fig. 7.7 on page 142 for the radial-velocity curve of HD 205478). Two sets of relative velocities were determined for HD 205478. The first set of velocities was determined *without* making allowance for the changing orbital velocity of the programme spectrum relative to the template. Cross-correlation was therefore carried out *without* using identical spectral features for the template and the programme image. The $n \times \lambda$ limits matched, but due to the relative Doppler-shift present, the spectral features included did not. As the velocity of the image relative to the template increased, more and more of each order was unmatched in the creation of the respective CCF peak and the related velocity measurement.

A second set of velocities was determined *with* allowance for the changing velocity, adjusting the wavelength window of the programme spectrum precisely to the relative Doppler-shift present. This adjustment was carried out internally by HRSP, but only after this anomaly in the measurement process was identified, and some suitable modifications to HRSP implemented.

The difference of the two velocities for each observation was then determined. The results for three orders are illustrated in Fig. 5.8(a). As the velocity of each image relative to the template increased, the systematic error that arose if the entire spectral map of the template was not included, increased in a linear fashion, in proportion to the relative velocity V. This is understandable, as with increasing V, there is a corresponding increase to the mismatch of the utilized spectral window.

The slope of each relative-velocity vs. systematic-error line has been determined by linear regression and the results of this part of the analysis are illustrated in Fig. 5.8(b). The behaviour differs from order to order. Inspection of the spectral features of each order for a spectrum of HD 205478 suggests that the largest systematic errors occur for those orders that have broad strong spectral features close to the order ends, as do, for instance orders $n = 110$ and 116. Orders that include sharp lines, no matter how numerous, e.g. as in the bluest orders, or have broad lines only in their central segments, e.g. Hβ in $n = 117$, are less sensitive to the mismatch of the template and programme images' spectral windows.

By carrying out the complete analysis twice, using two templates t_1 and t_2, obtained at the radial-velocity quadratures, both sides of the wavelength window have been assessed. The behaviour of the systematic errors (demonstrated by the scatter and slope of each order's difference velocities) is very similar regardless of which end of the order is analysed (using t_1 or t_2). This is to be expected as the velocity measured for each order must be dominated by the bulk of the spectral information between the order ends that is common to all images.

The velocity difference that occurs for order $n = 109$ of the HD 205478 spectra corresponds to a systematic error of about $1\,\mathrm{m\,s^{-1}}$ for each kilometre per second of relative velocity not allowed for in the cross-correlation process. For order 109, which has a total wavelength range of about 37 Å, $14\,\mathrm{km\,s^{-1}}$ corresponds to about 6.5 pixels or only $6.5/1024 \times 37\text{Å} \simeq 0.23$ Å. Therefore, for orders such as $n = 109$, it only requires a relatively small change to the wavelength window to cause a significant shift to the velocity measured. Additional comments relating to this matter

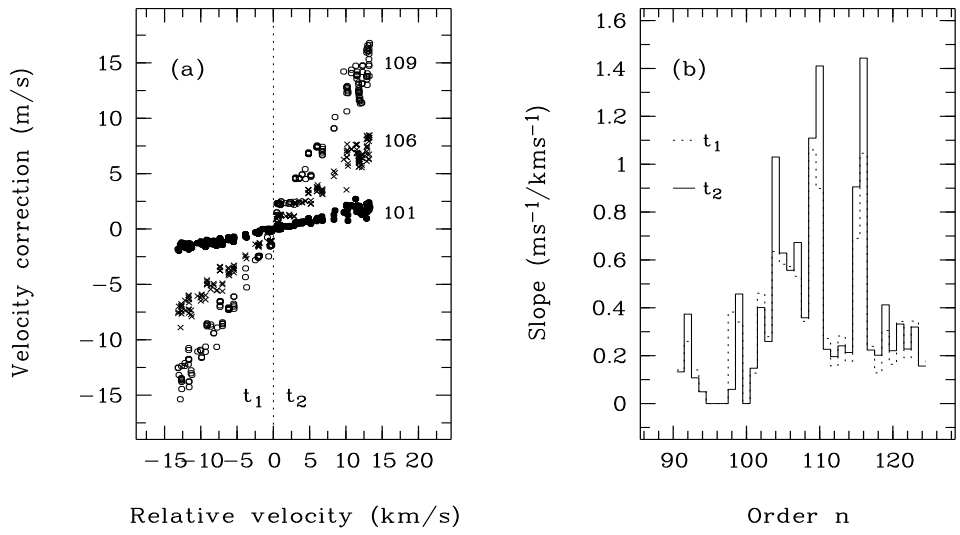

Figure 5.8: (a) The systematic errors that arise when the velocities of a series of spectra relative to a template, t_1 or t_2, are not taken into consideration in the cross-correlation process. The results for three typical orders are illustrated. The two templates were chosen close to the radial-velocity quadratures. The radial-velocity curve has a full-amplitude of about $14\,\mathrm{km\,s^{-1}}$. The central vertical line separates the results obtained using the two templates. (b) The slopes of the correction lines corresponding to each order. This example has used a series of 130 spectra of the SB1 HD 205478.

are included in § 5.10. Clearly, as the relative velocity between the template and programme image increases, the potential systematic error increases also. For a star like HD 205478, and if the image velocities are each determined as weighted means (see § 6.3 on page 110), the correction to the velocity for each observation is about $0.3\,\mathrm{m\,s^{-1}}/\,\mathrm{km\,s^{-1}}$ of relative velocity. This is a significant error if large relative velocities are measured, e.g. as with very close binary systems, and precise velocities are required.

5.7.2 Choosing the function to measure the CCF peak's maximum

Since the data is discrete rather than continuous, the maximum found for $c_\mathrm{d}(\Delta \ln \lambda)$ is unlikely to be the best estimate of $\Delta \ln \lambda$ and hence of $V = c(\mathrm{e}^{\Delta \ln \lambda} - 1)$. Hence, the next task is to decide which of the many functions available will best measure the CCF peak. Amongst the functions described in the literature for this purpose are lorentzian and gaussian profiles, and these convolved with rotational profiles (Hilditch 2001), synthetic profiles from a light-curve code and digital profiles using the CCFs of comparison stars (Hill 1993), as well as parabolic fits to the three CCF peak bins (e.g. Gullberg & Lindegren 2002).

HRSP provides a choice of algorithms for fitting the CCF peak. These include spline inter-

polation, parabolic interpolation and a gaussian profile determined by a least-squares fit. These algorithms use different portions of the CCF. The spline is computed using all available points of the CCF. The parabolic fit only uses the three uppermost bins nearest the CCF maximum, as described by Gullberg & Lindegren (2002). The gaussian fit is measured using a selected number of bins on either side of the discrete CCF maximum. This is the fitting window for the gaussian profile.

Since the gaussian fit could be adjusted according to the fitting window, it was first necessary to assess if a particular window width was preferable, so that the best of these could be used to compare gaussian fitting with the spline and parabolic methods.

Several single stars were selected that had at least 50 observations acquired reasonably uniformly over two years or more of this study. A similar series of daytime sky spectra were also included in this analysis. The latter were included so that any variation in the centering of the image on the fibre entrance could be safely neglected. The influence of the window width of the gaussian fit was assessed by measuring the velocity scatter for each order of each series of stellar spectra using several fitting-window widths. The sizes that are suitable for a given spectral type corresponds to the sharpness of the spectral features. Spectra with broader lines require a wider fitting window so that the gaussian fit can be achieved successfully. For a late-type star such as the Sun, the smallest fitting windows can be used.

Fig. 5.9 illustrates the daytime sky result for this analysis. The smallest velocity scatter was obtained when $\pm$ 3 bins were used, as shown. This strategy was applied to all of the series of spectra analysed in detail for this project. For instance, the fitting window that provided velocities that corresponded to the smallest r.m.s. to the fit, and the most precise orbital elements, for a spectroscopic orbital solution was the one employed.

The relative merit of the spline, parabola and gaussian fit (with an optimal fitting window) was next evaluated, again using several stars that each had a series of 50 or more observations available. For each series, two relative velocities, RV_1 and RV_2 , were measured based on two templates, t_1 and t_2 , chosen from the star's sample of spectra. The difference of these velocities, $\Delta RV = RV_1 - RV_2$, was measured for each spectrum. Since ΔRV is the difference of two velocity measures of the same observation, spectra belonging to SB1 systems could also be included. The resulting ΔRV values for the three fitting functions were then compared.

The theoretical expectation is that the velocity difference, ΔRV, would be a constant, equal to the relative velocity of the two templates, and independent of the fitting algorithm applied. Instead, a number of somewhat surprising results presented themselves that made it impossible to choose anything but the gaussian fitting algorithm for the measurement of radial velocities in this study. Two results for each of the SB1 HD 23817 and for the daytime sky are presented respectively in Fig. 5.10 and Fig. 5.11.

The examples chosen portray the extreme differences that can result when the three CCF

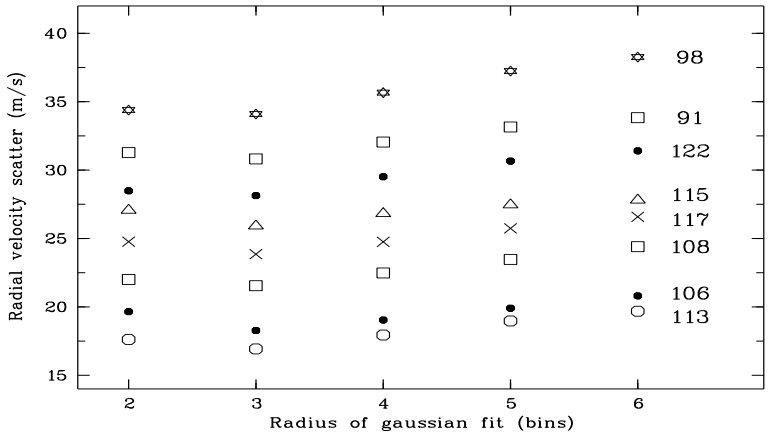

Figure 5.9: The radial-velocity scatter as a function of the number of bins on either side of the CCF maximum used for the gaussian fit. A series of 65 sky spectra acquired over approximately two years were analysed. The results computed for several representative orders are labelled.

peak fitting methods are compared using templates taken on different nights. However, it is important to realise that most other template choices produce plots that tell exactly the same story — if two templates are separated by a moderate time-span, it is likely that only the gaussian profile will provide an acceptable scatter for the velocity differences, ΔRV. The less chaotic scatter of ΔRV values for the series of sky spectra is an uncommon result, but is included to demonstrate the variety of possible outcomes.

These distributions for ΔRV cannot be due to such reduction steps as inclusion of the barycentric correction as the three fitting algorithms use the barycentric correction identically. Presumably, the underlying feature of these patterns is the changing shapes of the recorded spectra, possibly, in part as a result of changes to the spectrograph's instrument profile, as will be described shortly.

These four plots can be summarised as follows:

1. When the two template spectra are taken on different nights, ΔRV is more or less equal when the CCF peaks are measured with a gaussian profile. However, they can vary considerably when either the parabolic or the spline fitting algorithms are used. The scatter produced by the parabolic fit is approximately twice as great as that found for the spline algorithm.

2. When the two template spectra are taken on the same night, the scatter is low, regardless of the fitting method utilised. The lowest scatter is still provided by fitting a gaussian profile to the CCF peaks.

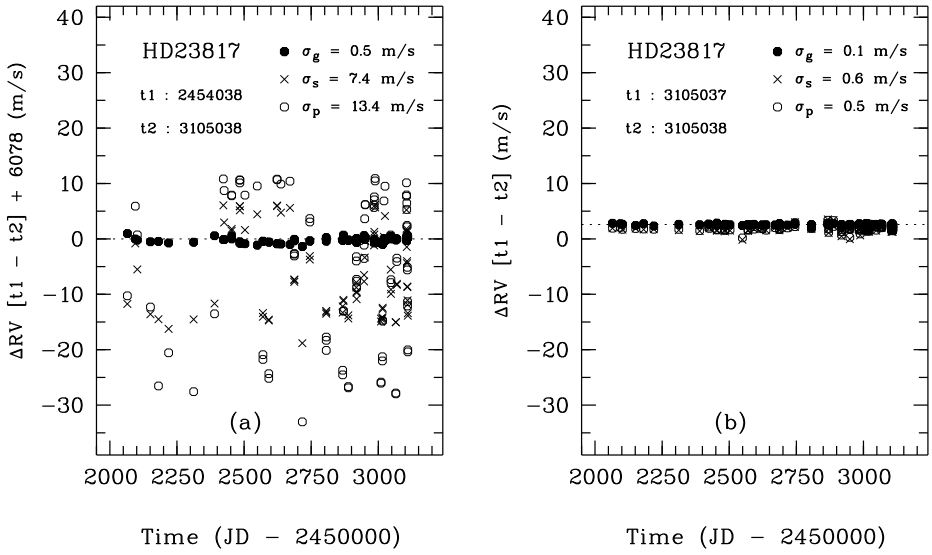

Figure 5.10: The difference velocities, $\Delta RV = RV_1 - RV2$, for two templates t_1 and t_2 , as a function of the date of observation for a series of 86 spectra of HD 23817: (a) templates taken several months apart, and (b) templates taken only minutes apart. In (a) the relative radial velocity of the two templates (using a gaussian fit) has been subtracted from ΔRV to bring the mean values closer to zero.

Finally, two further graphs illustrate that ΔRV for parabolic and spline interpolation does not change in a random manner, from night to night, as might appear in Fig. 5.10(a). Fig. 5.12 shows that the changes tend to be smooth.

The characteristics of Fig. 5.10 – Fig. 5.12 may be explained in terms of gradual changes to the asymmetry of the CCF peaks. When the template spectra are acquired within minutes of each other, as illustrated in Fig. 5.10(b) and Fig. 5.11(b), the two resulting CCF peaks for the two templates cross-correlated with any given programme spectrum can be expected to have almost identical profiles. However, when the two templates have been acquired on nights separated by longer intervals of time, the resulting CCF peaks can have quite different profiles. Apparently the spline and parabola fitting algorithms are more sensitive to these variations than are gaussian profiles. Such changes may be due to variations of the spectrograph's instrument profile or the star's line profiles, both of which are influenced by many factors. The instrument profile may vary as a result of changes in the ambient temperature or the aberrations created along the optical path. The stellar causes of spectral lines with variable asymmetry include non-radial pulsations and the rotation of a star with a non-uniformly luminous surface, for example, owing to starspots (see e.g. Toner & Gray 1988).

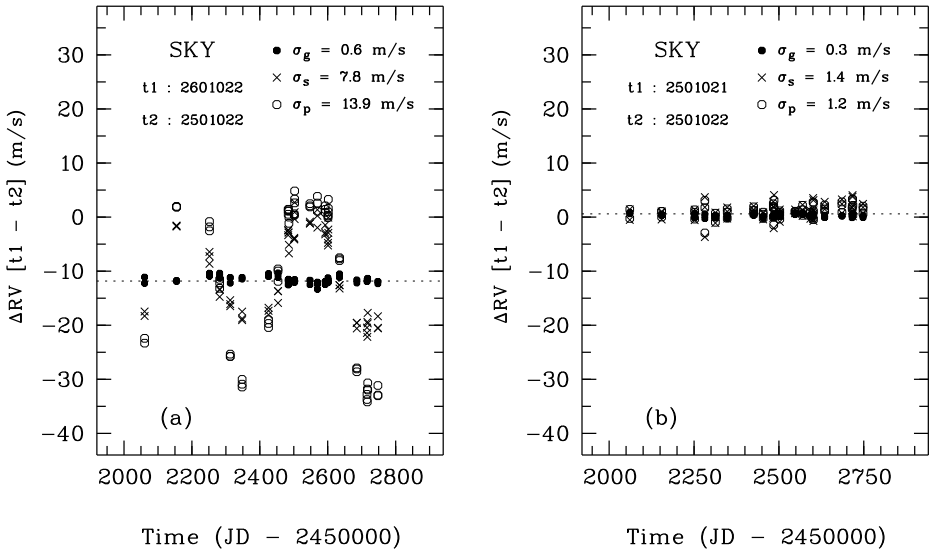

Figure 5.11: The difference velocities, $\Delta RV = RV_1 - RV2$, for two templates t_1 and t_2, as a function of the date of observation for a series of 65 spectra of the daytime sky: (a) templates taken several months apart, and (b) templates taken only minutes apart.

None of the three stellar examples illustrated are known to have significant photometric variability, the causes of which often also produce variable line asymmetry. Since the computed radial velocity is very sensitive to any change of the spectrograph's instrument profile (Queloz et al. 1999), it appears that many of the short- and long-term CCF profile changes implied in this section may be due to changes to the instrument profile of HERCULES. Mechanical and thermal effects must be minimised so as to achieve an instrument profile that is as stable as possible. One aspect of HERCULES operations that may deserve attention is the twice-daily refilling of the CCD detector's dewar with liquid nitrogen coolant. Whilst HERCULES is located in a thermally insulated room to minimise sudden temperature changes, the dewar is inside this room but is not itself insulated. The consequences to the instrument profile resulting from the thermal shock at the time of coolant refilling is presently unknown[13]. The coolant refilling, timed to occur at least one hour outside of each observing session, does not, though, seem to be related to the results illustrated in Fig. 5.12 on the next page. The discrete nature of CCD data may also have an influence on these results (Cummings 1998). Whilst we recognize that a gaussian profile does not match the shape of the CCF perfectly (Hill 1993), this analysis dictates that the most appropriate profile to use for HERCULES spectra and the present CCF fitting algorithms of HRSP is that of the gaussian function.

[13]The immediate effect upon the CCD detector due to the coolant entry into the CCD dewar is described in § 5.9.

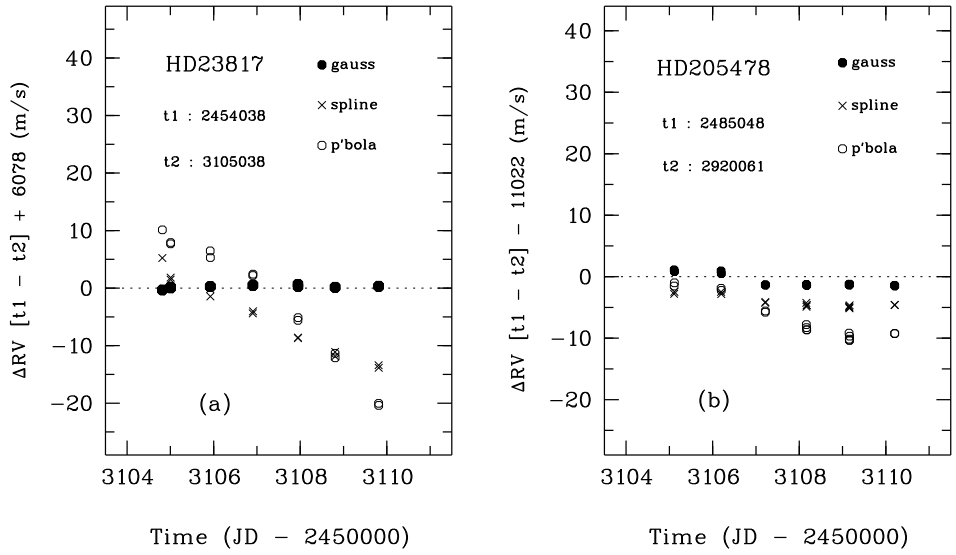

Figure 5.12: The difference velocity scatter, $\Delta RV = RV_1 - RV2$, for two templates t_1 and t_2 taken several months apart, as a function of the date of observation. Six consecutive nights of spectra of (a) HD 23817, and (b) HD 205478 are presented. In each plot, the relative velocity of the two templates (using a gaussian fit) has been subtracted from ΔRV to bring the mean values closer to zero.

5.8 Dispersion solution stability

The stability of the dispersion solutions measured throughout two routine observing sessions is illustrated in Fig. 5.13. The sessions selected had 12 hours or more of thorium spectra acquired using the more commonly used fibre 1. These two nights were also considered suitable as they included many thorium spectra separated by regular, generally brief, time intervals.

Each locus of datapoints has been created using a single stellar spectrum and a series of thorium spectra obtained during the given night. Each stellar spectrum was reduced to a logarithmic wavelength scale using a *single* thorium spectrum, these being acquired at different times throughout the night. As the spectra were taken on a typical observing night, the thoriums corresponded to the observations of other stars. They are identified in Fig. 5.13 as the first and second Th-Ar spectra. The resulting series of reduced spectra were then cross-correlated with a reference created using a thorium image obtained about midway through the observing session.

Since the same stellar spectrum is used for each locus of relative velocities, any variations must be due to differences of the dispersion solution produced by each Th-Ar spectrum. If the

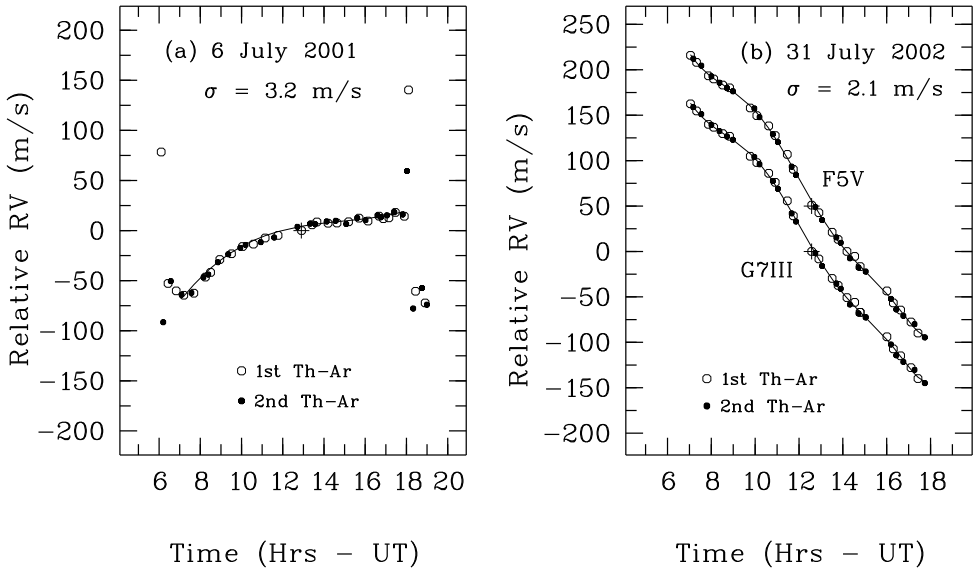

Figure 5.13: The stability of the dispersion solution using HERCULES spectra and the reduction package HRSP. The datapoints identify the observation times of a series of Th-Ar spectra taken throughout the given nights. These points represent the radial velocities of the same stellar spectrum reduced with each Th-Ar spectrum, relative to a reference thorium. The r.m.s. error of each polynomial fit is a measure of the uncertainty of each dispersion solution. The polynomial fit of (a) does not include the datapoints immediately after each abrupt velocity change, which are the result of disturbance to the detector by refilling of the CCD's dewar with liquid nitrogen coolant. The reference Th-Ar image is labelled with a '+'. The approximate time of the stellar observation corresponds to a relative velocity of zero.

dispersion solution had been constant throughout each night (as a result of the Th-Ar spectra always being projected onto exactly the same pixel positions of the CCD), the velocities measured would all be zero. Fig. 5.13 illustrates that this is not the case. There are changes to the dispersion solution during these nights, although they are mostly gradual. Occasionally, they are sudden and dramatic as is evident at the start and end of the observing night of 2001 July 6. The cause of the sudden changes was the unfortunate automatic refilling of the CCD system with liquid nitrogen coolant whilst observations were being acquired. This was a regrettable error early in the use of HERCULES and avoided thereafter, but put to good use in this analysis. The cause of the abrupt velocity change (due to the abrupt change to the dispersion solution) will be analysed in more detail in the next section. Its effects are neglected in the immediate discussion.

The two plots in Fig. 5.13 display quite different rates of change to the dispersion solutions. The cause of these different changes has not been identified. It does not seem to be the re-

sult of pressure or temperature changes, since HERCULES operates in a vacuum and the gradient of the two temperature records of these nights are similar ($\nabla T_{\rm cam,ech} \sim +0.02^{\circ}$/hr; see Fig. 5.14).

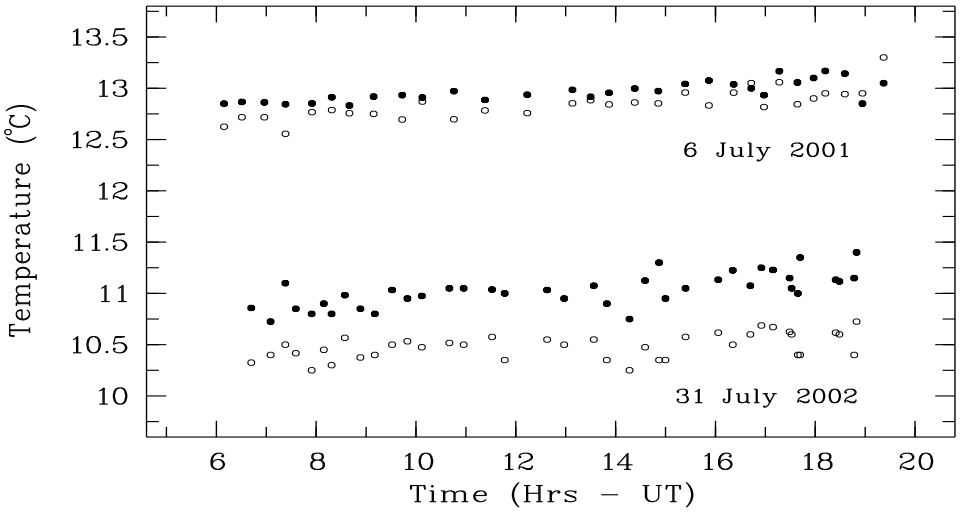

Figure 5.14: The HERCULES temperature record for the two nights presented in Fig. 5.13. Open circles: échelle grating, solid circles: primary mirror of Schmidt camera.

The temperatures were recorded by sensors on the échelle grating and the primary mirror of the Schmidt camera. The temperature variations corresponding to these two HERCULES elements generally mimic each other quite closely suggesting the sensors are reliable indicators. The obvious differences of these temperature records for the two nights is the slightly higher and less variable temperatures for 2001 July 6. It is not anticipated that these differences could influence the changing dispersion solutions in the way demonstrated.

The total drift of the dispersion solutions differs for the two nights, corresponding to about $80\,{\rm m\,s^{-1}}$ for 2001 July 6 and as much as $300\,{\rm m\,s^{-1}}$ for 2002 July 31. The larger drift is equivalent to a mean shift of the calibration lines by about 0.14 pixels. Drifts of either magnitude would be a serious problem for high precision velocity measures if only one or two thorium spectra were acquired each night. However, by recording pairs of Th-Ar spectra for each stellar spectrum, this effect is reduced considerably. The mean velocity drift rate for 2002 July 31 is about 25 $\rm ms^{-1}hr^{-1}$, or $8\,{\rm m\,s^{-1}}$ for a typical stellar exposure lasting 20 minutes. More importantly, the standard deviations of the r.m.s. errors of the polynomial fits are only $\sim$ 2–3 $\rm ms^{-1}$. By interpolating the two dispersion solutions to the flux-weighted time of the star's mid-exposure, it is believed that this is the lower limit to the precision of the (HERCULES + HRSP) radial velocities. For the night of 2002 July 31, [Fig. 5.13(b)], stellar spectra of two stars of spectral type F5V and G7III were analysed. Whilst the relative velocities do not have a constant difference,

it is evident that the general drift of the velocities/dispersion solutions is independent of the spectral type, as would be expected.

5.9 Coolant refilling of the HERCULES CCD dewar

The HERCULES CCD is maintained at a temperature of $\sim -95°$C to provide a low dark current. Liquid nitrogen is used for this purpose, pumped into the detector dewar approximately every 12 hours, although this time interval varies depending on the season. The consequences for stellar velocity precision, if observations are made when the refilling process takes place, have been emphasised by the results presented in Fig. 5.13(a).

The cause of the change to the velocity measured is illustrated in the set of plots presented in Fig. 5.15 for échelle order $n = 117$. A series of Th-Ar spectra were taken every 2–10 minutes over four hours. A liquid nitrogen refill was initiated after one hour. As soon as the coolant refilling began, the position of the calibration lines relative to the detector changed abruptly[14].

The *direction* and *magnitude* of the shift, as well as the extent of each pixel's *recovery* to its original position, is strongly correlated with the initial pixel position as defined by the calibration line initially projected onto it. Lines that initially project onto a low pixel number, project onto a higher pixel position immediately after coolant refilling. The recovery of the line position is initially rapid, but this slows after $\sim 1/2$ hour. Even after three hours, recovery is not complete. Lines that project onto a high pixel number project onto a lower pixel position. These pixels recover their original position more completely, and do so in about 1.5 hours. The uniformity of these changes in different orders is illustrated in Fig. 5.16. Clearly, the relative positions of the calibration lines differ before and after the refilling of the CCD coolant, particularly on opposite sides of the detector, and consequently the resulting dispersion solutions must also differ.

Such sudden changes to the line positions could only be attributed to a change in the position of the detector itself, or some portion of its support structure. It is difficult to imagine a mechanism by which the the image plane of the HERCULES spectrum or a large part of the spectrograph (for example, the tank, optical bench or floor) could change so rapidly. Therefore it is considered to be fixed for the following analysis.

Several possible physical changes that might describe what happens to the detector are illustrated in Fig. 5.17. These changes include expansion, contraction, rotation and detector translation. More than one of these re-alignments or others not illustrated may act at the time of coolant refilling. However, of the ones presented here, the surprising conclusion is that detector expansion provides the only scenario consistent with the results demonstrated in Fig. 5.15 and Fig. 5.16. This is an unexpected result, as the coolant would be considered more likely to

[14] After step(1) of a HRSP reduction (see § 5.5), the pixel coordinates (x, y) are measured so that the x-axis is along the main dispersion in the direction of increasing wavelength, while the y-axis is along the cross-dispersion in the direction of decreasing order number (increasing central wavelength). The pixel positions analysed here correspond to the x-axis only.

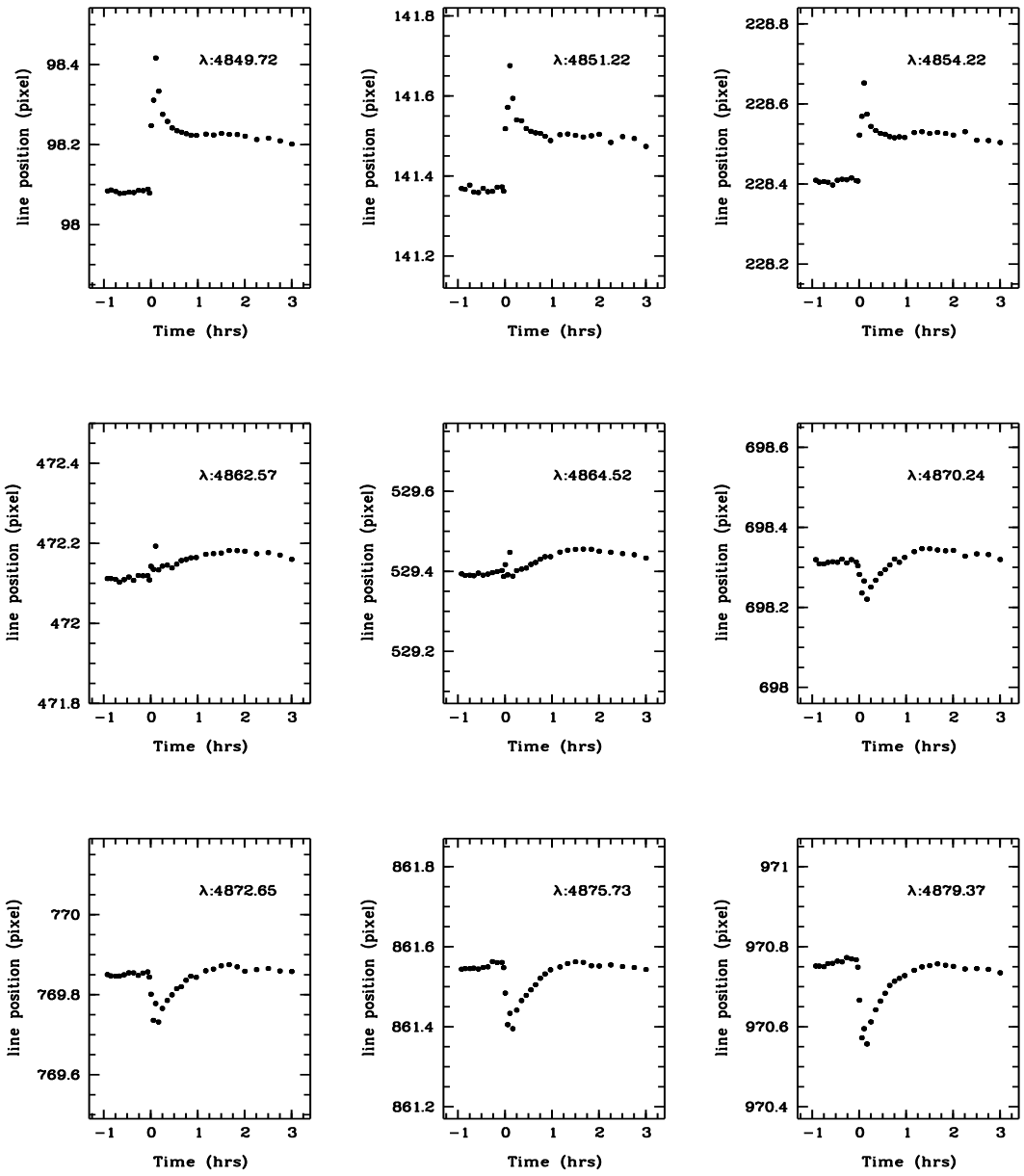

Figure 5.15: An example of the abrupt shift to nine calibration lines at the moment of liquid nitrogen refilling of the CCD system at $t = 0$ hrs. Each datapoint is the pixel position of a line (vacuum wavelength given) along order 117 as a function of time. By interpolation, lines falling close to pixel position 600 would appear to experience the least shift in their positions.

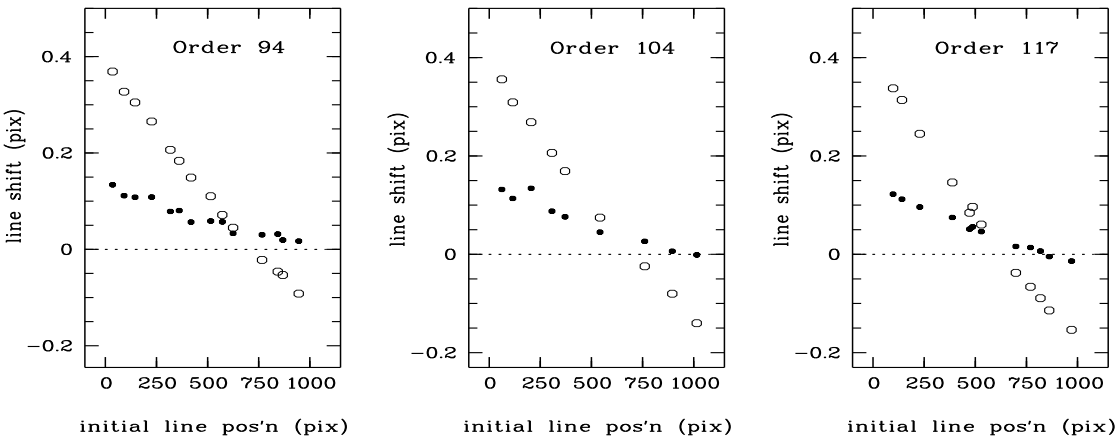

Figure 5.16: The typical shifts to the calibration lines for three échelle orders (94, 104, and 117), relative to each lines' position just prior to coolant refilling of the CCD dewar (line shift = 0). Open symbols: five minutes after refilling began; solid symbols: three hours later.

cause the chip to contract. One possibility is that the detector's own heating mechanism, which assists with maintaining the desired detector temperature, acts suddenly in response to the effect of the coolant. It is difficult to assess this possibility in more detail as the manufacturer has not made available the information required to do so.

These results demonstrate the importance of not attempting to acquire Hercules spectra for precise radial-velocity work until at least one, but preferably two hours have elapsed after the CCD has been refilled with coolant. From a practical point of view, if particular velocity measures are unusually disparate from expectations, or if thorium spectra are unusable or unavailable for a particular stellar image, the analyses described in this and the previous section, i.e. an unscheduled coolant refill (as was known to occasionally happen due to errors in the internal time-keeping mechanism), may provide a satisfactory explanation and/or solution.

5.10 Long-term changes to the position of the spectrum on the CCD

As described in § 5.1, the presently available CCD is too small to record the entire Hercules spectrum without moving the CCD to one of four discrete detector positions. The detector is also used regularly (usually at least once per month) for photometric observations that neces-

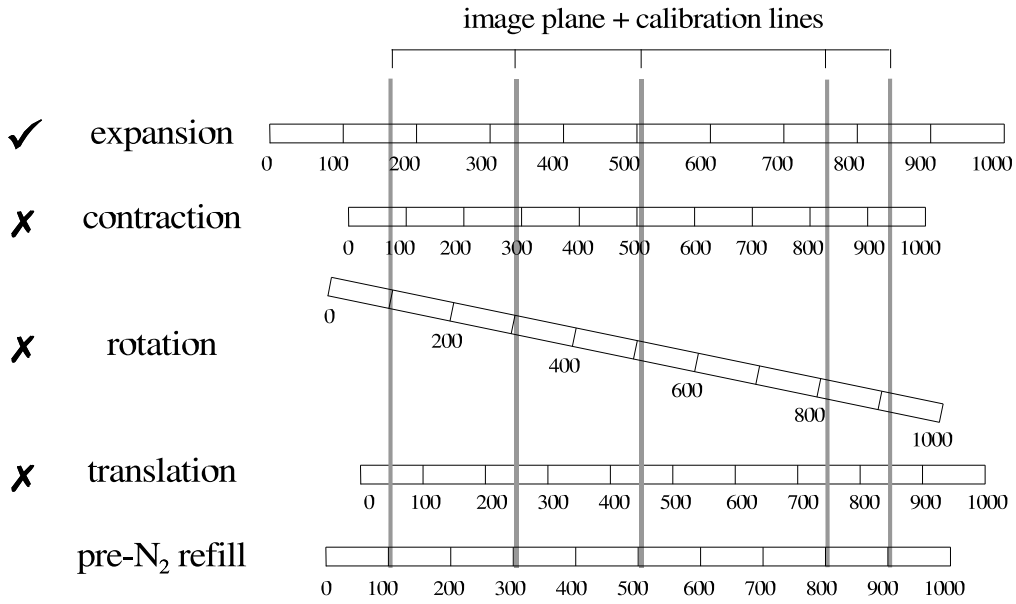

Figure 5.17: Four possible simple detector re-alignments relative to a fixed HERCULES image plane immediately after liquid nitrogen refilling of the CCD dewar. Pixel numbers along the five detector positions are labelled. Five calibration lines are included. The pixel position of zero-shift (Fig. 5.16) has been chosen to be at number 500 for three of the re-alignment scenarios. More than one of these re-alignments or others not illustrated may act at the time of coolant refilling. However, of the ones presented here, detector expansion provides the only scenario consistent with the results demonstrated in Fig. 5.15 and Fig. 5.16.

sitates removing it to another instrument platform. Therefore, the long-term stability of the HERCULES image plane relative to the detector deserved some consideration.

Approximately 400 Th-Ar spectra acquired after a vacuum was established in the HERCULES tank were cross-correlated with a reference spectrum. Two or three spectra were included from each available days' observing. Fig. 5.18 illustrates the changes that have occurred. The CCD plane is mounted such that the p-axis (across the échelle orders) is horizontal and the q-axis (along the échelle orders) is vertical[15]. In general, changes to the relative position in p are reflected in those in q, indicating that most changes are diagonally across the detector. The two larger changes, just before JD2200 and just after JD2600, occurred when minor work was carried out on the CCD dewar support platform. The first couple of months of HERCULES operation were also complicated by difficulties maintaining the tank vacuum due to a faulty seal. However, since these measurements are only relative ones, it is not known with certainty how

[15]In HRSP, the pre-reduction pixel coordinates (p, q) are measured in *raw* CCD images created at the time of acquisition at the observatory. In a typical situation, the physical pixel columns are measured along the p-axis, while pixel rows are counted along the q-axis. These coordinates are distinct from the previously described (x, y) coordinates which apply to CCD images that have been *prepared* by the initial HRSP reduction algorithms (Skuljan 2004). For more information, consult the detailed material in the HRSP User Manual prepared by J. Skuljan.

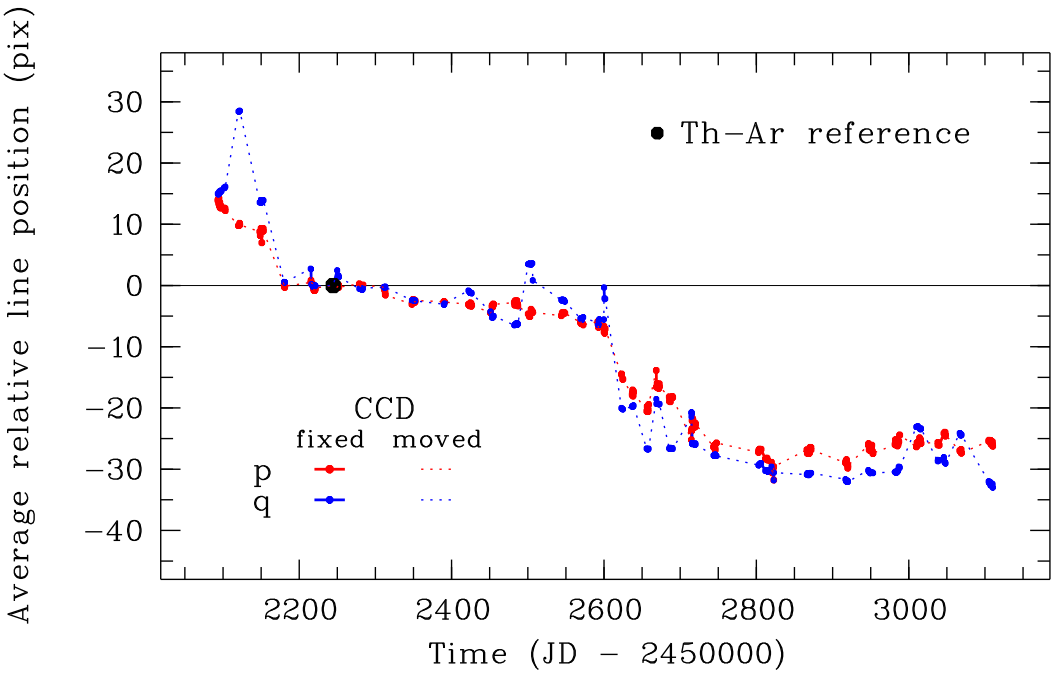

Figure 5.18: The position of the HERCULES spectrum relative to the detector as a function of time. The p-axis is horizontal across the échelle orders and the q-axis is vertical along the orders.

much the changes are due to the way the detector is positioned on its support platform or how much they are due to changes to the direction that the HERCULES spectrum is finally projected (see Fig. 5.19).

Whenever there is a shift in the relative position of the spectrum on the detector, the portion of the image recorded must change. The detector position across the orders determines the extreme order numbers for each spectrum, whilst along each order, n, the detector position determines the boundary values for $n \times \lambda$[Å] of the wavelength window. The extreme values of the orders and wavelengths for this study are presented in Table 5.4.

These changes have consequences for a long-term precise radial-velocity study such as the one described in this thesis. The important issue is that all spectra included in a cross-correlation series should have the same spectral features available for all orders involved in the velocity measurement. If this is not the case, systematic errors will occur. The errors that can arise when the spectral features of each order of the template and programme spectrum do not match were described earlier in § 5.7.1. Similarly, the inclusion or exclusion of entire orders will usually influence a spectrum's mean velocity. In Fig. 5.20, the velocities of 26 orders of a spectrum of HD 83610 illustrate the differences that can typically occur from one order to another. Clearly,

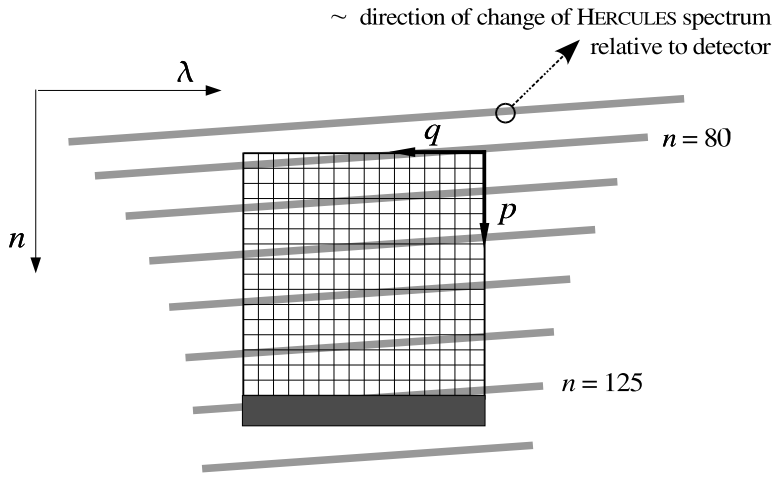

Figure 5.19: A schematic diagram of the HERCULES spectrum relative to the CCD detector. The change to the relative position of them, in pre-reducion pixel coordinates (p, q), is shown (see Fig. 5.18).

Date	Order n		$\lambda_{\rm vac}$ (Å)		$n \times \lambda$[Å]	
$JD - 2450000$	min	max	min	max	min	max
2102	79	124	4574	7227	567180	570930
2888	81	126	4503	7047	567380	570800

Table 5.4: The extreme order numbers and vacuum wavelengths of the HERCULES spectrum recorded by the detector during the course of this study. The $n \times \lambda$[Å] values are the boundary limits common to all orders of spectra for each date.

the mean velocity measured for this spectrum could change simply by altering the particular orders available or chosen.

5.11 Inadequate scrambling in the fibre: the need for continuous guiding

The original design strategy for HERCULES was to use intermittent guiding (described in § 5.1). This had a minimum inter-guide time of one minute. As observations using HERCULES accumulated, it became evident that the brightest stars also had the greatest velocity scatter. This result was initially revealed when consecutive observations of the zeroth-magnitude star α Cen A were compared (a spectrum with a $S/N \sim 100$ required an exposure of only several seconds).

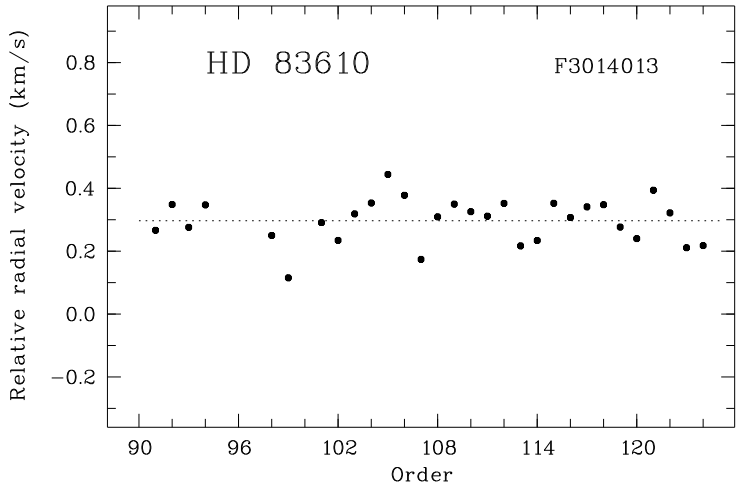

Figure 5.20: The relative radial velocity as a function of order number for HD 83610. The dotted line represents the unweighted mean velocity.

Similar results were found for bright radial-velocity standard stars such as HD 109379 (G5II, $m_{\rm v} = 2.6$; typical exposures 20–30 seconds). Even though the spectra had almost identical signal and the same pair of thorium spectra were used to derive the mean dispersion solution, velocity differences as large as 50–100 m s^{-1} could sometimes be measured. Imperfect telescope guiding, combined with inadequate scrambling of light by the optical fibre, were identified as the primary causes (Skuljan 2003).

Each time a new observation began, the stellar image was centred on the fibre input as accurately as possible using the exposure meter to determine the image position to achieve a maximum count rate. However, the image was rarely placed at exactly the same central position. If the stellar image is offset from the fibre centre, the fibre illumination becomes non-uniform and poor fibre scrambling results in the spectrum being shifted across the CCD chip, mimicking a Doppler-shift. The effect is especially prominent given these circumstances:

1. The stellar image is not positioned centrally on the fibre and the exposure is very short owing to the brightness of the star and the signal required.

2. If the telescope's tracking does not match the sidereal rate, the stellar image will tend to drift in right ascension across approximately the same edge of the fibre.

3. For a given star, the problem of non-uniform fibre illumination becomes worse as the seeing improves.

Longer exposures, with larger numbers of guiding corrections, and larger seeing images, reduce the non-uniformity of the fibre's input illumination. These circumstances are favourable for precise radial-velocity measurements and conceal the poor scrambling properties of the single

fibre.

Proof of the role of off-centre image positioning for creating less precise velocities was accomplished with a carefully conducted experiment involving two series of exposures of α Cen A. Before each series, the stellar image was intentionally positioned slightly to the east of the fibre's centre. The sidereal rate of the telescope was decreased so that the image slowly drifted westward. Without any guiding, a series of short exposures (duration $\sim$ three seconds) was obtained. The results are presented in Fig. 5.21. When the stellar image was east of the centre of the fibre the relative velocities were red-shifted, whereas when the image was west of the fibre the velocities were blue-shifted.

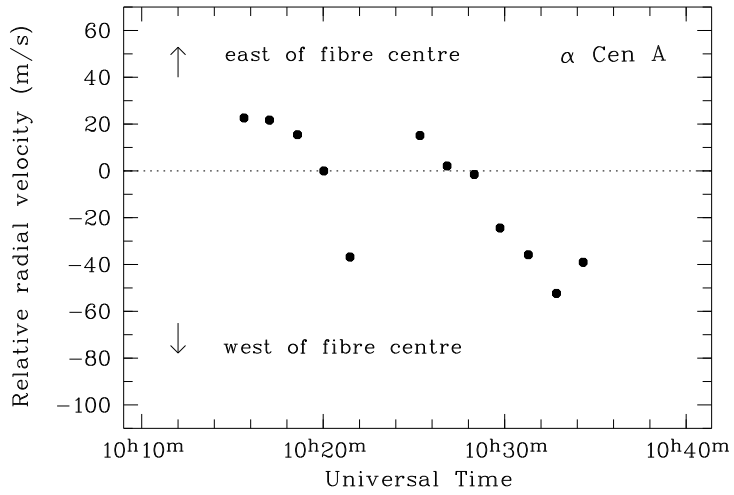

Figure 5.21: The effect of poor scrambling by the HERCULES optical fibre, due to intentional and variable off-centre positioning of the image of the bright star α Cen A (observations courtesy J. Skuljan).

Several solutions to this undesirable situation were considered:

1. a double-scrambling device could be inserted along the optical fibre so that more complete scrambling of the light could be achieved within the fibre (Queloz et al. 1999),

2. guiding could be executed more regularly so that the maximum count rate could be monitored more closely and image centring on the fibre better maintained,

3. the tracking accuracy and precision of the telescope could be improved, and/or

4. a neutral density filter could be inserted in the light path before the fibre input to increase the necessary duration of the exposure of bright stars (this was the least satisfactory solution).

The quickest satisfactory solution to the problem with the available expertise was to increase the guiding frequency by including a beamsplitter on the fibre-feed module's optical-bench turntable. This device allowed constant monitoring of the image position and guiding updates every few seconds by channeling most of the starlight to the fibre input throughout an exposure, but redirecting $\sim 8\%$ of the light to the guide camera. The usefulness of this approach is demonstrated in Fig. 5.22. For HD 109379, the velocity precision improved by a factor of nearly $4\times$ after the beamsplitter was installed. Use of the beamsplitter made it rather challenging to observe faint stars ($m_{\rm v}$ fainter than about 9th magnitude). However, these stars could still be observed using the original strategy of intermittent guiding without the beamsplitter in the lightpath.

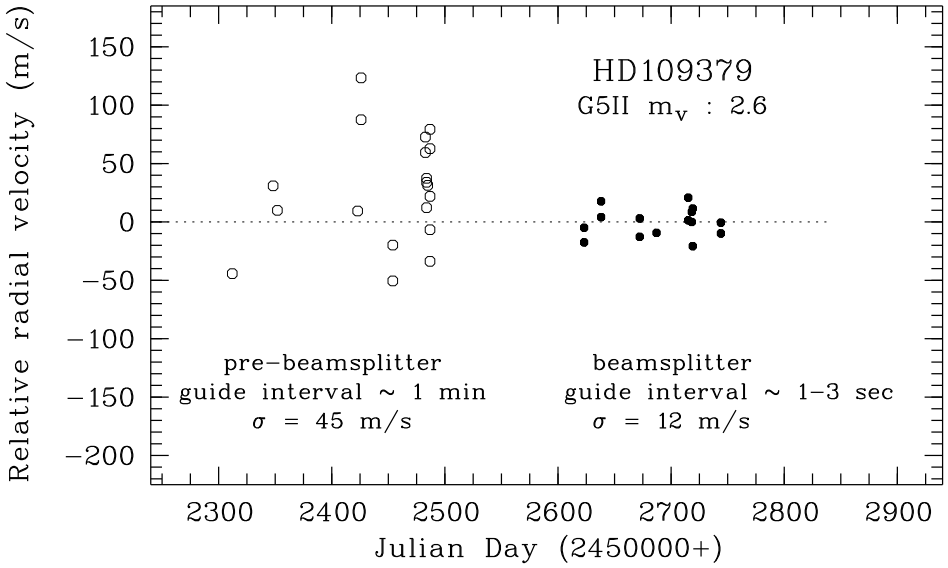

Figure 5.22: The improved precision of radial velocities for the bright radial-velocity standard star HD 109379 achieved by inclusion of a beamsplitter and frequent guiding during HERCULES observations.

These circumstances focussed attention upon the crucial need to obtain spectra with the most accurate and precise guiding possible, particularly when the seeing was better. To this end, the final months of observing were carried out with particular attention to the adjustment of the telescope's sidereal rate to match, as closely as possible, that of the given observation's direction in the sky.

Chapter 6

HERCULES radial velocities and orbital solutions

A number of additional steps are required during the reduction process so that the velocities measured for individual échelle orders, as well as the final mean velocity for a particular observation, is of as high a quality as the available techniques allow. These matters will be discussed in the present chapter. The methods used to determine the spectroscopic orbital elements and estimate the velocity zero-point are also included.

6.1 Avoidance of unwanted wavelength segments

Telluric lines

All HERCULES observations obtained for this thesis included 47 or 48 échelle orders, varying in wavelength space from about 50 Å for $n = 80$ to about 30 Å for $n = 125$. Some of the orders are contaminated by non-stellar absorption lines included in the recorded spectra as the starlight passes through the Earth's atmosphere. These telluric lines, typically due to water vapour and oxygen, can be relatively strong, numerous or both, and will have a velocity unrelated to the star. Inclusion of such lines will therefore result in a velocity measure for the corresponding cross-correlation function that will be inaccurate.

The HERCULES spectra recorded in this work using CCD position 2 have the telluric lines confined to several orders, typically in the red, and are easily avoided (for example, n =82, 83, 85, 86, 90, 95–97, and 100). Fortunately, these omissions leave many line-rich orders available for cross-correlation purposes in the late-type spectra studied in this thesis. When the telluric lines are confined to a relatively short portion of an order, the $n \times \lambda$ limits can be selected so that only the portion of the order contaminated is avoided.

Broad lines

The definition of each cross-correlation peak is also closely related to the sharpness of the spectral lines utilized. Certain spectral lines, such as those corresponding to hydrogen and the Mg I b triplet ($\lambda \sim 5170$ Å), significantly broaden the cross-correlation function (Hill 1993), so that the measured velocity can be expected to be less precise. When present in double-lined spectra, these strong lines may also cause the cross-correlation peak to be tilted away from an upright line of symmetry, as is illustrated in Fig. 6.1, resulting in the measured velocity being less accurate as well.

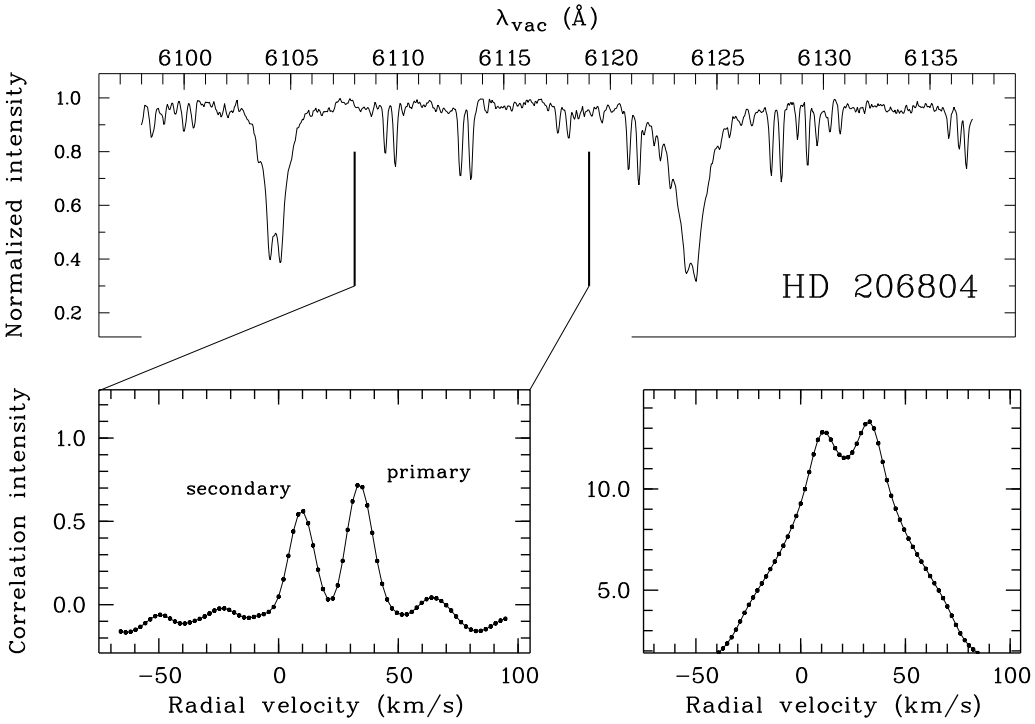

Figure 6.1: Example of the benefit obtained by removing broad spectral features from the cross-correlation (C-C) analysis. Top: The wavelength space of a HERCULES spectrum of the SB2 visual binary HD 206804 (K7V+K7V) for order 93. Bottom right: The more intense but broad and ill-defined C-C function that results when the entire order is included. The C-C peaks are also tilted away from vertical symmetry. Bottom left: The weaker but better-defined and more vertically symmetrical C-C peaks produced when only the wavelength segment indicated above is included.

6.2 The template spectrum

Any set of relative radial-velocity measurements of a series of observations requires a template spectrum (see § 5.6 beginning on page 86). The template image can be stellar or synthetic. Regardless of this choice, it is important that its spectral characteristics match that of the programme star as closely as possible so that each cross-correlation function is as well-defined and as symmetrical as possible about each peak-velocity axis (Hill 1993).

A stellar template can be one of the star itself, or of another star. The alternative is to use a synthetic spectrum created using an appropriate model of a stellar atmosphere. The template may be modified by its convolution with a suitable rotational profile (Hill 1993). Each of these choices has advantages and disadvantages. For instance, when the template is of the star itself, and if all spectra are single-lined, the template will be an almost perfect match for the series of

observations[1]. To minimize the introduction of undesirable noise into the cross-correlation, the stellar template should have a signal-to-noise that is as high as practicable. Furthermore, the velocity measures are unlikely to have barycentric values.

Alternatively, a synthetic spectrum will be noise-free but requires more effort to produce and also will not perfectly match the intended stellar spectrum, so that spectral mismatch is more likely. The measured velocities will, though, have approximately barycentric values[2].

The most challenging spectra for extracting accurate and precise velocities present themselves when both stars make a contribution that cannot be ignored, for example binary systems having a composite spectrum resulting from a hot dwarf and a cool giant or subgiant star (e.g. Griffin & Griffin 2004), or when the velocity difference between the stars is small enough that spectral-line blending becomes significant.

The latter situation has been addressed perhaps most successfully by Zucker, Mazeh and coworkers with their development of TODCOR: TwO-Dimensional CORrelation technique (e.g. see Zucker & Mazeh 1994). Rather than identifying the cross-correlation peaks of each dissimilar star using separate cross-correlations for each template, TODCOR applies the two templates simultaneously, with an appropriate relative Doppler-shift and flux-intensity ratio corresponding to the binary pair. The various parameters are adjusted until the two-dimensional correlation functions are maximised. The TODCOR procedure has also been favourably applied to triple-lined systems (Zucker et al. 1995). Zucker (2003) has described a method based on maximum-likelihood analysis for combining cross-correlation functions. This approach has already been successfully applied, in conjunction with TODCOR, for the detection of a very faint companion of a K star (Zucker et al. 2003).

When the spectra are single-lined, the analysis can proceed with relative ease once the template has been selected. However, when this is not the case, the analysis must consider the contributions that each star makes to the recorded spectrum, as well as the velocity difference that separates the two sets of spectral lines and therefore corresponding cross-correlation peaks. The subsequent analysis becomes easier the more similar the two spectral types are and the greater the velocity difference is between the two sets of spectral lines, such as when a classic double-lined spectrum results. In this situation, a single carefully chosen template spectrum should adequately match both stars, allowing each pair of adequately-separated cross-correlation peaks to be measured with confidence. All of the double-lined spectra that were analysed in detail for this thesis were of this type. They belonged to the binary systems HD 206804 (K7V+K7V), HD 217166 (G1V+G4V) and HD 181958 (F6V+F7V).

As there were no significant obstacles to obtaining high-quality stellar spectra, it was decided

[1] In reality, a strictly perfect match will not exist because of variations to the profiles and relative strengths of the spectral lines as a result of changes to the instrument profile, the star's photospheric behaviour and so on.

[2] Besides systematic errors, other complications such as stellar convective blueshifts and gravitational redshifts will mean that even these velocities cannot be claimed to be truely accurate for the star's centre-of-mass.

that all templates would be of this type. Each template spectrum had to be carefully acquired as it potentially had several important roles to play:

1. for cross-correlation purposes,
2. to determine the relative weights of each wavelength segment (or order) so that a weighted-mean velocity of each observation could be determined,
3. for comparing the MJUO velocity of the template to the published value and assessing the velocity zero-point of HERCULES observations, and
4. to determine the barycentric velocity of non-solar type stars.

The first point above has already been discussed. Comments with regard to the others will follow shortly.

The intended use of each template spectrum dictated that it be acquired with a signal-to-noise as high as possible, preferrably $S/N \sim 200$ or more. So as to obtain this image with the highest quality, the intention was to acquire it using as short an exposure as possible and therefore when the star was observable with a small airmass, as well as on a night with optimal seeing and transparency. The maximum exposure duration was nominally 20 minutes and therefore each star had to be reasonably bright (the faintest template star observed has $m_{\rm v} = 6\overset{\rm m}{.}4$). For the cases when the template was the visible star of a single-lined spectroscopic binary system, it was also desirable to acquire the image at an epoch when the star's orbital radial acceleration was minimal (i.e. during a quadrature phase)[3].

6.3 The weighted-mean velocity of each observation

The final radial velocity measured for each spectrum was calculated as a weighted mean of the velocities measured for each order or wavelength segment included. The weighting factors were calculated using the corresponding template spectrum. First, a large number ($N = 100$) of random copies of each wavelength segment were generated, each simulating the effect of photon noise, and then each random image was cross-correlated with the original. The standard deviation σ_k of each of the N radial velocities found for an order or wavelength segment k determined the weighting factor $w_k = 1/\sigma_k^2$. All random images were created so as to have the same signal-to-noise ratio as a spectrum typical for each star (which was nominally $S/N \sim 100$, as described in § 5.1 on page 72).

A particular set of weighting factors was determined by the choice of the template image, the characteristics of the fitting function used for the cross-correlation peaks and the $n \times \lambda$ limits for each wavelength segment. The fitting function was always a gaussian profile, but the fitting-window width varied from star to star, being primarily dependent upon the mean width of the

[3]For a typical visual binary, this issue is not significant, but it becomes increasingly important for close binary systems with very short orbital periods. Each star in a circular edge-on orbit with $\mathcal{M}_1 = \mathcal{M}_2 = 1\,\mathcal{M}_\odot$ and $P = 10$ days will have a maximum radial acceleration $\alpha \sim 0.5\ \mathrm{m\,s^{-2}} \Rightarrow \Delta\mathrm{RV} \sim 560\ \mathrm{m\,s^{-1}}$ during a 20 minute observation (see Eq. A.74 on page 228).

cross-correlation peaks associated with a star's analysis. For a given spectral type, the weights usually differed as a result of various factors, including the total number of absorption lines, their strength and the width of the order or wavelength segment (Murdoch & Hearnshaw 1991). For the same reasons, the weights for a particular order will differ for stars of different spectral types. For instance, the reddest orders acquire larger relative weights for correspondingly cooler stars. These variations are illustrated in Fig. 6.2 where the weights generated for three template stars of spectral types F5V (HD 693), G5V (HD 115617) and K5V (HD 209100) are presented.

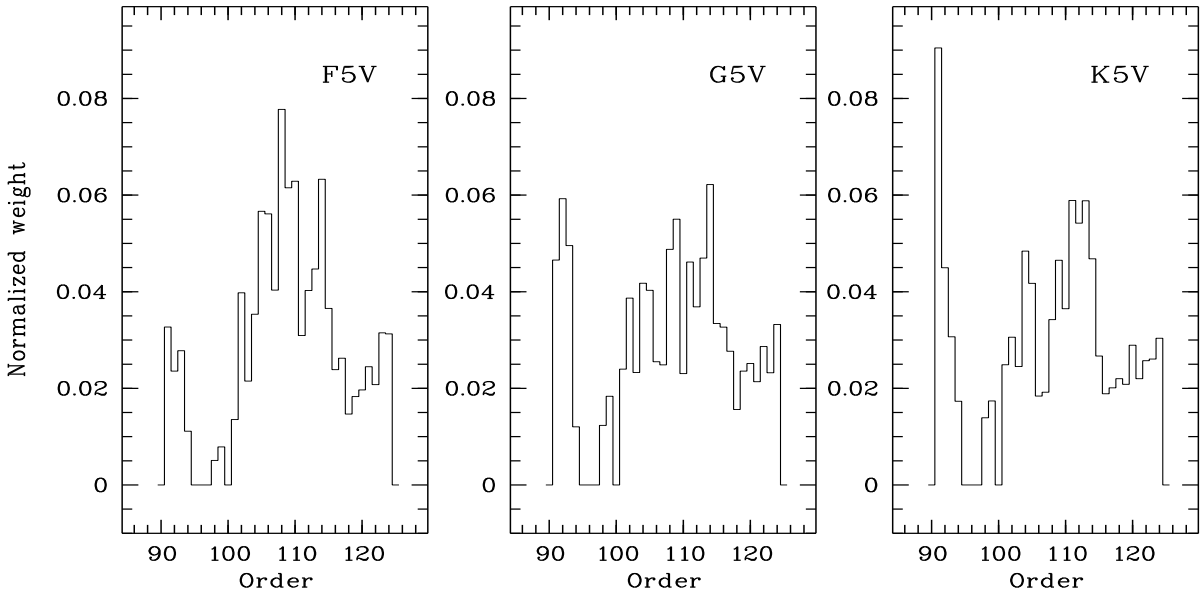

Figure 6.2: Normalized weighting factors generated for different échelle orders used to calculate the mean velocity of an observation. The weights for three spectral types, F5V, G5V and K5V, are illustrated. Orders disregarded due to the presence of telluric lines have zero weight.

All of the stars observed for this study had a spectral type of F5 or later. In general, for the single-lined spectra studied, there was very little radial-velocity information in the orders $n < 91$, several of which were also contaminated with telluric lines. Therefore none of these orders were included in the velocity measurements. Four additional orders, $n = 95$, 96, 97 and 100 also included telluric lines and were not used. Usually the highest order used was $n = 124$ so that 30 orders were included in the weighted-mean measurement. The complicated nature of the double-lined spectra (such as variable line blending) meant that the particular wavelength segments and their total number varied from system to system. These will be commented on in the respective detailed analysis of each.

6.4 The template library and radial-velocity standards

A total of 23 main-sequence and 15 evolved supposedly single stars were observed at least once for the purpose of having available a variety of potential template spectra. The stars had spectral types in the range from F5 to K5. All of the stars selected had a relatively small $v_{\rm equ} \sin i$ so that their spectra would include many sharp lines as do the spectra of the programme stars. Some of the templates were found in the lists for MK spectral type standards of Keenan & McNeil (1989) and for 'stable' stars with barycentric velocities with an r.m.s velocity scatter less than $100\,{\rm m\,s^{-1}}$ reported by Nidever et al. (2002). Four of the stars, HD 693, HD 80170, HD 102870 and HD 109379, are IAU radial-velocity standards (e.g., see Stefanik et al. 1999, Udry et al. 1999). Two other stars, HD 10700 and HD 115617, are candidate radial-velocity standards (Stefanik et al. 1999). Nidever et al. (2002) estimated that their FGK-dwarf velocities were precise to ~ 0.03 km s^{-1}and accurate to within about 0.3 km s^{-1}. They also reported that the 26 FGK stars on their list that are in common with the acknowledged radial-velocity standard star list of Udry et al. (1999), agreed in precision to 0.035 km s^{-1}and differed in zero-point by $+0.053$ km s^{-1}.

All of the template stars had their velocity, or when multiple spectra were available, their mean velocity, $V_{\rm sky}$, measured with respect to 30 HERCULES spectra of the blue-sky acquired over several observing runs at Mt John Observatory. A separate set of blue-sky spectra was used for each resolving power/fibre employed. The r.m.s. of the fibre 1 ($R \sim 41\,000$) blue-sky spectra was $\pm 13\,{\rm m\,s^{-1}}$, and for the fibre 3 ($R \sim 70\,000$) spectra, it was $\pm 8\,{\rm m\,s^{-1}}$. A larger series of nearly 100 blue-sky spectra acquired over the three years of this observing program using fibre 1 presented the same r.m.s. scatter as the smaller series, i.e. $\pm 13\,{\rm m\,s^{-1}}$. The barycentric velocities reported by Nidever et al. (2002) also had their zero-point velocity established by blue-sky spectra (four were used), together with two observations of Vesta.

The template stars are listed in Table 6.1 (main-sequence stars) and Table 6.2 (evolved stars), together with their spectral type, apparent magnitude, metallicity if available (Cayrel de Strobel et al. 2001), the published radial velocity (Barbier-Brossat & Figon 2000; unless otherwise indicated in table caption), the velocity measured from the HERCULES observation/s, the image number in the MJUO archive system and the HERCULES fibre used. When four or more observations have been made of a star, the r.m.s. scatter of the velocities is included instead of an archive number with the number of observations following in brackets. A comparison of the HERCULES velocities and the published values is illustrated in Fig. 6.3.

HD	Spectral type	m_v	[Fe/H]	V_{pub} ($km\,s^{-1}$)	V_{sky} ($km\,s^{-1}$)	image	HERCULES fibre
‡ 693	F5V	4.9	−0.49	$+15.0 \pm 0.3$	+14.933	±0.016(40)	1
7439	F5V	5.1	−0.38	+23.2	+21.837	2952059	1
203608	F6V	4.2	−0.60	−29.4	−29.889	2918049	1
					−29.961	2919015	3
210302	F6V	4.9	+0.07	−16.259	−16.295	2948017	1
					−16.292	2952062	3
38393	F7V	3.6	+0.01	−9.6	−9.196	2947048	1
48938	F7V	6.4	−0.50	−10.563	−10.558	2953030	1
					−10.580	3011023	3
7570	F8V	5.0	−0.07	+11.6	+11.837	2918057	1
					+11.839	2919060	3
10647	F8V	5.5	−0.07	+27.5	+27.706	2951004	1
					+27.678	2952073	3
45067	F8V	5.9	−0.20	+47.280	+47.303	2953041	1
					+47.301	3011017	3
‡ 102870	F8V	3.6	+0.20	+4.448	+4.501	2984084	1
				$+4.3 \pm 0.3$	+4.446	3015022	3
1581	F9V	4.2	−0.07	+8.9	+9.271	2918043	1
84117	G0V	4.9	−0.14	+34.8	+34.660	3187011	1
19994	G0V	5.1	−0.04	+19.331	+19.415	2953027	1
20807	G1V	5.2	−0.29	+11.5	+11.902	3190052	1
114613	G3V	4.9		−15.0	−13.023	3187023	1
102365	G3/G5V	4.9	−0.29	+15.3	+16.906	3187020	1
115617	G5V	4.7	+0.04	−7.850	−7.860	±0.0008(4)	1
					−7.869	3186068	3
18907	G8V	5.9	−0.69	+42.718	+42.447	2951027	1
					+42.429	2953038	3
10700	G8V	3.5	−0.42	−16.619	−16.655	3190071	1
20794	G8V	4.3	−0.48	+86.8	+87.812	3187094	1
177565	G8V	6.2	+0.05	+58.5	+60.065	2952044	1
131977	K4V	5.7	+0.03	+26.961	+26.953	3217052	1
209100	K5V	4.7	+0.04	-40.0	-40.075	2888030	1

Table 6.1: Template library of main-sequence stars. IAU standards are prefixed with a ‡. V_{pub} with error: Udry et al. (1999); V_{pub} to three decimal places: Nidever et al. (2002); otherwise V_{pub} from Barbier-Brossat & Figon 2000. [Fe/H] from Cayrel de Strobel et al. 2001.

HD	Spectral type	m_v	[Fe/H]	V_{pub} ($km\,s^{-1}$)	V_{sky} ($km\,s^{-1}$)	image	HERCULES fibre
109492	G4IV	6.2	−0.13	+6.0	+7.682	3217035	3
157347	G5IV	6.3	−0.04	−35.901	−35.894	3217046	3
140901	G6IV	6.0	+0.05	−5.2	−6.821	3187045	3
173791	G6IV	5.8		+9.7	+11.267	3214037	3
222803	G8IV	6.1		−30.8	−31.564	3214084	3
222805	G8IV	6.1		+20.2	+21.076	3217072	3
189005	G6III	4.9	−0.38	−51.1	−49.870	3214090	3
220957	G6/G8III	6.4		−81.264	−81.391	3217075	3
12055	G7III	4.8		+11.9	+12.305	3214090	3
29291	G8III	3.8	−0.09	−4.0	−3.275	2948055	3
115659	G8III	3.0	+0.06	−5.4	−4.884	3217049	3
223807	K0III	5.8	−0.10	−15.825	−15.806	3217078	1
					−15.799	3214087	3
25723	K1III	5.6		+26.748	+26.745	3217126	1
					+26.752	3218089	3
‡ 80170	K5III	5.3	−0.02	$+0.5 \pm 0.2$	+0.712	±0.022(46)	3
‡ 109379	G5II	2.6	−0.11	-7.6 ± 0.3	−7.390	±0.013(39)	1

Table 6.2: Template library of evolved stars. IAU standards are prefixed with a ‡. V_{pub} with error: Udry et al. (1999); V_{pub} to three decimal places: Nidever et al. (2002); otherwise V_{pub} from Barbier-Brossat & Figon 2000. [Fe/H] from Cayrel de Strobel et al. 2001.

The MJUO velocities agree very well with the published velocities for these stars. The stars that exhibit the largest differences are not radial-velocity standard stars. The mean residual for the four IAU standards in common with the MJUO list is $+5\,m\,s^{-1}$, with an r.m.s. scatter of $43\,m\,s^{-1}$. The corresponding uncertainty in the mean is therefore $43/\sqrt{4} \sim 21\,m\,s^{-1}$, so that the formal difference between the zero-points is $(V_{MJUO} - V_{IAU}) = +5 \pm 21\,m\,s^{-1}$, which is insignificantly different from zero. In addition, comparison of the MJUO velocities with the barycentric values reported by Nidever et al. (2002) presents a very similar picture, with one intriguing exception — HD 18907 (see Fig. 6.4). Excluding HD 18907, and HD 19994 which is now recognized as harbouring a Jupiter-mass extrasolar planet (Mayor et al. 2004), the mean residual for the remaining seven unevolved stars in common with the MJUO list is $+7\,m\,s^{-1}$, with an r.m.s. scatter of $24\,m\,s^{-1}$. This corresponds to a zero-point difference $(V_{MJUO} - V_{Nid}) = +7 \pm 9\,m\,s^{-1}$, and is also insignificantly different from zero.

HD 18907 presents a curious result. Whilst the velocities measured for the two MJUO spectra acquired on two separate nights differ from each other by only $18\,m\,s^{-1}$, they differ from the

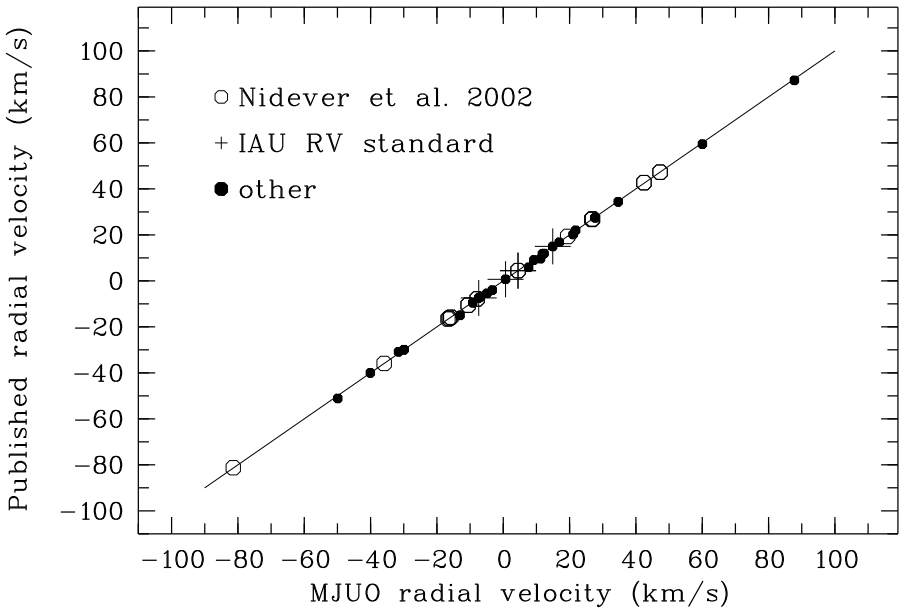

Figure 6.3: The MJUO velocities vs. the published velocities of the 37 template stars listed in Table 6.1 and Table 6.2.

Nidever et al. (2002) velocity by nearly $300\,\mathrm{m\,s^{-1}}$, or nearly 12σ, where $\sigma = 24\,\mathrm{m\,s^{-1}}$ for the corresponding residuals. Nidever et al. identified HD 18907 as a 'stable' star with $\sigma_{\mathrm{rms}} < 100$ $\mathrm{m\,s^{-1}}$. However, it seems they based this decision upon observations conducted on only two occasions, separated by only two nights. The residuals found here appear to be highly significant and suggest that HD 18907, an otherwise ordinary G8V star, has a variable radial velocity due to an orbiting mass, probably stellar. Indeed, examination of the radial velocities published for this star (SIMBAD) reveals considerable variability that supports this conclusion. At the time of writing, HD 18907 is not recognized as a spectroscopic binary.

To a first approximation, the velocities measured have barycentric values. However, as described in detail in, for instance, Nidever et al. (2002) and Lindegren & Dravins (2003), these velocities cannot be expected to be strictly absolute barycentric velocities. This is as a result of the many and varied astrophysical processes and measurement effects that influence the velocity derived for a given spectrum. Included in these effects are those due to the star's gravitational potential (resulting in a non-relativistic redshift $V_{\mathrm{grav}} = G\mathcal{M}/Rc$), movement of the stellar photosphere such as convective motions yielding a blueshift, rotation of a star whose surface is non-uniformily bright, relativistic effects arising from a star's transverse motion (Lindegren et al. 1999), and measurement errors as arise from mismatch of the template and programme star spectral types. Consequently, any similarity between the MJUO velocities and the published velocities does not indictate that the MJUO ones are accurate. The only claim that can be made is that, within the constraints of the measurements as outlined, they appear to have the

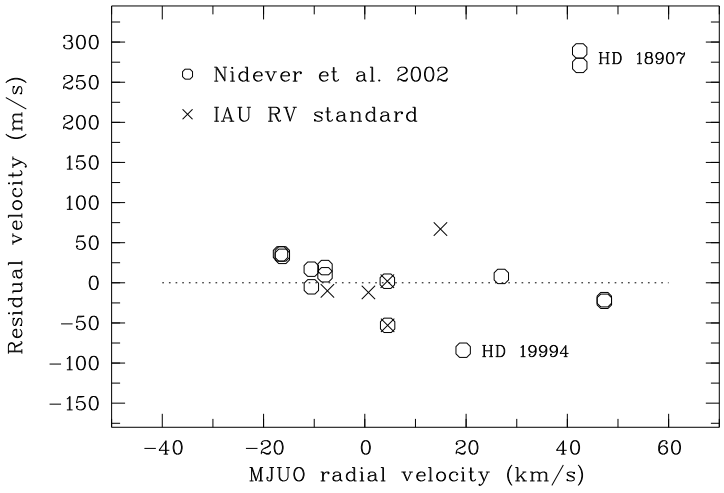

Figure 6.4: The residuals $V_{\rm MJUO} - V$pub for the IAU radial-velocity standards and the unevolved stars in common with the list of Nidever et al. (2002). HD 19994 is now known to harbour a Jupiter-mass companion. On the basis of the large residual velocity measured, HD 18907 is suspected of being a spectroscopic binary.

same velocity zero-point and systematic errors of the same magnitude as the published values.

Nidever et al. (2002) have derived calibration relations that estimate the total contribution made by the gravitational redshift and the convective blueshift in relation to $(B-V)$, allowing a corrected velocity, $V_{\rm corr}$, to be derived from the spectroscopic velocity, $V_{\rm spec}$:

$$\begin{aligned} V_{\rm corr} &= V_{\rm spec} - 2.317 \times (B-V) + 1.483 \ {\rm km\,s^{-1}}\,, & B-V < 0.64\ ; \\ V_{\rm corr} &= V_{\rm spec} - 0.642 \times (B-V) + 0.411 \ {\rm km\,s^{-1}}\,, & 0.64 < B-V < 1.3\ ; \\ V_{\rm corr} &= V_{\rm spec} \ {\rm km\,s^{-1}}\,, & B-V = 0.64\,. \end{aligned}$$

Nidever et al. (2002) estimated that these corrections brought their velocities within $0.15\,{\rm km\,s^{-1}}$ of their true values. It seems reasonable to suggest that this calibration is rather crude as it is based on only three data-points (at F5V, G2V and K0V) to determine the two lines of regression. In addition, no errors are given for the regression coefficients.

6.5 Relative and barycentric systemic velocities

As described in Item 12 on page 86, all of the velocities measured from HERCULES observations have had barycentric corrections applied to them. All of the weighted-mean velocities are relative to the chosen template spectrum. The only system for which the template was of solar origin is HD 217166, which comprises two solar-type stars. Therefore, only the velocities coresponding to this binary can be considered to have (approximately) barycentric values.

The decision to use relative velocities does not compromise the subsequent analysis of any of the binary systems for a number of reasons. First, the velocity zero-point is irrelevant with regard to the measurement of the orbital elements or mass ratio, or their errors. Second, none of the orbital solutions that will be derived include observations from other instruments in a manner that would require a common velocity zero-point. Finally, attempts to calibrate precise radial velocities against a purported standard star are significantly complicated by factors now well recognized, as has been described above. The only velocity that deserves further attention so that a barycentric velocity can be estimated is the adjustment of the relative systemic velocity, $\gamma_{\rm rel}$, to that of the true systemic velocity, γ. As recommended by Lindegren & Dravins (2003), this estimate is treated separately for each system. The way that this has been carried out is now outlined.

To estimate the true systemic velocity γ of the particular binary system, it was necessary to know the barycentric velocity of the template spectrum. There are two ways to go about achieving this, and both utilize the velocities prepared and listed above in Table 6.1 and Table 6.2:

1. Use the velocity measured for the template spectrum relative to the 30 sky spectra, $V_{\rm sky}$. This will be best suited to solar-type stars as these will have the smallest spectral-type mismatch. Since any mismatch correction is not known, the approximate systemic velocity is given by

$$\gamma = \gamma_{\rm rel} + V_{\rm sky} \,. \tag{6.1}$$

2. Cross-correlate the template spectrum with a spectrum of another star whose barycentric velocity, $V_{\rm bary}$ $(= V_{\rm pub})$, has been measured independently, to determine the velocity difference, $V_{\rm diff}$, between the two stars. This approach has the potential advantage that the comparison star can be carefully chosen to have a small or perhaps negligible spectral mismatch, but now three velocity values are required in the measurement of γ :

$$\gamma = \gamma_{\rm rel} + V_{\rm diff} + V_{\rm bary} \,. \tag{6.2}$$

This method is considered more appropriate when the spectral type of the stars is significantly non-solar.

6.6 The spectroscopic orbital solution

This project has had an observational time span of about three years. Those binary systems that have periods much more than about 5 – 6 years are unlikely to have sufficient orbital phase sampling to permit measurement of the majority of the system's orbital elements. The measurements achievable for the systems with longer orbital periods are limited to estimates of the system mass ratio, q, and the systemic velocity, γ, by methods described in § 3.2.2 on page 26.

However, when the orbital period is less than several years, adequate orbital phase sampling allows the spectroscopic orbital elements to be measured from the radial velocities obtained.

Measuring a binary system's orbital elements using spectroscopic observations may provide better precision for some elements than had been obtained by previous methods, e.g. astrometry, and therefore every effort should be made to achieve this worthwhile goal. As a result of any improvements, not only will the orbit be better defined, but better precision may also be attained for related parameters such as the component masses.

The elements of a single spectrum orbital solution are γ, e, P, T, ω_n, and K_n, where $n = 1$ or 2. Other quantities of astrophysical interest that can be derived from these elements include the mass function, $f_{\mathcal{M}}$ (Eq. 3.14 on page 28), and the projected semi-major axis

$$a_n \sin i = (9.1920 \times 10^{-5})\, K_n\, P\sqrt{1-e^2}\ \mathrm{AU}\,, \tag{6.3}$$

where K_n is given in kilometres per second and P is in days. Considerable advantage arises when the companion's orbital elements can also be deduced. Having both K_1 and K_2 makes it possible to determine the system mass and component masses, each scaled by $\sin^3 i$ (Eq. 3.13 on page 28). The companion's projected semi-major axis can now be measured and this leads to a value for the semimajor axis of the relative orbit, $a \sin i$. If the projected angular relative semimajor axis, $a'' \sin i$, is known from astrometry, the parallax of the system can also be deduced, since

$$p'' = \frac{a'' \sin i}{a \sin i\ (\mathrm{AU})} = 10,879 \times \frac{a'' \sin i}{(K_1 + K_2)\, P\sqrt{1-e^2}}\,. \tag{6.4}$$

In addition, the reader is reminded of a means to determine the parallax by linear regression using the relative orbit and radial velocities (Eq. 3.7 on page 24), even when a spectroscopic solution is not available.

Many methods have been devised for deducing spectroscopic orbital elements. The vast majority of these methods are based on an analysis of the properties of the radial-velocity equation, where the velocity V is expressed as follows:

$$V(t) = \gamma + K\Big\{e\cos\omega + \cos\big[\upsilon(t) + \omega\big]\Big\}\,. \tag{6.5}$$

The elements P, T and e determine the true anomaly, υ, at a given time t. This fundamental equation was first deduced by Lehmann-Filhés (1894) by differentiation of the space coordinate z (defined in § A.11 on page 223) and later by Paddock (1913) using the equations of motion of celestial mechanics. Numerous methods have been devised for determining the spectroscopic orbital solution for a binary system. In general, these may be divided into three categories:

1. graphical, in terms of geometric properties, e.g. see Binnendijk (1960; where descriptions of the methods of Lehmann-Filhés, Schwarzschild, and others may be found),

2. analytical, in terms of trigonometric series, e.g. Wilsing's method (which was extended by Russell 1902); Monet (1979); and Singh (1983),

3. differential, which use a least-squares solution for differential corrections to a preliminary set of orbital elements e.g. Lehmann-Fihlés (1894); Paddock (1915); Sterne (1941b).

The differential approach will be used in the following analyses.

6.6.1 Least-squares differential corrections

The size of the dataset, the precision of the velocities measured and the extent to which the orbit has been sampled by the observations will dictate the reliability and quality of the orbital solution. However, regardless of the underlying method used to estimate the orbital elements, improvement to them or at least confidence that they have been deduced with minimal personal judgment or bias, is usually pursued by subjecting the Q observations of (V, t) and the associated elements to an iterative least-squares analysis using a method known as differential corrections. This approach was also first described by Lehmann-Filhés (1894). The strategy of this method will now be outlined.

If $z = f(x, y)$ has continuous first derivatives at the point (x, y), then the *increment* $\Delta z = f(x + \Delta x,\ y + \Delta y) - f(x,\ y)$ can be written as

$$\Delta z = \frac{\partial f}{\partial x}\Delta x + \frac{\partial f}{\partial y}\Delta y + \epsilon_1 \Delta x + \epsilon_2 \Delta y = \frac{\partial f}{\partial x}\mathrm{d}x + \frac{\partial f}{\partial y}\mathrm{d}y + \epsilon_1 \mathrm{d}x + \epsilon_2 \mathrm{d}y = \Delta f$$

where $\epsilon_1 \to 0$, $\epsilon_2 \to 0$ as $(\Delta x, \Delta y) \to (0, 0)$. Δz is the change in z along the *surface* z produced by the changes Δx and Δy in x and y. The *differential* of z is

$$\mathrm{d}z = \frac{\partial f}{\partial x}\mathrm{d}x + \frac{\partial f}{\partial y}\mathrm{d}y\,,$$

which is also known as the *principal part* of Δz. Thus $\Delta z = \mathrm{d}z + \epsilon_1 \mathrm{d}x + \epsilon_2 \mathrm{d}y$. $\mathrm{d}z$ is the change in z along the tangent plane at (x, y) to the surface z. Thus, ϵ_1 and ϵ_2 are related to the distances between the surface and the tangent planes for x and y respectively. In the case when $\mathrm{d}x = \Delta x$ and $\mathrm{d}y = \Delta y$ are small, $\Delta z \approx \mathrm{d}z$ and the change in z along the surface and along the tangent plane are approximately equal.

For the more general case, the Taylor expansion of Δz in the neighbourhood of certain preliminary values (Δx, Δy) will be

$$\Delta z = \frac{\partial f}{\partial x}\Delta x + \frac{\partial f}{\partial y}\Delta y + \frac{1}{2}\left[\frac{\partial^2 f}{\partial x^2}(\Delta x)^2 + \frac{\partial^2 f}{\partial y^2}(\Delta y)^2 + 2\frac{\partial^2 f}{\partial x \partial y}(\Delta x)(\Delta y) + \ldots\right].$$

Similarly, $V = f(\gamma, K, e, \omega, T, P)$, which is analytic for $0 \leq e < 1$, can be written in differential form as follows

$$\Delta V \approx \mathrm{d}V = \frac{\partial f}{\partial \gamma}\Delta\gamma + \frac{\partial f}{\partial K}\Delta K + \frac{\partial f}{\partial e}\Delta e + \frac{\partial f}{\partial \omega}\Delta\omega + \frac{\partial f}{\partial T}\Delta T + \frac{\partial f}{\partial P}\Delta P\,, \tag{6.6}$$

where the higher terms have been neglected and ΔV is the change in the velocity produced by changes in the elements $\Delta\gamma$, ΔK,... ΔP. Substitution for the partial derivatives in Eq. (6.6) yields Lehmann-Filhés' (1894) equations of condition for the least-squares solution:

$$\begin{aligned}
\Delta V \approx \mathrm{d}V \;\; = \;\; & \Delta\gamma \\
& + \left[\cos(\upsilon + \omega) + e\cos\omega\right]\Delta K \\
& + K\left[\cos\omega - \frac{\sin(\upsilon+\omega)\sin\upsilon(2 + e\cos\omega)}{(1-e^2)}\right]\Delta e \\
& - K\left[\sin(\upsilon+\omega) + e\sin\omega\right]\Delta\omega \\
& + K\left[\left(\frac{2\pi}{P}\right)\frac{\sin(\upsilon+\omega)(1+e\cos\upsilon)^2}{(1-e^2)^{3/2}}\right]\Delta T \\
& + K\left[\left(\frac{2\pi}{P}\right)\left(\frac{t-T}{P}\right)\frac{\sin(\upsilon+\omega)(1+e\cos\upsilon)^2}{(1-e^2)^{3/2}}\right]\Delta P\,,
\end{aligned} \tag{6.7}$$

where it may be noted that the term

$$\left(\frac{2\pi}{P}\right)\frac{(1+e\cos\upsilon)^2}{(1-e^2)^{3/2}}$$

appearing with ΔT and ΔP is the expression for the time rate of change of the true anomaly, $\mathrm{d}\upsilon/\mathrm{d}t$ (Eq. A.52 on page 221).

The coefficient (ΔK, etc.,) of each element's differential, and the difference between the observed velocity (O) and the calculated velocity (C) obtained using Eq. (6.5), i.e. $\Delta V = (O - C)$, can be determined using an initial estimate for each orbital element (γ', K', etc.,). This process is undertaken for the Q observations at each time t so that a set of simultaneous equations results, each in terms of the six differential terms. Assuming there are more equations than differential terms (i.e. $Q > 6$), the simultaneous equations will be over-determined. If the initial estimates are sufficiently 'close' to a final solution, the first and subsequent iterations of a linear least-squares analysis of these equations will converge to a 'best' fit. Each iteration provides revised, and hopefully improved, values for each orbital element ($\gamma'' = \gamma' + \Delta\gamma$, $K'' = K' + \Delta K$, etc.), hence the method's name. With a greater number of observations and more accurate initial estimates, the convergence of the least-squares fitting algorithm to a complete solution will occur faster. When the corrections are large enough that the higher-order terms ($\partial^2 f/\partial K^2(\Delta K)^2$,

etc.,) cannot be neglected, convergence will not be achieved. This method and the one that follows has the added benefit that unequal weights can be assigned to the various observations.

6.6.2 Orbits with low eccentricity

Lehmann-Filhés' method works well for many orbits, in particular those that have an eccentricity $e \gtrsim 0.15$. This is because the time of periastron passage T and the longitude of periastron ω are adequately defined in these cases. However, as the eccentricity approaches zero, both T and ω become increasingly indeterminate. Thus the solution becomes more and more unstable.

The difficulty was addressed by Sterne (1941b) who replaced the reference time of periastron passage T with the *time of zero mean longitude* T_0. Sterne defined the *mean longitude* L by

$$L = \frac{2\pi}{P}(t - T) + \omega = \Phi + \omega \,,$$

where Φ is the mean anomaly (§ A.6.1 on page 215). The time of zero mean longitude T_0 occurs when $\Phi = -\omega$, which approaches the time of ascending-node passage, $t_{\rm asc}$ (when $\upsilon = -\omega$), as the eccentricity approaches zero. The advantage of this strategy is that $t_{\rm asc}$ is always defined as it coincides with the time of maximum positive velocity.

Two partial derivatives in the differential corrections Eq. (6.7) require modification to reflect the change of T to T_0. These are the coefficients for $\Delta\omega$ and ΔP. Thus, we have

$$\begin{aligned}
\Delta V \approx {\rm d}V \;\; = \;\; & \Delta\gamma \\
& + \left[\cos(\upsilon + \omega) + e\cos\omega\right]\Delta K \\
& + K\left[\cos\omega - \frac{\sin(\upsilon+\omega)\sin\upsilon(2 + e\cos\omega)}{(1-e^2)}\right]\Delta e \\
& - K\left[\sin(\upsilon+\omega) + e\sin\omega - \frac{\sin(\upsilon+\omega)(1+e\cos\upsilon)^2}{(1-e^2)^{3/2}}\right]\Delta\omega \\
& + K\left[\left(\frac{2\pi}{P}\right)\frac{\sin(\upsilon+\omega)(1+e\cos\upsilon)^2}{(1-e^2)^{3/2}}\right]\Delta T_0 \\
& + K\left[\left(\frac{2\pi}{P}\right)\left(\frac{t-T_0}{P}\right)\frac{\sin(\upsilon+\omega)(1+e\cos\upsilon)^2}{(1-e^2)^{3/2}}\right]\Delta P \,. \qquad (6.8)
\end{aligned}$$

After the least-squares solution has been obtained, determining the value for the conventional reference time, T, is straightforward. At $t = T_0$, $\Phi = -\omega$, and therefore

$$T = T_{0,\,\rm n} + \frac{\omega_{\rm n} P}{2\pi} \,, \qquad (6.9)$$

where $n = 1, 2$ for the primary and secondary components respectively. Hence, whereas T is common to both stars, T_0 differs for them by $P/2$. This is a very minor complication for a method

that is suitable for orbits of all eccentricities. However, since deriving the time of periastron passage T from T_0 relies on the period, the calculation of the error in T can be unnecessarily large if the period is very uncertain owing to an inadequate dataset. In these cases, particularly if e is considerably non-zero, the method of Lehmann-Fihlés may provide a more precise measure of T.

For the systems that provide velocities for both stars, the recommendations of Jones (1969) have been followed so as to obtain a simultaneous solution for both stars; namely, derive the mass ratio and systemic velocity by calculating the linear regression of the velocities (the results of which are independent of any subsequent measure of the elements; see § 3.2.2 on page 26), then convert the velocities of the secondary into velocities of the primary using Eq. (3.10). Finally, the method of differential corrections of Lehmann-Fihlés or Sterne was applied to estimate the orbital solution.

6.7 Error estimates

The proper estimation of the error of each orbital parameter is just as important as deriving the value of the parameter itself. In this thesis, whenever possible, the approach taken to estimate the errors of a parameter has been based upon numerical simulations (e.g. Nidever et al. 2002; Skuljan et al. 2004). We begin by assuming that the system parameters obtained from the least-squares fit describe the true situation, whether it is the radial-velocity curve, or the linear regression of the pairs of velocities of an SB2 to determine the system mass ratio q and systemic velocity γ (see § 3.2.2 on page 26). The r.m.s. error of the fit can be regarded as the standard deviation, σ, of a single observation around the fit. Many random copies ($N = 100$ always) of the original set of velocities were created for each binary system by replacing every observed velocity by a random value assuming a gaussian distribution $G(\mu, \sigma)$, where μ is the mean value obtained from the fit. Each random set is regarded as a possible outcome of the measurement process, and it has been used to derive a corresponding set of parameters. From the N values determined for each parameter, it is possible to calculate the associated standard deviation.

For the estimation of the errors of the mass ratio and systemic velocity determined by the linear regression of SB2 observations (using Eq. (A.76) on page 229), since random errors exist in both sets of velocities, the recommendations of Isobe et al. (1990a) were followed, and the r.m.s. error used for the numerical simulation was the pythagorean sum of both regressions, x vs. y and y vs. x. The final values for q, γ (or $\gamma_{\rm rel}$) and their errors obtained in this way was the weighted mean of each pair of values.

Conventional error propagation (e.g. Bevington 1969) was applied in the remaining appropriate circumstances, such as for the estimation of component masses from the system's total mass and mass ratio.

6.8 Fixing some orbital elements in the least-squares orbital fit

Not all of the differential terms need be kept as free variables in the least-squares fitting procedure. For instance, the period may have previously been accurately ascertained using photometric observations if the binary system displays eclipses. Fixing the period is advisable in such circumstances to give a better separation of the unknowns ΔT and ΔP (Petrie 1962).

Occasions may also arise when there are insufficient spectroscopic radial velocities and orbital phase sampling for convergence of the least-squares method to be achieved having all six orbital elements as free variables. Once again, an independent estimate of one of the orbital elements may provide the way forward. When varying velocities of both stars are available from SB2 observations, these will allow an estimate to be made of the systemic velocity by calculating the linear regression of the corresponding pairs of velocities.

6.9 Combining other datasets with the HERCULES observations

Combining datasets from the same or different methods of observation may yield more precise orbital parameters (e.g. Morbey 1975; Pourbaix 1998; Davis 1999, for spectroscopic and astrometric datasets; Wilson 1979, for spectroscopic and photometric datasets). Considerable advantage may be achieved with these methods, but some caution is appropriate should one dataset be of such poor quality that it simply degrades the better one.

In this thesis, the combination of other datasets with the MJUO observations was limited to other radial-velocity measurements. Before the final solution for a system was derived, it was sometimes possible to make use of the long timespan between the present HERCULES (V, t) set of observations and the one secured in the past, so that the period could be determined more accurately and with better precision. Consequently, the precision achieved for the other parameters improved as well. Whilst such 'historical' data may be of much lower precision, an advantage can arise in its use if a large number of orbital cycles have subsequently elapsed (as, for instance, was shown by Skuljan et al. 2004). The strategy used will be decribed shortly.

Three of the spectroscopic binary systems included in the final analysis to be described in Chap. 7 already had published spectroscopic orbital solutions. In each case these solutions have been derived using radial-velocity data acquired from 40–90 years ago, and are not considered to be definitive (Pourbaix et al. 2004). Since none of these historical measurements have precision anywhere near that of the HERCULES observations, it is not simply a matter of combining the historical and modern data into a single set and then deriving a new orbital solution. Two significant obstacles make this approach challenging. First, the velocities would have to be properly weighted (certainly the historical velocities would have a very low weight, since the orbital fits derived with the historical data always had an r.m.s. error that is typically 30–40 times greater than that of the modern observations). And second, the historical and modern values would have to be brought to the same velocity zero-point.

Instead, consideration is made of the possibility that the historical and modern series of observations are separated by an adequate interval of time so that a statistically useful number of complete orbital cycles separate the two data sets (Petrie 1962; Batten 1973). Naturally, a sensible time interval should include an integer number, or thereabouts, of complete orbital cycles. By selecting a suitable reference epoch $t_{\rm ep}$ for each dataset, an estimate of a mean period, $\bar{P}$, perhaps with a much reduced error, can be determined by comparing the historical and modern values of this time. There are four epochs that readily lend themselves to this approach:

1. the time of periastron passage, T,
2. the time of zero mean longitude, T_0,
3. a time of nodal passage, or
4. a time of ascending or descending radial velocity, close to the systemic velocity. This time is more suitable for SB1 systems.

The epochs that can be considered will depend upon the nature of the radial velocity curve and the orbital phase sampling available in the two datasets to be compared. For example, an orbital solution is needed to estimate T or T_0 , whereas the other two epochs only require sufficient observations in their vicinity to establish a reference value, perhaps by fitting a suitable function such as a cubic polynomial or a sinusoid to the available data. T_0 is often more precisely defined than T, regardless of the eccentricity of the orbit, so that again Sterne's method may be the most suitable to use if one of these strategies is to be pursued.

Once the most favourable epoch has been decided, the approach taken is as follows: we begin by dividing the time interval $\Delta t_{\rm ep} = t_{\rm ep(modern)} - t_{\rm ep(hist)}$ by the total number of complete cycles, $N_{\rm c}$, that the time interval contains to obtain a new mean period:

$$\bar{P} = \frac{\Delta t_{\rm ep}}{N_{\rm c}} \,. \tag{6.10}$$

Similarly, the corresponding error $\sigma_{\bar{\rm P}}$ is estimated as

$$\sigma_{\bar{\rm P}} = \frac{\sigma_{\Delta t_{\rm ep}}}{N_{\rm c}} \,, \tag{6.11}$$

where $\sigma^2_{\Delta t_{\rm ep}} = \sigma^2_{\rm t_{ep}(hist)} + \sigma^2_{\rm t_{ep}(modern)}$.

Chapter 7

Results and analysis

In some cases, insufficient observations were obtained of the binary systems included in the original list of programme stars to allow any meaningful analysis of them to be undertaken. Preliminary results are provided for two systems, θ Antliae and 94 Aquarii A in Appendix B.

Two additional systems were observed that had triple-lined spectra, HD 10800 (G2V $V = 5\overset{\mathrm{m}}{.}9$), and HD 118261 (F6V $V = 5\overset{\mathrm{m}}{.}6$). No attempt to determine the velocities for these systems has yet been attempted. Instead, the cross-correlation functions created for a single order for each series of observations are reproduced in Appendix B so that a preliminary insight into each system can be acquired (for HD 10800, see Fig. B.3–Fig. B.6, and for HD 118261, see Fig. B.7–Fig. B.9). Each cross-correlation diagram includes the observation's MJUO archive-file number.

HD 10800 was originally included as a possible radial-velocity standard star for HERCULES observers as its brightness, solar spectral-type and far southern declination, ($\delta \approx 83°$), made it a a convenient target from MJUO. Unfortunately, from the point of view of using it as a standard, we were unaware that its variablity in this regard had previously been noted (Buscombe & Morris 1958). The triple nature of the system has since been reported in the literature, after our first observation identified it as such (Wichmann et al. 2003).

The results arising from those systems observed adequately to yield measurements of orbital elements and component parameters such as the system mass ratio and component masses will now be presented. Three of the systems are SB1s and three are SB2s, one of the latter of which was discovered during the first week of HERCULES operations whilst the writer was assisting in another observing program.

The single-lined binary systems

Three SB1 binary systems were observed sufficiently to allow the spectroscopic orbital solution to be determined with substantially better precision than had been previously achieved.

β Reticuli and ν Octantis have many similar characterisitics which have presumably influenced the inclusion of both stars in various studies, including this one. Both have solar-metallicity, early K-type giant primary components that are bright — V magnitude about $3\overset{\mathrm{m}}{.}8$. Both stars are circumpolar at MJUO, and this, in addition to their brightness, was a significant factor in the final results obtained for both systems in this thesis. These factors allowed observations to be made more regularly and in conditions that were unsuitable for fainter objects.

Both β Ret and ν Oct are in the solar neighbourhood which contributes to the relatively large proper motion that each star has (β Ret: $\sim 0.3''\,\mathrm{yr}^{-1}$, ν Oct: $\sim 0.25''\,\mathrm{yr}^{-1}$; ESA 1997).

Neither star is recognized as being active in terms of Ca II (Warner 1969), radio (Slee et al. 1989; Beasley et al. 1992) or X-ray (Hünsch et al. 1996) emissions, and neither star has a significant lithium abundance (Costa et al. 2002). Each of these observations has been described as being consistent with the primary star's slow rotation, $v_{\mathrm{equ}} \sin i \lesssim 2\,\mathrm{km\,s}^{-1}$. Based upon photometric and spectroscopic data, both stars are believed to be members of the old disk population (Eggen 1993). β Ret and ν Oct have also been included studies of optical polarization (e.g. Tinbergen 1979, 1982). The first of these determined that β Ret and ν Oct could be considered as candidate stars to be used as zero-polarization standards. The second paper helped to establish the very low dust content of the local interstellar medium. Neither star exhibits an infra-red excess (Kwok et al. 1997), a result that is not surprising given the evolutionary stage of each giant star, when substantial mass loss (more typical of asymptotic giant branch stars) is not likely to be occurring.

The binary nature of β Ret and ν Oct was discovered as a result of radial-velocity observations acquired at the beginning of the 20th century on the D. O. Mills Expedition to Santiago, Chile. To date, the only spectroscopic orbital solution for each of these stars has been determined from these observations combined with others acquired at the Cape Observatory in South Africa, also secured during the first two decades of that century. The orbital grade of each system is currently classified as 'average', grade 3 (Pourbaix et al 2004). Each orbit has a period of about three years and is of moderate eccentricity ($e \sim 0.3$). For both systems, the unseen companion is likely to be a cool M-type dwarf or a white dwarf.

Subsequently, both β Ret and ν Oct have had a photocentric orbital solution derived. The solution for ν Oct has been derived solely from ground-based observations obtained a decade or so after the radial-velocity observations, whereas that of β Ret could only be determined by the combination of the historical spectroscopic solution and *Hipparcos* astrometry.

The third SB1 system, HD 159656 (G4IV–V), is also believed to have an M-dwarf or white dwarf companion. The orbital period is only about 10 days whilst the eccentricity is $e \sim 0.11$. As a result of the HERCULES observations acquired, a spectroscopic orbital solution of very high precision has been derived for this system. It appears that rapid rotation of the primary star, synchronized with the orbital period, has led to the considerable Ca II and X-ray activity observed for this system.

7.1 β Reticuli (HD 23817 HIP 17440 HR 1175; $3^{\mathrm{h}}44^{\mathrm{m}}12^{rms}$, $-64°48^{\mathrm{m}}25^{\mathrm{s}}$)

The precise V magnitude of β Ret is $V = 3\overset{\mathrm{m}}{.}840 \pm 0.006$ (Mermilliod 1987). Until *Hipparcos*, the parallax of β Ret had been estimated to be as large as 45.4 ± 6.9 mas (van Altena et al. 1995), which corresponds to a distance of only 22 pc. Fortuitously, this allowed the inclusion of β

Ret in several studies of stars within 25 pc (e.g. Gliese & Jahreiss 1988; Hünsch et al. 1996). Subsequently, however, *Hipparcos* measured the parallax to be 32.71 ± 0.46 mas, placing it at the greater distance of 30.57 ± 0.43 pc. Assuming no significant interstellar reddening ($E(b-y) = 0$; Eggen 1993), the absolute magnitude is then $M_{\rm V} = +1\overset{\rm m}{.}41 \pm 0.03$, where the error is estimated using $\sigma^2_{M_{\rm V}} = (\sigma_{m_{\rm v}})^2 + \left(5 \log_{10} {\rm e}\ \sigma_{p''}/p''\right)^2$.

The *Hipparcos* observations also identified this star as being very stable photometrically ($H_{\rm p} = 4\overset{\rm m}{.}0019 \pm 0.0005$ (ESA 1997); see also Adelman 2001). The $UBVRI$ colours of β Ret have also been measured in the Johnson and Cousins systems: $(B-V) = 1\overset{\rm m}{.}133 \pm 0.005$ and $(U-B) = 1\overset{\rm m}{.}107 \pm 0.005$ (Mermilliod 1987); $(R-I)_C = 0\overset{\rm m}{.}520 \pm 0.020$ and $(V-I)_C = 1\overset{\rm m}{.}105 \pm 0.020$ (Bessel 1990). The metallicity is estimated to be [Fe/H] $= -0.01$ (Eggen 1993).

The spectral type was initially described as K0IV (Evans et al. 1957), then as K1/K2III (Houk & Cowley 1975). More recently, Keenan & Barnbaum (1999) used the *Hipparcos* parallax to make a minor revision to a spectral type of K2IIIb:. The 'b' places β Ret in the luminosity class that defines members of the "clump" region of the H-R diagram, whilst the colon indicates that β Ret is not a reliable standard for stars of normal solar composition. The clump region is a relatively compact area that lies about 1 mag below the main giant branch, centred near $M_{\rm V} = +1$, $(B-V) = +1.0$ (Cannon 1970; Keenan & Barnbaum 1999), or at about $(R-I)_C = +0.46$. The clump is believed to be associated with the loops of evolutionary tracks of low-mass stars, where core helium burning may be prolonged by overshoot with semi-convective mixing (Tinsley & Gunn 1976).

There is only a moderate range of luminosity within clumps, which naturally suggests their use as indicators of Galactic and intergalactic distances as well as interstellar reddening. For example, red clump giants have been used in studies to estimate the Galactocentric distance (Paczyński & Stanek 1998), to map the interstellar extinction in Baade's window (Woźniak & Stanek 1996), and for estimating the distance modulus of the LMC, SMC and the Carina dwarf galaxy (Udalski Acta Ast. v.48 1998). However, caution in this regard has been recommended by others such as Giraldi & Salaris (2001), who have noted that the likely significant influence of interstellar extinction, population effects and the star formation history upon the red clump magnitude in these stellar systems, makes distance moduli measurements uncertain by up to ~ 0.3 magnitudes.

β Ret has a common proper-motion companion ($V = 7\overset{\rm m}{.}85$, CPD $-65°272$) at $24.4'$. Based on the available similar parallaxes, Gliese & Jahreiss (1988) estimated a projected separation of 33 000 AU, and hence suggested that they were one of 32 of the widest common proper-motion pairs in the solar neighbourhood. However, because of the disparity in the radial velocities, $\sim 32\,{\rm km\,s^{-1}}$, they considered that these stars did not form a physical system. Further support for this conclusion arises from the more recent *Hipparcos* astrometry of these stars (ESA 1997), which places them at significantly different distances. The companion, HIP 17748 ($m_{\rm v} \sim 8^{\rm m}$), has a parallax $p'' = 23\overset{''}{.}65 \pm 0.87$, so that the two stars are separated in space by about 12 pc.

Historical spectroscopic orbital solution

The variable radial velocity of β Ret was first detected by Palmer in 1906 from observations obtained at the San Cristobal Observatory, Santiago, Chile, during the first years of the Lick Observatory's D. O. Mills Expedition. Beginning with a preliminary solution derived using Russell's graphical method, followed by a differential correction procedure, Jones (1928) was able to determine an orbital solution (parameter set (1) in Table 7.1). He used 18 plates from these Lick observations and an additional 18 plates secured at the Cape Observatory, together obtained from 1903 to 1925.

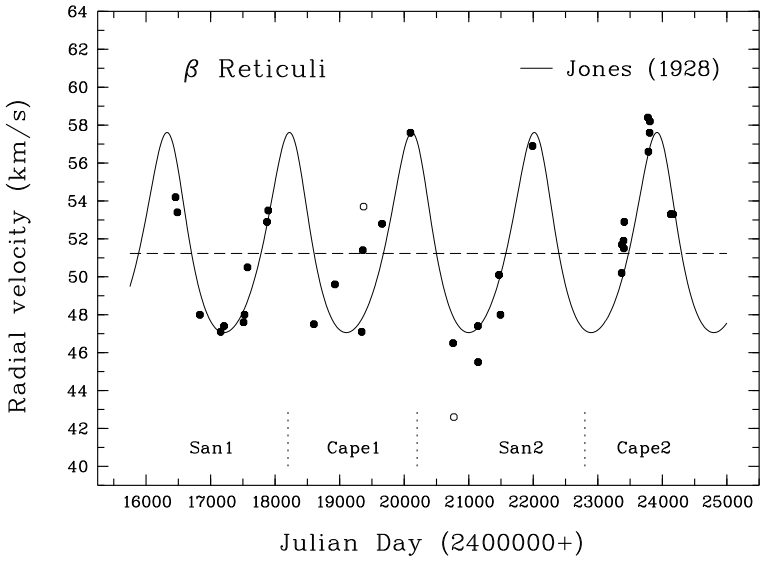

Figure 7.1: The historical radial velocities of β Ret and the velocity curve computed from the orbital elements. The solid symbols identify observations included in the solution (Jones, 1928) and the horizontal line corresponds to the systemic velocity γ. The labels San1...Cape2 identify the four series of plates used (see text).

It is interesting and easy to appreciate that there are considerable differences in the scatter of the velocities that Jones had to work with. The data included in Jones' solution was divided between four series of plates taken in the following order: from Santiago (1903–1907), the Cape Obs. (1909–1912), again from Santiago (1913–1919), and finally, once again from the Cape (1922–1925). These four time intervals are labelled on Fig. 7.1 respectively as San1, Cape1, San2, and Cape2. Clearly, the 'San1'and 'Cape2' velocities have much lower scatter that do the 'San2' and the 'Cape1' data. The differing precision of the velocities from the two observatories taken over separate time intervals may be attributed to changes to the personnel acquiring the spectra, those measuring the spectra, or the instrumentation employed.[1].

[1]See Hearnshaw (1986, pp.160–169) for further general historical comment with regards these two observatories

MJUO spectroscopic orbital solution

β Ret had 95 HERCULES spectra obtained of it between 2002 June 4 and 2004 August 1, or just over two years, using a resolving power of 41 000. The velocities measured are provided in Table C.1 in Appendix C. The radial velocities are plotted on Fig. 7.2 together with the best-fitting curve calculated from the orbital parameters derived using Sterne's method (§ 6.6.2 beginning on page 121). The corresponding residuals are also plotted on Fig. 7.2, and included in Table C.1 Appendix C. A periodogram analysis of the velocity residuals has not revealed any additional significant periodic behaviour. The time of periastron passage, T, the primary star's projected semi-major axis, $a_1 \sin i$, and the mass function, $f_{\mathcal{M}}$, have also been derived. The r.m.s. of this orbital solution is 24 $\mathrm{m\,s^{-1}}$ (see paramter set (3) in Table 7.1).

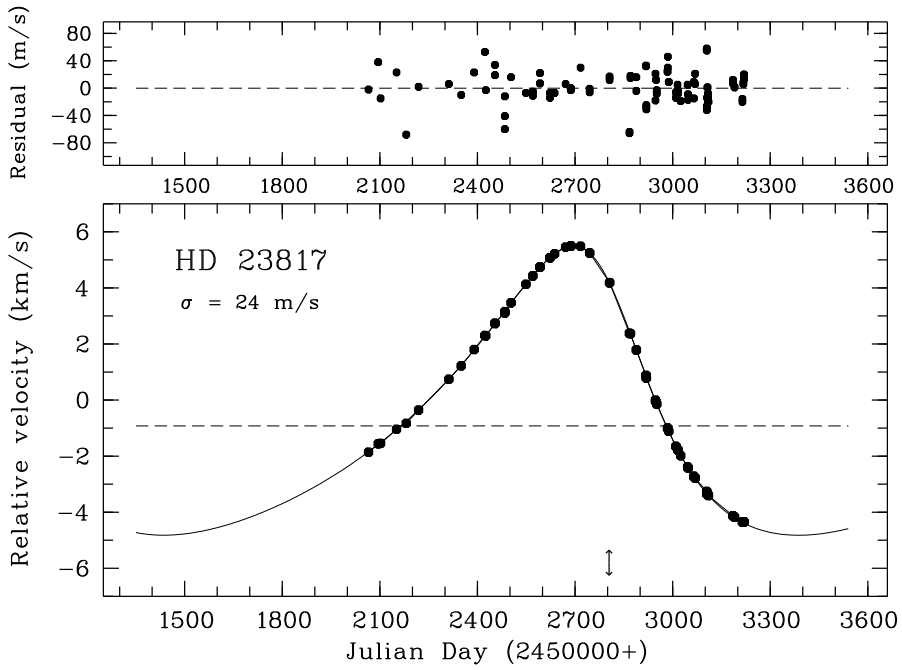

Figure 7.2: Bottom: The radial-velocities and corresponding curve for β Ret, from observations obtained at MJUO from 2002 June 4 to 2004 August 1. The dashed horizontal line identifies the relative systemic velocity, γ_{rel}. The '↕' symbol indicates a time of periastron passage. Top: The residual velocities.

and their contribution to early radial-velocity programs. Whether or not β Ret is an isolated case with regard the scatter of the velocities acquired from these two observatories during different time intervals (which seems unlikely) would require re-examination of other velocity data that is similarly divided in time. Lunt (1919), for instance, points out that the two datasets he was dealing with differed in precision as a result of differing spectrograph slit widths.

	β Reticuli	K_1 ($\mathrm{km\,s^{-1}}$)	e	ω_1 (°)	T_0 (JD 24...)	T (JD 24...)	P (day)	γ_{rel} ($\mathrm{km\,s^{-1}}$)	$a_1 \sin i$ (Gm)	$f_{\mathcal{M}}$ ($\mathcal{M}_\odot$)	fit rms ($\mathrm{km\,s^{-1}}$)
1.	Jones, 1928	5.19	0.210	13.8	–	20 086.1	1911.5	+51.11	133.4	0.025 95	–
		± 0.25	0.044	14.3	–	68.3	32.2	–	–	–	
2.	Cape1 & San2	5.36	0.238	18.16	20 012.0	20 092.9	1900.7	+51.17	135.9	0.0277	0.96
	with weight 0.3	± 0.35	0.049	15.9	17.0	75.1	8.0	0.23	8.5	0.0051	
3.	present work	5.135	0.3355	41.48	52 581.90	52 804.3	1929.9	−0.922	128.4	0.022 63	0.024
	(all elements free)	± 0.014	0.0029	0.38	0.82	1.1	15.3	0.030	1.2	0.000 29	
4.	combined	5.1236	0.333 01	41.79	52 582.64	52 805.07	1915.9	−0.8945	127.28	0.022 384	0.024
	(period fixed)	± 0.0046	0.000 98	0.14	0.28	0.58	(fixed)	0.0052	0.14	0.000 074	

Table 7.1: The spectroscopic orbital parameters for β Ret. The first sets of parameter are those due to Jones (1928). The second set (San1 & Cape2) is a solution determined using the computational methods of the present study, but including only the better precision velocity measurements published by Jones (1928); see text. The third parameter set uses only the velocities of the present work, and the fourth and final set is derived using a fixed period based on both the historical and modern measurements (see text for details). Note that the measures of the systemic velocity from the historical data alone are estimates of the barycentric value.

Combining the historical and modern velocities

The historical velocities include several complete orbits of the β Ret system, but result in an orbital solution of only moderate precision due to the poor precision of the velocities, in particular of the observations labelled on Fig. 7.1 as 'Cape1' and 'San2'. The observations obtained during this study yield an orbital solution with smaller errors, although the period is still known with relatively poor precision ($\pm$15.3 days). However, a solution of significantly better precision is possible if the historical and modern velocities are suitably combined.

If we apply our modern computational methods to these historical data, we can derive the elements and their errors in the same way that we have for the HERCULES observations. However, before we do this, it is appropriate that we weight the less precise historical data (corresponding to the time intervals 'Cape1' and 'San2') accordingly. These velocities have an r.m.s. that exceeds the better 'Cape2' and 'San1' data by a factor of about 1.8 times (r.m.s. 1.6 $\mathrm{km\,s^{-1}}$ vs. 0.9 $\mathrm{km\,s^{-1}}$). Therefore the 12 velocities of poorer precision are given weights of $1/1.8^2 \sim 0.3$.

When our modern computational methods are applied to the historical data, the orbital fit r.m.s is about 40 times greater than that of the HERCULES observations. Therefore, as described in the previous chapter (§ 6.9 beginning on on page 123), the most satisfactory way to achieve an improved result that is reliable, is to determine the binary's period with greater precision by making use of the sufficiently long interval of time between the historical and modern datasets.

The reference epoch chosen for this task is the time of zero mean longitude, T_0 , whose error is four times smaller than the corresponding value for T. The number of complete orbital cycles, $N_\mathrm{c} = 17$, is divided into the time interval between the two measured epochs of T_0 :

$$\bar{P} = \frac{52581.90 - 20012.04}{17} \approx 1915.87 \text{ days.}$$

The corresponding error $\sigma_{\bar{\mathrm{P}}}$ is estimated to be

$$\sigma_{\bar{\mathrm{P}}} = \frac{\sqrt{17.04^2 + 0.82^2}}{17} \approx 1.0 \text{ days,}$$

which is an order of magnitude improvement to the period precision when only the historical or the modern data were used in isolation. The relative error on the period is now $\sigma_{\bar{\mathrm{P}}}/\bar{P} \sim 0.0005$. Finally, with the period fixed at 1915.9 days, another orbital solution was derived (parameter set (4) in Table 7.1), where it is seen that all other parameters also have reduced errors. The largest changes to Jones's solution are for the eccentricity, which has increased from ~ 0.21 to ~ 0.33, and the position angle of periastron, which has increased by nearly 30° to $\sim 42°$.

The mass, age and radius of the primary star

The mass of the primary star can be estimated using measurements of suitable colour magnitudes of the star, and comparing these to the corresponding location on a colour-magnitude

diagram (CMD) with respect to evolutionary tracks for various stellar masses.

There are many conventional colour indices, each being sensitive to particular stellar properties such as luminosity and temperature. For instance, $(B-V)$ measures the slope of the Paschen continuum and is sensitive to temperature, whereas $(U-B)$ measures the height of the Balmer discontinuity and is very sensitive to temperature and somewhat so to luminosity, for late-type stars. The extension of the UBV system to include RI magnitudes gave astronomers another opportunity to investigate the far-red portion of the steller-energy distribution. The associated colour indices allow better temperature discrimination of the cooler stars (Hilditch 2001). Therefore, a more reliable position for an evolved star such as β Ret, on a colour-magnitude diagram with respect to evolutionary tracks and isochrones should be one of the red-wavelength indices, such as $(R-I)$. This index has been measured for β Ret by Bessell (1990) using the Cousins system: $(R-I)_C = 0^{\rm m}.520 \pm 0.020$.

The evolutionary tracks from the Geneva group (Lejeune & Schaerer 2001) are suitable for our purposes. These tracks have been computed for solar-metallicity stars ($Z = 0.02$, which is appropriate for β Ret), $(R-I)_C$, and for various masses that should adequately constrain the mass of the β Ret primary star (see Fig. 7.3), at least within the limits of accuracy that evolutionary tracks allow for this purpose.

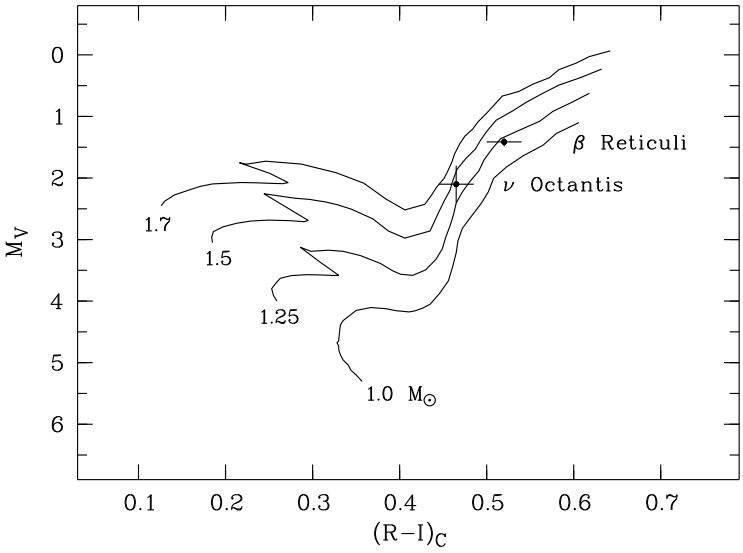

Figure 7.3: Colour-magnitude diagram with evolutionary tracks for stars of solar metallicity ($Z = 0.02$) for initial main-sequence masses 1–1.7 $\mathcal{M}_\odot$. The positions corresponding to $[(R-I)_C, M_{\rm V}]$ for the SB1 systems β Ret and ν Oct are shown, together with their respective 1-σ error bars.

The assumption is made that the contribution made by the unseen companion to the lumi-

nosity of the total magnitude of the observed system is insignificant. The validity of this will be checked after the character of the companion has been established. The 1-σ errors estimated for $(R-I)$ and $M_{\rm V}$ allow an estimate to be made of the precision of the evolutionary mass. The error for $M_{\rm V}$ is relatively small, as a result of the precise *Hipparcos* parallax (ESA 1997).

From this analysis, the mass of the primary star is estimated to be $\mathcal{M}_1 = 1.2 \pm 0.2\,\mathcal{M}_\odot$. Using the Geneva isochrone tables (Lejeune & Schaerer 2001), the isochrone age is estimated to be about 5.5 Gyr.

Another parameter that can be derived without additional orbital information is the primary star's radius. This can be estimated from the star's effective temperature, $T_{\rm eff}$, and $M_{\rm bol} = M_{\rm V} + BC$, where BC is the bolometric correction. Calibration relations have been derived for BC and $T_{\rm eff}$ based on the colour indices $(V-I)_C$ and $(B-V)$ respectively. BC can be calculated using $(V-I)_C = 1\overset{\rm m}{.}105 \pm 0.020$ (Bessell 1990) and the calibration relation of Bessell & Wood (1984):

$$BC = 0.3 - 0.62(V-I)_C - 0.14(V-I)_C^2\,, \tag{7.1}$$

which is valid for all late-type stars. The associated propagated error is estimated to be

$$\sigma_{BC} \simeq \sqrt{0.62^2 + 4 \times 0.14^2}\;\sigma_{(V-I)} \approx 0.68\,\sigma_{(V-I)}\,. \tag{7.2}$$

Therefore $BC \approx -0\overset{\rm m}{.}556 \pm 0.014$ and $M_{\rm bol} \approx 0\overset{\rm m}{.}86 \pm 0.03$ $(L \sim 36\,L_\odot)$.

The effective temperature is derived using the relation for G and K giants (McWilliam 1990):

$$T_{\rm eff} = 8351 - 4936(B-V) + 1456(B-V)^2 - 78(B-V)^3\,, \tag{7.3}$$

with an error

$$\begin{aligned} \sigma_{T_{\rm eff}} &\simeq \sqrt{4936^2 + 4 \times 1456^2 + 9 \times 78^2}\;\sigma_{(B-V)} \\ &\approx 5736\,\sigma_{(B-V)}\,. \end{aligned} \tag{7.4}$$

For β Ret, $(B-V) = 1\overset{\rm m}{.}133 \pm 0.005$ (Mermilliod 1987), so that $T_{\rm eff} \approx 4\,514 \pm 30$ K.

Finally, the star's radius is calculated using

$$\log \frac{R}{R_\odot} = \frac{4.74 - M_{\rm bol}}{5} - 2 \log \frac{T_{\rm eff}}{T_\odot}\,, \tag{7.5}$$

and

$$\begin{aligned}\sigma_R &\simeq R \times \sqrt{\left(\frac{\sigma_{M_{\rm bol}}}{5\log_{10}\mathrm{e}}\right)^2 + 4\left(\frac{\sigma_{T_{\rm eff}}}{T_{\rm eff}}\right)^2} \\ &\approx R \times \sqrt{\left(\frac{\sigma_{M_{\rm bol}}}{2.17}\right)^2 + 4\left(\frac{\sigma_{T_{\rm eff}}}{T_{\rm eff}}\right)^2}. \end{aligned} \tag{7.6}$$

Therefore, the radius of the primary star is found to be $R_1 \sim 9.8 \pm 0.2\,R_\odot$, assuming $T_\odot = 5780\,\mathrm{K}$. The angular diameter, $\theta_{\rm D}$, corresponding to the *Hipparcos* parallax is estimated to be $\theta_{D_1} = 2 \times R_1(\mathrm{AU}) \times p'' = 2.98 \pm 0.14$ mas. Both of these values are greater than the published ones: $R_1 = 7.6\,R_\odot$ (CADARS: Pasinetti-Fracassini et al. 2001, but which was based on the larger parallax reported in the introductory comments), and $\theta_{D_1} = 2.80 \pm 0.08$ mas (CHARM: Richichi & Percheron 2002). The radius of β Ret calculated here is about half that expected for a typical K2III star ($\sim 19\,R_\odot$; Drilling & Landolt 2000), but is consistent with a star of spectral type K2IIIb (as β Ret is presently classified), that is still evolving into a true giant.

The nature of the companion and other orbital parameters

An estimate of the secondary star's mass and consequently its general properties, as well as other orbital parameters, can be deduced with respect to the sytem's precise mass function, $f_{\mathcal{M}} = 2.2384 \pm 0.0074 \times 10^{-2}\,\mathcal{M}_\odot$, the primary star's CMD mass and the inclination of the orbit. The function (Eq. 3.16 on page 28)

$$f_{\rm q} = \frac{q^3}{(1+q)^2} = \frac{f_{\mathcal{M}}}{\mathcal{M}_1 \sin^3 i} \tag{7.7}$$

has been plotted in Fig. 7.4 for a range of conceivable inclinations. This curve shows that the minimum mass ratio consistent with these parameters, for $i \sim 90^\circ$ (the absence of eclipses dictates that the maximum inclination possible is a few degrees less than 90°), is $q_{\rm min} \sim 0.32$. The minimum orbital inclination, $i_{\rm min} \sim 23^\circ$, would only be possible if the companion had a mass comparable to the observed primary star. A normal star this massive would be more luminous than appearances allow, and hence, such a low inclination could only correspond to the companion being a massive white dwarf.

From a second statistical point of view, based on a recent survey of 152 white dwarfs (Bergeron et al. 2001), we can infer what the most likely white-dwarf mass might be. These authors used up-to-date evolutionary theory and took acount of the core and envelope composition of their sample to derive the mass of each star. A histogram representing their findings is presented in Fig. 7.5. As was also emphasized in Chapter 4, other strong biases that influence the study of probably all samples of astronomical objects are relative brightness and therefore proximity. This white-dwarf sample no doubt suffers in these and other ways (e.g. all members of this sample are close enough to have had their parallax and proper motion measured). However,

with this in mind, we can see from the histogram that there is a marked tendency for the white dwarfs we observe to have $\mathcal{M} \sim 0.6\,\mathcal{M}_\odot$, with relatively few having masses less than about $0.3\,\mathcal{M}_\odot$, or more than about $0.9\,\mathcal{M}_\odot$.

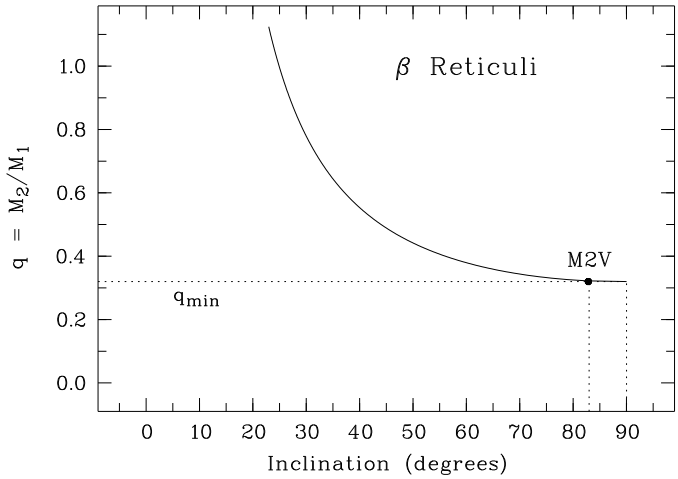

Figure 7.4: Curve defining the possible inclinations (prograde orbit assumed) and mass ratios with respect to the mass function and the primary star's estimated CMD mass ($\mathcal{M}_1 = 1.2\,\mathcal{M}_\odot$) for β Ret. The inclination of the orbit, $i \sim 83°$, derived with a photocentric orbital solution (ESA 1997), corresponds to a system mass ratio $q = 0.32 \pm 0.02$.

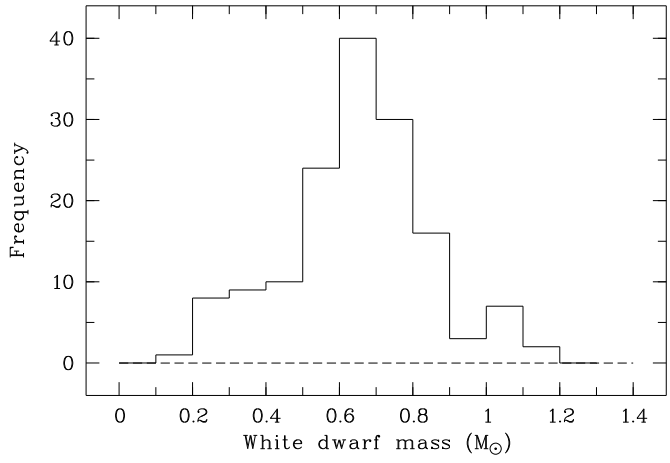

Figure 7.5: Histogram of the masses of a sample of 152 white dwarfs, based on a study conducted by Bergeron et al. (2001).

An estimate of the actual orbital inclination has been made by the *Hipparcos* consortium

(ESA 1997). Unfortunately, the *Hipparcos* observations were inadequate for a stand-alone solution and so relied heavily upon the spectroscopic orbit of Jones (1928), using the latter's values for P, e, and ω, and deriving i, T, $a_{\rm p}(\equiv a_0)$, and Ω (Table 7.2).

P	=	1911.5 days	(fixed)
e	=	0.21	(fixed)
ω_1	=	13.8	(fixed)
i	=	$82\overset{\circ}{.}85 \pm 3.36$	
T	=	JD $2\,448\,872.5 \pm 18.5$	
$a_{\rm p}$	=	$0\overset{''}{.}0271\ \pm 0.00250$	
Ω	=	$22\overset{\circ}{.}4 \pm 6.8$	

Table 7.2: The *Hipparcos* photocentric orbital solution for β Ret.

The merit of the *Hipparcos* solution must be carefully considered as it is based on three fixed orbital elements, two of which (e and ω), have been shown above to require some adjustment (Table 7.1). The *Hipparcos* value for the time of periastron passage also differs from the value derived from the HERCULES spectroscopic value (with allowance of two orbital cycles separating the values) by ~ 100 days. Furthermore, in their study of binary systems with a giant primary component and having both a spectroscopic and a *Hipparcos* orbital solution, Pourbaix & Boffin (2003) rejected the *Hipparcos* solution based upon a suite of statistical tests. Whether or not the present spectroscopic solution is consistent with the *Hipparcos* inclination is presently unknown.

A specific mass for the secondary star can be derived with respect to the inclination in Table 7.2. The corresponding errors were estimated using conventional error propagation, applied to Eq. (7.7) on page 134:

$$Q = \left(\frac{\sigma_{f_{\rm q}}}{f_{\rm q}}\right)^2 = 9\left(\frac{\sigma_q}{q}\right)^2 + 4\left(\frac{\sigma_q}{1+q}\right)^2 = \left(\frac{\sigma_{f_{\mathcal{M}}}}{f_{\mathcal{M}}}\right)^2 + \left(\frac{\sigma_{\mathcal{M}_1}}{\mathcal{M}_1}\right)^2 + 9\left(\frac{\sigma_i}{90}\right)^2$$

so that

$$\left(\frac{\sigma_q}{q}\right)^2 = \frac{Q(1+q)^2}{9(1+q)^2 + 4q^2}\,, \tag{7.8}$$

and

$$\sigma_{\mathcal{M}_2} = \mathcal{M}_2\sqrt{\left(\frac{\sigma_q}{q}\right)^2 + \left(\frac{\sigma_{\mathcal{M}_1}}{\mathcal{M}_1}\right)^2}\,. \tag{7.9}$$

Hence, $f_{\rm q} = 0.019 \pm 0.004$ and therefore $q = 0.32 \pm 0.02$. The unseen companion is estimated to have a mass $\mathcal{M}_2 = 0.38 \pm 0.07\,\mathcal{M}_\odot$. At the 1-$\sigma$ level of precision, this result corresponds to main-sequence stars of spectral type M1–M3, or white dwarfs of the same mass. An M2

dwarf has an absolute magnitude $M_{\rm V} \sim +9\overset{\rm m}{.}9$ (Drilling & Landolt 2000), which is about eight magnitudes fainter than the primary star. Therefore, the earlier assumption that the secondary star will not contribute any significant light to β Ret appears to be well justified.

Now that the mass ratio of the system has been estimated, it is possible to determine the corresponding angular size of the projected semimajor axis, as well as the linear size of the relative orbit. First,

$$a'' \sin i = \left(\frac{1+q}{q}\right)(a_1 \sin i)\, p'' \sim 0\overset{''}{.}115 \pm 0.007\,,$$

which is the minimum value for a''. The nodal separation

$$r''_{\rm ns} = \frac{a''(1-e^2)}{1 - e \parallel \cos\omega \parallel} \tag{7.10}$$

is about $0\overset{''}{.}14$. This estimate is consistent with one made by McAlister (1976; $r''_{\rm ns} = 0''.123$), but is about half that estimated by Halbwachs (1981; $r''_{\rm ns} = 0''.25$). McAlister's value was one of the largest he made in his survey of angular separations of spectroscopic binaries[2]. If the *Hipparcos* value for the inclination is accurate, the maximum angular separation of the components of β Ret is $a''(1+e) \sim 0\overset{''}{.}15$. The linear size of the relative orbit is

$$a = \frac{a'' \sin i}{p'' \times \sin i} = 3.54 \pm 0.26 \text{ AU}.$$

If the companion is a white dwarf, the mass of its precursor (which would have to exceed our estimate $\mathcal{M}_1 \sim 1.2\,\mathcal{M}_\odot$), and the linear separation would determine if mass exchange was possible during the giant phase of evolution of the presently unseen component (see § 2.2.1 on page 16 for estimating the size of the Roche lobes for various estimates of the mass ratio q and the separation a).

Future space-based astrometry missions will have unparalleled capabilities to detect faint companions close to bright primary stars. For instance, the Space Interferometry Mission instrument, SIM, is a nulling interferometer which has a mission goal for the nulling depth of 10^{-4}, i.e. 10 magnitudes, and an imaging resolution of $0''.010$ (Danner & Unwin 1999). These specifications should allow SIM to detect β Ret's faint companion allowing the relative orbit of the system to be determined for the first time.

The barycentric systemic velocity of β Ret

The most precise measure of the relative systemic velocity of β Ret, $\gamma_{\rm rel} = -0.8945 \pm 0.0052\,{\rm km\,s^{-1}}$, was determined when the period was fixed at the estimated mean value, $\bar{P}$. From the list of barycentric velocities reported by Nidever et al. (2002), a suitable star was identified that could

[2]Halbwachs (1981) also estimated the minimum mass ratio of β Ret to be $q_{\rm min} = 0.4$.

be used to measure $V_{\rm diff}$ (see Eq. 6.2 on page 117). This was HD 25723, which has a spectral type of K1III (see Table 6.2). Nidever et al. (2002) reported a barycentric velocity $V_{\rm bary} = +26.748\,{\rm km\,s^{-1}}$. Our measure of the barycentric velocity of HD 25723, $V_{\rm sky} = 26.745\,{\rm km\,s^{-1}}$, is in excellent agreement with this value. The velocity of the β Ret reference spectrum relative to the barycentric reference HD 25723 was measured to be $V_{\rm diff} = +25.138\,{\rm km\,s^{-1}}$. Neglecting the unknown contributions of the convective blueshift and other effects associated with evolved stars (Nidever et al. 2002), and assuming $V_{\rm diff}$ and $V_{\rm bary}$ each have a random error of $\pm 15\,{\rm m\,s^{-1}}$, our estimate of the barycentric velocity of β Ret is

$$\gamma = \gamma_{\rm rel} + V_{\rm diff} + V_{\rm bary} \approx -0.8945 + 25.138 + 26.748 = +50.992 \pm 0.020\ {\rm km\,s^{-1}}\,,$$

which is not significantly different from the value measured using the historical data available to Jones (1928; $\gamma = +51.17 \pm 0.23\,{\rm km\,s^{-1}}$).

7.2 ν Octantis (HD 205478 HIP 107089 HR 8254; $21^{\rm h}41^{\rm m}29^{\rm s}$, $-77^\circ23^{\rm m}24^{\rm s}$)

ν Oct is a bright SB1 system of spectral type K0III (Houk & Cowley 1975). The V magnitude is $V = 3\overset{\rm m}{.}731 \pm 0.002$ (Kharchenko 2001). The current trigonometric parallax of ν Oct is $p'' = 47.22 \pm 2.9$ mas (ESA 1997), which is not much different from that measured several decades ago ($p'' = 51$ mas; Woolley et al. 1970). The relatively poor precision of the *Hipparcos* parallax for such a close and bright star is consistent with ν Oct also having a stochastic solution to its *Hipparcos* astrometry (ESA 1997). The modern value for the absolute magnitude of the system is therefore $M_{\rm V} = 2\overset{\rm m}{.}10 \pm 0.13$. Based on 133 *Hipparcos* observations, the photometric stability of ν Oct, $H_{\rm p} = 3\overset{\rm m}{.}8981 \pm 0.0004$, also seems to be assured. Some of the colour indices measured for ν Oct are as follows: $(B-V) = 1\overset{\rm m}{.}004 \pm 0.003$ (ESA 1997); $(R-I)_C = 0\overset{\rm m}{.}465 \pm 0.020$ and $(V-I)_C = 0\overset{\rm m}{.}985 \pm 0.020$ (Bessell 1990). Eggen (1969) placed ν Oct in one of his largest moving groups, Wolf 630. The metallicity of ν Oct is estimated to be [Fe/H] $= -0.11$ (Eggen 1993).

Historical spectroscopic solutions

The variable radial velocity was first described by Wright in 1908. The Chilean observations provided a total of 11 spectra taken in the years 1904–1920. Six of these plates were measured more than once, and these had the mean velocity determined. The Cape observations contributed velocities from a further ten plates taken in the years 1909–1924.

The first two spectroscopic orbital solutions for ν Oct were determined within months of each other, by two astronomers working in different countries who no doubt were unaware that the other was occupied with the same task. Both used the same radial-velocity measures, and as was mentioned earlier, both solutions relied upon observations secured at San Cristobal Observatory, Chile, and the Cape Observatory, South Africa.

In March 1935, Colacevich (1935) submitted his single-lined spectroscopic solution[3], whilst that provided by Christie (1936) was submitted a few months later, in August 1935 (see Table 7.3). Neither author provided error estimates for their derived orbital elements, and only Christie (1936) mentions his method of analysis (graphical, and by comparison to standard radial-velocity curves). These two solutions and the observations employed are illustrated in Fig. 7.6. Whilst all elements other than the velocity semi-amplitude differ, it can be seen that the computed velocity curves are very similar and, without further analysis, equally plausible. When, as was done for β Ret , modern computational methods are applied to the same data set, a third solution is derived (Table 7.3). This solution more closely matches that due to Christie (1936). Only the period duplicates the Colacevich (1935) result[4].

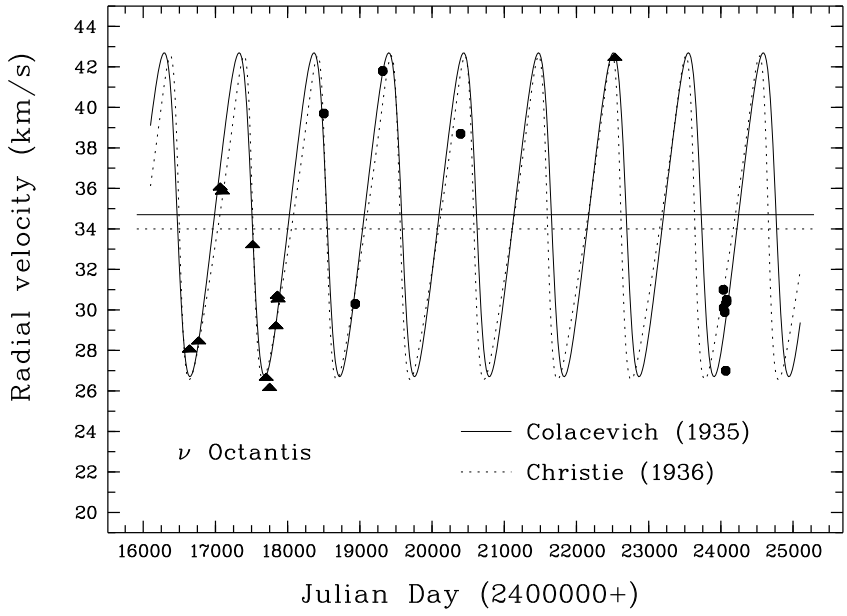

Figure 7.6: The historical radial velocities of ν Octantis and the velocity curve computed from the respective orbital solutions. The triangles identify observations secured at San Cristobal whilst the circles represent the velocity measures acquired at the Cape Observatory. The two major horizontal lines correspond to the systemic velocity γ of each solution.

[3]The value given for the time of periastron pasage T in Colacevich (1935) has a typographical error, since JD 2 317 506 corresponds to the year 1633!

[4]The division of observations over time at the two observatories is such that it has not been possible to compare the quality of the velocities acquired during different time intervals as was the case for β Ret, since very few observations were acquired between JD 2 418 000 and JD 2 423 000 for ν Octantis. However, a velocity measure with one of the largest residuals was acquired at the Cape Observatory ($\sim$ JD 2 421 400) during the same time when the β Ret velocities of poorest precision were also obtained (labelled 'Cape1' on Fig. 7.1.)

	ν Octantis		K_1 ($\mathrm{km\,s^{-1}}$)	e	ω_1 (°)	T_0 (JD 24...)	T (JD 24...)	P (day)	γ_{rel} ($\mathrm{km\,s^{-1}}$)	$a_1 \sin i$ (Gm)	f_{M} ($\mathcal{M}_\odot$)	fit rms ($\mathrm{km\,s^{-1}}$)
1.	Colacevich, 1935		8.0	0.25	90	–	17 506	1037	+34.7	110.4	0.050	–
		±	–	–	–	–	–	–	–	–	–	
2.	Christie, 1936		8.0	0.4	80	–	18 525	1020	+34.0	–	–	–
		±	–	–	–	–	–	–	–	–	–	
3.	historical data		7.95	0.401	82	18 289	18 534	1037	+34.17	103.9	0.042	1.4
	(Sterne's method)	±	0.90	0.084	14	18	26	5	0.40	8.7	0.011	
4.	present work		7.0477	0.238 08	74.76	52 959.51	53 177.31	1048.84	−6.4693	98.723	0.034 855	0.035
		±	0.0055	0.000 61	0.17	0.13	0.39	0.26	0.0033	0.075	0.000 076	

Table 7.3: The historical and MJUO spectroscopic orbital solutions for ν Octantis. The first two parameter sets are those due to Colacevich (1935) and Christie (1936). The third solution was determined by applying the computational methods of the present study to the historical data. The fourth parameter set uses only the velocities of the present work.

Photocentric orbital solutions of ν Oct

Soon after the spectroscopic solutions were published, Colacevich (1937) derived a provisional photocentric one. Subsequently, ν Oct was placed on the observing program of the Yale 26-inch refractor, and 38 astrometric plates were secured between June 1926 and October 1938, an interval of time that included approximately four and a half orbital cycles. Using 36 suitable plates, as well as Colacevich's spectroscopic solution, Alden (1939) derived a photocentric solution and parallax for the system. He may have fixed the period and eccentricity to the spectroscopic values as these are identical in the two solutions. The least-squares solution of the combined astrometric and spectroscopic observations are presented in Table 7.4. Many of the parameters used or derived in Alden's solution (e.g. the parallax, proper motions, eccentricity and period) do not differ significantly from the modern values.

P	=	1037 days	(fixed?)
e	=	0.25	(fixed?)
ω_1	=	37°	
i	=	65°	
T	=	JD 2 417 506	
a_p	=	$0\farcs052$	
Ω	=	118°	
p''	=	$0\farcs048 \pm 0.006$	

Table 7.4: The photocentric solution of ν Octantis (Alden 1939).

Alden also estimated the angular semi-major axis of the true relative orbit as well as the masses of the components. He achieved this by beginning with the assumption that the primary star had an effective temperature $T_\mathrm{eff} = 4000\,\mathrm{K}$, and, using a calibration table, a bolometric correction $BC = -0.62$. Using an unpublished mass-luminosity calibration, he then estimated the primary and secondary masses to be $M_1 = 2.7\,\mathcal{M}_\odot$ and $M_2 = 1.1\,\mathcal{M}_\odot$ respectively. Finally, Alden was able to estimate that the true semi-major axis was $a'' \sim 0\farcs18$ (although his values actually yield $a'' \sim 0\farcs15$), and that the secondary star was about three magnitudes fainter than the primary star.

Orbital solution using MJUO velocities

The first HERCULES spectra of ν Oct were acquired several days after a vacuum was established in the spectrograph in 2001 July. Spectra continued to be acquired until this project's last observing run in 2004 July–August, a duration of nearly three years. A total of 156 observations were recorded, all but two of which were with the higher resolving power, $R \sim 70\,000$. The dates and velocities corresponding to each observation are provided in Table C.2 Appendix C. The radial-velocity measurements are plotted in Fig. 7.7 together with the best-fitting curve

calculated from the orbital parameters derived using Sterne's method. The r.m.s. of this orbital solution was 35 $\mathrm{m\,s^{-1}}$ (see the final parameter set in Table 7.3), which is about 50% greater than that determined for the best-fit solution for β Ret.

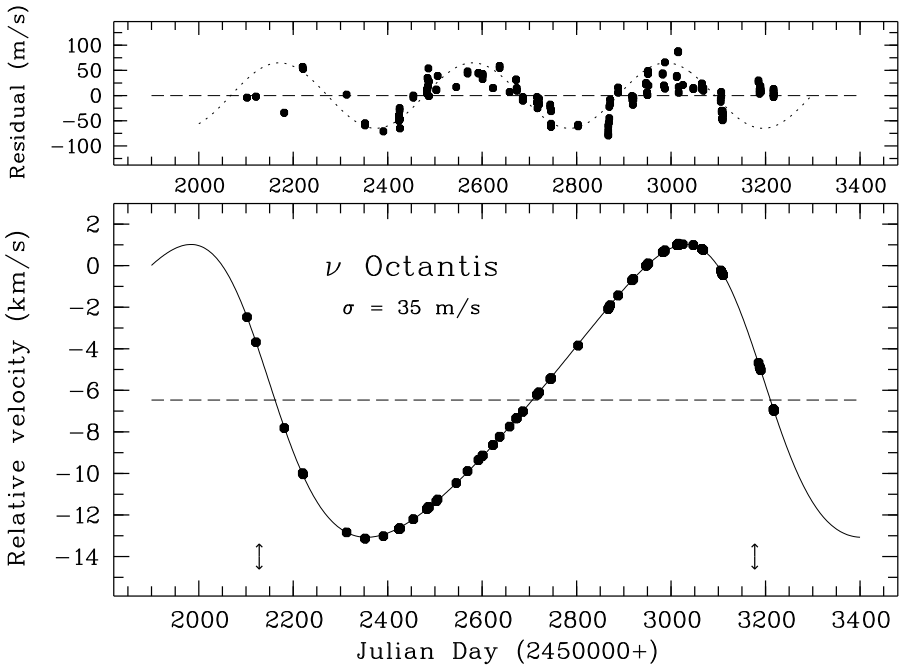

Figure 7.7: Bottom: The radial velocities and curve corresponding to the MJUO spectroscopic orbital solution for ν Octantis. The dashed horizontal line identifies the relative systemic velocity. The '↕' symbols indicate times of periastron passage. Top: The residual velocities. A sinusoidal curve has been fitted to them, centred near JD 2 452 600. See main text for a discussion of the possible relevance of this secondary curve.

The residuals arising from the best-fit computations are also plotted in Fig. 7.7 and included in Table C.2 Appendix C. The striking appearance of these residuals deserves some comment. First, these residuals are not as randomly distributed as was the case for β Ret, or indeed for any other star whose analysis will follow. Second, there is the suggestion that the residuals have cyclic behaviour, though it is also clear that it is not strictly periodic. A periodogram analysis of the residuals confirms the obvious $\sim$ 400 day cycle, most clearly defined between JD 2 452 400 and JD 2 452 800. No other significant periodicities were revealed. A sinusoidal curve has been fitted by eye to the residuals. This curve was computed for a period of 410 days and with a velocity semi-amplitude of 65 $\mathrm{m\,s^{-1}}$. The r.m.s. of the fit was 17 $\mathrm{m\,s^{-1}}$ for the residuals between the two dates mentioned.

If the residuals followed a periodic pattern, a single orbiting mass[5] or a large persistent

[5]If the residual velocities followed a strictly periodic sinusoidal curve with $P \sim 400$ days and $K \sim 60\,\mathrm{m\,s^{-1}}$,

surface feature, such as a 'starpatch' (Toner & Gray 1988), could be inferred. One way to distinguish between these two possibilities would be to examine the symmetry of the spectral lines. An orbiting mass should provide symmetrical spectral lines whereas a suitable surface feature should produce lines of variable asymmetry (Gray 1997). Another clue is the approximate duration of the two dominant cycles, each of which has a period of about 400 days. The rotational velocity of ν Oct has been estimated to be $v_{\rm equ} \sin i \sim 2\,{\rm km\,s^{-1}}$ (Costa et al. 2002). The inferred radius of a star star rotating with this period and velocity is about $16\,R_{\odot}$, which is consistent with a late-type evolved star (Drilling & Landolt 2000). A starpatch as described by Toner & Gray (1988) has been used to explain the long-term ~ 6.4 day periodic velocity variations of the G8 dwarf ζ Bootis A. The velocity semi-amplitude for ζ Bootis A was about $60\,{\rm m\,s^{-1}}$, just as is evident for the residuals computed for ν Oct. A detailed analysis of the HERCULES spectra has not been undertaken to explore further this possible and apparently meritorious explanation. A longer series of velocity measurements would also be advantageous, particularly in view of the apparent substantial shift to the residual velocities of the final 24 observations of the present series. This shift is strong evidence to discredit the possibility of a single orbiting mass. The possibility of shorter-timescale, similarly low-amplitude, velocity variations as a result of pulsational behaviour, well-recognized in K-giants, should also be considered, (e.g. Cummings et al. 1999; Larson et al. 1999).

Combining the historical and modern velocities

The spectroscopic solution derived by Colacevich (1935) is seen to more closely approximate the HERCULES solution than does that determined by Christie (1936). Fortunately, it was the Colavevich solution that was used to facilitate Alden's (1939) photocentric solution.

Unlike the opportunity provided by β Ret, the historical and modern observations of ν Oct cannot be combined in any useful manner to improve the result obtained using only the modern velocities. There are several reasons for this: 1. the historical velocities have much poorer precision with respect to the modern data (the orbital fit historical r.m.s/modern r.m.s. $= 40$) so that the weights given to the historical velocities would be tiny, i.e. , $\sim 1/40^2$, 2. the estimated error, σ_{T_0}, of the more precise epoch, the time of zero mean longitude, is 140 times greater for the historical data than that estimated for the modern observations, whilst, 3. there are only about $N_{\rm c} = 33$ orbital cycles separating the two data sets. Therefore, the error estimated for the mean period, $\bar{P}$, would be $\sigma_{\bar{P}} = \sigma_{T_{0({\rm hist})}}/N_{\rm c} \approx 0.55$ days, or twice the error estimated using only the HERCULES data.

The mass, age and radius of the primary star

The CMD mass of the primary star, as well as its age and radius, can be estimated using the same procedures, evolutionary tracks and isochrone tables as were applied to β Ret, since ν Oct

an orbiting body, corresponding to the estimated mass of the primary star ($\mathcal{M}_1 \sim 1.4\,\mathcal{M}_{\odot}$, as will presented shortly), would have a minimum mass of about $\mathcal{M}_{\rm p} \sim 3$ Jupiter masses.

is also a solar-metallicity star and the required information is available. For the CMD mass, the relevant colour index is $(R-I)_C = 0^{\rm m}.465 \pm 0.020$ (Bessell 1990). Unlike β Ret, though, ν Oct thas a rather less precise parallax so that the 1-σ error bar for $M_{\rm V}$ is consequently larger. The mass of the primary star of ν Oct is estimated to be $\mathcal{M}_1 = 1.4 \pm 0.4\,\mathcal{M}_\odot$. The isochrone age is estimated to be about 3.3 Gyr.

The primary star's radius was estimated based on the two colour indices, $(V-I)_C = 0^{\rm m}.985 \pm 0.020$ (Bessell 1990), and $(B-V) = 1^{\rm m}.004 \pm 0.003$ (ESA 1997). Using the various expressions beginning on page 133, the following parameters relating to ν Oct can be deduced: $BC \approx -0^{\rm m}.447 \pm 0.014$, $M_{\rm bol} \approx 1^{\rm m}.65 \pm 0.13$ ($L \sim 17\,L_\odot$), $T_{\rm eff} \approx 4\,784 \pm 20\,{\rm K}$, and hence finally, the radius of the primary star is estimated to be $R_1 \sim 6.1 \pm 0.4\,R_\odot$. The angular diameter of ν Oct corresponding to its parallax is therefore $\theta_{D_1} = 2.6 \pm 0.2$ mas. The published values are $R_1 = 7.6\,R_\odot$ (Pasinetti-Fracassini et al. 2001), and $\theta_{D_1} = 2.42 \pm 0.06$ mas (Richichi & Percheron 2002). The estimated radius of ν Oct is about 60% less than that expected for a typical K0III star ($\sim 15\,R_\odot$; Drilling & Landolt 2000). With regard to the approximate 400-day cycles found in the velocity residuals (Fig. 7.7), the estimated $6.1\,R_\odot$ radius of ν Oct's primary star corresponds to a rotational velocity of about $1\,{\rm km\,s^{-1}}$, very much in agreement with the measured value (Costa et al. 2002). If the photometric data and calibration relations that led to the CMD location and radius estimate for ν Oct are accurate, they suggest that the red-clump luminosity-class, IIIb, might be more appropriate for ν Octantis.

The nature of the companion

Using the modern values determined for the mass function, $f_{\mathcal{M}} = 3.4855 \pm 0.0076 \times 10^{-2}\,\mathcal{M}_\odot$, and the primary star's CMD mass, $\mathcal{M}_1 = 1.4 \pm 0.4\,\mathcal{M}_\odot$, the expression Eq. (7.7) on page 134 has been plotted for a range of possible orbital inclinations for the ν Oct system (Fig. 7.8). The minimum mass ratio consistent with these parameters, for $i \sim 90°$ (as was the case for β Ret, the absence of eclipses requires that i is at least a few degrees from an edge-on orbit), is $q_{\rm min} \sim 0.36$. The minimum orbital inclination is $i_{\rm min} \sim 25°$, which, given the absence of detectable light from the companion, would only be consistent with a massive white dwarf. Fig. 7.5 on page 135 illustrates the statistical unlikelihood of the companion being so massive.

The photocentric orbital solution derived for ν Oct by Alden (1939) provides an estimate of the true inclination of its orbit, $i = 65°$. Unfortunately, this value has been reported without an error. We can only hope that the error is no worse than the earlier estimate made by Colacevich (1937; $\sigma_i = 16°$) in his provisional photocentric solution. Therefore, if we use $i = 65° \pm 16$, $f_{\rm q} = 0.033 \pm 0.02$ and therefore $q = 0.40 \pm 0.08$. The unseen companion is estimated to have a mass $M_2 = 0.56 \pm 0.20\,\mathcal{M}_\odot$. At the 1-$\sigma$ level of precision, this result corresponds to main-sequence stars of spectral type K1–M2, or white dwarfs of the same mass. The spectral type corresoponding to an unevolved star of mass $\mathcal{M}_2 = 0.56\,\mathcal{M}_\odot$ is about K7V. Such a star has an absolute magnitude $M_{\rm V} \sim +8^{\rm m}$ (Drilling & Landolt 2000), which is about six magnitudes fainter than the primary star. Shortly, evidence will be given that lends support to the companion being a more luminous main-sequence star, rather than a white dwarf.

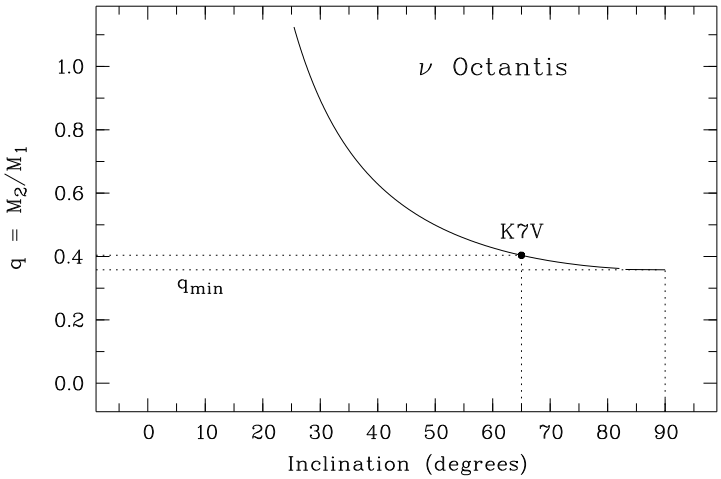

Figure 7.8: Curve defining the possible inclinations (prograde orbit assumed) and mass ratios with respect to the mass function and the primary star's estimated CMD mass ($\mathcal{M}_1 = 1.4\,\mathcal{M}_\odot$) for ν Oct. The inclination of the orbit, $i = 65°$, derived with a photocentric orbital solution (Alden 1939), corresponds to a system mass ratio $q = 0.40 \pm 0.08$.

Size of the relative orbit

The corresponding angular size of the projected semimajor axis of the ν Oct system is determined as it was for β Ret:

$$a'' \sin i = \left(\frac{1+q}{q}\right)(a_1 \sin i)\, p'' \sim 0''.109 \pm 0.024\,.$$

The nodal separation is about $0''.12$ or twice that estimated by McAlister (1976; $a'' \sim 0''.077$) and Halbwachs (1981; $a'' \sim 0''.063$). If the inclination is accurate, the maximum angular separation of the components of ν Oct is about $0''.15$. The linear size of the relative orbit is estimated to be

$$a = \frac{a'' \sin i}{p'' \times \sin i} \sim 2.6 \pm 0.5 \text{ AU}\,.$$

There have been three attempts to resolve ν Oct using speckle interferometry. The first of these was successful (Morgan et al. 1980; BLM 6), and the separation measured was $\rho = 0''.104 \pm 0.016$. According to the HERCULES spectroscopic solution, this observation, on about JD 2 442 950, would have been made at close to a time of descending nodal passage, when we would predict this separation. Unfortunately, no estimate of the magnitude difference was reported. However, resolution of the two components suggests that the companion is not a white

dwarf, but rather, is a more luminous K-dwarf, which would be 4–6 magnitudes fainter than the primary star. The other two interferometric observations of ν Oct were not able to resolve the components (Bonneau et al. 1980), but estimated that $\rho < 0''.029$. These null results are also consistent with the spectroscopic solution, since both were made at times very close to periastron passage.

It is a pity that further interferometric observations of this binary system have not been made since the apparent success of Morgan et al. (1980). However, with a high-precision orbital solution now available because of the work carried out here, greater confidence for success with further interferometric observations would not seem unreasonable. Furthermore, with the single ground-based observation, which is consistent with the refined orbital solution, ν Oct should be an excellent target for future space-based interferometric instruments.

The barycentric systemic velocity of ν Oct

The relative systemic velocity of ν Oct was measured to be $\gamma_{\rm rel} = -6.4693 \pm 0.0033\,{\rm km\,s^{-1}}$. From the list of barycentric velocities reported by Nidever et al. (2002), a suitable star was identified that could be used to measure $V_{\rm diff}$ (see Eq. (6.2) on page 117). This was HD 223807, which has a spectral type of K0III (Table 6.2 on page 114). Nidever et al. (2002) measured a barycentric velocity $V_{\rm bary} = -15.825\,{\rm km\,s^{-1}}$. The barycentric velocity of HD 223807 measured using HERCULES spectra, $V_{\rm sky} = -15.799\,{\rm km\,s^{-1}}$, is in excellent agreement with this value. The velocity of the ν Oct reference spectrum relative to the barycentric reference HD 223807 was measured to be $V_{\rm diff} = +57.532\,{\rm km\,s^{-1}}$. Neglecting the unknown contributions of the convective blueshift and other effects associated with evolved stars (Nidever et al. 2002), and assuming $V_{\rm diff}$ and $V_{\rm bary}$ each have a random error of $\pm 15\,{\rm m\,s^{-1}}$, the estimate of the barycentric velocity of ν Oct is

$$\gamma = \gamma_{\rm rel} + V_{\rm diff} + V_{\rm bary} \approx -6.4693 - 15.825 + 57.532 = +35.238 \pm 0.020\ {\rm km\,s^{-1}}\,.$$

This measurement of the sytemic velocity of ν Oct is about 0.5–1 $\rm km\,s^{-1}$ greater than the values based on the historical observations.

7.3 HD 159656 (HIP 86289; $17^{\rm h}37^{\rm m}54^{\rm s}, -42^\circ34^{\rm m}00^{\rm s}$)

HD 159656 is a seventh magnitude single-lined spectroscopic binary system located in the tail of Scorpius, about 1/2 degree N.E. of θ Sco. The primary component is a slightly evolved star of spectral type G4 that moves in an orbit of low eccentricity ($e \sim 0.1$) and with a period of about 10 days. Several of its characteristics make it an object of somewhat greater interest than might normally be the case for a typical single-lined spectroscopic binary.

The spectral type of HD 159656 has been classified between G2 and G5, for instance, as G5V (Evans 1961), G4IV–V (Barker et al. 1967) and G2/3V (Houk 1978). Cousins & Stoy (1962)

assigned the system magnitudes of $V = 7^{\rm m}\!.15$ and $(B - V) = 0.65$. Before *Hipparcos* astrometry became available, HD 159656 appeared in various nearby-star catalogues, for example, Woolley et al. (1970) and Gliese & Jahreiss (1991; CNS3) based on a trigonometric parallax of 45 mas which placed it at a distance of 22 pc. These two catalogues were intended to include all known stars within 25 parsecs of the Sun. However, for instance, the CNS3 based a star's inclusion only upon its trigonometric parallax even though it may have been evident from photometry that a star might be more distant. This was occasionally the case, and HD 159656 is an example.

It was fortuitous that HD 159656 appeared in the CNS3 as this led to its selection for subsequent investigations, for example, pre-IRAS infrared predictions (Johnson & Wright 1983), $BVRI$ photometry (Bessell 1990), and the 'ROSAT All-sky Survey Catalogue of Nearby Stars' (Hünsch et al. 1999). The last named authors were aware of its greater distance with the availability of *Hipparcos* parallax measures. HD 159656 was also considered as a possible nearby solar twin (Hardrop 1982; Fracassini et al. 1988), and was included in surveys for target stars suitable for SETI programmes (Fracassini et al. 1988; Henry et al. 1996) even though the existence of the short-period stellar companion had been recognized for many years (Barker et al. 1967).

Eventually, *Hipparcos* measured the trigonomtric parallax of HD 159656 to be 29.80 ± 0.93 mas (ESA 1997), in close agreement with a photometric parallax of 32 mas, reported by Eggen (1998). The *Hipparcos* value corresponds to a distance of 33.56 ± 1.05 pc. HD 159656 was included in a large Strömgren photometric study by Olsen (1994), who measured $V = 7^{\rm m}\!.169 \pm 0.004$, $(b - y) = 0^{\rm m}\!.407 \pm 0.003$, $m_1 = 0^{\rm m}\!.205 \pm 0.004$, and $c_1 = 0^{\rm m}\!.339 \pm 0.005$. Hence, the absolute magnitude is $M_{\rm V} = +4^{\rm m}\!.540 \pm 0.068$.

More recently, this binary system appeared in the comprehensive Geneva-Copenhagen survey ($\sim 14\,000$ essentially unevolved F and G stars) of the solar neighbourhood (Nordström et al. 2004). The study used various calibration relations to determine the effective temperature and metallicity based on the *uvby* photometry just mentioned, and deduced $\log T_{\rm eff} = 3.751$ and $[{\rm Fe/H}] = -0.11$. On the assumption that the secondary star makes no significant contribution to these parameters, they correspond to those of the primary component. The temperature and absolute magnitude are consistent with the primary star having a spectral type G4IV–V, as assigned by Barker et al. (1967).

Nordström et al. (2004) also estimated that HD 159656 has evolved approximately $0^{\rm m}\!.77$ from the theoretical zero-age main-sequence (ZAMS). This figure was based on their comparison between the system's absolute magnitude and the ZAMS at the same colour and metallicity, and could only have any validity if the secondary star made no significant contribution to the total light of the system. They also determined that the most-likely isochrone age was $t_{\rm iso} = 12.1$ Gyr (with a lower confidence age limit of 8.2 Gyr), using the theoretical evolution models from the Padova group (e.g. Girardi et al. 2000). This age is somewhat more than the age of 5.98 Gyr estimated by Ibukiyama & Arimoto (2002). The ages derived by Nordström et al. (2004) had good agreement with the older age stars in common with the study conducted by Edvaards-

son et al. (1993). The considerable age of HD 159656 is consistent with the G4IV–V spectral type of this primary star which, having a sub-solar mass, $\mathcal{M}_1 = 0.93 \pm 0.05\,\mathcal{M}_\odot$ (Nordström et al. 2004), would evolve away from the main-sequence rather slowly, only after having moved along the main-sequence for the initial but extended early part of its life.

The Geneva-Copenhagen survey also assessed the kinematic characteristics of their large stellar sample. Based on the accepted systemic radial velocity of HD 159656, $V_\mathrm{r} = +3.77\,\mathrm{km\,s^{-1}}$ (Pourbaix et al. 2004), Nordström and co-workers estimated the heliocentric space velocities $U = -9\,\mathrm{km\,s^{-1}}$, $V = -32\,\mathrm{km\,s^{-1}}$, $W = -55\,\mathrm{km\,s^{-1}}$, and the projected maximum distance that the binary travels from the Galactic plane ($z = 0.95$ kpc). This distance was one of the very largest estimated in the Geneva-Copenhagen survey[6] (see their Fig. 21.).

Several of the parameters reported above place HD 159656 in the thick disk population (Eggen 1998; Ibukiyama & Arimoto 2002). Thick disk stars are believed to have ages ranging from $\sim$ 2 to 10 or 12 Gyr, whereas those of the thin disk have a maximum age of 2 Gyr (Eggen 1998). The space velocities of HD 159656 place it outside the thin/young disk velocity 'ellipse' in (U, V) velocity space (Eggen 1969). In addition, the predicted orbital path of HD 159656 carries it well beyond the boundary of thin disk stars, which is expected to have a scale height of only 100–300 pc, and into the territory of the thick disk, whose scale height is believed to be 800–1300 pc (Bensby et al. 2003).

The photometric stability of HD 159656 have led to it being recognized as a standard star since the pioneering work of Cousins (1962), this taking place before the first spectroscopic orbit had been determined (Barker et al. 1967). HD 159656 occupies one of the nine Harvard E-regions which are centred on about declination $\delta \approx -45°$ and are evenly spaced around the sky, about 2–3 hours apart in right ascension. HD 159656 is a recognized standard in the UBV $(\mathrm{RI})_\mathrm{C}$ (Menzies et al. 1989), Strömgren *uvby* (Cousins 1987; Kilkenny & Laing 1992), Hβ (Cousins 1990), and Vilnius (Forbes et al. 1997) photometric systems. More recently, Gil-Hutton & Benavidez (2003) identified HD 159656 as a candidate for use as an unpolarized standard.

Historical spectroscopic orbital solutions

The variable radial velocity of HD 159656 was first reported by Evans (1961), who used 12 radial-velocity measures to determine a mean velocity of $+1\,\mathrm{km\,s^{-1}}$ and a velocity semi-amplitude $K_1 = 15\,\mathrm{km\,s^{-1}}$. A spectroscopic orbital solution for the system was subsequently provided by Barker et al. (1967) based on these and a further ten observations, acquired over about 13 years (1951–1964), or nearly 500 orbital cycles. This is the solution included in the 'Ninth Catalogue of Spectroscopic Binary Orbits' (Pourbaix et al. 2004). The mean weight assigned to the 11 observations acquired before mid-1956 (JD 2 435 600) was 4.5 times smaller than that assigned

[6]Nordström et al. (2004) defined (U, V, W) according to a right-handed Galactic coordinate system with $+U$ directed toward the Galactic centre, $+V$ in the direction of Galactic rotation, and $+W$ towards the north Galactic pole. Some authors direct $+U$ toward the Galactic anti-centre (e.g., Eggen 1998).

to the following 11 observations (Fig. 7.9). The cause of this dramatic change in precision can only be guessed at, but maybe the result of an instrument modification[7]. The orbital elements derived, as well as the projected semi-major axis of the primary star and the mass function, $f_{\mathcal{M}}$, are presented in Table 7.5. The phased radial-velocity curve corresponding to these orbital elements is found in Fig. 7.9.

K_1	=	$13.36 \pm 0.59\,\mathrm{km\,s^{-1}}$	P	=	$10.089\,99 \pm 0.000\,45$ days
e	=	0.142 ± 0.046	ω_1	=	$133\overset{\circ}{.}0 \pm 14.5$
T	=	JD $243\,3798.24 \pm 0.45$	γ	=	$+3.77 \pm 0.42\,\mathrm{km\,s^{-1}}$
$a_1 \sin i$	=	1.834 Gm	$f_{\mathcal{M}}$	=	$2.42 \times 10^{-3}\,\mathcal{M}_\odot$

Probable error of an observation of unit weight = $9.72\,\mathrm{km\,s^{-1}}$

Table 7.5: The spectroscopic orbital solution and related orbital parameters for HD 159656 derived by Barker et al. (1967).

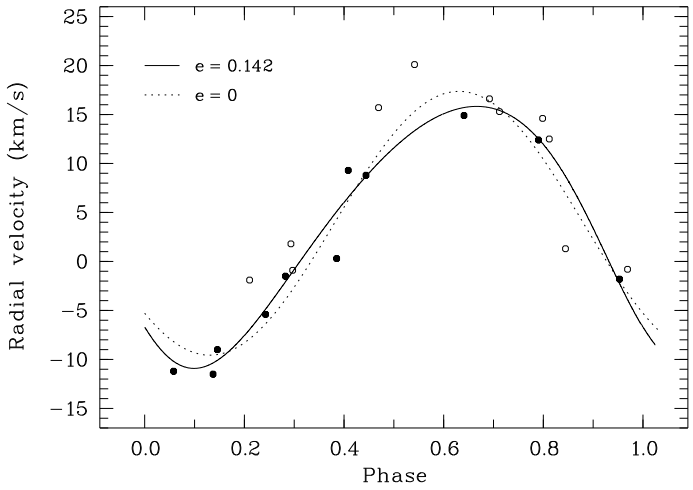

Figure 7.9: Phased radial-velocity curves of HD 159656. Solid line: based on the orbital solution reported by Barker et al. (1967). Dotted line: based on the solution we have derived using the historical observations but with the assumption that the orbit is circular as suggested by Lucy & Sweeney (1971). The open symbols represent observations given less relative weight (∼0.2) by Barker et al. (1967) than those corresponding to the solid symbols.

[7]D.S.Evans contributed several of the observations to the earlier and the later series, so a change of observers seems unlikely to be responsible.

HD 159656 next entered the astronomical literature in the often-cited study conducted by Lucy & Sweeney (1971). The purpose of their work was to identify which low but non-zero eccentricity spectroscopic orbital solutions as found in the 'Sixth Catalogue of the Orbital Elements of Spectroscopic Binary Systems' (Batten 1967) were perhaps erroneous and instead should be assigned a circular orbit. Their study was motivated by the findings of previous workers, for example, Luyten (1936), Sterne (1941a) and Savedoff (1951). Sterne's (1941a) investigations were entirely theoretical. He argued that consideration should be given to the non-spherical shape and non-uniform illumination of stars in close binary orbits leading to systematic errors in the measured velocities and subsequent orbital solution. Sterne concluded that when spurious low eccentricities arise in such situations, the position angle of periastron, ω, is likely to be 90° or 270°.

Savedoff (1951) compared the measured values of $e\cos\omega$ for eclipsing binary systems that had both photometric and spectroscopic orbital solutions. His investigations revealed that $(e\cos\omega)_{\rm ph}$ and $(e\cos\omega)_{\rm sp}$ were poorly correlated, and that the differences between the two values were typically greater for stars of spectral type earlier than A5. Since photometric orbital solutions are usually more accurate than spectroscopic ones, his results suggested that many spectroscopic solutions with $e \lesssim 0.05$ should instead be assigned circular orbits.

Luyten (1936) also argued that many small eccentricities were not statistically significant. Hence, Lucy & Sweeney embarked upon their own assessment of the situation, basing their investigation purely on statistical considerations. After recomputing the orbits of 213 single-lined spectroscopic binaries using Sterne's (1941b) approach to differential corrections for the best-fit solution, Lucy & Sweeney identified only 110 solutions that passed their statistical test, namely, that at the 5% level of significance, the hypothesis that the eccentricity was zero could be rejected (i.e., the eccentricity had to exceed 2.45 times its standard error or 3.63 times its probable error). One of their conclusions was that all orbits with a period less than about five days were circular. There was no long-period cut-off in their investigation, and the orbit ($e = 0.1$) with the longest period which Lucy & Sweeney (1971) re-assigned as being circular was for the visual binary HD 219834 (94 Aqr A; $P \sim 6.3$ years)[8].

HD 159656 was one of the binary systems that Lucy & Sweeney suggested should be reassigned a circular orbit until evidence to the contrary was available. We have computed the corresponding orbital elements for a circular orbit using the historical observations and weights and have included the phased velocity curve on Fig. 7.9. Comparison of the two curves illustrates that there is little to choose between the $e = 0.142$ and the $e = 0$ solutions. Indeed, the r.m.s. of the two fits ($\sim 1.45\,{\rm km\,s^{-1}}$) differ by only $\sim 60\,{\rm m\,s^{-1}}$.

[8]HD 219834 was also included in this study. Using a mean period derived by comparison of historical and recent MJUO velocities of the system, a provisional spectroscopic orbital solution has been derived. The eccentricity measured, $e = 0.198 \pm 0.018$, is clearly non-circular, and is consistent with the astrometric value (see Appendix B and the corresponding tables and figure).

Basis for MJUO selection

HD 159656 was selected for observation towards the end of this study for several reasons. First, observations of a number of other binary systems in this study ceased either because their orbital phases were no longer suitable or because of the increasing awareness that their continued observation would be unlikely to deliver useful results. At about this time, a very successful programme of investigation to determine a high precision orbital solution for another single-lined spectroscopic binary, ζ Trianguli Australis, was also coming to an end (Skuljan et al. 2004). Therefore, as a way to make use of potentially unused telescope time, another binary system was sought. HD 159656 was chosen to take advantage of the anticipated opportunity.

HD 159656 had a certain appeal as its eccentricity was one of the largest that Lucy & Sweeney (1971) advocated being changed to a value of zero. The orbital period of about 10 days, the abundant sharp lines offered by a G4IV–V star, and the velocity semi-amplitude of about $13\,\mathrm{km\,s^{-1}}$ suggested that a precise orbital solution should be achievable in a relatively short timespan, given adequate orbital phase sampling. In terms of the orbital characteristics, the 10-day period (and anticipated mass ratio) meant that the primary star should not be rotating unusually fast for its spectral type, even if synchronization of the axial rotation and orbital period existed. This was confirmed with the first observations which revealed sharp-lined spectra, as illustrated in Fig. 7.10. Finally, the period of HD 159656 places it in an important region of the well-studied $e - \log P$ distribution (see Fig. 4.18 on page 62, or Appendix D).

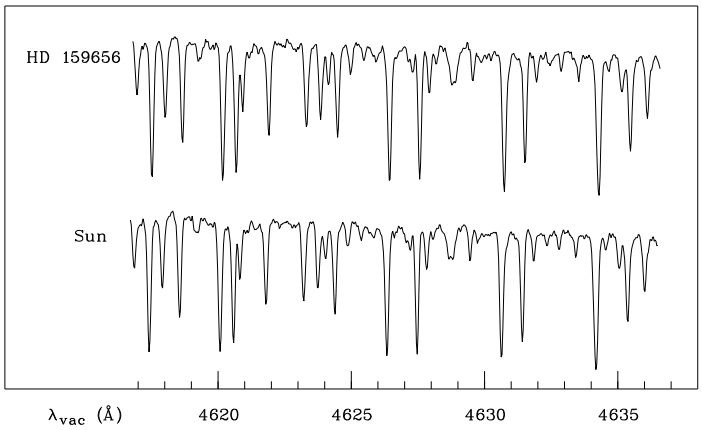

Figure 7.10: The normalized spectrum of HD 159656 and the Sun (blue-sky) in order $n = 123$. The similarity of the two spectra in terms of lines present, relative line strengths and line widths is evident. In particular, the line widths indicate that HD 159656 has a low $v_{\mathrm{equ}} \sin i$.

The MJUO radial velocities and orbital solution

The 121 velocity measurements from the HERCULES observations of HD 159656 were acquired over about six months, between 2004 February 11 and 2004 August 1, using fibre 1 ($R \sim 41\,000$). The velocities and radial-velocity curve corresponding to the orbital solution are plotted on Fig. 7.11. The velocities and their residuals are listed in Table C.3 in Appendix C. Two observations were rejected from the best fit solution as their residuals exceeded 3σ, where $\sigma \approx 15\,\mathrm{m\,s^{-1}}$ is the r.m.s. of the orbital solution.

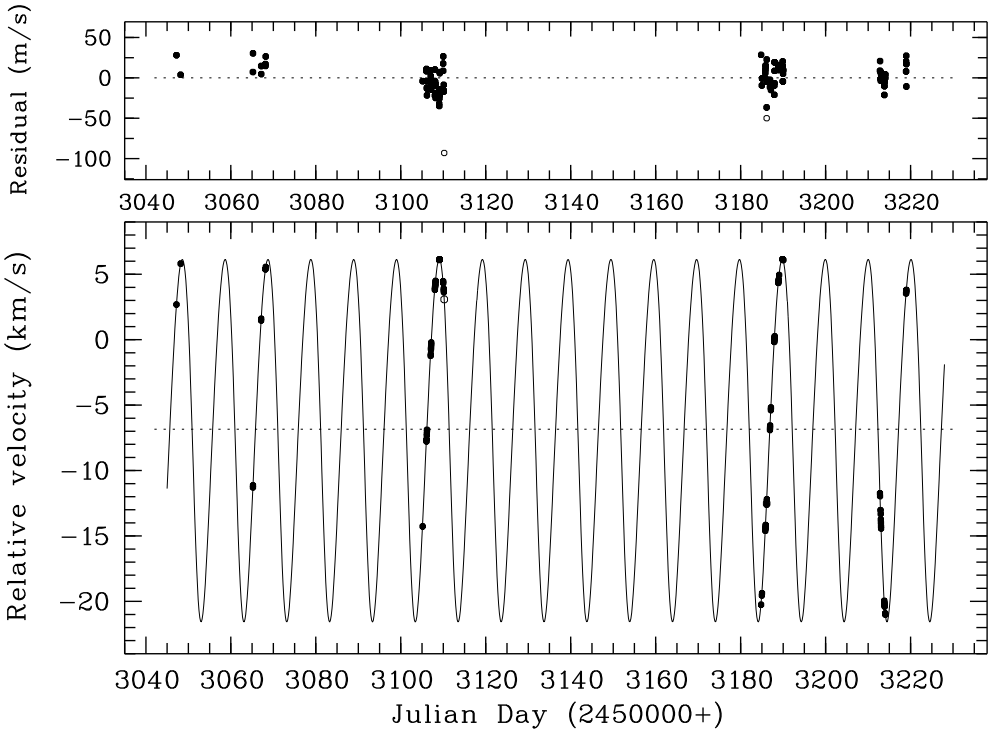

Figure 7.11: Bottom: The MJUO radial velocities of HD 159656 together with the radial-velocity curve computed from the derived spectroscopic orbital elements. The open symbols identify the two observations not included in the orbital solution. Top: The velocity residuals.

The high-precision of the orbital solution presented in Table 7.6 makes it certain that the orbit of HD 159656 is non-circular ($e \sim 0.12$), which is consistent with the original though poorer-precision solution of Barker et al. (1967). The non-sinusoidal appearance of the phased velocities presented in Fig. 7.12 are clear evidence of this.

As was the case for ν Octantis, the historical data for HD 159656 provides an orbital solution best-fit r.m.s. that is much worse than that obtained for the HERCULES observations. Similarly, there are insufficient orbital cycles elapsed ($N_c = 1\,914$), relative to the error measured for the the total time elapsed separating the two zero mean longitude epochs to improve the error on

K_1	=	$13.8590 \pm 0.0024\,\mathrm{km\,s^{-1}}$	P	=	$10.090\,862 \pm 0.000\,067$ d
e	=	$0.115\,83 \pm 0.000\,16$	ω_1	=	$123\overset{\circ}{.}01 \pm 0.10$
T_0	=	JD $245\,3108.79192 \pm 0.000\,53$ d	γ_{rel}	=	$-6.8451 \pm 0.0019\,\mathrm{km\,s^{-1}}$
T	=	JD $245\,3112.2399 \pm 0.0031$			
$a_1 \sin i$	=	$1.910\,12 \pm 0.000\,32$ Gm	f_{M}	=	$2.7274 \pm 0.0013 \times 10^{-3}\,\mathcal{M}_\odot$
	$\approx$	0.013 AU			
		r.m.s. of best fit = $15\,\mathrm{m\,s^{-1}}$			

Table 7.6: The spectroscopic orbital solution for HD 159656 derived from MJUO observations.

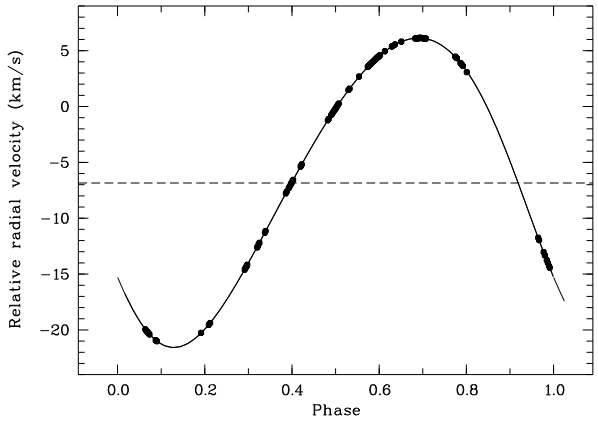

Figure 7.12: The phased MJUO observations of HD 159656 and the corresponding computed radial-velocity curve. The horizontal dashed line represents the relative systemic velocity, γ_{rel}.

a mean period calculation ($\sigma_{\bar{P}} \approx 0.00015$ d, which is twice the error obtained using only the HERCULES data.

The barycentric systemic velocity

As was the case for the binary solutions previously analysed, the systemic velocity of HD 159656 is relative to the velocity of the reference image. Since the observed star has a spectral type similar to that of the Sun, it is reasonable to estimate the barycentric systemic velocity, γ, using either of the methods described in § 6.5 on page 116, i.e., by measuring the barycentric velocity of the reference spectrum relative to the Sun, V_{sky}, or by measuring the velocity, V_{diff}, of the reference image relative to another star of a more similar spectral type whose barycentric velocity, V_{bary}, has also been determined.

Thus, we find, using Eq. (6.1) and 30 sky spectra acquired during the same period that HD 159656 was observed:

$$\gamma = \gamma_{\rm rel} + V_{\rm sky} \approx -6.8451 \pm 0.0019 + 12.260 \pm 0.013 = +5.415 \pm 0.013 \ {\rm km\,s^{-1}}\,,$$

where the precision of this measure reflects principally the scatter of the sky spectra velocities. Using Eq. (6.2) and the G4IV star, HD 109492 (see Table 6.2 on page 114), as the barycentric reference,

$$\gamma = \gamma_{\rm rel} + V_{\rm diff} + V_{\rm bary} \approx -6.845 + 4.569 + 7.682 = +5.406 \ {\rm km\,s^{-1}}\,.$$

The mean of these two values provides the final estimate of the systemic velocity of HD 159656, $\gamma = +5.411 \pm 0.030\,{\rm km\,s^{-1}}$, as usual neglecting the the various complications of such a measurement, including systematic errors arising from spectral mismatch, differences of each star's gravitaional redshift, convective blueshift and other stellar surface anomalies. This velocity is slightly greater than the value, $\gamma \sim +3.8\,{\rm km\,s^{-1}}$ (measured by Barker et al. 1967), the latter of which is included in the radial-velocity catalogue of Barbier-Brossat & Figon (2001).

The true orbital period

Having the period measured with such high precision makes it realistic to consider whether or not the system's systemic velocity could have a significant influence upon our measure of the true orbital period, P_0, as a result of the light-travel-time effect (Kopal 1959). For a binary system moving with a systemic velocity γ, the true period P_0 is related to the observed period P as follows:

$$P_0 = P/(1 + \frac{\gamma}{\rm c})\,. \tag{7.11}$$

The true period of HD 159656 is therefore

$$P_0 = 10.090\,862 \times \left(1 + \frac{5.411}{299\,792.458}\right) = 10.091\,044 \pm 0.000\,067{\rm days},$$

where the error in P_0 is entirely a result of the error in P since σ_γ is negligible owing to its division by c. The value for P_0 differs from P by about $2.7\sigma_P$.

Other characteristics of the primary star

One parameter that can be derived without additional orbital information is the radius of the primary star. This can be estimated from its observed properties, namely $M_{\rm bol}$ and $T_{\rm eff}$, using the methods described earlier (beginning on page 133). For HD 159656, $(V-I)_C = -0.692 \pm 0.020$ (Bessell 1990), so that $BC \approx -0\overset{\rm m}{.}196 \pm 0.014$ and $M_{\rm bol} \approx 4\overset{\rm m}{.}34 \pm 0.07$, or $L \sim 1.45\,L_\odot$. The effective temperature of HD 159656 has been estimated by Nordström et al. (2004) to be

$\log T_{\rm eff} = 3.751 \Rightarrow T_{\rm eff} = 5\,636\,{\rm K}$. Therefore, our estimate for the radius is $R_1 \approx 1.3\,R_\odot$. This measure of the primary star's radius is 30% greater than the value catalogued by Pasinetti-Fracassini et al. (2001) based on Gray's (1967; 1968) method. Gray compared the energy distribution in the entire visual spectrum to a theoretical one so that the angular diameter of a star could be estimated. The radius he deduced for HD 159656, $R_1 = 0.9\,R_\odot$, was consistent with the spectral type accepted at the time (G4V). This radius corresponds to an angular measure of $\sim 0''.004$ which leads to a smaller estimate of R_1 presumably because the parallax was over-estimated by $1 - (29.8/45) \sim 30\%$, as described earlier. The luminosity and radius deduced gives further support to the claim that HD 159656, a mid-G type star, has evolved beyond the main sequence. As noted in the introducion to this system, the isochrone mass of the observed star has been estimated by Nordström et al. (2004) to be $\mathcal{M}_1 = 0.93 \pm 0.05\,\mathcal{M}_\odot$.

The nature of the companion

The expression relating the mass ratio, q, in terms of the orbital inclination, i, (Eq. 7.7 on page 134) has been plotted according to the mass function, $f_\mathcal{M} = 2.7274 \pm 0.0013 \times 10^{-3}\,\mathcal{M}_\odot$ and the estimated mass of the primary star (Fig. 7.13 on the following page). Extreme values of the system mass ratio, the mass of the secondary star and the orbital inclination can be estimated based on various reasonable assumptions. From these values, further characteristics of the HD 159656 binary system can be estimated. Characteristics of interest for this system, with its short 10-day orbital period, are the time required for synchronization of the axial rotation with the orbital period, $t_{\rm sync}$, and the time for an eccentric orbit to circularize, $t_{\rm circ}$.

First, consideration is given to the range of possible mass ratios this binary system may have, which in turn dictates the range of masses the companion will be limited to based on the primary star's mass. In principle, the minimum mass ratio, $q_{\rm min}$, that our orbital solution allows corresponds to an edge-on orbit, i.e. $i = 90°$, and therefore $q_{\rm min} \approx 0.16$. In fact, the $(i,\, q)$-curve demonstrates that, even for orbits with inclinations considerably less inclined than those which are edge-on, have $q \sim q_{\rm min}$. However, the maximum inclination is actually constrained by photometric observations. To a first approximation, and assuming a prograde orbit, to be consistent with the observed lack of eclipse behaviour imposed by HD 1596565's stable photometric record, the orbital inclination cannot exceed

$$i = 90° - \sin^{-1}\left(\frac{R_1 + R_2}{r}\right)$$

for two stars of radii R_1 and R_2 and separation r (see Eq. 2.5 on page 13). The anticipated size of the stars and their minimum separation means that the restricted values of the inclination will amount to no more than a few degrees and therefore this will make no significant difference to $q_{\rm min}$. However, to estimate more accurately the highest inclination consistent with what we know about this binary, we proceed as follows: the theoretical $q_{\rm min}$ corresponds to a secondary mass $M_{2,\,\rm min} \sim 0.15\,\mathcal{M}_\odot$, which may be a white dwarf or a main-sequence star. It has already been demonstrated, in Fig. 7.5 and the related text on page 134, that a white dwarf of this low mass is extremely unlikely. If, instead, the companion is substantially unevolved, this low mass

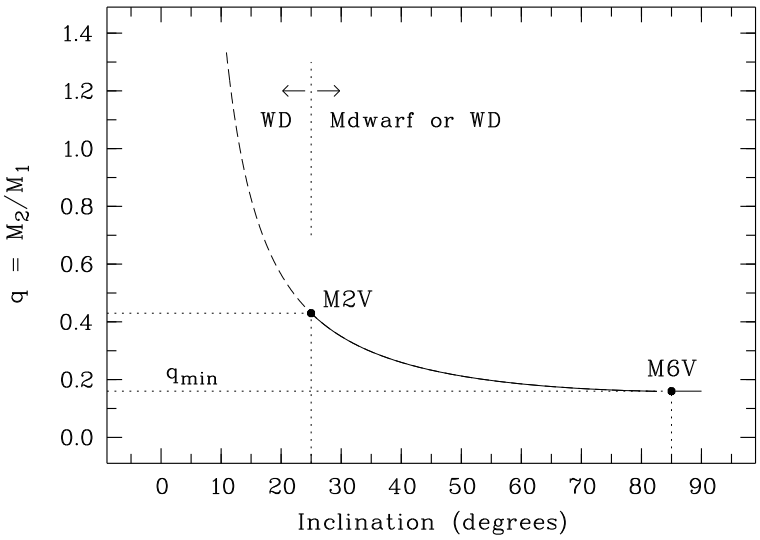

Figure 7.13: The predicted possible range of orbital inclinations and corresponding mass ratios for HD 159656 in a prograde orbit, based on estimates of the mass of the primary star, and the mass function derived from the HERCULES radial velocities. The limits for an unevolved M dwarf companion are represented by the solid symbols. A white dwarf (WD) companion might be more massive than the observed primary star which would require (statistically less likely to be observed) lower inclinations (dashed curve).

corresponds to a star of spectral type M6V ($M_{\rm V} \sim +13$ mag), which is expected to have a radius $R_{2,\,\rm min} \sim 0.2\,R_{\odot}$ (Drilling & Landolt 2000). For an edge-on system, primary mid-eclipse occurs when $v + \omega = 90°$. However, for an inclined eccentric orbit, it is only true that $v + \omega \sim 90°$. The separation, r, can be approximated using Eq. (A.23) on page 215, to get

$$r = a_1 \left(\frac{1 + q_{\rm min}}{q_{\rm min}} \right) \left(\frac{1 - e^2}{1 + e \sin \omega} \right) . \tag{7.12}$$

Therefore, using our estimate for $a_1 \sin i$, and assuming $i \sim 90°$, $r \sim 18\,R_{\odot}$. Therefore, the maximum inclination the binary orbit can have if the unseen companion is an M6 dwarf, is $i_{\rm max} \sim 85°$, and Fig. 7.13 shows that the corresponding mass ratio is insignificantly different from the minimum value. In addition to this estimate for $i_{\rm max}$, we can determine a corresponding size for the true relative orbit, namely, $a_1(1+q_{\rm min})/q_{\rm min} = a \sim 0.09$ AU. The maximum angular separation these components would achieve, for their orbit with a parallax of $p'' = 29.8$ mas, is about 3 mas to an observer on Earth.

The assessment needed to estimate the maximum mass ratio, $q_{\rm max}$, for the unevolved and degenerate companion scenarios follows a different path of reasoning. For the unevolved case, $q_{\rm max}$ is constrained by the lack of spectroscopic evidence of any companion in the highest S/N observations acquired of HD 159656 using HERCULES. If detection were to be possible, two

ways to achieve this would be: 1. to recognize the companion's sufficiently prominent lines in a single high S/N spectrum, or, more likely for a faint companion, 2. to detect the relatively inconspicuous presence of the companion's spectrum by its movement relative to the primary lines as a result of an adequate velocity change, $\delta V = V - V'$, between two observations. The velocity change for the companion would be greater, since $\delta V_2 = -\delta V_1/q$, and therefore $\delta V_2 - \delta V_1 = -\delta V_1(1+q)/q$. A third strategy is to look for evidence of the companion in CCFs created using a suitable template, in this case, that of an M-dwarf[9]. For these investigations, programme spectra obtained at opposite quadrature phases are most suitable as the velocity difference between the components is greatest (see also footnote (10) below).

If the companion's spectrum is unrecognizable, this suggests that its spectral lines are lost in the noise. The S/N in the continuum of an observation can give a clue to the maximum flux ratio (f_1/f_2) between the spectra of the binary pair. Let us assume that any weak absorption lines can be detected only when they are deeper than, say 5σ, where $\sigma = (S/N)^{-1}$, is the standard deviation in the continuum. If those lines have a typical relative intensity of ~ 0.5, then the base level of the secondary spectrum must be at least at 10σ below the continuum. For a given photometric passband, Λ, the magnitude difference, $M_{\Lambda_2} - M_{\Lambda_1}$, corresponding to a flux ratio, f_1/f_2, is $M_{\Lambda_2} - M_{\Lambda_1} = 2.5\log(f_1/f_2)_\Lambda$.

The two images used for this purpose have $S/N \approx 450$ in the red orders, $\lambda \sim 7000$ Å (middle of the R filter), where an M dwarf's spectral lines would be more easily recognized than at shorter wavelengths. Each image was created by co-adding several spectra, each with moderate signal ($S/N \sim 200$ in the red)[10].

Therefore, the brightest absolute V magnitude that the faint secondary can have is

$$\begin{aligned} M_{\mathrm{V}_2} &= \Big[M_{\mathrm{V}_1} - (V-R)_1)\Big] + (V-R)_2 + 2.5\log\left(f_1/f_2\right)_{\mathrm{R}} \\ &= \Big[M_{\mathrm{V}_1} - (V-R)_1)\Big] + (V-R)_2 + 2.5\log\left(\frac{S/N}{10}\right). \end{aligned} \tag{7.13}$$

Again, we take advantage of the tables of Drilling & Landolt (2000) as well as Bessell's (1990) measure for $(V-R)_1 = +0^{\mathrm{m}}.356$. As the nature of the secondary star is yet to be determined, we must guess $(V-R)_2$, and iterate Eq. (7.13) until $(V-R)_2$ for a given spectral type is

[9] This approach was also explored, using as template a $S/N \sim 200$ spectrum of the M1/M2 dwarf HD 202560. No recognizable signal of the companion was evident in any of the CCFs produced.

[10] The contributing spectra in each case were acquired when the system was close to quadrature so that the velocity differences between the co-added images was minimised ($\Delta V \lesssim 100\,\mathrm{m\,s^{-1}}$) during the time interval required to acquire the spectra (~ 2 hours). The highest S/N obtained with a *single* observation ($S/N \sim 250$ in the red orders), was acquired with an exposure time of 30 minutes. This was recorded on another night, when HD 159656 was close to the zenith and when the seeing, $\theta_* \sim 3''$, was slightly better than its median value (see § 5.2 on page 72 for comments relating to the seeing at MJUO).

consistent with the derived M_{V_2}. The magnitudes that are consistent with this analysis[11] are $(V-R)_2 \approx 1\overset{\mathrm{m}}{.}5$ and $M_{V_2} \approx 9\overset{\mathrm{m}}{.}8$. For an unevolved companion, these magnitudes correspond to it having a spectral type no earlier than about M2V. A star of this spectral type has a mass $\mathcal{M}_2 \sim 0.4\,\mathcal{M}_\odot$. Therefore, $q_{\max} \sim 0.43$, $i_{\min} \sim 25^\circ$ and $a \sim 0.1$ AU. The radius this companion is predicted to have is $R_{2,\,\max} \sim 0.5\,R_\odot$ (Drilling & Landolt 2000).

What chance is there that a more massive companion might be a white dwarf? Evidence from studies of open clusters suggest that the white-dwarf progenitor upper-mass limit could be as much as 4–5 $\mathcal{M}_\odot$ (Liebert 1980). HD 159656 has an estimated age of about 10 Gyr, which is more than enough to accommodate the evolution of a sufficiently massive, faster evolving, companion to such a remnant, assuming that the components are coeval. A white dwarf's intrinsic faintness is also consistent with the absence of the secondary spectrum. If a planetary nebula had been formed during the progenitor's evolution, the nebulosity would have had ample time to dissipate since these features are predicted to be evident for less than 100 000 yr. The white dwarf remaining would have to have a mass less than the Chandrasekhar limit, $\mathcal{M} \sim 1.44\,\mathcal{M}_\odot$ (Hilditch 2001), a limit which depends, in part, on the composition of the stellar remnant.

One argument against a white dwarf with a mass greater than that of the speculated more massive M-dwarf companion, is that a greater companion mass dictates a smaller orbital inclination, which for statistical reasons are increasingly less likely to be observed. However, this argument per se has no validity for masses equal to the possible M-dwarf masses outlined above. The possibility that the companion is a neutron star is even slimmer, as, for instance, these stellar remnants have masses believed to start at the upper limits of white dwarfs and also evolve from less common, more massive stars.

Finally, it is straightforward to show that the primary star and its companion, whatever the nature of the latter may realistically be, are each *presently* substantially detached from their predicted Roche surfaces. The formula reported by Eggleton (1983; see Eq. 2.6 on page 16), predicts that R_*/R_{L}, which is dependent on the mass ratio of the system, is no greater than about 0.1. Obviously, that may not have always been the case, if the companion is a white dwarf that evolved from a rather more massive progenitor.

The preceeding results that have been obtained with the assumption that the companion is unevolved, are summarized in Table 7.7.

An attempt to detect the secondary star in HD 159656 by optical speckle interferometry was unsuccessful (Mason et al. 1998a). The detection limits for this study were $\Delta V \leq 3\overset{\mathrm{m}}{.}0$ and the component separations had to lie between $0\overset{''}{.}035$ and $1\overset{''}{.}08$. In the case of HD 159656, the magnitude difference $\Delta V \geq 5\overset{\mathrm{m}}{.}3$ and the earlier estimate for the maximum angular separation of the components, $\rho \sim 0\overset{''}{.}003$, both made it impossible for detection of the companion to have been

[11] $M_{V_2} \sim (+4.540 - 0.356) + \underline{1.50} + 2.5 \times \log(450/10) \approx \underline{9\overset{\mathrm{m}}{.}8}$, where both $(V-R) = 1\overset{\mathrm{m}}{.}50$ and $M_{\mathrm{V}} = 9\overset{\mathrm{m}}{.}8$ are consistent with a star of the same spectral type.

	primary	secondary	
spectral type	G4IV-V	M6V	M2V
M_V	+4.54	+13	+9.8
q	→	0.16	0.43
$\mathcal{M}$ ($\mathcal{M}_\odot$)	0.93	0.15	0.4
R ($R_\odot$)	1.3	0.2	0.5
i (°)	→	85	25
a (AU)	→	0.09	0.10
a ($R_\odot$)	→	20	22.5

Table 7.7: Some parameters of the primary and possible unevolved secondary components of HD 159656.

achieved, a fact that was recognized by the authors but which did not deter them from trying. Detection of such a faint close companion will have to await the next generation of space-based astrometric instruments such as SIM or GAIA (Global Astrometry for Interferometric Astrophysics).

The Mason et al. (1998a) study also compared the relative multiplicity fractions for binary systems that had chromospherically active or inactive components, and estimated the ages of the systems based on the strength of their chromospheric emission. They estimated the mean age of their active and inactive samples as about 1 Gyr and 4 Gyr respectively. These authors noted that chromospheric activity is a poor indicator of age when the stars are *very* active e.g. when in RS CVn systems, but seem to have considered that the activity would be a reliable indicator of age otherwise. As will shortly be revealed, HD 159656 is just such a system where the chromospheric age is markedly less than has been deduced by other methods. Just how many other active but *not* young systems were in their sample is unknown, but clearly their final statistics with regards to multiplicity and binary age may be distorted.

The times for orbit synchronization and circularization

Synchronization of a given star's axial rotation with its orbital period, and circularization of the mutual orbits, each require the action of both a frictional mechanism and a tidal component. Synchronization requires that there is exchange between the spin angular momentum of the star and the orbital angular momentum. For a given orbital angular momentum, circular orbits have the least orbital energy. The energy in excess of the minimum amount for the system's angular momentum produces the eccentricity, and any process that reduces the energy can facilitate the circularization phenomenon (Lubow 1993; and see Appendix D beginning on page 259).

There have been numerous investigations into the synchronization and circularization time scales of binary systems (see below and Appendix D for references). One of the most active

workers in this field of study is J. -P. Zahn. As have other workers since (e.g. Goldman & Mazeh 1991; Tassoul 1995; Claret & Cunha 1997), Zahn (1977) has provided formulae that make it possible to estimate the time it might take for synchronization, $t_{\rm sync}$, and the time required to circularize the orbit, $t_{\rm circ}$. Separate formulae are available for stars with convective envelopes (for which the most efficient dissipation mechanism is claimed to be turbulent friction retarding the equilibrium tide), and for those with radiative envelopes (for which the principle dissipative mechanism is claimed to be radiative damping on the dynamical tide[12]).

HD 159656, as well as all other late-type stars studied during this thesis, has a convective envelope. The approximation $t_{\rm sync}$ and $t_{\rm circ}$ formulae for convective envelope stars reported by Zahn (1977) are:

$$t_{\rm sync} \approx 10^4 \left(\frac{1+q}{2q}\right)^2 P^4 \text{ years}, \tag{7.14a}$$

$$\text{and} \qquad t_{\rm circ} \approx 10^6 q^{-1} \left(\frac{1+q}{2}\right)^{5/3} P^{16/3} \text{ years}, \tag{7.14b}$$

where P is in days. Therefore, the estimates for the times for synchronization and circularization depend on the mass ratio q. The maximum time required to synchronize the primary star's axial rotation to the orbital period corresponds to the minimum mass ratio, $q_{\rm min} \sim 0.16 \Rightarrow t_{\rm srnc,\,max} \sim 1.4\,$Gyr. However, the predicted minimum time to circularize the orbit, which corresponds to the maximum mass ratio, $q_{\rm max} \sim 0.43$ (assuming $i_{\rm min} \sim 25^\circ$), is $t_{\rm circ,\,min} \sim 300$ Gyr, which far exceeds the age of the universe[13]. Typically, alternate theories for calculating the circularization time, predict smaller values. For instance, Goldman & Mazeh (1991) claim $t_{\rm circ} \sim 10^{10/3}$, which for $q_{\rm max} = 0.43$ as used above, we get $t_{\rm circ} \sim 3\,$Gyr. In fact, based on observational evidence from other studies of circularization times for binary systems of various ages, Zahn's predictions definitely appear to be excessive, as the following comments emphasize.

For over a century, it has been increasingly recognized that binary systems with short period orbits ($\lesssim 10$ days) are likely to have orbits which are circular rather than eccentric (see Duquennoy & Mayor 1992, for proceedings of a conference substantially devoted to matters relating to orbital circularization and synchronization). Circumstances that occasionally arise to upset this trend include the presence of a distant third star which might induce the orbit to remain or become eccentric (e.g., see Mazeh 1990). Over the past couple of decades, many studies have

[12]Using a classical approximation, the equilibrium tide is the adjustment of a star's equilibrium shape in response to tidal distortions caused by a close companion. The dynamical tide describes various other processes, such as modes of oscillations, and the increased dissipation of energy in the star resulting from compression of the heated gases, i.e., radiative damping (see Hilditch 2001, p. 141–142, for further details).

[13]If the companion is a white dwarf, the post-main-sequence evolution of the more massive precursor would have provided a much deeper convective zone during its giant phase, and therefore we would expect any circularization to occur more rapidly. However, the evolution of these more massive stars would probably lead to the complex interactions of Roche lobe overflow which would greatly complicate any analysis of the possible orbital history.

investigated samples of spectroscopic binaries with a view to establishing the orbital period that corresponds to the maximum period below which all orbits in the sample are circular. This so-called cut-off period, $P_{\rm cut}$, is typically $\sim$ 6–20 days, depending on the mean age of the sample, spectral type and so on.

For instance, for young open clusters such as Praesepe and the Hyades, $P_{\rm cut} \sim 5.7$– 8 d (age 0.8 Gyr; Mayor & Mermilliod 1984; Mermilliod 1997), for the much older open cluster M67, $P_{\rm cut} \sim 12.4$ d (age 4 Gyr; Latham et al. 1992) and for the halo, $P_{\rm cut} \sim$ 19–20 d (Latham et al. 1992; Latham et al. 2002). Both of the older samples drawn from M67 and the halo, have stars with ages comparable to that predicted for HD 159656. However, unlike the shorter period members of these samples, HD 159656, with its 10.1-day period, and its somewhat deepened convective zone owing to its evolutionary stage (which should assist the circularization process), retains an orbit with an eccentricity that is significantly non-zero ($e \sim 0.12$). Therefore, HD 159656 has an orbit that occupies a significant and interesting location in the $e - \log P$ distribution (see Fig. 4.18 on page 62, or Appendix D).

The possibility exists that the eccentric orbit of HD 159656 is the result of a distant faint third star, perhaps another red or white dwarf. This is a reasonable suggestion, as it is believed 20–50% of binary stars are members of triple or multiple systems (Batten 1973; Mazeh 1990). If a third companion exists in this binary system, it may reveal itself by inducing nodal precession in the orbital plane (Mazeh & Shaham 1976). For very close binary pairs, apsidal motion can have a rotational period as short as a few years. Apsidal motion can also provide the opportunity to investigate the density distribution within a star, an important test of stellar-structure theory (Hilditch 2001). Unfortunately, the precision of the historical orbital solution is inadequate to allow a reliable assessment of any change of this kind at present. However, the HERCULES result addresses this situation, and future high-precision solutions may demonstrate a significant and tell-tale change to ω.

If we accept the predicted value for $t_{\rm sync,\,max} \sim 1.4$ Gyr as being valid, then the anticipated synchronization of HD 159656 allows the rotational velocity, $v_{\rm equ} \sin i$, of the primary star to be estimated, based on its radius $R_1 \sim 1.3\,R_\odot$, and period $P \sim 10.09$ days. Thus, we determine $v_{\rm equ} \sim 2\pi R/P \sim 7\,{\rm km\,s^{-1}}$. This velocity is consistent with the sharp-lined spectra recorded for HD 159656 (Fig. 7.10). It is well-recognized that single late-type main-sequence stars have very low rotational velocities. Evolution of these stars away from the main-sequence slows them even further as a result of magnetic braking due to the deepening of the convective envelope, and the reduction of angular momentum as a result of mass loss in a stellar wind. The mean value of rotational velocities of subgiants decreases gradually from about $6\,{\rm km\,s^{-1}}$at G0IV, to about $1\,{\rm km\,s^{-1}}$at K5IV (Lèbre et al. 1999). The estimated axial rotation of HD 159656 does not differ significantly from these values for $v_{\rm equ} \sin i$. One may therefore speculate whether or not the axial rotation has increased as a result of tidal locking and spin-up as a consequence of the synchronization process. This possibility is supported by the observed activity of HD 159656, as will now be discussed.

HD 159656 as an active star

During the past decade, HD 159656 has been identified as an active star based on ultraviolet (UV) and X-ray emissions. UV emissions have been observed in the Ca II H and K lines. These spectral features are used as indicators of chromospheric emission (CE). CE is observed in stars later than about F0–F2, that is, in stars that have non-negligible convective envelopes. In general, for single stars, rapid rotation and youth is associated with greater CE activity (Baliunas et al. 1995). Stars in very close binary systems, where rapid rotation due to synchronization of the axial rotation with the orbital period is present, are more likely to be CE active, for instance, as is observed for RS CVn or W UMa types (Henry et al. 1996). Evolved stars are also typically more active than main-sequence stars of the same rotation period (Stassmeier et al. 1990).

Examples of the Ca II H and K emissions of HD 159656 acquired with HERCULES[14] are presented in Fig. 7.14. The chromospheric emission ratio, $\log R'_{\rm HK} = -4.57$ (Henry et al. 1996), indicates that HD 159656 belongs to the population of CE active stars (Fig. 7.15a). CE activity has been classified into four groups based on a star's $R'_{\rm HK}$. Thus, we have: very active, $\log R'_{\rm HK} < -4.25$; active, $\log R'_{\rm HK}$ extends between -4.25 and -4.75; inactive, $\log R'_{\rm HK}$ varies between -4.75 and -5.1; and finally inactive, $\log R'_{\rm HK} > -5.1$ (Henry et al. 1996)[15].

HD 159656 was also included in a study investigating the X-ray luminosity of nearby stars (Hünsch et al. 1999). This work relied on observations acquired by the ROSAT All-Sky Survey, combined with *Hipparcos* parallaxes. All of the 3 802 stars included in the CNS3 (Gliese & Jahreiss 1991) were assessed for X-ray emissions. Approximately 33% of the CNS3 stars were detected. The X-ray luminosity of HD 159656 was measured to be $L_{\rm x} = 108.2 \times 10^{27}\,{\rm erg\,s^{-1}}$. Only 283 ($\sim 25\%$) of the stars with a detectable X-ray flux were found to be more luminous[16] than HD 159656 (see Fig. 7.15b). Therefore, this binary system is more X-ray luminous than about 92% of CNS3 stars. The fact that HD 159656 has substantial X-ray luminosity is consistent with the finding of Makarov (2003), who reported that at least 40% of the most X-ray luminous sources within ~ 50 pc are spectroscopic binaries. HD 159656 was not identified in the

[14]Unfortunately, the detector position used in this study for radial-velocity observations does not include the Ca II H or K lines. Therefore, the Ca II lines could only be recorded if the CCD was moved, a requirement not well-suited to precise radial-velocity work. An attempt was made by another observer to record the Ca II emission at opposite quadratures so as that it would be possible to make the additional useful distinction as to whether the emission belongs to the primary or the secondary star. The spectrum illustrated in Fig. 7.14 is courtesy of S.Barnes. Unfortunately, the spectrum acquired at one quadrature was lost because of chip readout failure. Two other spectra were obtained, but on occasions when the binary was close to the systemic velocity, when $V_{\rm r2} - V_{\rm r1} \approx 0$. Whilst this present outcome is regrettable, nonetheless, it is irrefutable that at least one of the components displays activity at UV wavelengths.

[15]The emission ratio $\log R'_{\rm HK} = -4.75$ is coincident with the so-called Vaughan-Preston 'gap' or transition zone (vaguely recognizable in Fig. 7.15a), wherein lie the relatively few stars of intermediate activity. By comparison, the solar cycle causes the relatively inactive Sun's $\log R'_{\rm HK}$ to vary between -4.78 and -5.00 (Baliunas et al. 1995). A similar distribution of $\log R'_{\rm HK}$ values has been reported by other workers, for example, Gray et al. (2003).

[16]For comparison, the solar X-ray luminosity varies between about 3×10^{25} and $10^{27}\,{\rm erg\,s^{-1}}$ (Hünsch et al. 1999) during the solar cycle.

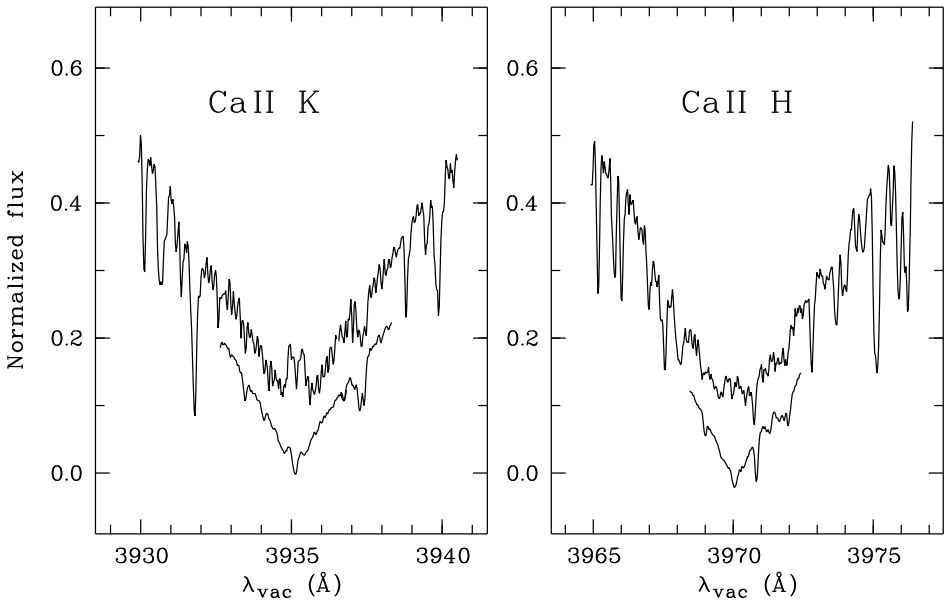

Figure 7.14: Ca II H and K line profiles. On each plot, the upper spectrum is of HD 159656 revealing its Ca II emission. The lower smaller spectral segment is from a solar (blue-sky) observation, which demonstrates the relative Ca II emission of the two stars. (HD 159656 observation date: JD 2 453 256.82)

survey of ROSAT data by Fuhrmeister & Schmitt (2003) as having variable X-ray output.

Both the UV and the X-ray emission findings are generally regarded as good indicators of magnetic activity and stellar youth (e.g., Baliunas et al. 1995). Since the earliest investigations (e.g. Wilson 1963) a correlation between Ca II emission strength with stellar age has been suggested, presumably due to the relationships between a star's rate of rotation, magnetic field strength and chromospheric activity (Noyes et al. 1984). A few close binaries were recognized that disageed with this trend, with the view that the emission may be due to mass exchange (Warner 1969). This cannot be the case for HD 159656 as its components presently exist in a well-detached system.

The relationship between age and CE continues to be explored, (e.g., Soderblom et al. 1991; Donahue 1993; Rocha-Pinto & Maciel 1998). Each of these studies suggested relations that calibrated the chromospheric age, $t_{\rm CE}$, against $\log R'_{\rm HK}$ or equivalently $R_5 = R'_{\rm HK} \times 10^5$ (= 2.69 for HD 159656). For instance:

$$\log t_{\rm CE} = -1.50 \log R'_{\rm HK} + 2.25 \qquad \text{(Soderblom et al. 1991)}, \tag{7.15a}$$

$$\log t_{\rm CE} = 10.725 - 1.334 R_5 + 0.4085 R_5^2 - 0.0522 R_5^3 \qquad \text{(Donahue 1993)}, \tag{7.15b}$$

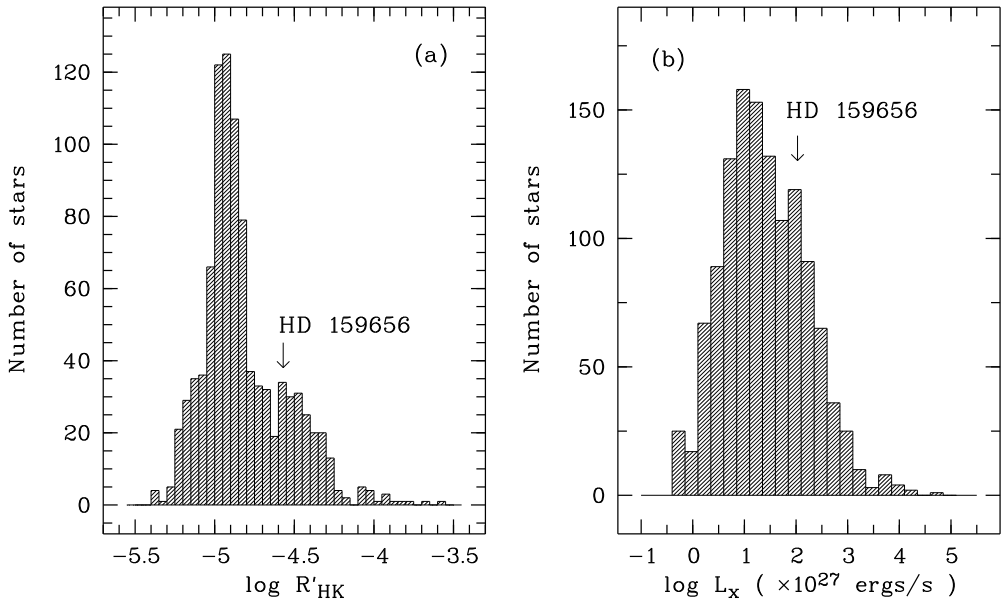

Figure 7.15: (a) A histogram of the chromospheric emission ratio for a sample of 800 southern stars (Henry et al. 1996). The transition between active stars such as HD 159656, and inactive stars such as the Sun occurs at $\log R'_{\rm HK} = -4.75$. (b) The luminosity in X-rays of a sample of 1 252 stars observed by the ROSAT X-ray all-sky survey. The activity of HD 159656 in terms of these indicators is identified.

These relations has been used by other investigators, for example, Henry et al. (1996), Mason et al. (1998a); Mayor et al. (2004), and Wright et al. (2004), each of whom used the Donahue expression. Henry et al. (1996) pointed out that, given the variable solar CE activity, the Sun's chromospheric age could be estimated between 2.2 and 8 Gyr. Mayor et al. (2004) and Wright et al. (2004) both made their chromospheric age estimates in the context of extrasolar planet search lists of stars not believed to include close binary systems[17].

The chromospheric age deduced for HD 159656 is $\log t_{\rm CE}\,({\rm Gyr}) \sim 9.1$, or $t_{\rm CE} \sim 1.3$ Gyr, a value which is considerably lower than our previously cited estimates of its isochrone age. The estimate of $t_{\rm CE}$ places HD 159656 in the young disk population and hardly gives it time as a subsolar-mass star to evolve at all away from or even along the main-sequence, which is quite at odds with other observational material. This clearly suggests that HD 159656 is not a valid

[17]In can be seen by inspection of the respective curves in Fig. 7.16 that there is no significant difference between the ages derived using the much simpler Soderblom et al. (1991) expression as compared with the Donahue expression (1993) for the range of $\log R'_{\rm HK}$ between -5.3 and -4.5, a range that includes the majority of stars in the 800 star sample of Henry et al. (1996; see Fig. 7.15a).

object to which to apply these CE-age calibration relations.

Rotational period and CE

We have predicted that HD 159656 is more than old enough to achieve a synchronized orbit within its lifetime. Noyes et al. (1984), found that $R'_{\rm HK}$ was well correlated with the parameter $P_{\rm rot}/\tau_{\rm c}$ for a sample of main-sequence stars. $P_{\rm rot}$ is the rotation period and $\tau_{\rm c}$ is a function of $(B-V)$ (see their equations (3) and (4)). τ is the theoretically-derived convective overturn time which is related to the depth of the convection zone of the star. The slightly evolved nature of HD 159656 may make valid application of this relationship uncertain. However, with this possibility in mind, we can derive the expected rotational period for HD 159656 based on $(B-V) = 0\overset{\rm m}{.}641 \pm 0.008$ (ESA 1997) and $R'_{\rm HK}$ using the expressions provided by Noyes and co-workers. The value we get is $P_{\rm rot} \sim 11.3\,{\rm d}$ (see Fig. 7.16). This is in excellent agreement with our estimate based on the assumption that the axial rotation is synchronized with the orbital period $P \sim 10.1$ days and well within the error margin of 0.08 dex given for this calibration relation.

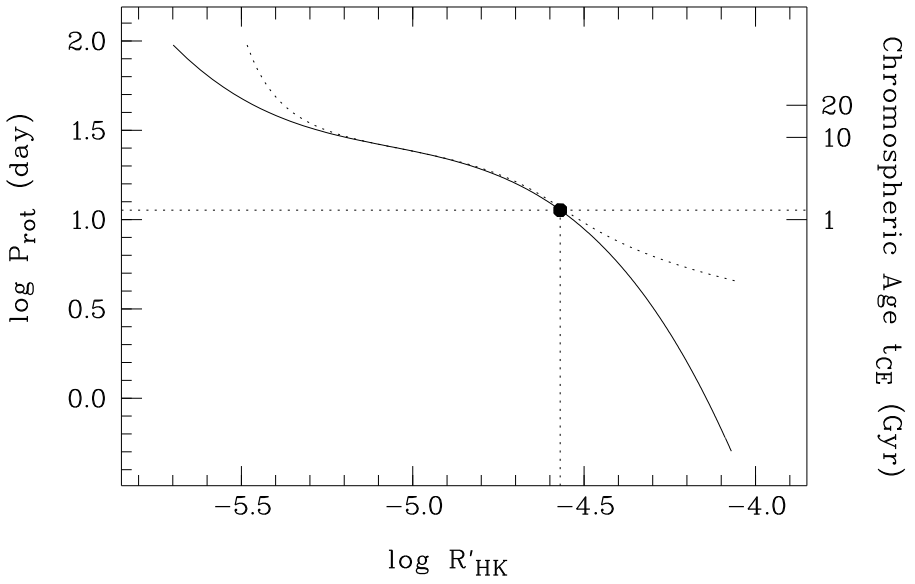

Figure 7.16: The predicted rotational period, $P_{\rm rot}$, and the chromospheric age, $t_{\rm CE}$, as a function of $\log R'_{\rm HK}$. The solid curve has been generated using the expressions found in Noyes et al. (1984) that relate $P_{\rm rot}$ to $\log R'_{\rm HK}$. The corresponding values for $t_{\rm CE}$, on the right axis, have been calculated using Eq. (7.15b); Donahue (1993). The dotted curve was then generated using these ages in Eq. (7.15a); Soderblom (1991). The solid symbol represents the published value for $\log R'_{\rm HK}$ for HD 159656 (Henry et al. 1996).

The tightness of the CE vs. $P/t_{\rm c}$ relationship was considered by Noyes et al. (1984) to

provide strong support for the idea that the ratio of rotation period to convection overturn time (the Rossby number *Ro*) is a significant determinant of magnetic field amplification in rotating stars with convective envelopes. Such a relationship is to be expected from standard dynamo theory. The unexpected activity of a binary system as old as HD 159656 supports the possibility of a synchronized orbit since the spun-up star/s can be expected to acquire this greater magnetic field strength.

Balinus et al. (1995) notes that it is common for the two components in a binary system (at least 18 of 22 systems sampled in their study) to have CE levels that places both stars in the same activity class. Henry et al. (1996) reported that these systems yield CE ages that differed by less than 0.5 Gyr. However, in terms of determining the validity and reliability of these CE-age relationships, an equally important test must be that the chromospheric ages are accurate. HD 159656 is likely to be an example were that would not be the case.

Summary

A high-precision spectroscopic orbital solution for the single-lined binary system HD 159656 has been described, and is presented in Table 7.6 on page 153. This solution confirms the low-eccentricity ($e \sim 0.12$) solution originally reported by Barker et al. (1967) but brought into doubt by the statistical study of Lucy & Sweeney (1971).

HD 159656 is an interesting and enigmatic object for several reasons:

1. The system appears to be very old, having an isochrone age perhaps as great as ~ 12 Gyr (Nordström et al. 2004). Its subsolar-mass evolutionary state (G4IV-V), deduced radius, space velocities (Eggen 1998) and the predicted height of its Galactic orbit (Nordström et al. 2004) are all consistent with a considerable age.

2. HD 159656 occupies a significant corner of the $e - \log P$ distribution. Its 10.1 day period places it in an interesting position on the $e - \log P$ distribution, separating the young open cluster systems with $P_{\rm cut} \sim 8$ d (Mermilliod 1997), from the old halo objects that have $P_{\rm cut} \sim 20$ d (Latham et al. 2002). The estimated age of HD 159656 is closer to that of the halo sample. If we assume the considerable age is accurate, the possibility exists that the significantly non-circular orbit is the result of a distant third stellar companion and the consequent possibility of detection of apsidal motion.

3. This binary system displays evidence of considerable UV and X-ray activity that might imply it is instead as young as ~ 1 Gyr. Active stars are more likely to present variable behaviour and be associated with relatively greater levels of magnetic activity. The ROSAT observations identified HD 159656 as being more X-ray luminous than $\sim 92\%$ of all stars listed in the Nearby Star Catalog (Gliese & Jahreiss 1991).

4. HD 159656 is probably a clear example of the caution that should be exercised when considering chromospheric activity as a trustworthy indicator of age.

5. The axial-rotation period of HD 159656 is predicted to be synchronized with the orbital period. The measured chromospheric activity is consistent with, and indirect support for, a synchronized rate of rotation (Noyes et al. 1984), suggesting its active nature is a result of enhanced dynamo processes due to tidal locking and spin-up, rather than youth. Enhanced activity due to mass exchange would be limited to captured stellar winds since the components are presently significantly detached from their Roche surfaces.

6. The primary star has been recognized as a standard star in several photometric systems for several decades (e.g., Cousins & Stoy 1962; Forbes et al. 1997). Recently, HD 159656 was suggested as a candidate as an unpolarised standard (Gil-Hutton & Benavidez 2003). The stability of HD 159656 in both of these regards suggest that its magnetic activity is not large.

7. The various scenarios for the allowed unseen companion include an M dwarf of spectral type M2–M6 or a white dwarf. The considerable age of HD 159656 makes it possible that both a degenarate white dwarf or an unevolved M2–M6 dwarf is consistent with this analysis.

The double-lined binary systems

Three SB2 systems have been analysed in detail. Two of these are the visual binaries HD 206804 (K7V+K7V) and HD 217166 (G1V+G4V). The third system is a newly discovered binary, HD 181958 (F6V+F7V), which should be suitable for investigation by present ground-based high-angular resolution techniques. All of these binaries have periods that are unusually long $\gtrsim 3$ years, as compared to other SB2 systems reported in the literature (Pourbaix et al. 2004). These binaries have been the subjects of two accepted publications (Ramm et al. 2004; Ramm et al. 2005).

7.4 HD 206804 (HIP 107522; $21^{\rm h}46^{\rm m}36^{\rm s}$, $-57^\circ42^{\rm m}12^{\rm s}$)

HD 206804 is a visual binary whose components are a pair of almost equal ninth-magnitude K7 dwarf stars in a moderately eccentric ($e \sim 0.6$) orbit with a period of about six years. The system resides in the inconspicuous southern constellation of Indus close to its border with Tucana, whose brightest star, α Tucanae, is about 8° eastward. About a degree to the north of HD 206804 is ϵ Indi, a bright K5 dwarf ($V \sim 4\overset{\rm m}{.}7$) that has the distinction of being the sixth closest naked-eye star to the solar system, and the only K5–K7 solitary dwarf brighter than sixth magnitude in the southern sky (ESA 1997). More importantly for this work, ϵ Indi's brightness and similar spectral type made it a suitable choice for the template spectrum for the cross-correlation of the double-lined spectra of HD 206804 obtained with the HERCULES spectrograph.

HD 206804 is listed in the 'Henry Draper Catalogue' (Cannon & Pickering 1918) with a photometric V magnitude of $8\overset{\mathrm{m}}{.}6$ and spectral class Ma. This spectral class, first introduced by Edward Pickering and Williamina Fleming in their 'Draper Memorial Catalogue', is equivalent to the modern Draper classification M0. The spectral type of HD 206804 was re-classified to K7V (Eggen 1955), where it is now generally regarded to be best placed. Somewhat surprisingly, it was described as having a composite spectrum, K5V + G/KIII, by Houk et al. (1975). The possibility of this binary harbouring a giant component is entirely inconsistent with the apparent magnitude and parallax of the system. Edwards (1976) undertook an investigation into the spectral types of *each* component of 208 visual binaries and assigned both stars of HD 206804 a spectral type of K7V on the basis that only two stars were present and the magnitude difference was only $\Delta m = 0\overset{\mathrm{m}}{.}15$. HD 206804 is included in a list of near-infrared standard stars (McGregogor 1994; see therein for various magnitudes).

HD 206804 was included in Luyten's (1955) catalogue of stars with high proper-motions ($\mu > 0\overset{''}{.}5\,\mathrm{yr}^{-1}$). The modern values for the proper motions of this binary system are $(\mu_\alpha \cos\delta, \mu_\delta) \approx (0\overset{''}{.}09, -0\overset{''}{.}91)\,\mathrm{yr}^{-1}$ (ESA 1997). Eggen (1971) placed HD 206804 in one of his smaller moving groups of old disk stars, the η Cephei group. Using *Hipparcos* and *Tycho* data (ESA 1997), Kharchenko (2001) derived the combined V and B apparent magnitudes for HD 206804: $V = 8\overset{\mathrm{m}}{.}790 \pm 0.011$ and $B = 10\overset{\mathrm{m}}{.}108 \pm 0.014$, so that $(B - V) = 1\overset{\mathrm{m}}{.}318 \pm 0.017$.

HD 206804's binary nature was discovered by W. S. Finsen (ϕ 283). The first astrometric orbital solution, computed by van den Bos (1950), included the orbital elements $P = 6.32$ yr and $a'' = 0\overset{''}{.}2335$ for the nearly equal components. The accepted trigonometric parallax of the time, 46 ± 7 mas, implied an improbable total mass for the system, $\mathcal{M}_\mathrm{S} = 3.28\,\mathcal{M}_\odot$. In his catalogue of visual binaries of spectral type later than K8, Baize (1966) pointed out that a dynamical parallax $p''_\mathrm{dyn} = 63$ mas was more consistent with a realistic total mass of about $1.3\,\mathcal{M}_\odot$ (modern value: $\mathcal{M}_\mathrm{S} \sim 1.2\,\mathcal{M}_\odot$, Drilling & Landolt 2000). A subsequent increase of the value measured for the trigonometric parallax to 52 ± 6 mas (Woolley et al. 1970) reduced the system mass to $\mathcal{M}_\mathrm{S} = 2.27\,\mathcal{M}_\odot$, which still exceeded the anticipated value by about one solar mass. The modern trigonometric parallax is 52.56 ± 1.88 mas (ESA 1997).

The next astrometric orbital solution for HD 206804 was computed by Finsen (Rossiter 1977). On this occasion, two solutions were offered. These solutions differed in a way common for visual binaries harbouring equal components; namely, one solution of moderate eccentricity, and the other nearly circular but with a period twice as long. These two solutions are listed in Table 7.8.

The most recent attempts to improve the astrometric orbital solution of HD 206804 relied on *Hipparcos* observations. Martin et al. (1997) identified HD 206804 as one of 18 binary systems that might provide the opportunity accurately to measure the system mass ratio using these data, provided the elements of the relative orbit were known. Their method of investigation, which was related to the determination of photocentric orbital solutions, relied upon the components having an orbital period less than about 20 years but with an angular separation in

	Solution 1	Solution 2
P (yr)	6.25	12.48
a''	0.205	0.315
e	0.551	0.024
i (°)	130.90	117.00
ω (°)	358.00	278.70
T	1945.500	1945.840
Ω (°)	110.00	112.00
$\mathcal{M}_{\rm S}$ ($\mathcal{M}_\odot$)	1.57	1.43

Table 7.8: Astrometric orbital solutions for HD 206804 as computed by Finsen (Rossiter 1977). The respective mass-sum values are also given.

excess of $0''.3$. Finsen's second solution met these requirements.

Subsequently, Martin & Mignard (1998) identified HD 206804 as one of 145 binary systems whose *Hipparcos* data might allow an improved orbital solution, or measurement of a system's mass ratio, or at least the difference between the mass fraction $B = q/(1+q)$ and the intensity ratio $\beta = L_2/(L_1 + L_2)$ (see Eq. (2.2) on page 10). However, whilst they had varying success in their attempts for 46 of the 145 binary systems that they analysed, HD 206804 was not so accommodating. As will soon be revealed, this was no doubt in part due to the fact that Finsen's first solution was the one that was closer to the truth.

Another investigation into visual binary orbits and the component masses using *Hipparcos* data was conducted by Söderhjelm (1999). He derived new orbital solutions for 205 binary systems by combining the *Hipparcos* astrometry with existing ground-based observations. Included in this solution was a revised parallax and a magnitude difference for the componenets. He was unable to derive an astrometric mass ratio, but instead, estimated the component masses from his solution's magnitude difference, the combined $(V-I)$ magnitude and an iterative fit to theoretical isochrones and evolutionary tracks. HD 206804 was one of 27 systems whose orbital sampling by *Hipparcos* was also able to provide an astrometric mass ratio, $q = \mathcal{M}_2/\mathcal{M}_1$.

Söderhjelm was apparently unable to distinguish which of Finsen's solutions was valid, and altered the respective elements very little (see Table 7.9). Each solution included a new estimate of the system parallax, which was used in his mass-sum estimate. Both solutions have been classified as 'reliable' (grade 3) by Hartkopf & Mason (2004), who consider that the longer period orbit corresponds most closely to the available astrometric data. The apparent inconsistency of classifying two such solutions as being 'reliable' is recognized. The discrepancy is clearly inherent in the grading system.

Söderhjelm (1999) identified HD 206804 as an interesting system whose orbital solutions gave mass ratios that implied the system was actually a triple, with the secondary star itself a double.

	Solution 1	Solution 2
P (yr)	6.21	12.46
a''	0.205	0.324
e	0.59	0.00
i (°)	129	113
ω (°)	347	0
T	1988.9	1986.0
Ω (°)	103	109
Δm	$0\overset{\mathrm{m}}{.}13$	$0\overset{\mathrm{m}}{.}13$
p'' (mas)	53.38 ± 1.63	53.30 ± 1.41
$\mathcal{M}_1$ ($\mathcal{M}_\odot$)	0.56 ± 0.08	0.50 ± 0.07
$\mathcal{M}_2$ ($\mathcal{M}_\odot$)	0.91 ± 0.11	0.95 ± 0.10
$\mathcal{M}_\mathrm{S}$ ($\mathcal{M}_\odot$)	1.47 ± 0.13	1.45 ± 0.13
q	1.61 ± 0.30	1.88 ± 0.34

Table 7.9: Two strometric orbital solutions for HD 206804 as computed by Söderhjelm (1999). The derived magnitude difference, parallax, individual masses, mass-sum and mass ratio are also given.

The primary star would be a late-K (solution 1, consistent with the accepted spectral type) or an early-M dwarf (solution 2). Since it was already well established that the visible components had almost equal magnitudes, the third star was constrained in terms of its mass and its luminosity. The total mass of the subsystem would be $M_{2+3} \sim 0.91$–$0.95\,\mathcal{M}_\odot$. If $\mathcal{M}_2$ is also a late-K dwarf, the third star would have to be a late-M dwarf or a white dwarf. If $\mathcal{M}_2$ is an early-M dwarf, the third star would have to be likewise, for example a pair of M0V stars. Söderhjelm did not anticipate the subsystem would be resolvable by interferometry, but felt it may be revealed by spectroscopy.

The two astrometric solutions computed by Söderhjelm (1999) correspond to two quite different radial-velocity curves, and these are illustrated in Fig. 7.17.

Radial velocities of HD 206804

When the HERCULES spectrograph began operation in 2001 ($\sim$ JD 2 452 000), the distinction between the radial-velocity curves predicted by Söderhjelm's (1999) study were such that a single observation should be able to recognize, in principle, which orbital solution was more likely to be valid. The first observation secured a double-lined spectrum, implying that the moderate eccentricity orbit with the shorter period was the more likely. Using HERCULES at a resolving power of 41 000 (fibre 1), a total of 19 spectra of this ninth-magnitude binary system were obtained over a timespan of about three years. Twelve of these spectra were double-lined, all of which were obtained within the first five months of observations, and these demonstrated the near-equality of the two spectral types recorded (see Fig. 7.18). The double-lined spectra were

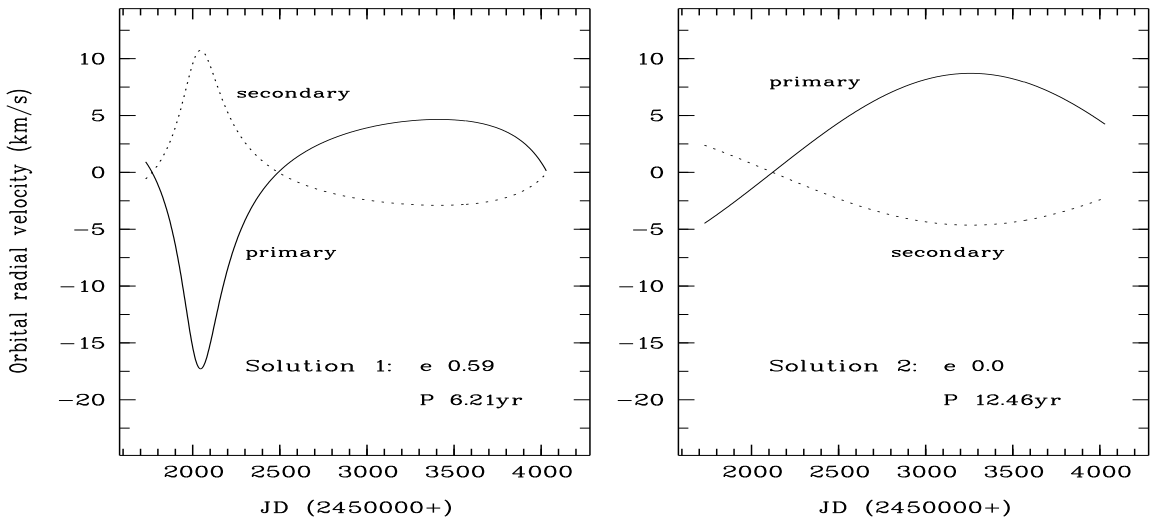

Figure 7.17: The radial-velocity curves of HD 206804 for the two orbital solutions computed by Söderhjelm (Table 7.9). If the secondary mass is itself a double system, as implied by q, the curve corresponding to the secondary would approximate the motion of its centre of mass.

used to determine the binary system's mass ratio, q, and a spectroscopic orbital solution. The remaining seven spectra were obtained close to the systemic velocity making measurement of the velocities of each star highly uncertain; these were treated as single-lined and are reported, but excluded from further analysis.

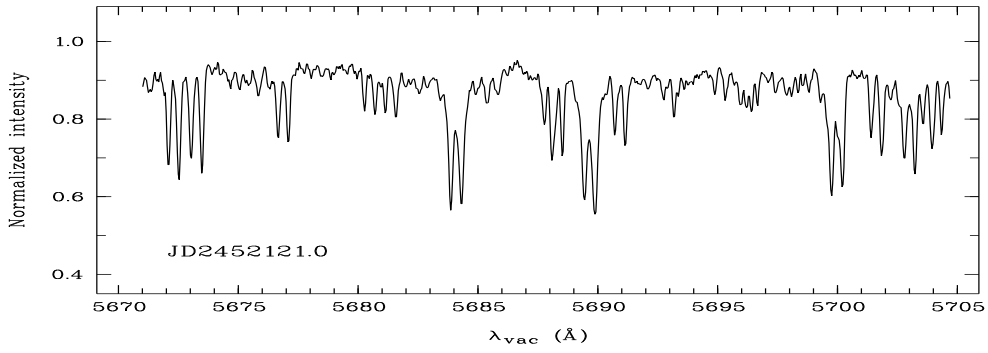

Figure 7.18: A segment of a HERCULES spectrum recorded when the near-equal components of HD 206804 were close to their maximum velocity separation.

A template spectrum was also required for the purpose of digital cross-correlation. As it had been established that the two components of this binary system had almost identical spectra,

a single template was justified. The double-lined spectra were cross-correlated with a HERCULES spectrum of the K5V star ϵ Indi (HD 209100), as mentioned in the introduction. This template provided well-defined cross-correlation peaks for the radial-velocity measurements. After the template spectrum was chosen, the cross-correlation peaks had their definition further enhanced by the careful removal of broad and heavily blended features from the wavelength segments used (e.g. see Fig. 6.1 on page 108). Wavelength segments isolated from 19 échelle orders were used to determine the weighted-mean velocity of each observation. All of the single-lined cross-correlation peaks were never more than about 10% broader than the peaks measured at maximum-velocity separation of the double-lined spectra. This is expected from the orbital solution subsequently derived. The relative velocities are listed in Table C.4 Appendix C.

The challenge of separating the closely blended cross-correlation peaks is demonstrated in Fig. 7.19, which includes a cross-correlation function for each quadrature phase. It is evident from inspection of this figure that the cross-correlation function corresponding to the quadrature phase $\Delta V \sim K\|e\cos\omega - 1\|$ at $\sim$ JD 2 453 220, is only very slightly wider than the individual peaks seen at maximum velocity separation when $\Delta V \sim K(e\cos\omega + 1)$ at $\sim$ JD 2 452 122. The relatively narrow and tightly blended peaks were found for all cross-correlation functions created after $\sim$ JD 2 452 250. The tight blending of the corresponding spectral lines is indirect support for the spectroscopic orbital solution derived.

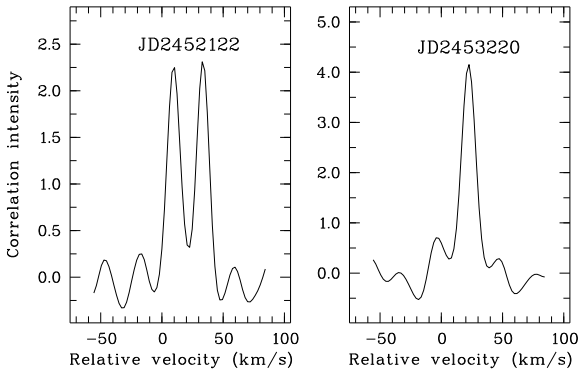

Figure 7.19: Cross-correlation functions for HD 206804 at both quadrature phases (order 99).

The spectroscopic mass ratio

The HERCULES radial-velocity observations provide very little orbital phase sampling for this system. Consequently, it was not possible to derive a spectroscopic orbital solution directly. Instead, it was necessary to derive at least one of the solution parameters independently of the orbital elements so that it could be fixed whilst the orbital solution was determined. The orbital element that suits this purpose is $\gamma_{\rm rel}$, the relative systemic velocity. This parameter can be derived with no knowledge of the orbital elements (Paddock 1915; see Eq. (3.10) on page 26

and the related comments), by calculating the linear regression of the component velocities. Additional benefits of this approach are that it provides a measure of the system's mass ratio, q, and therefore it identifies which star is the primary, on the basis that $\mathcal{M}_1 \geq \mathcal{M}_2$. The results of this analysis are presented in Fig. 7.20.

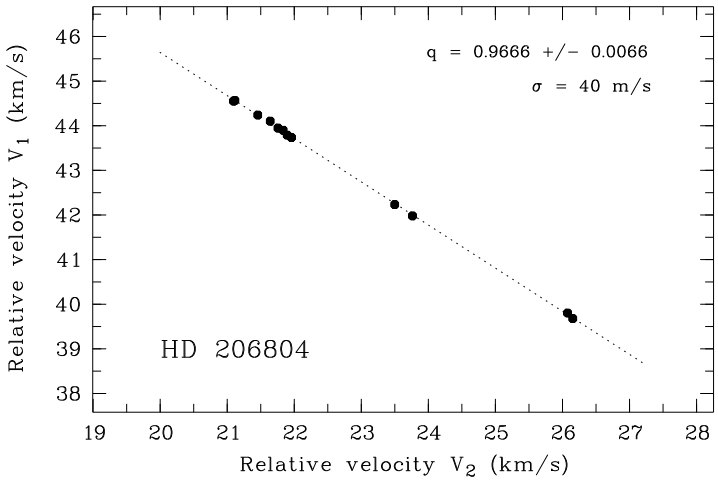

Figure 7.20: Derivation of the mass ratio, q, and the relative systemic velocity, $\gamma_{\rm rel}$, for HD 206804 using linear regression applied to the radial velocities of the components.

The mass ratio derived from HERCULES data differs noticeably from those reported by Söderhjelm (1999). Furthermore, the observed spectra and the high precision with which $q = 0.9666 \pm 0.0066$ has been measured appears to refute the possibility of any third stellar mass in this system. However, q can be used to estimate the mass of each star, based on the mass sum corresponding to the more accurate astrometric solution provided by Söderhjelm (1999; his solution 1). The mass sum is given as $\mathcal{M}_{\rm S} = 1.47 \pm 0.13\,\mathcal{M}_\odot$, but should be considered with caution as the corresponding mass ratio estimate has already been shown to be incorrect. The component masses are determined to be $\mathcal{M}_1 = 0.75 \pm 0.07\,\mathcal{M}_\odot$ and $\mathcal{M}_2 = 0.72 \pm 0.06\,\mathcal{M}_\odot$. Both of these estimates are about 20% larger than the accepted masses for stars of spectral type K7V or thereabouts ($M \sim 0.61\,\mathcal{M}_\odot$), implying that the mass sum is excessive to the same degree.

The component's V and B magnitudes

To extend our understanding of the absolute properties of this binary system we can assume that both stars conform statistically to the same empirical mass-luminosity relation[18], for instance, as described in § 3.3 on page 30, namely, $L \sim \mathcal{M}^\alpha$, and that these stars belong to the same

[18] Kopal (1959) describes a similar statistical approach for eclipsing binaries with photometric elements, pp. 472–476.

stellar population that generated the mean-magnitude values that will be introduced shortly.

The spectroscopic mass ratio can be used to estimate the magnitude difference of the stars and the corresponding individual $M_{\rm V}$ and $M_{\rm B}$ magnitudes and spectral types, using empirical values for $M_{\rm V}$, $(B-V)$ and BC (e.g. from Drilling & Landolt 2000) to derive suitable calibration relations. Subsequently, the corresponding positions of the components can be located on a $(M_{\rm V}, B-V)$ CMD diagram. We have

$$\begin{aligned} \Delta M_{\rm bol} = M_{\rm bol,\,2} - M_{\rm bol,\,1} &= 2.5\,\log\,(L_1/L_2) \\ \therefore \qquad \Delta M_{\rm V} = M_{\rm V,\,2} - M_{\rm V,\,1} &\approx -\,(BC_2 - BC_1) - 9.5\,\log\,q\,, \end{aligned} \tag{7.16}$$

assuming $L \sim M^{3.8}$ for an average sample of main-sequence stars[19]. The term

$$(BC_2 - BC_1) = \Delta BC = \frac{{\rm d}BC}{{\rm d}M_{\rm V}} \times \Delta M_{\rm V}\,,$$

can be estimated after deducing an expression for ${\rm d}BC/{\rm d}M_{\rm V}$. By fitting a suitable polynomial to a series of $(M_{\rm V}, BC)$ data (see the top diagram in Fig. 7.21 on the next page), we find

$$BC \approx 0.1155 - 0.1892 M_{\rm V} + 0.0546 M_{\rm V}^2 - 0.0060 M_{\rm V}^3\,.$$

We have to expect that the bolometric corrections will have systematic errors, but for two similar stars, it is reasonable to assume that these errors will more or less cancel when their difference is calculated. We next derive

$$\Delta M_{\rm V} = -\left(\frac{{\rm d}BC}{{\rm d}M_{\rm V}}\right)\Delta M_{\rm V} - 9.5\log q$$

so that

$$\Delta M_{\rm V} \approx \frac{-\,9.5\log q}{0.811 + 0.109\overline{M}_{\rm V} - 0.018\overline{M}_{\rm V}^{\,2}}\,, \tag{7.17}$$

where $\overline{M}_{\rm V}$ is the *mean* magnitude of the components of the binary system. This approach will be most suited to pairs of stars that are approximately equally luminous (since such stars should be about equally evolved and also conform to the same mass-luminosity relation), as are the components of many SB2 systems, such as HD 206804. Hence, for the purposes of estimating $\Delta M_{\rm V}$ using Eq. (7.17), $\overline{M}_{\rm V} \approx M_{\rm V,\,c} + 0\overset{\rm m}{.}75$, where $M_{\rm V,\,c} \equiv M_{\rm V}$ (combined), and the error in $\overline{M}_{\rm V}$ is the same as in $M_{\rm V,\,c}$.

[19] Drilling & Landolt (2000) claim that a power index of 3.8 is suitable for $M > 0.2\,\mathcal{M}_\odot$. Similarly, Lampens et al. (1997) used *Hipparcos* parallaxes and 170 visual binaries with well known orbits to assess the mass-luminosity relation and derived $L \sim M^{3.9}$ for $0 < M_{\rm bol} < 7$ mag. The Drilling & Landolt value will be used as all of the other average magnitude values for the present analysis have been sourced from their tables.

Since q and $\overline{M}_{\rm V}$ are uncorrelated, the propagated error corresponding to the expression for $\Delta M_{\rm V}$ is

$$\left(\frac{\sigma_{\Delta M_{\rm V}}}{\Delta M_{\rm V}}\right)^2 = \left(\frac{\log_{10}{\rm e}}{q\log q}\right)^2\sigma_q^2 + \left(\frac{0.1148}{0.811+0.109\overline{M}_{\rm V}-0.018\overline{M}_{\rm V}^{\,2}}\right)^2(\sigma_{\overline{M}_{\rm V}})^2$$

$$\approx \left(\frac{\log_{10}{\rm e}}{q\log q}\right)^2\sigma_q^2 + \left(\frac{0.0121\Delta M_{\rm V}}{\log q}\right)^2(\sigma_{\overline{M}_{\rm V}})^2\,,$$

where the last term was produced by reference to Eq. (7.17).

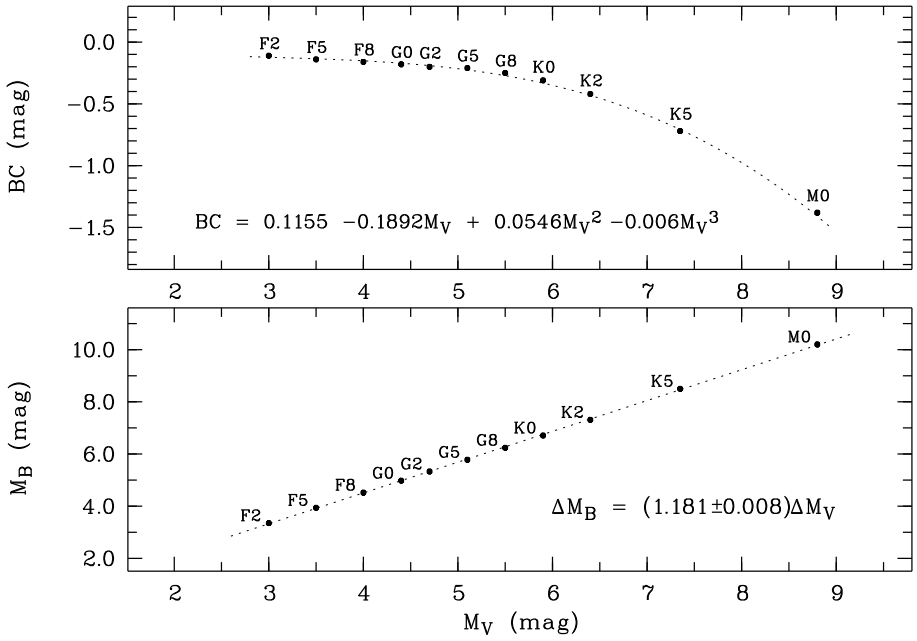

Figure 7.21: Top: Empirical values of $M_{\rm V}$ vs BC for F2–M0 main-sequence stars. The cubic polynomial that gives a least-squares best-fit is given. Bottom: Empirical values of $M_{\rm V}$ vs $M_{\rm B}$. Data from Drilling & Landolt (2000).

Using the combined V and B apparent magnitudes provided on page 168 (Kharchenko 2001) and the *Hipparcos* parallax $p'' = 52.56 \pm 1.88$ mas, the corresponding $M_{\rm V}$ for HD 206804 is $M_{\rm V,c} = 7\overset{\rm m}{.}393 \pm 0.078$, so that our estimate for $\overline{M}_{\rm V}$ is $8\overset{\rm m}{.}143 \pm 0.078$. Therefore, $\Delta M_{\rm V} = 0\overset{\rm m}{.}278 \pm 0.059$, which compares favourably with the most recently published value ($\Delta m = 0\overset{\rm m}{.}2$; Worley 1989). We can calculate the individual magnitudes, m, using Δm and the combined magnitude, $m_{\rm c}$, to get

$$m_2 = m_{\rm c} + 2.5\log\left(1+10^{0.4\Delta m}\right) \qquad \text{and} \qquad m_1 = m_2 - \Delta m\,, \tag{7.18}$$

whose respective errors are estimated using

$$\sigma_{m_2}^2 = \sigma_{m_c}^2 + \left(\frac{10^{0.4\Delta m}}{1+10^{0.4\Delta m}}\right)^2 \sigma_{\Delta m}^2 \qquad \text{and} \qquad \sigma_{m_1}^2 = \sigma_{m_2}^2 + \sigma_{\Delta m}^2\,,$$

since (m_c, Δm) and (m_2, Δm) are each also uncorrelated.

Therefore, the estimates for the V magnitudes of the components of HD 206804 are $M_{V,1} = 8^m.02 \pm 0.10$ and $M_{V,2} = 8^m.29 \pm 0.08$. These magnitudes, for unevolved stars, correspond to a spectral type of about K7V for both components, which is consistent with their present classification. The respective apparent V magnitudes are $9^m.4$ and $9^m.7$, based on the *Hipparcos* parallax $p'' \sim 0''.053$.

The B magnitudes can be estimated using an expression that calibrates B against V for main-sequence stars (see the bottom diagram in Fig. 7.21). Again using empirical data, it is easily revealed that $\Delta M_B = (1.181 \pm 0.008) \times \Delta M_V$. Therefore, we can estimate $\Delta M_B \approx 0^m.328 \pm 0.070$ for the components of HD 206804. The combined absolute B magnitude is $M_{B,c} = 8^m.711 \pm 0.079$, so that $M_{B,1} = 9^m.31 \pm 0.11$ and $M_{B,2} = 9^m.64 \pm 0.09$.

The $(B-V)$ colour index will be calculated for HD 206804 in the final section of this chapter, together with the following two SB2 systems that will be analysed in the same way. The corresponding pairs of ($B-V$, M_V) values have been placed in a colour-magnitude diagram that includes some related evolutionary tracks for comparison (see Fig. 7.31 on page 199).

Spectroscopic orbital solution

Assisted with a value for γ_{rel} measured independently of any orbital elements, the spectroscopic orbital solution could be derived. However, being mindful of the small portion of the radial-velocity curve sampled, it was decided that some prudence was merited with regard to pursuing this goal. Therefore two solutions have been derived, one with only the systemic velocity fixed, for which we provide our complete solution, and a second solution that also has the period fixed to that from the more accurate astrometric solution (Table 7.9), i.e. solution (1) with $P = 6.21$ years.

For both analyses, the classic approach of differential corrections first developed by Lehmann-Filhés (1894) was used. Sterne's (1941b) method was considered less suitable for HD 206804 for several reasons. First, any final orbital solution should include the full set of standard parameters, namely K_n, P, e, ω, γ, and the time of periastron passage, T. However, Sterne's approach provides T indirectly using the time of zero mean longitude T_0 as well as P and ω: $T = T_0 + \omega P/2\pi$. Once an initial solution was derived, it was clear that the element with the largest relative error was that for the period P. This is not surprising given the small fraction of the radial-velocity curve for which double-lined spectra could be extracted for radial-velocity analysis. The large error associated with the period measurement will propagate into the error determined for T if Sterne's method is used first to derive T_0. Second, the orbit is decidedly

P	=	$2\,138 \pm 135$ d $(5.85 \pm 0.37$ yr)	e	=	0.634 ± 0.016
K_1	=	$7.075 \pm 0.072\,\mathrm{km\,s^{-1}}$	K_2	=	$7.319 \pm 0.089\,\mathrm{km\,s^{-1}}$
ω_1	=	$352\overset{\circ}{.}87 \pm 0.77$	ω_2	=	$172\overset{\circ}{.}87 \pm 0.77$
T	=	JD $245\,2112.76 \pm 0.96$ d	γ_{rel}	=	$+33.04\,\mathrm{km\,s^{-1}}$ (fixed)
		r.m.s. of best fit $= 17\,\mathrm{m\,s^{-1}}$			
$a_1 \sin i$	=	160.1 ± 5.8 Gm	$\mathcal{M}_1 \sin^3 i$	=	$0.155 \pm 0.013\,\mathcal{M}_\odot$
$a_2 \sin i$	=	165.6 ± 6.1 Gm	$\mathcal{M}_2 \sin^3 i$	=	$0.150 \pm 0.012\,\mathcal{M}_\odot$
$a \sin i$	=	2.18 ± 0.11 AU	$\mathcal{M}_\mathrm{S} \sin^3 i$	=	$0.305 \pm 0.017\,\mathcal{M}_\odot$
q	=	0.9666 ± 0.0066	γ	=	$-7.03 \pm 0.23\,\mathrm{km\,s^{-1}}$

Table 7.10: The spectroscopic orbital solution for HD 206804 using MJUO velocities with only the relative systemic velocity fixed.

P	=	2 268.2 d (6.21 yr) (fixed)	e	=	0.64908 ± 0.00079
K_1	=	$7.0100 \pm 0.0025\,\mathrm{km\,s^{-1}}$	K_2	=	$7.2522 \pm 0.0026\,\mathrm{km\,s^{-1}}$
ω_1	=	$353\overset{\circ}{.}45 \pm 0.34$	ω_2	=	$173\overset{\circ}{.}45 \pm 0.34$
T	=	JD $245\,2113.62 \pm 0.43$ d	γ_{rel}	=	$+33.04\,\mathrm{km\,s^{-1}}$ (fixed)
		r.m.s. of best fit $= 17\,\mathrm{m\,s^{-1}}$			

Table 7.11: The spectroscopic orbital solution using MJUO velocities for HD 206804 derived with both the relative systemic velocity and the period fixed.

non-circular, making Sterne's approach less advantageous.

The spectroscopic elements for HD 206804 derived from the HERCULES observations and using a fixed value for the systemic velocity, $\gamma_{\mathrm{rel}} = +33.04\,\mathrm{km\,s^{-1}}$, are given in Table 7.10. The radial velocities are plotted with the computed velocity curves in Fig. 7.22. The orbital period, $P = 5.85 \pm 0.37$ years, is similar to the astrometric value of solution 1. The solution derived with the period also fixed to the astrometric value is found in Table 7.11.

Three comparisons can readily be made between the two spectroscopic solutions. First, the r.m.s. error of the two best-fits is the same ($17\,\mathrm{m\,s^{-1}}$). Second, the values of the respective orbital elements do not differ significantly. And third, the precision with which K_1, K_2 and e are measured with the period fixed improves considerably. We felt that the second solution that yields this exceptional precision deserved mention, but that the errors derived with only γ_{rel} fixed were more realistic considering the extent of our velocity dataset.

Only a few per cent of double-lined spectroscopic orbits have a period greater than HD 206804 (Pourbaix et al. 2004), so that this spectroscopic solution to the orbit is a welcome addition to the relatively bare segment of the period histogram presented in Fig. 4.17 on page 56. Clearly,

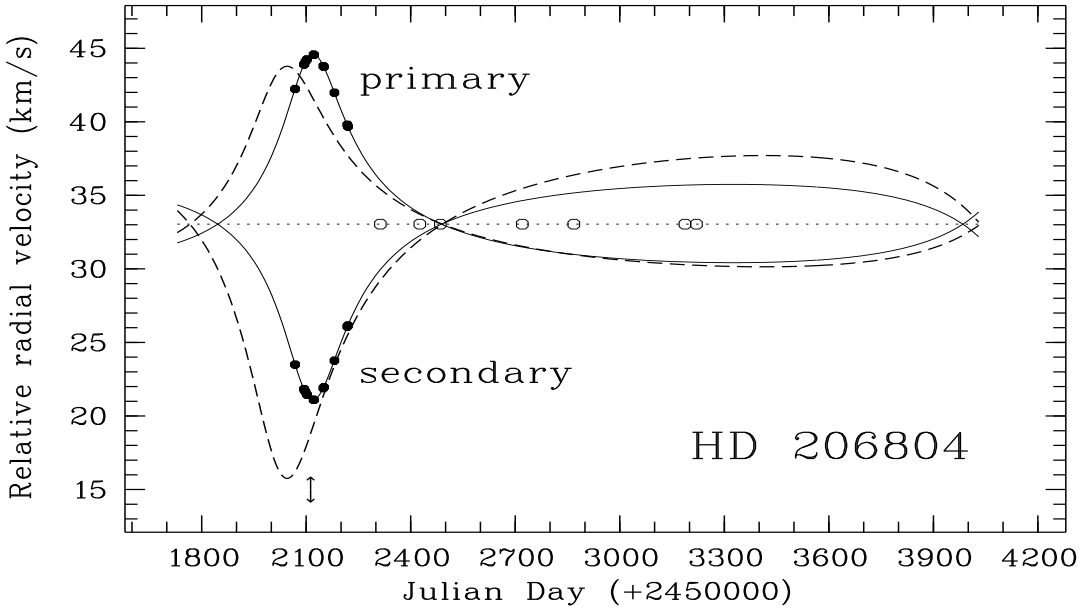

Figure 7.22: Solid lines: The radial-velocity curves for HD 206804 corresponding to the solution in Table 7.10. The solid symbols represent the double-lined observations used to derive the spectroscopic orbital solution. The open symbols identify observations obtained with closely-blended spectra and treated as single-lined. The dashed curves correspond to astrometric solution 1 in Table 7.9 and the left figure in Fig. 7.17. Note that the astrometric curves are reversed owing to Ω having been placed in the wrong quadrant. The '$\updownarrow$' symbol indicates a time of periastron passage.

the approach used here, i.e., to select and observe potential long-period SB2s based upon velocity predictions from astrometric data, can be very successful for investigating binaries whose spectroscopic orbits are otherwise elusive.

An astrometric orbital solution cannot distinguish between the ascending and descending nodes of an orbit, and therefore there is an ambiguity of 180° in the value of Ω. Until radial-velocity observations identify the respective nodes, it is conventional to assign the ascending node to the one that is closest to north, hence $0° \leq \Omega < 180°$. The spectroscopic solution has now revealed that, since $\omega_2 = \omega \approx 173°$, the incorrect node was chosen for the previous astrometric solutions, and Ω must have 180° added to it. Söderhjelm's first solution would be more accurate if $\Omega = 283°$.

The measured total semi-amplitude of the radial-velocity curve, $K = K_1 + K_2 \sim 14.4\,\mathrm{km\,s^{-1}}$, is also about 20% smaller than that predicted, $K = 17.7\,\mathrm{km\,s^{-1}}$, based on the astrometric solution with $P \sim 6.2$ years, owing to further inaccuracies in the values of the contributing

parameters. We can also estimate the system's parallax using $p'' = a'' \sin i / a \sin i$ from the two orbital solutions: $p'' \sim 73$ mas, which is significantly more than the *Hipparcos* value.

The inclination and an adjustment to the astrometric solution

The spectroscopic orbital solution allows the component masses to be derived using the orbital inclination, i, rather than the mass sum as previously shown. The inclination used, $i = 129°$, is taken from Söderhjelm's more accurate astrometric solution 1. Unfortunately, this parameter was published without an error estimate. The masses derived are $\mathcal{M}_1 = 0.33\,\mathcal{M}_\odot$ and $\mathcal{M}_2 = 0.32\,\mathcal{M}_\odot$. On this occasion, the values are about half as large as expected for stars with a spectral type K7V. Furthermore, the corresponding unevolvd stars ($\sim$ M3V) would be a couple of magnitudes fainter than is observed.

More realistic masses would result if the inclination was increased to $i \sim 140°$. This seems to be a reasonable approach, as it appears to be quite certain that the stars present do have spectral types of about K7V. This estimate for i, combined with our precise measure for e, considerable confidence that $P \sim 6.2$ years, and a rather precise parallax and estimate for K, allows us to determine a corresponding value for the semimajor axis: $a = KP\sqrt{1-e^2}/2\pi \sin i \approx 3.6$ AU and therefore $a'' \approx 0\farcs19$. This latter value is not much smaller than those published previously, and is quite likely within the associated error. Naturally, these values for a and a'' are consistent with the *Hipparcos* parallax and the anticipated component masses $\mathcal{M} \sim 0.6\,\mathcal{M}_\odot$, since p'' and and our estimates for $\mathcal{M}$ have assisted in the formers' calculation. A summary of our new estimate for the orbital solution for HD 206804 is provided in Table 7.12.

P (yr)	=	6.21 *	i (°)	=	140.7
e	=	0.634 ± 0.016	T	=	2001.55
ω (°)	=	172.87 ± 0.77	Ω (°)	=	283
K ($\mathrm{km\,s^{-1}}$)	=	14.394 ± 0.114	a'' (mas)	=	190
a (AU)	=	3.6	p''_{Hip} (mas)	=	52.56 ± 1.88 *
$q = 0.9666 \pm 0.0066$			$\Delta m = 0\fm28 \pm 0.06$		
Kepler's 3rd law: $\mathcal{M}_\mathrm{S}$ ($\mathcal{M}_\odot$) ≈ 1.2			$\mathcal{M}_1 \approx 0.6(1)\,\mathcal{M}_\odot$ K7V		
q + photometry: $\mathcal{M}_\mathrm{S}$ ($\mathcal{M}_\odot$) ≈ 1.2			$\mathcal{M}_2 \approx 0.5(9)\,\mathcal{M}_\odot$ K7V		

Table 7.12: The orbital solution for HD 206804 that corresponds to the MJUO velocities, spectroscopic mass ratio, and the period reported by Söderhjelm (1999), which is identified with a ' * ' to remind the reader that this value was fixed from the astrometric solution.

Barycentric systemic velocity

The barycentric radial velocity of HD 206804's centre-of-mas, γ, is deduced in the same fashion employed earlier in this thesis. As HD 206804 is about 15 spectral sub-types different from the Sun, it was considered inappropriate to estimate γ using sky spectra. Instead, a HERCULES spectrum of the K4V star HD 131977 was used to determine the velocity difference, $V_{\rm diff}$, between it and the ϵ Indi reference spectrum, since the former has a published barycentric radial velocity ($V_{\rm bary} = +26.961\,{\rm km\,s^{-1}}$; Nidever et al. 2002) [20]. The velocity of our template star relative to HD 131977 was measured to be $V_{\rm diff} = -67.030\,{\rm km\,s^{-1}}$. We expect that any errors relating to the relative velocities of the reference spectra will be dwarfed by the error accompanying our measure of the relative systemic velocity of HD 206804 , $\gamma_{\rm rel} = 33.04 \pm 0.23\,{\rm km\,s^{-1}}$. Therefore, the barycentric systemic velocity of HD 206804 is estimated to be $\gamma = \gamma_{\rm rel} + V_{\rm diff} + V_{\rm bary} = +33.04 - 67.030 + 26.961 = -7.03 \pm 0.23\,{\rm km\,s^{-1}}$. This measure of the systemic velocity is substantially more precise than the value listed in 'Mean Radial Velocities Catalogue' (Barbier-Brossat & Figon 2000), which gives $\gamma = -7.0 \pm 3\,{\rm km\,s^{-1}}$.

Summary

The visual binary system HD 206804 has had a spectroscopic orbital solution derived for the first time. This solution corresponds more closely to the previous astrometric solutions that claimed an orbital period of about six years, which is one of the longest measured for an SB2 system. The radial-velocity observations have disproven the alternative suggestion that the orbit might be circular with a period of ~ 12 years.

The orbit is moderately eccentric ($e \sim 0.63$) and is oriented towards the Earth so that only a small fraction of the orbital cycle is suitable for recording double-lined spectra. Their is no spectroscopic evidence to support the claim of a possible third stellar component, which had been based on astrometrically derived mass ratios of $q = 1.61$ and 1.88 (Söderhjelm 1999). Instead, the spectroscopic mass ratio $q = 0.9666 \pm 0.0066$ has been found. This value is in excellent agreement with the photometric appearance of the two nearly-equal ninth-magnitude K7-dwarf components.

The more accurate astrometric solution also leads to component mass estimates that are inconsistent with those expected for such stars. This is the case regardless of whether the published mass sum or inclination is used for the mass calculation. However, if the spectroscopic solution, predicted masses, *Hipparcos* parallax and a period of 6.2 years are assumed valid, the astrometric solution can be modified to allow the solution to be self-consistent. A new value for $i = 140.7°$ leads to a predicted semimajor axis of $a'' \approx 0\farcs19$, so that $\mathcal{M}_1 \sim \mathcal{M}_2 \sim 0.6\,\mathcal{M}_\odot$ (see Table 7.12 on the preceding page).

[20] Our estimate of the barycentric velocity of HD 209100, using 30 sky spectra, was $V_{\rm sky} = +26.953\,{\rm km\,s^{-1}}$ (see Table 6.1 on page 113), which is in excellent agreement with the published value.

Unfortunately, the error corresponding to the period measured from the radial-velocity observations is presently of a relatively low precision, ($P = 5.85 \pm 0.37$ yr). This should be addressed by an adequate observing programme to coincide with the opportunity to record spectra of HD 206804 during its next phase of maximum velocity separation, predicted to occur in mid-2007. Now that the nature of the orbit has been established, a similar astrometric observing programme aimed at improving the precision of the astrometric orbit would provide a more precise total mass for the system, as well as making it possible to determine the parallax, luminosities and component masses with the high precision desired.

7.5 HD 217166 (HIP 113445 ADS 16417 HR 8737; $22^{\rm h}58^{\rm m}35^{\rm s}$, $+9°21^{\rm m}25^{\rm s}$)

The visual binary HD 217166 was discovered by Otto Struve (Σ 536). The similar unevolved solar-type seventh-magnitude stars are in a moderately eccentric ($e \sim 0.5$) orbit of 26 years duration that is practically edge-on to the plane of the sky. The system is located in Pegasus, about 6° south of α Pegasi, very close to the western-most border of Pisces[21].

HD 217166 was given a spectral type of G0V in the 'Henry Draper Catalogue' (Cannon & Pickering 1918). The principal components of HD 217166 have been assigned individual spectral types of G2V and G4V (Christy & Walker 1969), based on a composite spectrum of G3V, the available magnitude difference ($\Delta m = 0\overset{\rm m}{.}3$), and a luminosity calibration of the MK system. Eggen (1971) considered that HD 217166 was a member of the old disk population and placed the system in the ζ Herculis moving group. Recently, Nordström et al. (2004) gave HD 217166 an isochrone age of 10.3 Gyr. However, this estimate was based on the system having an absolute magnitude $M_{\rm V}$(combined)$= 3\overset{\rm m}{.}99$ which suggested that it was $1\overset{\rm m}{.}38$ evolved from the ZAMS. Since the absolute magnitude used for the isochrone fitting was that of the combined pair, the evolutionary stage reported must be incorrect. Based on available *uvby* photometry and their derived calibration relation, Nordström et al. (2004) also calculated [Fe/H] $= -0.17$ and derived $\log T_{\rm eff} = 3.750$.

HD 217166 has an angular semi-major axis, $a'' = 0\overset{''}{.}35$, that lends itself to astrometric investigation using the full range of techniques from classical visual astrometry to the modern techniques employing interferometry and adaptive optics. Its relatively short period and equatorial position in the sky has provided the opportunity for several complete orbital cycles to be observed. Unfortunately, these favourable circumstances have not allowed a definitive orbit to be determined to date (Hartkopf & Mason 2004).

During the first few decades of observation of this binary system, it was recognized that the

[21] Two other stars share the same listing as HD 217166 in the Catalogue of Components of Double and Multiple Stars, CCDM 22586+0921, with separations of $206''$ (component C, $V = 9\overset{\rm m}{.}2$) and $141''$ (component D, $V = 11\overset{\rm m}{.}0$). The proper motion of component C is known and this places it on a completely different trajectory in space to that of HD 217166 (ESA 1992). If component D is single and is bound to the HD 217166 system, it would be a star of spectral type $\sim$ M0V and presently be about 4 300 AU distant from HD 217166.

position angle of the components was more or less constant, so that HD 217166 presented an orbit where $i \sim 90°$. The small difference in brightness, $\Delta m \sim 0^{\rm m}.3$ (Mason & Wycoff 2004), of the stars meant that it was difficult correctly to determine to which quadrant each star should be assigned[22]. The first orbit computed by van den Bos (1934) interpreted the available observations by assuming the orbit was highly eccentric ($e = 0.98$) with a period of 27 years and $\omega = 180°$. Therefore, HD 217166 was expected to present a double-occultation, separated by a short time interval every orbital cycle, with the companion thereafter observed in the same quadrant until the stars next approached each other. However, van Biesbroeck realized that this solution did not correspond to the observation that the binary pair approached each other very closely every 13 years or so, rather than van den Bos' prediction that this would occur in about 27 year cycles. Thus, van Biesbroeck (1936) revised van den Bos' solution, making the only substantial change to the orbital elements in the history of their determination, and deduced the elements listed in Table 7.13. Crawford (1937) noted HD 217166 has a distinctive orbit that is (approximately) both edge-on and whose semi-major axis is directed toward the Earth. Van Biesbroeck's solution was subsequently modified slightly by Cester (1962): $P = 26.5$ years, $e = 0.55$ and $a'' = 0''.39$.

P (yr)	=	27.0	T	=	1927.00
e	=	0.65	i (°)	=	90
ω (°)	=	267	Ω (°)	=	166
a''	=	$0''.41$	$p''_{\rm dyn}$	=	$0''.037$

Table 7.13: The astrometric orbital solution for HD 217166 computed by van Biesbroeck (1936)

Van Biesbroeck's (1936) increase to the estimated semi-major axis, slightly more than tripled the dynamical parallax, $p''_{\rm dyn}$, which was then more in accord with the trigonometric parallax $p''_{\rm tr} = 27$ mas and the spectroscopic parallax $p''_{\rm sp} = 26$ mas (Baize 1950). The modern value for the trigonometric parallax, as determined by *Hipparcos* (ESA 1997) is 32.32 ± 0.89 mas.

Observation of HD 217166 using interferometric techniques began with Tokovinin's work (1982). He used a photoelectric phase-grating interferometer of his own design. This instrument was a simplified version of a speckle interferometer. The speckle instruments soon followed, beginning with observations conducted by McAlister et al. (1984). Subsequently, at least 15 additional interferometric studies have included HD 217166 in their target lists, two-thirds of them being conducted by McAlister, Hartkopf and co-workers. Adaptive optics have been employed on at least one occasion (ten Brummelaar et al. 2000).

[22]This confusion has continued into recent times as illustrated, for instance, by speckle observations of HD 217166 reported by Isobe et al. (1990b) and Scardia et al. (2000), both of whose reported observations place HD 217166 out of phase by 180° in a (ρ, θ) diagram, relative to their accepted positions.

The most recent attempts to improve the astrometric orbital solution of HD 217166 relied on *Hipparcos* observations and the efforts of Martin and co-workers, and Söderhjelm, as was the case for HD 206804, and described earlier in this thesis (see comments beginning on page 168 for a summary of their methodologies). HD 217166 was one of only five systems that fulfilled the separation criterion, $a'' \gtrsim 0''.3$, set by Martin et al. (1997) and Martin & Mignard (1998), but its period was apparently too long for the *Hipparcos* observations to yield any useful results with their approach (Martin et al. 1998).

Söderhjelm's (1999) study, which incorporated ground-based observations with the *Hipparcos* astrometry, resulted in a new but only slightly modified orbital solution for HD 217166 (see Table 7.14). Whilst this orbital solution was initially considered 'definitive' (grade 1; Hartkopf et al. 2001), the orbital quality was more recently down-graded (grade 2; Hartkopf & Mason 2004). Söderhjelm was unable to derive an astrometric mass-ratio for HD 217166, but he estimated the evolutionary masses in relation to a colour-magnitude diagram (CMD), isochrone tables, and based his analysis on the available magnitude difference, the combined $(V - I)$ index and the photometric mass-ratio.

P (yr)	=	26.0	T	=	1978.1
e	=	0.5	i (°)	=	89
ω (°)	=	262	Ω (°)	=	166
a''	=	0.35	p'' (mas)	=	32.6 ± 0.9
Δm	=	$0^{\mathrm{m}}.58$	$q_{\mathrm{photometric}}$	=	0.92
$\mathcal{M}_{\mathrm{S}}$ ($\mathcal{M}_{\odot}$)	=	1.83 (orbit)	1.93 ± 0.19 (CMD)		

Table 7.14: The most recent astrometric orbital solution for the orbit of HD 217166 (Söderhjelm 1999).

The photometric record

The sub-arcsecond separations that the components of HD 217166 present to observers are insufficient to allow the easy measurement of the individual magnitudes, colours and spectra. Instead, the combined values are more readily estimated. It is perhaps this difficulty that has led to two mostly unsubstantiated claims regarding HD 217166 existing for nearly three decades. These are the possibility of photometric variability and the presence of a third close eclipsing companion.

The suspicion of variability apparently originated during an early photometric survey using the Strömgren *uvby* and Hβ systems (Heck 1977). HD 217166 was identified as a possible variable star on the basis of five observations that showed excessive scatter for the measure of H$\beta = 2^{\mathrm{m}}.650 \pm 0.015$. At this point, HD 217166 appears to have entered the 'Catalogue of Suspected Variables' (CSV 8809), where it has remained ever since. Starikova (1979) re-classified

HD 217166 as a 'miscellaneous' variable in an investigation into the astrophysical properties of visual binaries with at least one variable component. This was done on the basis, apparently, of it being listed by Walker (1978) as a suspected eclipsing variable. This latter assignment may have been motivated by reports of occultation behaviour in the first decades of the 20th century.

In a study of possible solar analogues, Neckel (1986) gave HD 217166 the status of a triple system. More recently, Hartkopf & Mason (2004) included a comment in the 'Sixth Catalog of Orbits of Visual Binary Stars' that one of the components of HD 217166 is an eclipsing binary. Thus, there is also a persistent belief that HD 217166 is actually a triple system, with one of its components in fact a close sub-system. Presumably as a result of these claims, Tokovinin & Smekhov (2002) included HD 217166 in their spectroscopic study of possible sub-systems in visual binaries. They did not observe any radial-velocity variability that exceeded their expectations for the established binary pair, measuring a mean heliocentric velocity for the system $V \equiv \gamma = -21.58 \pm 0.18\,\mathrm{km\,s^{-1}}$ from nine observations.

Interestingly, other than the original claim made by Heck (1977), there does not appear to be any further *evidence* in the literature that HD 217166 is in any way variable or accompanied by a third close stellar mass. Subsequent independent photometric studies do not disclose any support for this possibility (e.g., Sowell & Wilson 1993; Olsen 1994; ESA 1997). With regard to the *Hipparcos* observations, 74 photometric measures of HD 217166 yielded $H_\mathrm{p} = 6\overset{\mathrm{m}}{.}5710 \pm 0.0008$, which led to the binary pair being recognized as one of the *least* variable bright stars in the sky (Adelman 2001). The combined apparent magnitudes for HD 217166 are $V = 6\overset{\mathrm{m}}{.}433 \pm 0.007$ and $B = 7\overset{\mathrm{m}}{.}086 \pm 0.005$, so that $(B-V) = 0\overset{\mathrm{m}}{.}653 \pm 0.008$ (Kharchenko 2001). The *uvby* colour indices are $(b-y) = 0\overset{\mathrm{m}}{.}407 \pm 0.002$, $m_1 = 0\overset{\mathrm{m}}{.}197 \pm 0.003$ and $c_1 = 0\overset{\mathrm{m}}{.}340 \pm 0.004$ (Olsen 1994).

Radial-velocity observations: past and present

Several studies have acquired radial-velocity measures of HD 217166, these beginning just over one orbital cycle before the HERCULES observations began at MJUO. Abt et al. (1980) included HD 217166 in a sample of 160 visual binaries with known orbital elements in an attempt to derive the spectroscopic orbital elements, or at least detect radial-velocity variations of accommodating systems. Based on the presently accepted orbital solution, the final of six observations of HD 217166 would have taken place at the time of ascending node passsage, when the greatest velocity difference of the binary pair would occur (see Fig. 7.24 on page 186). All spectra were considered to be single-lined. A suspicion of a small-amplitude variation was reported for the series of velocities obtained.

Heintz (1981) followed with a similar study and reported two velocities ($\sim$JD 244 3500) obtained from single-lined spectra. These were acquired one week apart and had a velocity difference of $6\,\mathrm{km\,s^{-1}}$, which is not possible at any phase of the orbit of HD 217166. Heintz believed his observations had been acquired at the time of nodal passage, but this is not consistent with the present orbital solution, which instead has each component moving at close to the systemic

velocity on the dates reported.

The last series of historical radial-velocity measures of HD 217166 were acquired in a large survey ($\sim$ 16 000 observations) conducted at the Fick Observatory (Beavers & Eitter 1986). These observations, using a vacuum photelectric radial-velocity spectrometer inspired by the work of R. F. Griffin, started in 1976 and continued for eight years. Their 21 observations of HD 217166 included several that were acquired at the time of nodal passage but were also all reduced as single-lined. The mean velocity measured was $-21.3 \pm 2.2\,\mathrm{km\,s^{-1}}$.

No further radial-velocity measures of HD 217166 have appeared until the present series obtained using HERCULES at MJUO. These began at the most recent nodal-passage phase (predicted to occur from mid-2001), several months after HERCULES became operational. As had been the case for the previously discussed visual binary system, the K-dwarf pair of HD 206804, HD 217166 had been carefully selected based on the radial-velocity curves computed for the system from the astrometric solution.

Easily discernible double-lined spectra were immediately acquired (see Fig. 7.23), using a resolving power of $R \sim 41\,000$, and further observations were pursued. Unfortunately, the northern declination of HD 217166 restricted these opportunities somewhat.

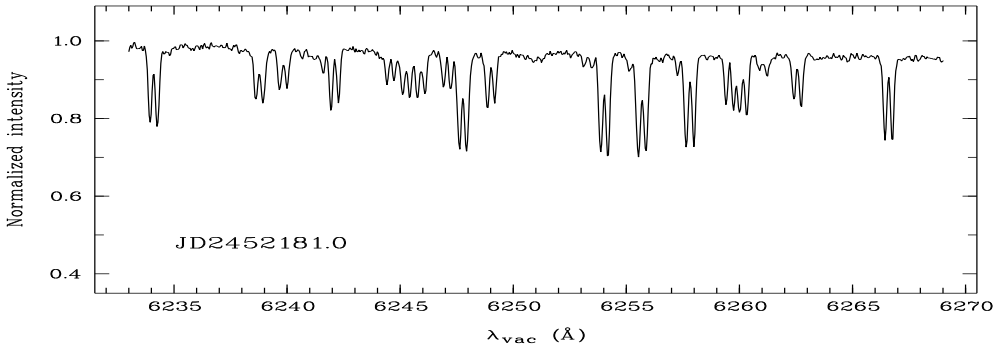

Figure 7.23: A segment of a HERCULES spectrum recorded when the similar solar-type components of HD 217166 were close to their maximum velocity separation.

Eventually, 14 double-lined spectra were secured between 2001 August and 2002 October, a timespan that represents only $\sim 4.5\%$ of the total orbital cycle. As the components of HD 217166 are both unevolved solar-type stars, the template spectrum on this occasion was a high signal-to-noise dome-flat illuminated by the Sun. The velocities measured are listed in Table C.5 Appendix C, and included on Fig. 7.24 on the next page. Since barycentric corrections have been applied to all spectra, the resulting velocities measured for the components of HD 217166 are considered to be barycentric (neglecting the contributions of the gravitational redshift and so on).

Whilst few in number, and extending over only $1\,\mathrm{km\,s^{-1}}$ or so of velocity space for each component, there is sufficient precision in the radial velocities to derive a spectroscopic mass ratio, establish the ascending node of the orbit, and provide estimates of other astrophysical properties of the components.

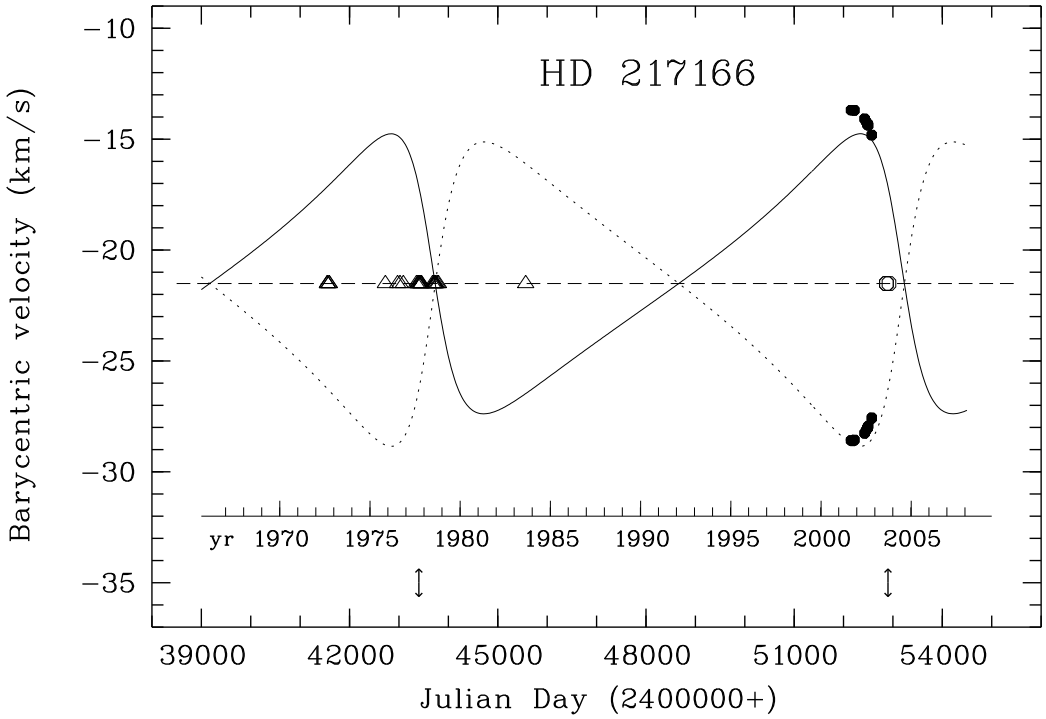

Figure 7.24: The radial-velocity curves for the primary (solid line) and secondary (dotted line) of HD 217166 based on the astrometric orbital solution (Söderhjelm 1999). HERCULES observations are circles (velocities of primary star are more −ve), historical measures are triangles. Observations reduced as single-lined are represented with open symbols. The '↕' symbols indicate times of periastron passage.

The system mass ratio and identification of the primary component have been determined by deriving the linear regression of the primary star's velocities against those of the secondary (Fig. 7.25). The mass ratio is measured to be $q = 0.906 \pm 0.025$, which is consistent with the photometric mass ratio reported by Soderhjelm (1999; see Table 7.14 on page 183). The somewhat poorer precision obtained for the mass ratio of HD 217166 as compared to HD 206804 can be attributed, in part, to the lesser velocity separation provided by this system's components. The primary star has the more negative velocities which is in contrast to the situation predicted by the present astrometric solution's choice of the ascending node (Table 7.14). Therefore the node is 180° out of phase and instead $\Omega = 346°$ and $\omega = 82°$ would be more appropriate for HD 217166.

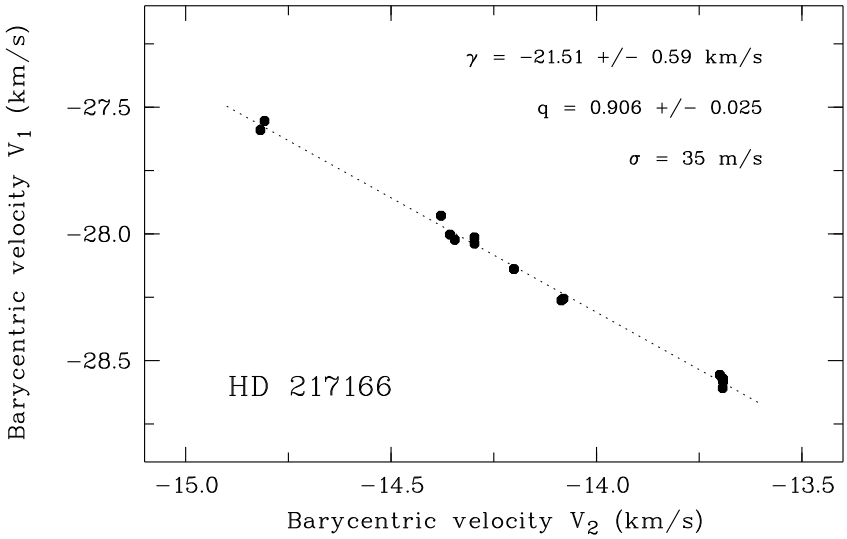

Figure 7.25: The relative velocities of HD 217166 measured from MJUO observations. The mass ratio, q, of the binary pair and the systemic velocity are derived from the linear regression of these velocities.

The systemic velocity derived from the linear regression is $\gamma = -21.51 \pm 0.59\,\mathrm{km\,s^{-1}}$, which is in excellent agreement with the mean velocity measured by Tokovinen & Smekhov (2002) mentioned earlier, i.e., $\gamma = -21.58 \pm 0.18\,\mathrm{km\,s^{-1}}$. However, these authors did not provide observation dates, so that the extent of line broadening in their spectra, which they treated as single-lined, cannot be estimated. The precision of the MJUO systemic velocity is considerably poorer than typically measured with HERCULES spectra, and is owing to the nature of the approach taken to acquire it.

An alternate estimate is to use the velocities measured for the HERCULES spectra that were reduced as single-lined (see the last three velocities in Table C.5 Appendix C). These show a suspicious trend to less negative values, which may be a result of the measurement process for these unresolved spectra. The velocity acquired on the date closest to when the components will actually being moving at $V = \gamma$ is $V \approx -21.25\,\mathrm{km\,s^{-1}}$. This value is consistent with the estimate made from the linear regression method, and is perhaps the more accurate of them.

If a second series of observations can be acquired at the coming opposite quadrature phase in 2007, as is presently planned, both the mass ratio and the systemic velocity can be expected to be determined with substantially greater accuracy and precision, as the line of regression should be 10–15 times longer.

It is also interesting to note the apparent contradiction between the luminosity differences of the two stars implied by the mass ratio, and the appearance of the double-lined spectra

(e.g. Fig. 7.23 on page 185) that reveal spectral lines of very similar strength. This can be ascribed to two competing processes relating to spectral line formation. The first is that hotter stars of the same luminosity class will be more luminous than cooler ones, so that, for the case of HD 217166, $q = 0.906 \Rightarrow L_1/L_2 \sim 1.5$, assuming the same mass-luminosity relation used in Eq. (7.16) on page 174. However, the equivalent widths of cooler late-type dwarf stars are expected to be greater than those that are slightly hotter because of the increased density of neutral absorbers in the lower temperature atmosphere. These two processes approximately compensate for each other so that the spectral lines resulting from them appearing together appear about equal, as is found for HD 217166.

Component magnitudes, spectral types and age for HD 217166

The magnitude difference of the components of HD 217166 has proven to be elusive. This is illustrated by inspection of the range of the measured values for this quantity in the 'Second Photometric Magnitude Difference Catalog' (Mason & Wycoff 2004), where it is found that Δm ranges between 0.0 and 0.7 magnitudes, with a mean measure of $\sim$ 0.3–0.4. As demonstrated previously (beginning on page 174), on the understanding that the components of HD 217166 obey the same mass-luminosity relation, the parallax is valid, and various other assumptions outlined there, the mass ratio, $q = 0.906$, can be used to estimate their magnitude difference. The corresponding individual $M_{\rm V}$ and $M_{\rm B}$ magnitudes can be deduced, and therefore the corresponding spectral types.

We start with the combined V and B apparent magnitudes (see on page 184), as well as the *Hipparcos* parallax, $p'' = 32.32 \pm 0.89$ mas, and deduce that the combined absolute magnitudes for HD 217166 are $M_{\rm V,\,c} = 3\overset{\rm m}{.}980 \pm 0.060$ and $M_{\rm B,\,c} = 4\overset{\rm m}{.}633 \pm 0.060$. Therefore, our estimate for the mean value of $M_{\rm V}$ is $\overline{M}_{\rm V} = 4\overset{\rm m}{.}730 \pm 0.060$, which is almost the same as that of the Sun. Using Eq. (7.17) on page 174 and the relation for $(\Delta B,\, \Delta V)$, we then deduce $\Delta M_{\rm V} = 0\overset{\rm m}{.}441 \pm 0.123$ and $\Delta M_{\rm B} = 0\overset{\rm m}{.}521 \pm 0.145$ for the components of HD 217166. Therefore, we can estimate, for the primary star: $M_{\rm V,\,1} = 4\overset{\rm m}{.}53 \pm 0.16$ and $M_{\rm B,\,1} = 5\overset{\rm m}{.}16 \pm 0.18$, and for the secondary: $M_{\rm V,\,2} = 4\overset{\rm m}{.}98 \pm 0.10$ and $M_{\rm B,\,2} = 5\overset{\rm m}{.}68 \pm 0.11$ The V magnitudes and known parallax correspond to apparent magnitudes $7\overset{\rm m}{.}0$ and $7\overset{\rm m}{.}4$, for the primary and secondary respectively. The V and B magnitudes are consistent with stars of spectral types G1V and G4V, and place both components of HD 217166 on the main sequence. These spectral types are in excellent agreement with the types assigned these stars by Christy & Walker (1969, G2V+G4V; see second paragraph of the introduction to HD 217166). A more precise estimate of the evolutionary stage of these stars will be described at the end of this chapter, where each star will be placed in a colour-magnitude diagram based on the estimates for $M_{\rm V}$ and $(B - V)$.

The masses of the components and a self-consistent orbit for HD 217166

The masses of the components can be estimated from empirical values for their derived spectral types (Drilling & Landolt 2000). The mass of a G1V star is predicted to be about $\mathcal{M}_1 \sim 1.03\,\mathcal{M}_\odot$

and that for a G4V star, it is $\mathcal{M}_2 \sim 0.94\,\mathcal{M}_\odot$. The total mass is $\mathcal{M}_S \sim 1.97\,\mathcal{M}_\odot$, which agrees very well with the evolutionary total mass derived by Söderhjelm (1999, $\mathcal{M}_S \sim 1.93\,\mathcal{M}_\odot$; Söderhjelm did not report his estimates of the individual masses).

The system mass corresponding to the astrometric orbital solution, $\mathcal{M}_S = 1.83\,\mathcal{M}_\odot$, is somewhat less than the value calculated from the spectroscopic mass ratio and available photometric data. The component masses derived with regard to the astrometric total mass are $\mathcal{M}_1 = 0.96\,\mathcal{M}_\odot$ and $\mathcal{M}_2 = 0.87\,\mathcal{M}_\odot$, which are reasonably consistent with our expectations from current knowledge relating to the masses of solar-type stars. However, these masses correspond to slightly later unevolved stars of spectral types G4V and G7V. Such a pair of stars would have a combined magnitude $\sim 0^{\rm m}.4$ fainter than is measured, assuming that the parallax is accurate. Furthermore, the composite spectrum is reported to be at least as early as about G3V (Christy & Walker 1969).

The apparent under-estimate of the system mass, $\mathcal{M}_S$, implies that the value for a'', p'' and/or P are erroneous. Unfortunately, without an SB2 orbital solution, we cannot estimate the parallax using $p'' = a'' \sin i / a \sin i$. Further evidence that the present orbital solution has some inaccurate elements comes from inspection of the radial-velocity curves corresponding to the change of phase of Ω, so that $\omega = 82°$. This is demonstrated in Fig. 7.26. There is considerable improvement to the fit of the radial-velocity curves (represented by the dashed curves) to the Hercules observations, though, a noticeable discrepancy still exists. Can the relatively few radial-velocity measures guide a suitable adjustment to the orbital elements to provide a self-consistent solution, in terms of the Hercules velocities and the implied masses involved?

Without additional velocity measures and a rigouress least-squares analysis of all of the associated parameters (e.g. see Pourbaix 1998), any attempt here to improve the orbit must be limited to fixing some of the elements to their published values and adjusting the remainder. Since HD 217166 has been observed for over 150 years, and there is no doubt that it presents an almost edge-on orbit to observers, it seems justified to fix the period and inclination to the astrometric values: $P = 26$ years, and $i = 89°$. Furthermore, since $i \sim 90°$, its value would have to be moderately inaccurate to alter $\sin i$ (as it enters various calculations), in a significant way. In contrast, ω enters our calculations as $\cos\omega$, which is very sensitive to small changes in ω when $\omega \sim 90°$, as appears to be the case for HD 217166.

One way to estimate ω is to make use of another orbital parameter, as yet not considered. This is the velocity difference, ΔV, of the components at either quadrature phase. If we accept that our few Hercules observations include the important phase when the stars are at the ascending node passage as they appear to be, and as the modified astrometric solution suggests, then the velocity difference of the components at this time is

$$\Delta V_{\rm asc} = K(1 + e \,\|\cos\omega\|\,) \approx 14.9 \text{ km s}^{-1}\,,$$

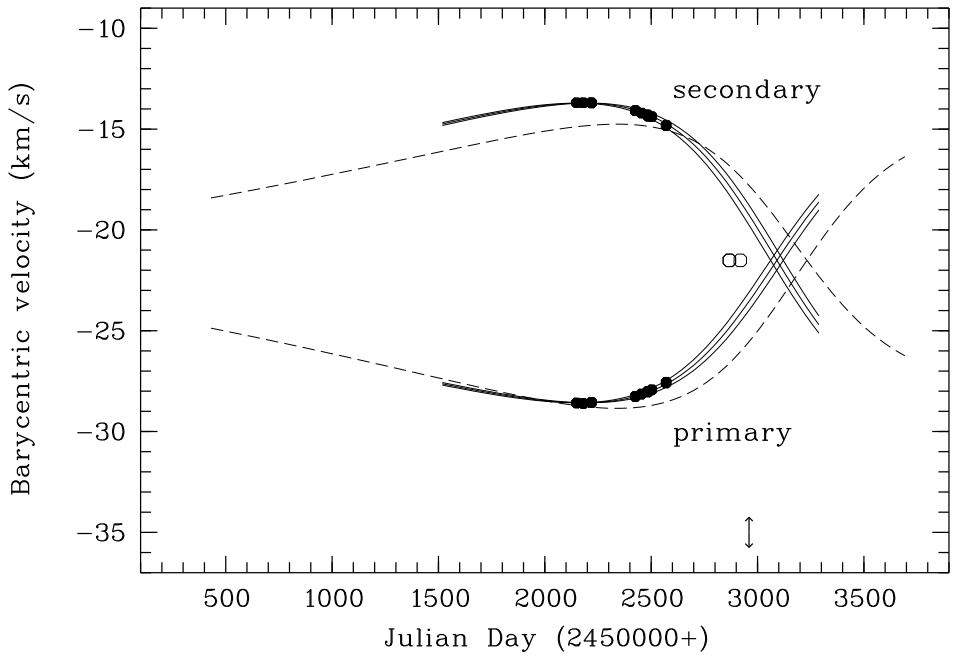

Figure 7.26: Improvement of the astrometric orbital fit of HD 217166 to the HERCULES observations. Dotted line: (Soderhjelm's (1999) solution except that $\omega = 82°$. Inner solid line: $\omega = 87°$, $T = 2003.87$, $K_1 + K_2 = 14.5\,\mathrm{km\,s^{-1}}$ and $q = 0.906$. The outer two solid lines correspond to $T \pm 30$ days. The '$\updownarrow$' symbol indicates the new estimate for T.

by inspection of the relevant velocities (note that $K = K_1 + K_2$). We could calculate a value for K corresponding to the astrometric solution, but that would include elements that we presently do not favour. However, if we make one final decision and fix the eccentricity as well, K can be deduced using P, i, e, and our previous estimate for the system mass, $\mathcal{M}_\mathrm{S} = 1.97\,\mathcal{M}_\odot$. The eccentricity of the orbit does not enter the calculation of the total mass of the system, and it's value has received only minor revision since the solution of Cester (1962). Therefore, we assume $e = 0.5$ is also accurate for this orbit. The first expression in Eq. A.66 on page 227 relates these parameters as is required:

$$K = \frac{2\pi \sin i}{\sqrt{1-e^2}} \sqrt[3]{\frac{\mathcal{M}_\mathrm{S}}{P}}\,,$$

and we deduce $K \approx 14.5\,\mathrm{km\,s^{-1}}$. Since this calculation incorporates Kepler's third law, we expect that this easily acquired result should ultimately lead to a self-consistent orbital solution. For comparison, Söderhjelm's solution corresponds to $K \approx 14.2\,\mathrm{km\,s^{-1}}$.

The new estimate for the position angle of periastron is therefore $\omega = 87°$, which differs from the previously published value by only 5 degrees (not including the phase change to Ω). Now we can re-calculate the radial-velocity curves for each component, based also on the spectroscopically derived value $q = 0.906$, and adjust the last orbital element, T, to achieve a satisfactory

fit. The position of each radial-curve is also quite sensitive to T, as is demonstrated by the three 'best-fit' curves in Fig. 7.26. The two outer curves that correspond less well with the HERCULES velocities differ from the estimated best-fit T =JD 245 2960 ($\equiv$ 2003.87 or 1977.87) by only $\pm$30 days. This comparison is considered to be valid, as the plotted solid symbols for the HERCULES observtions are equivalent to error bars of about $\pm 200\,\mathrm{m\,s^{-1}}$, which far exceeds the r.m.s. fits of other HERCULES double-lined spectra of late-type stars (e.g. HD 206804 described earlier, for which the r.m.s. error was $17\,\mathrm{m\,s^{-1}}$). The revised value for T is about 90 days earlier than the published value.

Using the larger value for K, and the *Hipparcos* parallax, the corresponding linear and angular semi-major axis can be derived: $a = 11$ AU and $a'' = 0\overset{''}{.}356$. The latter value is very close to the value reported in Söderhjelm's (1999) solution. However, combined with the *Hipparcos* parallax, the total mass increases to $\mathcal{M}_\mathrm{S} = 1.97\,\mathcal{M}_\odot$, as suggested by the estimated spectral types of the stars. The complete set of orbital elements and related parameters corresponding this analysis are found in Table 7.15.

P (yr)	=	26.0 *	i (°)	=	89 *
e	=	0.5 *	T	=	2003.87
ω (°)	=	87	Ω (°)	=	346
K ($\mathrm{km\,s^{-1}}$)	$\approx$	14.5	a'' (mas)	$\approx$	356
a (AU)	$\approx$	11	p''_Hip (mas)	=	32.32 ± 0.89 *
$q = 0.906 \pm 0.025$			$\Delta M_\mathrm{V} \approx 0\overset{\mathrm{m}}{.}44$		
Kepler's 3rd law: $\mathcal{M}_\mathrm{S}$ ($\mathcal{M}_\odot$) ≈ 1.97			$\mathcal{M}_1 \approx 1.03\,\mathcal{M}_\odot$		G1V
q + photometry: $\mathcal{M}_\mathrm{S}$ ($\mathcal{M}_\odot$) ≈ 1.97			$\mathcal{M}_2 \approx 0.94\,\mathcal{M}_\odot$		G4V

Table 7.15: The orbital solution for HD 217166 that corresponds to the MJUO velocities, spectroscopic mass ratio, and some of the astrometric orbital elements derived by Söderhjelm (1999). Values that are unaltered from their previously published ones are marked with a '*'.

Summary

HD 217166 is another binary system where the claimed presence of a third close star, apparently owing to spurious photometric evidence, appears to be unfounded. A spectroscopic mass ratio has been measured, $q = 0.906 \pm 0.025$, with precise radial velocities corresponding to a small fraction of the orbital cycle. This measurement emphasizes the results that are possible even when only a small fraction of the orbit has been observed and a small change in the components' velocities has occurred.

Based on the photometric measures of the combined light and the mass ratio, the component

magnitudes and spectral types (G1V and G4V) have been estimated. The age of the system appears to be similar to the Sun, about 4–5 Gyr. A minor modification to the astrometrically derived values for T and ω, together with the apparently reasonable assumption that the ascending node passage of HD 217166 has been sampled with HERCULES observations, has led to a self-consistent orbital solution for this binary system.

The next quadrature phase, predicted to occur in 2007, will provide excellent opportunities to improve the accuracy and precision of the mass ratio and, without necessarily enabling a spectroscopic orbital solution to be derived, will at least allow the measurement of an independent value for the radial-velocity semi-amplitude, K.

7.6 HD 181958 (HIP 95718; $19^{\rm h}28^{\rm m}6^{\rm s}$, $-69°37^{\rm m}55^{\rm s}$)

The first programme of study undertaken with HERCULES was actually one to obtain precise radial velocities of solar-type stars. HD 181958 was one of the first stars observed, initially presenting itself with the anticipated single-lined spectrum but when next observed, revealing its double-lined characteristics and the near equality of the two F-dwarf stars.

HD 181958 is in the constellation Pavo, about midway between δ and ζ Pavonis. It is listed in the 'Henry Draper Catalogue' (Cannon & Pickering 1918) as $6^{\rm m}\!.\!76$, type F8. Based upon published *uvby* photometry, Marsakov & Shevelev (1995) calculated [Fe/H] $= -0.11$, $M_{\rm V} = 3^{\rm m}\!.\!65$, and unaware that HD 181958 was the combined light of two stars, placed it at a distance of 41 pc. They also derived an isochrone age of 3.17 Gyr and assigned it a spectral type of F7V. Kharchenko (2001) derived $V = 6^{\rm m}\!.\!720 \pm 0.003$ and $B = 7^{\rm m}\!.\!234 \pm 0.003$, thus $(B-V) = 0^{\rm m}\!.\!514 \pm 0.004$, for the combined light of both stars.

Hipparcos (ESA 1997) obtained 273 acceptable photometric observations of HD 181958 ($H_p = 6^{\rm m}\!.\!8318 \pm 0.0007$) which demonstrated its stability in this regard. *Hipparcos* also measured the parallax $p'' = 18.19 \pm 0.77$ mas, corresponding to the somewhat greater distance of 55.0 ± 2.3 pc, and an absolute total magnitude $M_{\rm V} = 3^{\rm m}\!.\!02 \pm 0.09$. The mean absolute magnitude of one star is $\overline{M}_{\rm V} = 3^{\rm m}\!.\!77$, indicating evolution above the ZAMS of about $0^{\rm m}\!.\!5$ (Allen 1973). No evidence of duplicity was found in *Hipparcos* or *Tycho* data.

At the time the binary nature of HD 181958 was discovered, the SIMBAD database listed only two papers relating to it, each describing large photometric programmes, one made in the *uvbyβ* photometric system (Twarog 1980) and the other in the *uvby* system (Olsen 1994). In the more recent of these publications, which also provides more precise measures: $(b-y) = 0^{\rm m}\!.\!327 \pm 0.003$, $m_1 = 0^{\rm m}\!.\!158 \pm 0.004$, and $c_1 = 0^{\rm m}\!.\!406 \pm 0.005$. The $(B-V)$ and $(b-y)$ are consistent with a spectral type of F8V. Other than the values described here, there are no apparent published radial velocities for this object (e.g. Barbier-Brossat & Figon 2000; Malaroda et al. 2003).

Radial velocities and orbital solution

The recognition that HD 181958 is a spectroscopic binary meant that it no longer suited the original programme of study at MJUO. However, it was decided to continue observing it whenever opportunities arose with a view to determining the orbital parameters. Beginning in 2001 April, over the next ~ 2.5 years, 33 spectra were obtained using HERCULES at a resolving power of $R \sim 41\,000$. These observations provided adequate phase coverage so that, combined with the precision of the velocities, it was possible to compute a satisfactory orbital solution.

There are 27 double-lined spectra which were used to derive the orbit. The remaining six spectra were obtained close to the systemic velocity making measurement of the velocities of each star highly uncertain; these were treated as single-lined and excluded from the orbital solution. A segment of the spectrum of HD 181958 (see Fig. 7.27), illustrates the similarity of the spectral lines found for each star.

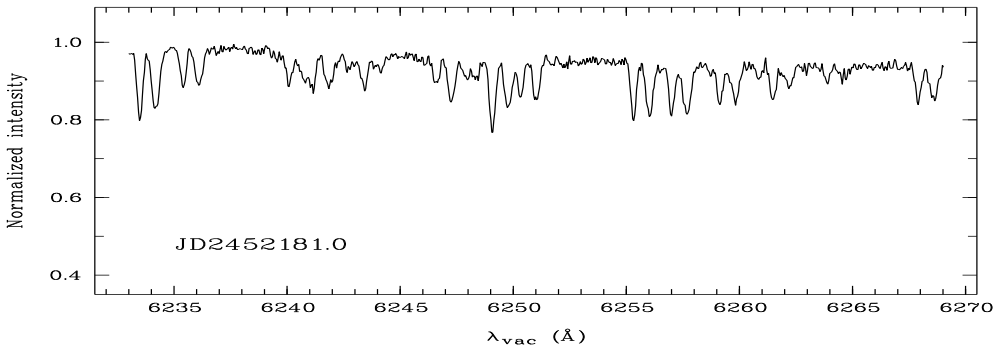

Figure 7.27: A segment of a HERCULES spectrum recorded when the similar F-dwarf components of HD 181958 were close to their maximum velocity separation.

A template spectrum was also required for the purpose of digital cross-correlation. Eight F-dwarf spectra were available in the HERCULES template library at the time the final analysis of the HD 181958 spectra took place (Table 6.1 on page 113). The star that provided the best template in terms of maximizing the separation, strength and quality of the cross-correlation peaks, was the F8V star, HD 7570. Using this template, a typical cross-correlation function at close to maximum velocity separation is shown in Fig. 7.28. The correlation peaks at this phase are similar in intensity, though, in all échelle orders, the width of the primary peak is ~ 20 per cent greater than that of the secondary.

The weighted-mean velocities are listed in Table C.6 Appendix C. The differential-correction method of Lehmann-Fihlés (1894) was used to derive the corresponding orbital solution. The velocities are plotted in Fig. 7.29, together with the computed radial-velocity curves. The residuals of the two stars are not significantly different, and are also listed in Table C.6. The typical

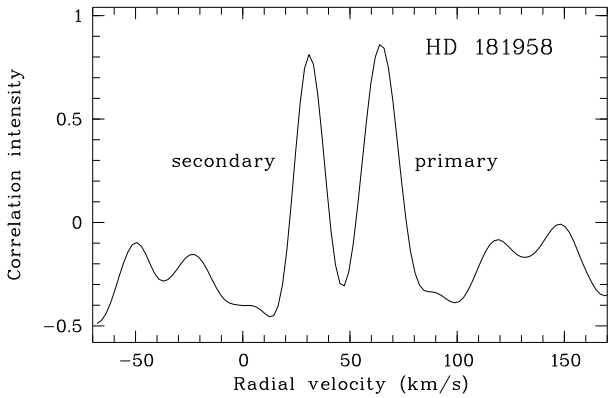

Figure 7.28: Correlation function of HD 181958 near maximum separation.

random error of one data point is $56\,\mathrm{m\,s^{-1}}$. This precision is somewhat worse than that achieved for the previous two SB2 systems analysed. This can be attributed, in part, to the broader and fewer spectral lines provided by HD 181958, as compared to these other two systems (see Murdoch & Hearnshaw 1991). For examples of the respective maximum-velocity separation spectra, see Fig. 7.18 on page 171 for HD 206804 (K7V+K7V), and Fig. 7.23 on page 185 for HD 217166 (G1V+G4V).

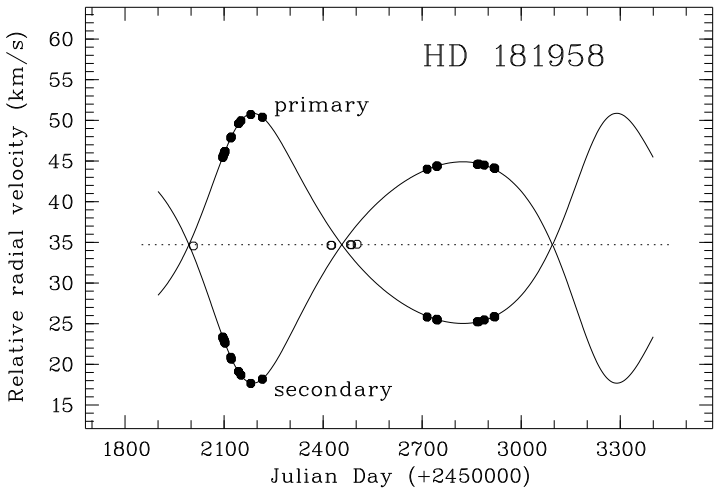

Figure 7.29: The relative radial velocities of HD 181958 and velocity curves computed from the orbital elements. The open symbols identify blended observations which were reduced as single-lined and not used in the orbital solution.

The elements and related parameters of the spectroscopic orbital solution are given in Ta-

P	=	$1\,101.7 \pm 3.2$ d $(3.016 \pm 0.009$ yr)	e	=	0.2772 ± 0.0012
K_1	=	$12.926 \pm 0.014\,\mathrm{km\,s^{-1}}$	K_2	=	$13.617 \pm 0.014\,\mathrm{km\,s^{-1}}$
ω_1	=	$334\overset{\circ}{.}71 \pm 0.70$	ω_2	=	$154\overset{\circ}{.}71 \pm 0.70$
T	=	JD $245\,2145.2 \pm 2.9$ d	γ_{rel}	=	$+34.71 \pm 0.050\,\mathrm{km\,s^{-1}}$
		r.m.s. of best fit $= 56\,\mathrm{m\,s^{-1}}$			
$a_1 \sin i$	=	188.0 ± 0.6 Gm	$\mathcal{M}_1 \sin^3 i$	=	$0.971 \pm 0.005\,\mathcal{M}_\odot$
$a_2 \sin i$	=	198.1 ± 0.7 Gm	$\mathcal{M}_2 \sin^3 i$	=	$0.922 \pm 0.005\,\mathcal{M}_\odot$
$a \sin i$	=	2.581 ± 0.006 AU	$\mathcal{M}_{\mathrm{S}} \sin^3 i$	=	$1.893 \pm 0.007\,\mathcal{M}_\odot$
q	=	0.9492 ± 0.0018	γ	=	$+53.30 \pm 0.40\,\mathrm{km\,s^{-1}}$

Table 7.16: The spectroscopic orbital solution for HD 181958 based on MJUO observations.

ble 7.16. As was the case for HD 206804, the solution for HD 181958 is notable in that its period is one of the longest ones so far measured for an SB2 system (∼93% of SB2 solutions are for binary systems with a shorter period; Pourbaix et al. 2004).

In the same manner as was used for HD 206804 and HD 217166, this measure of the mass ratio, q, was derived without any knowledge of the orbital elements, by calculating the linear regression of the component velocities. The diagram that illustrates this analysis, with the associated results, is presented in Fig. 7.30.

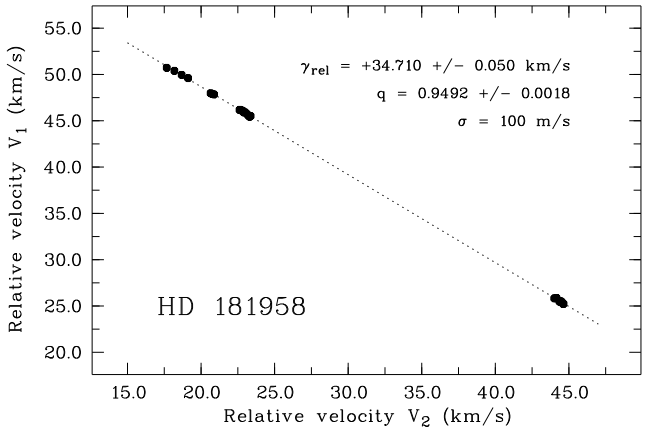

Figure 7.30: Derivation of the mass ratio, q, and the relative systemic velocity, γ_{rel}, for HD 181958 using linear regression applied to the radial velocities of the components.

Barycentric systemic velocity

An estimate of the true systemic velocity γ of HD 181958 was determined with the aid of a spectrum of the F8V star HD 45067. The published barycentric velocity measure of HD 45067 is $+47.280$ km s^{-1} (see Table 6.1 on page 113). The HERCULES measure of the barycentric velocity of HD 45067 is $V_{\rm bary} = +47.290 \pm 0.018$ km s^{-1}, in excellent agreement with the result of Nidever et al. (2002). The radial velocity of our template star, HD 7570, relative to the barycentric reference HD 45067, was measured to be $V_{\rm diff} = -28.689$ km s^{-1}. Hence the estimated sytemic velocity of HD 181958 is $\gamma = +34.710 + 47.280 - 28.689 = +53.30 \pm 0.40$ km s^{-1}. Whilst unusual for a star as bright as seventh-magnitude, this appears to be the first measure of the radial velocity of HD 181958.

Estimates of additional stellar & orbital parameters

The reported values for the various parameters presented in the introduction to this stellar system result from the combined light of two stars. The most reliable guides for the determination of additional parameters to better describe this new binary are presumably the well-defined mass ratio and the combined V and B absolute magnitudes. The strategy will be the same as described earlier (beginning on page 174).

We know from the HERCULES spectra and the derived mass ratio, $q = 0.9492 \pm 0.0018$, that the two components of HD 181958 are quite similar and have spectral types that are approximately F7V. The combined $M_{\rm V}$ and $M_{\rm B}$ magnitudes can be calculated using the apparent magnitudes derived by Kharchenko (2001): $M_{\rm V,\,c} = 3\overset{\rm m}{.}019 \pm 0.092$ and $M_{\rm B,\,c} = 3\overset{\rm m}{.}533 \pm 0.092$. The mean magnitude of the former is $\overline{M}_{\rm V} = 3\overset{\rm m}{.}769 \pm 0.092$, so that, we deduce that $\Delta M_{\rm V} \approx 0\overset{\rm m}{.}223 \pm 0.008$ and $\Delta M_{\rm B} = 0\overset{\rm m}{.}263 \pm 0.010$. Therefore, for the primary star, the magnitudes are $M_{\rm V,\,1} = 3\overset{\rm m}{.}67 \pm 0.09$ and $M_{\rm B,\,1} = 4\overset{\rm m}{.}16 \pm 0.09$, and for the secondary: $M_{\rm V,\,2} = 3\overset{\rm m}{.}89 \pm 0.09$ and $M_{\rm B,\,2} = 4\overset{\rm m}{.}42$. The apparent V magnitude for the primary is $7\overset{\rm m}{.}4$ and for the secondary it is $7\overset{\rm m}{.}6$.

The absolute magnitudes can be used to estimate each star's spectral type and mass. The respective spectral types and corresponding masses are, for the primary star, F6V and $\mathcal{M}_1 = 1.3(3)\,\mathcal{M}_\odot$, and for the secondary star, F7V and $\mathcal{M}_2 = 1.2(6)\,\mathcal{M}_\odot$.

The estimates of the component masses allow an approximation of the orbital inclination, i, and combined with the *Hipparcos* parallax, the orbit's angular semi-major axis, a''. The total mass of the system is $\mathcal{M}_{\rm S} \approx 2.6\,\mathcal{M}_\odot$, so from our measurements of $\mathcal{M}_{1,\,2}\sin^3 i$ we derive $i \sim 64°$. In turn, from $a_{1,\,2}\sin i$ we derive $a = a_1 + a_2 \sim 2.9$ AU and from the parallax $p'' = 0\overset{''}{.}01819$, $a'' \sim 0\overset{''}{.}05$. The nodal separation is about $0\overset{''}{.}065$. An under-estimate of the system's total mass will only separate the components further. An over-estimate by as much as $0.6\,\mathcal{M}_\odot$ (which would require the spectral types to be in error by an unlikely 4–5 sub-types), whilst increasing the inclination to nearer 80 degrees, will not significantly reduce the angular separation. These estimates of properties of the binary system HD 181958 are listed in Table 7.17.

Table 7.17: The orbital solution for HD 181958 that corresponds to the HERCULES velocities, spectroscopic mass ratio, and estimates of the magnitudes of the components.

P (days)	=	1101.7 ± 3.2	i (°)	$\approx$	64
e	=	0.2772 ± 0.0012	T	=	2001.64
ω (°)	=	154.71 ± 0.70	K ($\mathrm{km\,s^{-1}}$)	=	26.543 ± 0.020
a (AU)	$\approx$	2.9	a'' (mas)	$\approx$	50
p''_{Hip} (mas)	=	18.19 ± 0.77			

$q = 0.9492 \pm 0.0018$ $\quad$ $\Delta M_{\mathrm{V}} = 0\overset{\mathrm{m}}{.}22 \pm 0.01$

$\mathcal{M}_1 \approx 1.3(3)\,\mathcal{M}_\odot$ F6V $\quad$ $\mathcal{M}_2 \approx 1.2(6)\,\mathcal{M}_\odot$ F7V

Kepler's 3rd law: $\mathcal{M}_{\mathrm{S}}\ (\mathcal{M}_\odot) \approx 2.6$

Summary

The recently discovered double-lined spectroscopic binary HD 181958 has been described comprising nearly equal seventh magnitude F-type dwarf stars in an orbit of eccentricity 0.277 and period of 1102 days. Together with the angular size of the orbit which is estimated to be $\sim 0''.05$, this binary system appears to be a very worthwhile target for investigation with current high-angular resolution techniques, such as interferometry, and certainly future space-based instruments.

Should HD 181958 be a favourable interferometric object with separate component detection achieved, the considerable benefits of combined interferometric and spectroscopic data would result (Davis 1999). HD 181958 would provide a welcome addition to the growing list of binary systems allowing measurement of the stellar masses, which is a fundamental stellar quantity. The estimate of $a \sin i = 386.1 \pm 0.9$ Gm, corresponds to a percentage error of only 0.23%. If the prospective interferometric observations can match this precision for the angular measure, the precision of the orbital parallax would improve to about 0.3%, which is an order of magnitude better than that achieved by *Hipparcos*.

7.7 The $(B-V)$ magnitudes and CMD positions of the SB2 stars

The previous estimates for M_{V} and M_{B} can be used to estimate the $(B-V)$ colour index of each component of the three SB2 systems described above. The results of the previous calculations for M_{V} and M_{B}, and the corresonding $(B-V)$ values are listed in Table 7.18. Since it is unclear the extent to which random errors and systematic errors contribute to the error estimates, it is possible that these are over-estimated.

The last diagram of this chapter (Fig. 7.31), records the derived positions in a colour-magnitude diagram (CMD) of the K-dwarf (HD 206804), G-dwarf (HD 217166) and F-dwarf

(HD 181958) SB2 binary systems. The diagram includes the evolutionary tracks for stars of masses $\mathcal{M} = 0.8$–$1.5\,\mathcal{M}_{\odot}$ from Lejeune & Schaerer (2001), and a curve representing the empirical ZAMS (Allen 1973).

HD	Sp. type	$M_{\rm B}$	$M_{\rm V}$	$(B-V)$
206804	K7V	$9^{\rm m}\!.31 \pm 0.11$	$8^{\rm m}\!.02 \pm 0.10$	$1^{\rm m}\!.30 \pm 0.15$
	K7V	$9^{\rm m}\!.64 \pm 0.09$	$8^{\rm m}\!.29 \pm 0.09$	$1^{\rm m}\!.35 \pm 0.12$
217166	G1V	$5^{\rm m}\!.16 \pm 0.18$	$4^{\rm m}\!.53 \pm 0.16$	$0^{\rm m}\!.62 \pm 0.24$
	G4V	$5^{\rm m}\!.68 \pm 0.11$	$4^{\rm m}\!.98 \pm 0.10$	$0^{\rm m}\!.70 \pm 0.14$
181958	F6V	$4^{\rm m}\!.16 \pm 0.09$	$3^{\rm m}\!.67 \pm 0.09$	$0^{\rm m}\!.50 \pm 0.13$
	F7V	$4^{\rm m}\!.43 \pm 0.09$	$3^{\rm m}\!.89 \pm 0.09$	$0^{\rm m}\!.54 \pm 0.11$

Table 7.18: The $M_{\rm B}$, $M_{\rm V}$, and $(B-V)$ magnitudes for three SB2 systems, based on each system's combined V and B magnitudes, and the spectroscopic mass ratio.

For HD 206804, the magnitudes are consistent with both stars still being substantially unevolved from the ZAMS, as would be expected for such relatively low-mass stars. The components of HD 217166 are about $0^{\rm m}\!.2$ evolved above the ZAMS. The mean magnitude difference from the ZAMS is similar to the Sun, which we know has an age of about 4.5 Gyr. Therefore a more accurate estimate of the age of these two stars should be 4–5 Gyr, or about half of the age predicted by Nördstrom et al. (2004).

The third SB2 system is HD 181958. These stars have CMD positions that appear to be even more evolved ($\sim 0^{\rm m}\!.5$) from the ZAMS than HD 217166, although the errors make it impossible to draw any particular conclusions. The estimated isochrone age is about 3.5–4 Gyr (using the isochrone tables provided by Lejeune & Schaerer 2001). The younger ages of these stars, if accurate, but greater distance above the ZAMS, would reflect their somewhat faster evolution, owing to their greater masses relative to HD 217166.

The CMD positions of each star, relative to the evolutionary tracks in Fig. 7.31, suggest slightly different masses for the four hotter stars, when compared to the values estimated earlier in this chapter. Our estimates have been based upon the comparison of the $M_{\rm V}$ and $(B-V)$ colours of the stars with empirical tabulations of these parameters (Allen 1991; Drilling & Landolt 2000). When allowance is made for the inherent assumptions, inaccuracies and random errors present in this work on the one hand, and in the evolutionary-track data available on the other, the differences are not sufficiently different that the results described would alter in any substantial way. The difficulties encountered by evolutionary models were outlined at the start of this thesis, and are the result of the complex contributions to the evolutionary path of a star

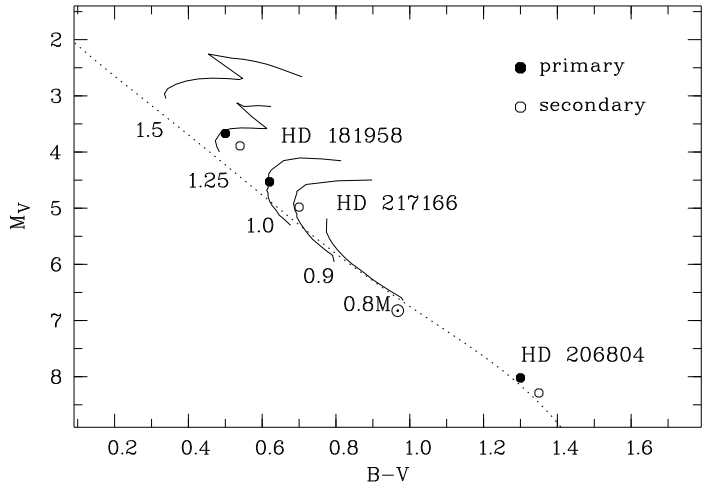

Figure 7.31: Colour-magnitude diagram including the corresponding positions for the components of the three SB2 systems labelled. Included are some evolutionary tracks (Lejeune & Schaerer 2001), and the empirical ZAMS (Allen 1973).

of a given mass owing to, for instance, the star's composition, age, axial rotation, and energy transport mechanisms (e.g. see Kippenhahn & Weigert 1994).

Chapter 8

Summary and conclusions

The research described in the preceeding pages has been divided primarily between the following tasks:

1. assessing the new échelle spectrograph, HERCULES, at the Mt John University Observatory,
2. assessing the associated software, HRSP, which was developed for reducing and analysing the échelle spectra, and
3. studying detached binary systems in a number of ways, including acquiring high-resolution spectra for the purpose of measuring precise radial velocities of the stars. The observational programme of 20 or so of these systems was of about three years' duration.

The following sections will summarize the results of this work, comment upon some subsequent conclusions, and recommend possible avenues for future research.

8.1 Assessment of HERCULES and HRSP

In the first place, this work has demonstrated the successful implementation of the new high-resolution échelle spectrograph, HERCULES. Its successful design has been guided, in part, by the relatively small aperture of the 1-metre McLellan telescope with which it is operated.

Whilst the observational programme and related analyses were being carried out, the assessment of the HERCULES spectrograph and the related reduction software, HRSP, was also pursued. Of course, since both of these research tools were new and untested, the origin of some problems was far from obvious. This was particularly the case for the primary goal of this project's observational programme, namely high-precision radial velocities.

The design prediction for the radial-velocity precision of HERCULES was $\lesssim 10\,\mathrm{m\,s^{-1}}$, for late-type stars with small $v_{\mathrm{equ}} \sin i$. During the first months of operations, it became increasingly evident that this precision was not being approached, especially for brighter stars. In particular, spectra acquired of α Cen A, separated by a timespan of only minutes, sometimes yielded velocity differences as large as 50–100 $\mathrm{m\,s^{-1}}$. Ultimately, the cause of this serious problem was recognized as being due to inadequate guiding of the stellar image on the optical fibre input, combined with insufficient scrambling by the fibre itself (Skuljan 2003). A beamsplitter and more frequent guiding was implemented to address this situation, and as shown in Fig. 5.22 on page 106, the velocity precision improved considerably, particularly, as anticipated, for brighter

stars. At present, the resulting typical long-term velocity precision achieved by HERCULES is about $15\,\mathrm{m\,s^{-1}}$, for late-type unevolved stars with small $v_{\mathrm{equ}} \sin i$.

These circumstances focussed attention upon the crucial need to obtain spectra with the most accurate and precise telescope guiding possible, particularly when the seeing was at its best, if the most precise velocity measures were to be obtained. To this end, the final months of observing were carried out with particular attention to the adjustment of the telescope's sidereal rate to match that of the given observation's direction in the sky. Whilst insufficient observations were obtained to demonstrate that this improved the long-term precision, there can be no doubt, from the earlier experiences, that the accuracy and precision of the guiding are highly significant aspects of this type of research. These are important matters for consideration when instrument upgrades are possible at Mt John. Not only would a dedicated detector that was large enough to record the entire HERCULES spectrum be desirable (and plans for which are well advanced), but the telescope's guiding performance and the light scrambling properties of the fibres should also be given their due attention.

As the project progressed, a couple of problems with the reduction algorithms of HRSP became apparent. First, as described in § 5.7.2 beginning on page 90, the instability of interpolating splines (and later parabolas) for measuring the velocity corresponding to the CCF peak, was demonstrated. Gaussian-profile fitting did not present the same problem, so these were used routinely thereafter. It was also shown that, to get the most precise radial velocities, it was necessary for the final velocity to be measured (by the method of digital cross-correlation), only after allowance was made for any relative velocity between the template and the progamme star's spectrum. As Fig. 5.8 on page 90 illustrates, if this is not done, the systematic error that occurs can be of the order of $\sim$1 part in 10^3 of relative velocity.

An investigation into the possibility of an improved table of Th–Ar calibration lines (see comments beginning on page 77 in § 5.3), for the dispersion-solution algorithm used by HRSP, led to the production of a HERCULES 'Thorium-Argon Atlas', and the recognition of an unexpected relationship between a Th–Ar line's species (ThI, ThII, ArI or ArII), and its intensity properties. The Atlas (Appendix E includes several pages from it) is a four volume document that includes, amongst other data, the wavelengths in air and vacuum for 8806 Th–Ar lines in the range $3527 \lesssim \lambda_{\mathrm{vac}} \lesssim 7638$ Å. This is a major fraction of the present image plane of HERCULES. To assist with the identification of lines with regard to blending and relative strengths, spectral maps are provided for each échelle order. These maps include all but a couple of dozen of these lines, which are absent owing to the minor incomplete overlap of the HERCULES detector positions.

For reasons not yet understood, but which are anticipated to be complex, it was found that a simple statistical analysis of certain series of Th–Ar spectra could be used to identify, with considerable confidence, the exact species that an emission line belongs to (§ 5.4 on page 82). As a consequence, it has been possible to infer the species of all of the nonspecific thorium lines

in a preliminary calibration table, as well as the erroneous labelling of one thorium line in the literature (see Table 5.3 on page 84).

8.2 Binary system orbits and related properties

Spectroscopic orbital elements and/or related parameters have been determined for eight binary systems. All of the observed components were late-type main-sequence or evolved stars. The orbital periods of these systems range from about 10 days to 26 years, with a median of about 6 years. Orbital solutions were determined for the seven systems with shorter periods, using the method of differential corrections. The measurement of the mass ratio of the longest-period system, HD 217166, demonstrates that this important astrophysical quantity can be estimated in a model-free manner with less than 10% of the orbital cycle observed spectroscopically, and relatively little velocity change ($\sim 1\,\mathrm{km\,s^{-1}}$).

Single-lined orbital solutions have been derived for five of the binaries. Two of these, β Ret and ν Oct, are astrometric systems, each with K-giant primary stars and orbital periods of about three years. The other systems studied were 94 Aqr A ($P \sim 6.3$ years), θ Ant ($P \sim 18$ years), and the 10-day system, HD 159656. The preliminary spectroscopic solution for θ Ant is the first one derived for this system. On the other hand, the orbital solution determined for HD 159656 is of very high precision. For instance, $e = 0.115\,84 \pm 0.000\,16$, $P = 10.090\,862 \pm 0.000\,067$ days, and $\omega = 123\overset{\circ}{.}0 \pm 0.1$. The improvement to the precision achieved for the elements of the this and the other three systems was typically between 1–2 orders of magnitude. The K-giant, ν Oct, has been found to have a long-term additional irregular periodicity, attributed, for the time being, to the rotation of a large surface feature.

Double-lined solutions were obtained for HD 206804 (K7V+K7V; $P \sim 6$ years) and HD 181958 (F6V+F7V; $P \sim 3$ years). Until this work, HD 206804 had two competing astrometric solutions but no spectroscopic solution. The valid solution has been identified here. HD 181958 is a newly discovered seventh-magnitude system. It has the distinction of having components and an orbit whose study should be possible with present ground-based interferometers. The considerable benefits of being able to combine the astrometric and spectroscopic data would result. This system would provide a welcome addition to the growing list of binary systems allowing accurate and precise measurement of the parallax and masses of these stars. Both of these systems have an orbital period that is unusually long for a binary with an SB2 orbital solution.

All eight of the binaries have had their system mass ratio and the masses of their components estimated. Unfortunately, none of the final mass estimates can be considered particularly accurate or precise, owing, in part, to the lower precision of the corresponding astrometric parameters. However, the precision of the spectroscopic orbital solutions range from moderate to very high. The choice of the ascending node for the visual binaries HD 206804 and HD 217166 have been shown to be incorrect, so that each respective value for Ω is 180° out of phase.

A significant number of observations was acquired of two triple-lined systems, HD 10800 (50 spectra) and HD 118261 (41 spectra). The analysis of these systems has not yet begun, but as an indication of their nature, the cross-correlation functions, for one order, have been provided (Appendix B).

8.3 Velocity zero-point and template library

A concurrent sample of several IAU radial-velocity standards, as well as a dozen other late-type main-sequence and evolved stars with precise barycentric velocities, was also observed. Based upon the HERCULES velocities, it has been established that the velocity zero-point of the HERCULES system is insignificantly different from that of these other surveys (see § 6.4 beginning on page 112). These observations, together with those of about twenty other similar stars, form the foundation of a library of high-resolution template spectra for HERCULES users, at least, until a detector upgrade is carried out.

8.4 Statistics of the observed properties of binary stars

Another area of binary star research that attracted some attention during this thesis was the statistics of the observed properties of two large samples of binary systems, one comprising visual and unresolved astrometric orbital solutions (Hartkopf & Mason 2004), and the other devoted to spectroscopic orbital solutions (Pourbaix et al. 2004). This work was considered especially relevant, as the challenges of the complementary approach to determining, as completely as possible, a binary system's parameters, hinges on the selection effects that influence the respective observational methods differently. Chapter 4 was devoted to a presentation of this work. Whilst the general conclusions in that chapter differ little from the conclusions of previous similar surveys, these were the largest samples for which a comparison of these properties has, apparently, been made to date. Unfortunately, from this analysis, it appears that the binary samples allowing spectroscopic and astrometrically determined orbital solutions continue to be substantially independent of each other.

8.5 Future work

There are considerable opportunities for future work resulting from the research that has been undertaken during this thesis. Whilst the spectroscopic orbital solutions derived so far are satisfying, there is no doubt that the only ones that could be described as definitive are those belonging to the SB1 systems analysed in detail in Chapter 7, namely those corresponding to β Ret, ν Oct and HD 159656. The latter binary has an unusual orbit which, for the system's predicted considerable age ($\sim 10\,\mathrm{Gyr}$) and short period ($P \sim 10\,\mathrm{days}$), is not circular ($e \sim 0.1$). Thus, HD 159656 appears to be an excellent candidate for further spectroscopic observations to assess the possibility of apsidal motion.

The preliminary orbital solutions for θ Ant and 94 Aqr A are based on radial velocities for only part of each respective orbit; about 15% of that for θ Ant, and about half of that for 94 Aqr A. The θ Ant system has the distinction of having a composite spectrum, although the exact nature of the spectral types are presently uncertain. A full description of this binary requires disentanglement of the two spectra present, the identification of them, and radial-velocity observations throughout the remaining orbital cycle. Careful analysis of the spectra will hopefully permit the measurement of velocities for both components so that a model-free precise estimate of the system mass ratio and other desirable parameters can be derived.

The three SB2 systems, HD 206804, HD 217166 and HD 181958 (the newly discovered seventh-magnitude F-dwarf pair) would all benefit from further observations. HD 217166 continues to lack a spectroscopic solution, however, a preliminary mass ratio with moderately high precision has been derived. The masses derived for its components, $\mathcal{M}_1 = 0.96\,\mathcal{M}_\odot$ and $\mathcal{M}_2 = 0.87\,\mathcal{M}_\odot$, based on the astrometric orbit and spectroscopic mass ratio, are reasonably consistent with our expectations from current knowledge relating to stellar masses. The opportunity to improve the precision of the mass ratio substantially will present itself in 2007, when the stars in this 26-year period system approach the opposite quadrature phase to the one observed here. Unfortunately, the velocity separation is predicted to be somewhat less, but modern techniques, e.g. TODCOR, should have no difficulty extracting the velocities from both spectra. It is coincidental, of course, that the other SB2 visual binary, HD 206804, will also be in a favourable phase during 2007, when the orbital phase observed here repeats itself. In the meantime, the orbital solutions of all three SB2 systems may be improved by the application of TODCOR to the blended cross-correlation functions that are already available, and this is the author's intention in the near future.

The consequences for future work resulting from this research are not limited to spectroscopic investigations. Several of the solutions presented here should assist investigators employing high-angular resolution techniques, such as interferometry. This appears to be particularly so for the recently discovered SB2 system HD 181958, the apparently once-resolved SB1 binary HD 205478, and the K-dwarf pair HD 206804, which has had the more accurate of its two astrometric solutions identified.

In general, this research demonstrates the potential and cost-effective advantage of small telescopes for doing fundamental science. As a specific example, the the radial-velocity study of the relatively long-period visual binary, HD 217166, shows that when carefully chosen and observed at favourable phases, previously unobtainable data, such as precise mass ratios, can be determined for them with relatively few observations acquired over a small fraction of the orbital cycle.

Finally, the series of spectra acquired of the two triple-lined systems provide an excellent starting point for the proper and complete study of either of these astrophysically interesting systems. Indeed, this possibility is already being pursued by another colleague.

Appendix A

Definitions and theoretical background

The purpose of this appendix is to place before the reader definitions of the many terms used and derivations of a number of equations encountered in the study of bound orbital motion. The equations derived include those that are commonly associated with Kepler's three laws of planetary motion, Kepler's equation, and equations relating to the calculation of radial-velocity parameters.

A.1 Choosing which star to label the *primary* component

It is worthwhile to begin by considering this aspect of binary star nomenclature. Unfortunately, which star is designated the primary component in an orbital pair can change from aythor to author, so that different labels can arise for the same system. Generally this is due to differing labelling conventions as a result of the various methods of study aimed at deducing the parameters that describe binary systems. The primary star is typically identified with a subscript label '1' or 'A' whilst the secondary is labelled '2' or 'B'.

For visual binary systems the primary star is the brighter star. When the components are more or less equally bright, the choice is not so obvious. An important issue that arises for equally bright pairs is the possibility that the stars may be confused and the labels exchanged during two or more observing programs of the same system. When confusion occurs for one observer but not another, so that for instance, one orbit is assigned a relatively circular orbit, and another orbital solution is assigned a high eccentricity, it is typical that the circular solution has a period double that of the eccentric one. Many pairs of orbital solutions exist as a result of this situation arising (e.g. see the 'Sixth Catalog of Orbits of Visual Binary Stars', Hartkopf & Mason 2004.)

A spectroscopic binary may be assigned a single-lined or double-lined orbital solution (§ 2.1.3 beginning on page 11). The primary star of a double-lined spectroscopic binary is the component with the smaller radial-velocity amplitude, so that $\mathcal{M}_1 \geq \mathcal{M}_2$ and $q \leq 1.0$ always. When a single-lined system is studied, the observed star may be regarded as the primary component unless additional reliable data indicates that for $q \leq 1.0$, the other star should be regarded as the primary. Usually the more massive star will also be the more luminous, but this may not be the case either, for example when the binary includes a degenerate star such as a white dwarf.

The convention for photometric orbital studies is to designate the star being eclipsed at

primary minimum i.e. the star of greater surface brightness, as the primary component.

Finally, the definition of the primary from the point of view of evolutionary studies, such as those that incorporate Roche models (see § 2.2 on page 14) is usually the component that was initially the more massive i.e. before mass transfer may have reversed the mass balance. However, when only one component is a degenerate object, the compact object is regarded as the secondary (Vanbeveren et al. 1998), so that in such cases, $q > 1$ is possible.

None of these conventions are set in stone, so it is prudent to ascertain the convention used for each publication studied. Combining orbital data arising from different methods of study necessitates the careful and consistent labelling of the components[1]. The standard spectroscopic conventions for labelling the components and numerical labels will be used in this thesis.

A.2 Orbits and orbital elements

Orbital motion is one of the central features of astronomy. In its simplest form it involves two point masses moving relative to each other about their common centre of mass as a result of the gravitational force. Consider two masses $\mathcal{M}_1$ and $\mathcal{M}_2$ in orbit about their common centre of mass or barycentre **C**. The general nature of the orbit described depends on whether the barycentre or a given body is used as a reference point for the orbit. An absolute or barycentric orbit is that which is traced out by either mass around the barycentre, hence there are two such orbits in whatever plane of motion is being considered. Each orbital parameter or element associated with an absolute orbit is labelled with a '1' or '2' using the same convention as for the masses. If one body is considered fixed, the relative orbit is traced out by the orbiting body. Relative orbital elements are without subscripts.

In the case of binary stars, the conventional orbital elements are:

1. the *semimajor axis* of the true relative orbit, a
2. the *eccentricity*, e
3. the *time of periastron passage*, T
4. the *inclination* of the orbital plane to the sky plane, i
5. the *longitude* or *position angle of periastron* of the true relative orbit, ω
6. the *longitude of the line of nodes*, Ω, and
7. the *orbital period*, P. A particular epoch t on the respective orbits of the two stars may be defined in various ways, for instance, in terms of P, T, and the mean anomaly Φ (related by Eq. A.25 on page 215). An alternate epoch is the time of zero mean longitude, T_0,

[1] See § A.11.1 on page 224 for the example of the differing conventions for designating the longitude of periastron ω.

which is described in § 6.6.2. The period P is related to the binary's total mass by the general form of Kepler's third law (Eq. A.49 on page 220) and the semimajor axis a.

Each of these terms and many others will be defined in the following. The typical measures of T and P are given as the observed values, rather than the true values, as they disregard the inherent light-travel-time effect corresponding to the binary's *systemic radial velocity*, γ, relative to the Earth[2].

A.3 The gravitational force and orbital masses

The gravitational force $\boldsymbol{F}_{\rm grav}$ is observed to have several important properties, each of which has a role to play in the following. In the first place, the gravitational force is attractive. It is also directed radially along the line connecting the two masses and therefore it is a central force. In addition, it is a conservative force, which can be defined as a force which is independent of time, or one that does work that is independent of the path taken by a mass that moves in the force field. The gravitational force on a body that lies outside a closed uniform spherical shell is the same as it would be if all the matter were concentrated at one point at the centre of the shell. Hence the following assumes uniform spherical bodies which will considerably simplify the subsequent derivations.

For a relative orbit, the motion of either body is as though the central fixed body **f** has the system's total mass

$$\mathcal{M}_{\rm S} = \mathcal{M}_1 + \mathcal{M}_2 \,, \tag{A.1}$$

and the orbiting body has a *reduced mass*, μ, given by

$$\mu = \frac{\mathcal{M}_1 \mathcal{M}_2}{\mathcal{M}_1 + \mathcal{M}_2} \,. \tag{A.2}$$

In this way, for instance, the gravitational force remains the same between the fixed and orbiting masses. The division of mass between the fixed body and the orbiting body is always the same so that there is only one relative orbit. As only one mass is moving, a relative orbit permits an easier analysis of the motion involved. In the following discussion, the orbiting body has constant mass and a relative orbit is assumed unless otherwise stated.

A.4 Coordinate systems and conservation laws in the orbital plane

The fundamental quantities energy and angular momentum and their respective conservation laws are relevant to any discussion of periodic orbital motion. Furthermore, the physics of a problem must be independent of the coordinate system used as a reference frame. The priorities

[2] A calculation of the true period, P_0, is made for the single-lined spectroscopic binary HD 159656, based on γ and the high-precision observed period P (see § 7.3 on page 154).

for this appendix are to determine the nature of the curves that orbiting bodies follow, and to be able to deduce the positions and motions of the bodies at particular times. The equations required to achieve these goals can be derived using a combination of rectangular and polar coordinates, which for convenience, will have a common origin **O**. The coordinate systems and hence solutions can be simplified considerably by showing that the orbital motion must be confined to a single plane, so that plane coordinate systems can be utilised.

A.4.1 Conservation of angular momentum

Let **r** be the *position* or *radius vector* from the origin to the reduced mass μ on the orbit at the point **Q** (see Fig. A.1 on page 214). Let this orbiting mass have instantaneous velocity **v**. By definition, the *angular momentum* $\boldsymbol{J}$ of a body with linear momentum $\boldsymbol{p}$ relative to the origin is $\boldsymbol{J} = \boldsymbol{r} \times \boldsymbol{p}$. The angular momentum of the orbiting mass is therefore

$$\boldsymbol{J} = \mu\,(\boldsymbol{r} \times \boldsymbol{v})\,. \tag{A.3}$$

The *torque* $\boldsymbol{T}$ is defined as the time rate of change of $\boldsymbol{J}$ so that $\boldsymbol{T} = \mathrm{d}\boldsymbol{J}/\mathrm{d}t = \mu\,\mathrm{d}(\boldsymbol{r} \times \boldsymbol{v})/\mathrm{d}t$. Thus $\boldsymbol{T} = \boldsymbol{r} \times \boldsymbol{F}$ where the force $\boldsymbol{F}$ for an orbiting body is the gravitational force $\boldsymbol{F}_{\mathrm{grav}}$. As the gravitational force is a central force, $\boldsymbol{F}_{\mathrm{grav}} \parallel \boldsymbol{r}$ and the torque is zero. Therefore *the orbital angular momentum is conserved*. Consequently, $\boldsymbol{r}$ must always be in the same plane as the velocity vector $\boldsymbol{v}$ (whose normal is always parallel to $\boldsymbol{J}$). Assuming no external forces act on the orbiting mass, its motion must be confined to a single plane, which is known as the orbital plane.

If **Q** is a point in the orbital plane with *rectangular coordinates* $(X',\, Y',\, Z' = 0)$ associated with the unit vectors $\hat{\mathbf{X}}'$, $\hat{\mathbf{Y}}'$, $\hat{\mathbf{Z}}'$, its position vector can be defined by $\boldsymbol{r} = X'\hat{\mathbf{X}}' + Y'\hat{\mathbf{Y}}'$. The instantaneous velocity of a body at **Q** is

$$\boldsymbol{v} = \frac{\mathrm{d}\boldsymbol{r}}{\mathrm{d}t} = \dot{\boldsymbol{r}} = \dot{X}'\hat{\mathbf{X}}' + \dot{Y}'\hat{\mathbf{Y}}'\,. \tag{A.4}$$

Alternatively the point **Q** can be defined with plane *polar coordinates* $(r,\, \upsilon)$ where the radius vector $\boldsymbol{r}$ subtends the angle υ to the polar axis. In orbital motion studies υ is known as the *true anomaly*. This angle is measured from the polar axis in the direction of orbital motion with $0 \le \upsilon < 2\pi$. The associated unit vectors are $\hat{\mathbf{r}} = \cos\upsilon\hat{\mathbf{X}}' + \sin\upsilon\hat{\mathbf{Y}}'$ and $\hat{\boldsymbol{\upsilon}} = -\sin\upsilon\hat{\mathbf{X}}' + \cos\upsilon\hat{\mathbf{Y}}'$, with $\boldsymbol{r} = r\hat{\mathbf{r}}$. In terms of polar coordinates the velocity of the body at **Q** is

$$\boldsymbol{v} = \boldsymbol{v}_{\mathrm{r}} + \boldsymbol{v}_{\upsilon} = \frac{\mathrm{d}(r\hat{\mathbf{r}})}{\mathrm{d}t} = \dot{r}\hat{\mathbf{r}} + r\dot{\upsilon}\hat{\boldsymbol{\upsilon}}\,. \tag{A.5}$$

The magnitude of the angular momentum $\boldsymbol{J}$ of the orbiting mass is therefore

$$J = \|\boldsymbol{J}\| = \mu r\|\boldsymbol{v}_{\upsilon}\| = \mu r^2\dot{\upsilon} = \text{constant}\,. \tag{A.6}$$

A.4.2 Conservation of energy

The time derivative of Eq. (A.5) provides an expression for the vector acceleration of the orbiting mass:

$$\ddot{\boldsymbol{r}} = \frac{\mathrm{d}\dot{\boldsymbol{r}}}{\mathrm{d}t} = (\ddot{r} - r\dot{\upsilon}^2)\hat{\mathbf{r}} + \frac{1}{r}\frac{\mathrm{d}}{\mathrm{d}t}\left(r^2\dot{\upsilon}\right)\hat{\boldsymbol{\upsilon}}\,. \tag{A.7}$$

The attractive gravitational force obeys Newton's second law so that

$$-F_{\mathrm{grav}}\hat{\mathbf{r}} = \mu\ddot{\boldsymbol{r}} = \mu\,(\ddot{r} - r\dot{\upsilon}^2)\hat{\mathbf{r}} + \frac{\mu}{r}\frac{\mathrm{d}}{\mathrm{d}t}\left(r^2\dot{\upsilon}\right)\hat{\boldsymbol{\upsilon}}\,,$$

which can be separated into its vector components. The components for $\hat{\boldsymbol{\upsilon}}$ represent the conservation of angular momentum as already deduced since

$$\frac{\mu}{r}\frac{\mathrm{d}}{\mathrm{d}t}\left(r^2\dot{\upsilon}\right) = 0 \tag{A.8}$$

implies $r^2\dot{\upsilon} =$ constant, as expressed in Eq. (A.6).

The components for $\hat{\mathbf{r}}$ yield

$$\mu\,(\ddot{r} - r\dot{\upsilon}^2) + F_{\mathrm{grav}} = 0\,,$$

which with the identity $\ddot{r} = \dot{r}\mathrm{d}\dot{r}/\mathrm{d}r$ becomes

$$\mu\,(\dot{r}\frac{\mathrm{d}\dot{r}}{\mathrm{d}r} - r\dot{\upsilon}^2) + F_{\mathrm{grav}} = 0\,.$$

Integrated with respect to r, this equation gives

$$\frac{1}{2}\mu(\dot{r}^2 + r^2\dot{\upsilon}^2) + \int F_{\mathrm{grav}}\,\mathrm{d}r = \text{constant}\,. \tag{A.9}$$

The gravitational force is conservative and therefore it must be the gradient of some scalar function of position i.e. $\boldsymbol{F}_{\mathrm{grav}} = -\nabla U(\boldsymbol{r})$. U is called the *potential energy*. Eq. (A.9) is therefore recognizable as a statement of the *conservation of energy* since the first term represents the *kinetic energy* S in polar coordinates and the remaining integrand represents the potential energy. The constant value that the orbital energy E has will be derived in § A.9.

A.5 Elliptical orbits: Kepler's first law

Another consequence of the gravitational force being a central force is that Bertrand's theorem applies to it. Bertrand's theorem states that the only central forces that result in closed orbits for all bound particles are forces F that are either 1. directly proportional to the radial distance r e.g. Hooke's law, or 2. the attractive inverse-square law i.e. $F \propto 1/r^2$ (Goldstein et al. 2002).

Gravitational forces are observed to act over vast distances and a force increasing indefinitely to infinity (as would $F \propto r$) would be unrealistic. Therefore the gravitational force must act like $F_{\rm grav} \propto 1/r^2$. If the proportionality constant is k then

$$F_{\rm grav} = \|\boldsymbol{F}_{\rm grav}\| = \frac{k}{r^2} \qquad \text{and therefore} \qquad U = -\frac{k}{r} \tag{A.10}$$

with the integration constant for U chosen to be zero, since its zero-point is arbitrary. By definition of the gravitational mass and Newton's third law it follows that $F_{\rm grav} \propto \mathcal{M}_1\mathcal{M}_2$, and therefore $k \propto \mathcal{M}_1\mathcal{M}_2$ and with a new proportionality constant, G, known as the *gravitational constant*

$$k = G\mathcal{M}_1\mathcal{M}_2\,. \tag{A.11}$$

In polar coordinates the total energy $E = S + U$ of the reduced mass μ moving with orbital speed $V_{\rm orb} = \|\boldsymbol{v}\|$ is

$$E = \frac{1}{2}\mu V_{\rm orb}^2 + U(r) = \frac{1}{2}\mu\big(\dot{r}^2 + r^2\dot{\upsilon}^2\big) + U(r)\,. \tag{A.12}$$

From the expression for J from Eq. (A.6) and the expression for $U(r)$ from Eq. (A.10)

$$E = \frac{1}{2}\mu\dot{r}^2 + \frac{1}{2}\frac{J^2}{\mu r^2} - \frac{k}{r}\,. \tag{A.13}$$

Solving this equation for $\dot{r}$, we have

$$\dot{r} = \frac{{\rm d}r}{{\rm d}t} = \sqrt{\frac{2}{\mu}\left(E + \frac{k}{r} - \frac{J^2}{2\mu r^2}\right)}\,. \tag{A.14}$$

We let $r = 1/h$ so that ${\rm d}r = -{\rm d}h/h^2$ and invert the result to give

$$h^2{\rm d}t = -\frac{{\rm d}h}{\sqrt{\frac{2}{\mu}\left(E + kh - \frac{J^2h^2}{2\mu}\right)}}\,. \tag{A.15}$$

For the next change of variable of differentiation, one uses Eq. (A.6) to substitute $\mu{\rm d}\upsilon/J$ for ${\rm d}t/r^2 = h^2{\rm d}t$. Some minor re-arrangement yields

$$-{\rm d}\upsilon = J\frac{{\rm d}h}{\sqrt{2\mu E + 2\mu kh - J^2h^2}}\,. \tag{A.16}$$

As J, E, μ and k are all constants of the motion, the indefinite integral of Eq. (A.16) has a standard form in h of second degree[3] that leads to the solution

[3] If u is a differentiable function of x, $\int \frac{1}{\sqrt{1-u^2}}\frac{{\rm d}u}{{\rm d}x}{\rm d}x = -\cos^{-1}u$.

$$\upsilon - \upsilon_0 = -\cos^{-1}\left(\frac{\frac{J^2 h}{\mu k} - 1}{\sqrt{1 + \frac{2EJ^2}{\mu k^2}}}\right), \tag{A.17}$$

where υ_0 is a constant.

Finally, the equation of the orbit is determined by re-defining it in terms of $h = 1/r$:

$$\frac{1}{r} = \frac{\mu k}{J^2}\left(1 + \sqrt{1 + \frac{2EJ^2}{\mu k^2}}\cos(\upsilon - \upsilon_0)\right) \tag{A.18}$$

which can be recognized as a conic section, whose general form in polar coordinates is

$$\frac{1}{r} = \frac{1}{s}[1 + e\cos(\upsilon - \upsilon_0)]\,. \tag{A.19}$$

There are three constants in the general solution Eq. (A.19) — s, e, and υ_0. The first constant we shall consider is υ_0. Any conic section has a symmetry axis about the line $\upsilon = \upsilon_0$. This line is called the *major axis* and υ_0 determines the orientation of the major axis to the polar axis $\upsilon = 0$. Since the general properties of any conic section are not influenced by this constant, the following discussion is not compromised by setting $\upsilon_0 = 0$ so that now the major axis of the conic is coincident with the polar axis.

The constant e is known as the *eccentricity* of the conic section and has the non-negative value

$$e = \sqrt{1 + \frac{2EJ^2}{\mu k^2}}\,. \tag{A.20}$$

For the orbit to be bound, the orbit must have $E < 0$, i.e. $e < 1$. For Eq. (A.20) to have a real value $E \geq -\mu k^2/2J^2$. Therefore all bound orbits must have an eccentricity between $0 \leq e < 1$. For the special case when $e = 0$, $r = s = J^2/\mu k$ which is a constant, so that this orbit is a circle. When $-\mu k^2/2J^2 < E < 0$ the eccentricity falls between $0 < e < 1$ and therefore $1/r$ is always positive and is a periodic function of υ with a period P of 2π. Such a closed curve is called an ellipse. **Kepler's first law** — the orbit of each planet is an ellipse with the Sun at one focus — is a special case of this general result for bound orbits.

A.6 More ellipse definitions and properties

Having determined that all closed orbits follow curves that are in general represented by ellipses, it is possible to utilise a particular definition that will assist in understanding some of

their features: an ellipse is the locus of all points such that the sum of the distances from two given fixed points, f_1 and f_2, to any point **Q** on the curve so formed is a constant (Fig. A.1). We let this constant be $2a$ so that $f_2Q + f_1Q = r' + r = 2a$. Each fixed point is known as a focus of the ellipse and by symmetry will be equidistant from **G**, the geometric centre of the ellipse[4].

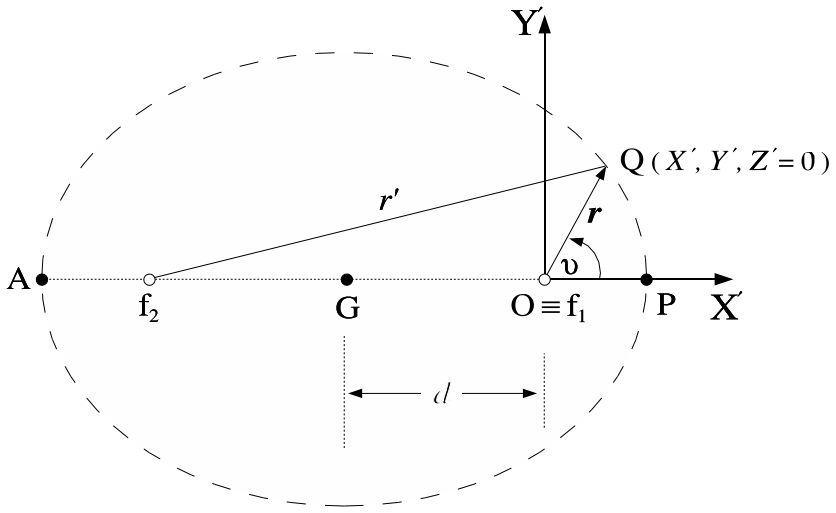

Figure A.1: Parameters for the construction of an ellipse.

This definition also lends itself to deriving an equation of an ellipse using rectangular coordinates (X', Y') with the X′-axis coincident with the previously described polar axis. Let the distance between the foci be $2d$ where $d < a$ by necessity of the definition. Then position the focus f_1 also at the origin **O** of these two reference systems, and form two right-angled triangles such that $r'^2 = (2d + X')^2 + Y'^2$ and $r^2 = X'^2 + Y'^2$. It is then possible to derive

$$\frac{(X' + d)^2}{a^2} + \frac{Y'^2}{(a^2 - d^2)} = 1\,. \tag{A.21}$$

Several important features of ellipses readily arise from this equation. First, the ellipse is symmetrical about the lines $y = 0$ and $x = -d$, which are clearly normal to one another. When $d = 0$ the locus of points is a circle. For $d \neq 0$, $a^2 > a^2 - d^2$ always, and the axis of greater

[4]There are many ways to define an ellipse in geometric terms. For instance, an alternate way is to define an ellipse as the locus of points whose distance from a given fixed point (the focus) bears a constant ratio (the eccentricity) to the distance from a given fixed line (the directrix). The major axis will be normal to the directrix.

length is also the major axis of the ellipse, upon which sit the two foci. The length a is known as the *semimajor axis* of the ellipse. The length of the *semiminor axis* is $b = \sqrt{a^2 - d^2}$. The two axes meet at **G** at the point $(-d, 0)$.

So that all features of the ellipse can be defined in terms of the geometric constants of the general ellipse, we first return to its polar form [Eq. (A.19)]. The end-points of the major axis are $[\, s/(1+e),\, 0\,]$ and $[\, s/(1-e),\, 0\,]$. The semimajor axis $a = s/(1-e^2)$. The constant s can now be expressed in terms of the dynamical properties of the orbit represented in [Eq. (A.18)] and also in terms of the geometric properties of the ellipse as follows

$$s = \frac{J^2}{\mu k} = a(1-e^2)\,. \tag{A.22}$$

The line $r = s$ is known as the semi-latus rectum. The geometric significance of s is that it represents the distance from the focus to the ellipse perpendicular to the major axis since $r = s$ when $\upsilon = \pi/2$ and $3\pi/2$. The usefulness of the latter expression for s is that it allows the polar equation of the orbit to be represented in another common form:

$$r = \frac{a(1-e^2)}{1 + e\cos\upsilon}\,. \tag{A.23}$$

The minimum and maximum distance between the ellipse and a focus (when $\mathrm{d}r/d\upsilon = 0$), are the end-points of the major axis. When $\upsilon = 0$ the distance $r = a(1-e)$ is a minimum and when $\upsilon = \pi$ the distance $r = a(1+e)$ is a maximum. On the relative orbit, each end-point is known as an apsis and the respective distances as *apsidal distances*. In a binary system the closest and furthest apsidal points are known respectively as periastron **P** and apastron **A**.

The centre of the ellipse is found at the mid-point of the major axis. Due to the underlying symmetry, the distance of the mid-point to either focus is $d = a - a(1-e) = ae$. The length of the semi-minor axis is now determined to be

$$b = \sqrt{a^2 - d^2} = a\sqrt{1-e^2}\,. \tag{A.24}$$

A.6.1 Auxiliary angles: the mean anomaly and eccentric anomaly

Let r have an initial value r_0, which by convention is at periastron when $\upsilon = 0$ and the time $t = T$ is a time of periastron passage. The angular fraction, in radians, of one orbital period P, as the orbiting mass μ moves from periastron to some other position on the orbit at time t is the *mean anomaly*

$$\Phi = \frac{2\pi}{P}(t-T) = n(t-T)\,, \tag{A.25}$$

where $n = 2\pi/P$ is the *mean annual motion*.

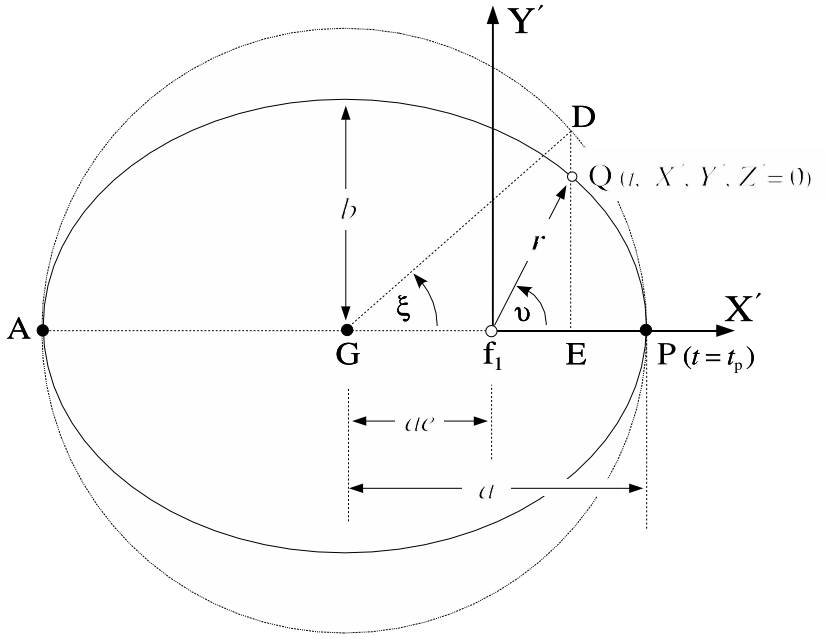

Figure A.2: Construction to determine the eccentric anomaly ξ and expressions for other ellipse parameters. The position of f_1 has been shifted toward **G** so that the various lines and labels are more evenly spaced.

Next, we introduce the auxiliary angle ξ known as the *eccentric anomaly*. This angle is formed as follows: produce an *auxiliary circle* of radius a whose centre is coincident with the geometric centre, **G**, of the ellipse representing the orbit (Fig. A.2). One draws a line from a point **D** on the auxiliary circle to the major axis such that it is normal to the axis at **E** and it also passes through the point where a radius vector meets the ellipse. A second line connecting **G** and **D** subtends the angle ξ with the polar axis. The eccentric anomaly ξ has the same angular range and zero-point as the true anomaly υ.

The ellipse can be thought of as a projection of the auxiliary circle onto another plane rotated about the major axis through an angle

$$\cos\phi = \frac{b}{a} = \frac{\mathbf{EQ}}{\mathbf{ED}} = \frac{Y'}{\mathbf{ED}}\,. \tag{A.26}$$

Consequently $e = \sin\phi$.

A number of useful expressions incorporate ξ. Since $\cos\xi = (ae + X')/a$ and $\sin\xi = \mathbf{ED}/\mathbf{GD} = Y'/b$ (using $\mathbf{ED} = aY'/b$ from Eq. (A.26)), the rectangular coordinates $(X',\, Y')$ can be expressed in terms of ξ as follows

$$X' = a(\cos\xi - e) \qquad \text{and} \qquad Y' = b\sin\xi\,. \tag{A.27}$$

As $X' = r\cos\upsilon$, Eq. (A.23) and the trigonometric identity $\cos^2\psi + \sin^2\psi = 1$ can be used to derive

$$\cos\upsilon = \frac{\cos\xi - e}{1 - e\cos\xi} \tag{A.28a}$$

$$\text{and} \qquad \sin\upsilon = \frac{\sqrt{1-e^2}\sin\xi}{1 - e\cos\xi}\,. \tag{A.28b}$$

Therefore, when $e \neq 0$ the anomalies υ and ξ are only equal at periastron and apastron when $\sin\xi = 0$. When the orbit is circular $\Phi = \upsilon = \xi$.

The equalities in Eq. (A.28) can be re-arranged to give ξ in terms of υ:

$$\cos\xi = \frac{e + \cos\upsilon}{1 + e\cos\upsilon} \tag{A.29a}$$

$$\text{and} \qquad \sin\xi = \frac{\sqrt{1-e^2}\sin\upsilon}{1 + e\cos\upsilon}\,. \tag{A.29b}$$

Finally, a standard trigonometric formula for half-angles in terms of an angle θ is $\tan^2\dfrac{\theta}{2} = \dfrac{1-\cos\theta}{1+\cos\theta}$, can be used to deduce another useful expression relating ξ and υ:

$$\tan\frac{\xi}{2} = \sqrt{\frac{1-e}{1+e}}\tan\frac{\upsilon}{2}\,. \tag{A.30}$$

A.7 Conservation of angular momentum: Kepler's second law

From arguments presented in § A.4.1 we know that the total orbital angular momentum is conserved and from Eq. (A.6) we have $r^2\dot{\upsilon} = J/\mu = \text{constant}$. Since the differential area dA swept out in time $\mathrm{d}t$ is $dA = \frac{1}{2}r^2 d\upsilon$, it follows that

$$\frac{\mathrm{d}A}{\mathrm{d}t} = \frac{1}{2}r^2\dot{\upsilon} = \frac{J}{2\mu} = \text{constant}\,. \tag{A.31}$$

This expression states that the areal velocity is constant. It is the general form of **Kepler's second law** — the radius vector to a planet sweeps out equal areas in equal times. This is a general property of an orbit governed by a central force and is not restricted to an inverse-square law.

The expression for the constant value of J is easily determined. The area swept out by the radial vector $\boldsymbol{r}$ is πab in the time P so that

$$\frac{\mathrm{d}A}{\mathrm{d}t} = \frac{\pi ab}{P}\,, \tag{A.32}$$

and therefore

$$J = \frac{2\pi}{P}\,\mu a^2\sqrt{1-e^2} = \frac{2\pi\,a^2\sqrt{1-e^2}\mathcal{M}_1\mathcal{M}_2}{P(\mathcal{M}_1+\mathcal{M}_2)}\,. \tag{A.33}$$

A.8 Absolute and relative orbits in the orbital plane

The principal reference plane for a binary system is its orbital plane, within which the three true orbits (relative and absolute) lie. The radial distances in the two absolute orbits sum to the radial distance in the relative orbit

$$r = r_1 + r_2 \tag{A.34}$$

for which the apsidal distances are a special case and

$$a = a_1 + a_2\,. \tag{A.35}$$

Consider the two masses $\mathcal{M}_1$ and $\mathcal{M}_2$ orbiting their common barycentre $\mathbf{C}$ at respective distances r_1 and r_2. By the definition of centre of mass

$$\frac{r_1}{r_2} = \frac{\mathcal{M}_2}{\mathcal{M}_1}\,. \tag{A.36}$$

The mass ratio of the orbital system is defined as the ratio of the secondary mass to the primary mass

$$q = \frac{\mathcal{M}_2}{\mathcal{M}_1}\,. \tag{A.37}$$

Therefore the proportions of the radial distances on the respective true orbits are

$$r_1 \;:\; r_2 \;:\; r \;=\; \mathcal{M}_2 \;:\; \mathcal{M}_1 \;:\; (\mathcal{M}_1+\mathcal{M}_2) \;=\; q \;:\; 1 \;:\; (1+q)\,. \tag{A.38}$$

The proportions of the respective semimajor axes are naturally identical:

$$a_1 \;:\; a_2 \;:\; a \;=\; \mathcal{M}_2 \;:\; \mathcal{M}_1 \;:\; (\mathcal{M}_1+\mathcal{M}_2) \;=\; q \;:\; 1 \;:\; (1+q)\,. \tag{A.39}$$

Since the gravitational force is a central force, $\mathcal{M}_1$ and $\mathcal{M}_2$ must always be on opposite sides of the barycentre, always separated according to Eq. (A.38), and completing one orbit in the same time, the orbital period P. Consequently, the eccentricity e of each true orbit will be identical and for convenience, this should also be true of the time of periastron passage T. Similarly, at a given time, the three true orbit values of each of the three angles, υ, ξ and Φ must be equal e.g. $\upsilon = \upsilon_1 = \upsilon_2$.

A.8.1 Orbital speed

In terms of polar coordinates, the orbital speed of the reduced mass μ in the relative orbit $V_{\rm orb} = \|\boldsymbol{v}\|$ according to Eq. (A.5) is

$$V_{\rm orb}^2 = \dot{r}^2 + r^2\dot{\upsilon}^2 \,. \tag{A.40}$$

An expression for $\dot{\upsilon}$ is provided by combining Eq. (A.31) and Eq. (A.32):

$$\dot{\upsilon} = \frac{\mathrm{d}\upsilon}{\mathrm{d}t} = 2\frac{\mathrm{d}A}{\mathrm{d}t}\frac{1}{r^2} = \frac{2\pi ab}{P}\frac{1}{r^2} = \frac{nab}{r^2} \,, \tag{A.41}$$

from which $\dot{r} = \dot{\upsilon}\,\mathrm{d}r/d\upsilon$ can be deduced using the derivative of Eq. (A.23). Therefore

$$V_{\rm orb}^2 = \frac{n^2a^2}{1-e^2}\left(1 + 2e\cos\upsilon + e^2\right) . \tag{A.42}$$

Finally by the substitution for $e\cos\upsilon$ from Eq. (A.23) it is possible to deduce that the total speed in the relative orbit is given by

$$V_{\rm orb}^2 = n^2a^3\left(\frac{2}{r} - \frac{1}{a}\right) . \tag{A.43}$$

Using the proportional relationships of Eq. (A.38) and Eq. (A.39), the orbital speeds with respect to each true orbit can be shown to have the same proportions as do the radial distances in terms of the component masses:

$$V_{\rm orb\,1} \;:\; V_{\rm orb\,2} \;:\; V_{\rm orb} = \mathcal{M}_2 \;:\; \mathcal{M}_1 \;:\; (\mathcal{M}_1 + \mathcal{M}_2) \;=\; q \;:\; 1 \;:\; (1+q) \,. \tag{A.44}$$

A.9 Conservation of energy: Kepler's third law

The total orbital energy E of a pair of bodies in a mutual orbit is given by the sum of the kinetic energy S and the potential energy U. The kinetic energy is

$$\begin{aligned} S &= \frac{1}{2}\mathcal{M}_1 V_{\rm orb\,1}^2 + \frac{1}{2}\mathcal{M}_2 V_{\rm orb\,2}^2 \\ &= \frac{1}{2}\mu V_{\rm orb}^2 \,, \end{aligned} \tag{A.45}$$

which is the kinetic energy of the reduced mass μ in the relative orbit. The orbital speed is given by Eq. (A.43) and the potential energy U of the reduced mass is given by Eq. (A.10) so that

$$E = \frac{1}{2}\mu\, n^2a^3\left(\frac{2}{r} - \frac{1}{a}\right) - \frac{k}{r} \,.$$

Let $W = \mu\, n^2a^3$ to simplify this equality to

$$E = \left(\frac{W-k}{r}\right) - \frac{W}{2a}\,. \tag{A.46}$$

Energy conservation strictly implies $\mathrm{d}E/\mathrm{d}t = 0$. An expression for $\mathrm{d}E/\mathrm{d}t$ can be derived using the chain rule for differentiation:

$$\begin{aligned}\frac{\mathrm{d}E}{\mathrm{d}t} &= \frac{\mathrm{d}E}{\mathrm{d}r} \times \frac{\mathrm{d}r}{\mathrm{d}\upsilon} \times \frac{\mathrm{d}\upsilon}{\mathrm{d}t} \\ &= \left(\frac{k-W}{r^2}\right)\left(\frac{re\sin\upsilon}{1+e\cos\upsilon}\right)\left(\frac{nab}{r^2}\right) \\ &= (k-W)\left(\frac{nabe\sin\upsilon}{r^3(1+e\cos\upsilon)}\right)\,. \end{aligned} \tag{A.47}$$

The solutions to $\mathrm{d}E/\mathrm{d}t = 0$ are $(k-W) = 0$, $e = 0$ and $\sin\upsilon = 0$. The latter two are special cases. The only general solution is

$$k = W = \mu\, n^2 a^3\,, \qquad \text{or}$$

$$P^2 = 4\pi^2\,\frac{\mu}{k}\,a^3\,. \tag{A.48}$$

Eq. (A.48) is the general form of **Kepler's third law** — the squares of the sidereal periods of the planets are proportional to the cubes of the semimajor axes of their orbits. Eq. (A.48) is seen to be not just a consequence of energy conservation. It is the strict criterion that allows the orbital energy to be conserved, as it must for isolated orbital motion [as was shown in § A.4.2 and Eq. (A.9)].

Kepler's third law is an approximation, since it assumes that the proportionality constant is the same for each planet, when in fact it is not. Replacing the constants μ and k using the relations from Eq. (A.2) and Eq. (A.11) brings us to the general form of Kepler's third law for a relative orbit

$$P^2 = \frac{4\pi^2}{G(\mathcal{M}_1+\mathcal{M}_2)}\,a^3\,. \tag{A.49}$$

The true value of the proportionality constant is now seen to be proportional to the system mass, not the primary mass. When the mass ratio q of the orbital system is also known, the masses of the components can be deduced. If the semimajor axis is given in astronomical units (AU) and the period is given in mean solar years the system mass will have solar mass ($\mathcal{M}_\odot$) units

$$\mathcal{M}_1 + \mathcal{M}_2 = \frac{a^3}{P^2}\,\mathcal{M}_\odot\,. \tag{A.50}$$

Having deduced the criterion for energy conservation to hold, it remains to determine the constant value of E. We return to Eq. (A.46) and since $W = k$, the total orbital energy must be

$$E = -\frac{k}{2a} = -\frac{G\mathcal{M}_1\mathcal{M}_2}{2a}\,, \tag{A.51}$$

since $k = G\mathcal{M}_1\mathcal{M}_2$ from Eq. (A.11). Therefore, for a given pair of bound orbiting masses, the total orbital energy depends only on the semimajor axis.

A.10 Kepler's equation

Once an orbital solution has been determined, Kepler's equation provides a means to determine the orbital position in terms of the eccentric anomaly ξ at any time t. Its importance cannot be over-estimated as to determine the orbital position directly in terms of the true anomaly υ, at least until the advent of modern computers, would be an enormous task as will first be shown.

Finding an expression for the time t in terms of the true anomaly is itself a relatively straightforward task. First we substitute the expression for r from Eq. (A.23) into Eq. (A.41) to derive

$$\frac{\mathrm{d}\upsilon}{\mathrm{d}t} = \frac{2\pi}{P}\frac{(1+e\cos\upsilon)^2}{(1-e^2)^{3/2}}\,. \tag{A.52}$$

Inversion of this expression to get the time t in terms of the true anomaly υ leads to one of the standard integral forms. In going from $\upsilon = 0$ at $t = T$ to υ at time t the orbital position changes according to

$$\int_T^t \mathrm{d}t = \frac{P}{2\pi}\int_0^\upsilon \frac{(1-e^2)^{3/2}}{(1+e\cos\upsilon)^2}\,\mathrm{d}\upsilon\,,$$

and therefore

$$t = T + \frac{P}{2\pi}\left\{2\tan^{-1}\left[\sqrt{\frac{1-e}{1+e}}\tan\left(\frac{\upsilon}{2}\right)\right] - \frac{\sqrt{1-e^2}(e\sin\upsilon)}{1+e\cos\upsilon}\right\}\,. \tag{A.53}$$

Deducing υ for a given t is rather more challenging! Only when the orbit is circular does the task become simple since then we have

$$\upsilon = \frac{2\pi}{P}(t-T) = \Phi \qquad (e=0)\,. \tag{A.54}$$

The alternate strategy is to derive an expression for the orbital position in terms of the eccentric anomaly, ξ, for each epoch desired. If we begin with Eq. (A.53) and make substitutions

using Eq. (A.29b) and Eq. (A.30), we immediately derive Kepler's equation, which relates motion in the unit ellipse to motion in the unit circle:

$$t = T + \frac{P}{2\pi}(\xi - e \sin \xi) ,$$

and therefore

$$\frac{2\pi}{P}(t - T) = \Phi = \xi - e \sin \xi . \tag{A.55}$$

We note therefore, that the expression within the curly brackets of Eq. (A.53) equates to the mean anomaly, Φ, but in terms of υ rather than ξ, as is the case for Kepler's equation. Next, if we substitute the expression for $\cos \upsilon$ given in Eq. (A.28a) into Eq. (A.23) we get

$$r = a(1 - e \cos \xi) , \tag{A.56}$$

which will determine (r, ξ) at time t, and with Eq. (A.30) will also determine (r, υ).

Since Kepler (1619) introduced this equation, it has attracted frequent attention over the ensuing three centuries, leading to hundreds of publications relating to various general strategies for its solution[5]. As a brief example, one of the iterative approachs (the strategy employed by Kepler himself) will be described. We guess an approximate solution $\xi_0 = \Phi$ so that the first iteration of

$$\xi_m = \Phi + e \sin \xi_{m-1} ,$$

yields $\xi_1 = \Phi + e \sin \Phi$. Each subsequent iteration results in a more accurate value for ξ and iterations are continued until the desired accuracy is achieved, which is a relatively simple task for a modern computer.

A.11 The sky plane

The restriction of our attention to the orbital plane is not realistic as the stars will be perceived to be in the plane of the sky, which is unlikely to be coincident with the orbital plane. The sky plane is the plane tangential to the celestial sphere and it is here that the stars and orbits appear to be. In each such plane, the absolute and relative orbits are known as apparent orbits.

The research described in this thesis is based primarily on radial-velocity measurements. By definition, the radial velocity of an object is the velocity component along the line of sight,

[5]The derivation of Kepler's equation presented here relies on calculus, which was not presented to the world by Newton and Liebnitz until the late 1600s. Kepler's derivation instead relied upon geometric methods. Colwell (1993) provides a detailed account and divides the many solutions into seven primary categories: geometric, graphical, infinite series, iteration, universal form, diverse methods and parabolic approximation. Five secondary categories of methods of solution are also identified.

whose direction must be normal to the sky plane. The 2-dimensional coordinate system used so far has been satisfactory as the motions considered have been confined to a plane so that the more general 3-dimensional reference frame (X′, Y′, Z′) would always have $Z' = 0$. To allow computation of radial velocities it is now necessary to include the third space dimension (Fig. A.3).

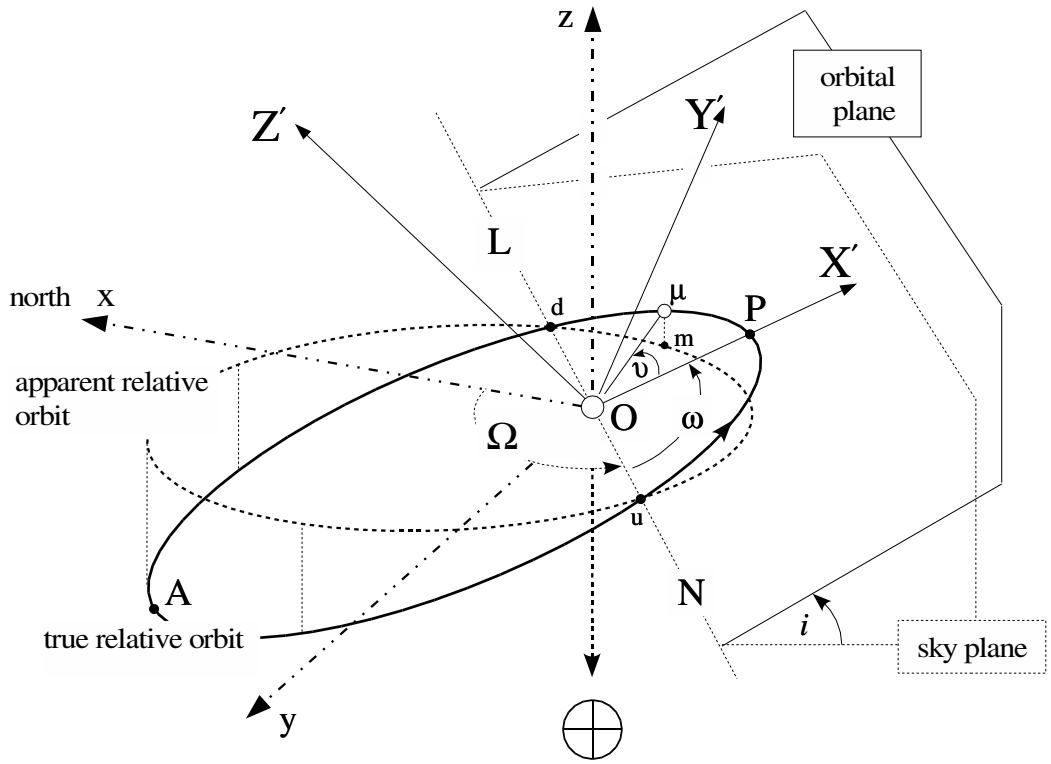

Figure A.3: The relationship of the orbital plane coordinates (X', Y', Z') to the sky plane coordinates (x, y, z). The ascending node **u**, descending node **d**, line of nodes **LN**, and the position angles i, ω and Ω are also identified. The relative orbit illustrated has the reduced mass μ travelling about the fixed system mass which is at the origin **O**.

We create a second 3-dimensional rectangular coordinate system (x, y, z) that has one axis (chosen to be **z**) parallel to the radial direction. We make both rectangular systems right-handed with their origins coincident and the xy-plane coincident with the sky plane. Direct the +**z**-axis away from the observer toward the sky plane so that all radial velocities measured will be consistent with positive doppler shifts being due to receding bodies. The +**x**-axis is chosen to point to the north. The locus of intersection of the orbital plane and the sky plane is the line of nodes **LN**, upon which are the ascending node **u** and the descending node **d**. The ascending node is where the orbiting mass passes through the sky plane in the direction away from the

observer i.e. with positive radial velocity. The descending node is where the orbiting mass passes through the sky plane in the direction toward the observer i.e. with negative radial velocity. For a relative orbit, the line of nodes passes through the system mass $\mathcal{M}_{\rm S}$, whereas for an absolute orbit, the line of nodes will pass through the system's barycentre.

A.11.1 The dynamical and geometric elements

Additional orbital parameters are required to define observations of binary stars whose motions are perceived in the sky plane. These parameters are also needed to define precisely the relationship between the sky plane and the orbital plane. The polar coordinates in the sky plane are the *angular separation* $\rho = \overline{\mathbf{Om}}$ in arcseconds, and the *position angle* θ measured in degrees from north through east with $0 \leq \theta < 2\pi$. When the relative motion is toward increasing position angle θ, the motion is direct or prograde. When the motion is toward decreasing θ, the orbit is retrograde.

To orient the orbital plane with respect to the sky plane in 3-space requires three position angles. The angle subtended by the orbital plane to the sky plane is the orbital *inclination* i. When the orbital motion is direct, $0 \leq i < \pi/2$ whereas when the motion is retrograde, $\pi/2 \leq i \leq \pi$. The longitude of the line of nodes, Ω, is measured in the sky plane from north through east. With only astrometry data available, Ω is ambiguous by 180 degrees. The convention is to chose the ascending node so that $\Omega < \pi$, until radial velocities can resolve the issue[6]. Thus $\Omega = \angle\mathbf{xOd}$ in Fig. A.3. The longitude or position angle of periastron, ω, is measured in the orbital plane from the ascending node **u** to periastron **P** in the direction of motion, with $0 \leq \omega < 2\pi$. A comparison of the relative and absolute orbits will show

$$\omega = \omega_2 = \omega_1 \pm \pi\,. \tag{A.57}$$

By convention, astrometric orbital solutions quote the value $\omega = \omega_2$ since for visual observers the relative orbit is defined as that of the fainter secondary orbiting the primary star. Spectroscopic and photometric orbital solutions usually quote the value of the primary star ω_1 since, typically for SB1 systems, that will be the object dominating the spectrum (Batten 1973).

When $e = 0$ two orbital elements become undefined since peristron is no longer unique. By convention, ω should be taken to be zero, so that the time of periastron passage, T becomes the time of ascending node passage.

The position angles i, ω, and Ω are observer-dependent and are known as the geometric elements. Precession changes Ω and ω. The orbital elements a, e, T, and P are independent of the observer and are known collectively as the dynamical elements.

[6]This is demonstrated for two of the visual binary systems studied in this thesis — HD 206804 (discussed on page 178) and HD 217166 (see page 186).

A.12 Transforming the reference frame of the orbital plane into the sky plane

In view of the likelihood that the orbital plane coordinate system (X', Y', Z') and the sky plane coordinate system (x, y, z) are not coincident, it is useful to be able to transform positions and velocities from one system to the other. Elementary rotation matrix multiplication is one way to achieve this goal. As the necessary rotations are passive i.e. the reference frame is rotated and not the physical object, the general form of the matrix for rotation by angle ψ about the x-axis is

$$\mathsf{R}_x(\psi) = \begin{bmatrix} 1 & 0 & 0 \\ 0 & \cos\psi & \sin\psi \\ 0 & -\sin\psi & \cos\psi \end{bmatrix} .$$

The matrices relevant to rotations about the y- and z-axes can be deduced by symmetry. Analysis of Fig. A.3 will show that one total rotation R_T that rotates the (X', Y', Z') coordinate system into the (x, y, z) system is

$$\mathsf{R}_\mathrm{T} = \mathsf{R}_{\mathrm{Z}'}(-\Omega)\,\mathsf{R}_{\mathrm{X}'}(-i)\,\mathsf{R}_{\mathrm{Z}'}(-\omega)\,, \tag{A.58}$$

where each successive rotation is about the new orientation of the particular axis. Thus

$$\begin{aligned} \mathsf{R}_\mathrm{T} &= \begin{bmatrix} \cos\Omega & -\sin\Omega & 0 \\ \sin\Omega & \cos\Omega & 0 \\ 0 & 0 & 1 \end{bmatrix} \begin{bmatrix} 1 & 0 & 0 \\ 0 & \cos i & -\sin i \\ 0 & \sin i & \cos i \end{bmatrix} \begin{bmatrix} \cos\omega & -\sin\omega & 0 \\ \sin\omega & \cos\omega & 0 \\ 0 & 0 & 1 \end{bmatrix} \\ &= \begin{bmatrix} \cos\Omega\cos\omega - \sin\Omega\sin\omega\cos i & -\cos\Omega\sin\omega - \sin\Omega\cos\omega\cos i & \sin\Omega\sin i \\ \sin\Omega\cos\omega + \cos\Omega\sin\omega\cos i & -\sin\Omega\sin\omega + \cos\Omega\cos\omega\cos i & -\cos\Omega\sin i \\ \sin i\sin\omega & \sin i\cos\omega & \cos i \end{bmatrix} \end{aligned} \tag{A.59}$$

A.12.1 Thiele-Innes constants

The position vectors in the sky plane

$$\begin{bmatrix} x \\ y \\ z \end{bmatrix} = \mathsf{R}_\mathrm{T} \begin{bmatrix} X' \\ Y' \\ Z' \end{bmatrix}$$

allow the relative position of the binary components to be determined on the sky plane using

$$\left.\begin{aligned} x &= \rho\cos\theta = AX + FY \\ y &= \rho\sin\theta = BX + GY \\ z &= CX + HY\,, \end{aligned}\right\} \tag{A.60}$$

where (from Eq. A.27 on page 216)

$$\left.\begin{aligned} X = \frac{X'}{a} = \frac{r\cos\upsilon}{a} &= \cos\xi - e\,, \\ Y = \frac{Y'}{a} = \frac{r\sin\upsilon}{a} &= \sqrt{1-e^2}\sin\xi\,. \end{aligned}\right\} \tag{A.61}$$

The constants *A, B, G, F, C, H* are the Thiele-Innes constants. These are alternatives for the geometric elements (see § A.11.1 on page 224). The Thiele-Innes constants can be produced using the total rotation matrix elements as follows: $A = aR_{\mathrm{T}\,11}$, $B = aR_{\mathrm{T}\,21}$, $F = aR_{\mathrm{T}\,12}$, $G = aR_{\mathrm{T}\,22}$, $C = aR_{\mathrm{T}\,31}$ and $H = aR_{\mathrm{T}\,32}$. For a description of their application see, for example, Binnendijk (1960), or van den Bos (1962).

A.13 The radial velocity

The quantity that attracts our primary attention is $\dot{z}$, the velocity measured in the radial direction. The velocity vectors in the sky plane are

$$\begin{bmatrix} \dot{x} \\ \dot{y} \\ \dot{z} \end{bmatrix} = \mathsf{R}_{\mathrm{T}} \begin{bmatrix} \dot{X}' \\ \dot{Y}' \\ \dot{Z}' \end{bmatrix}\,.$$

Once again we call upon Eq. (A.27), but now the derivatives with respect to time are used:

$$\left.\begin{aligned} \dot{X}' &= -a\dot{\xi}\sin\xi \\ \dot{Y}' &= b\,\dot{\xi}\cos\xi \\ \dot{Z}' &= 0 \qquad\qquad (\text{since} \qquad Z' = 0)\,, \end{aligned}\right\} \tag{A.62}$$

together with an expression for $\dot{\xi}$ provided by the time derivative of Kepler's equation [Eq. (A.55)], namely $\dot{\xi} = n/(1 - e\cos\xi)$. Therefore, the radial velocity is

$$\begin{aligned} \dot{z} &= \dot{X}'\sin i\sin\omega + \dot{Y}'\sin i\cos\omega \\ &= a\sin i\,\dot{\xi}(\sqrt{1-e^2}\cos\xi\cos\omega - \sin\xi\sin\omega) \\ &= \frac{na\sin i}{1-e\cos\xi}\left(\sqrt{1-e^2}\cos\xi\cos\omega - \sin\xi\sin\omega\right)\,. \end{aligned} \tag{A.63}$$

Eq. (A.63) provides a suitably direct route to computer generated values of $\dot{z}$ since ξ can be derived from Kepler's equation and the definition of the mean anomaly Φ [Eq. (A.25)] for any time t. However, it is an otherwise cumbersome expression that can be simplified considerably using Eq. (A.29). As $\dot{z}$ is the radial velocity of the orbiting mass relative to the fixed mass, let $\dot{z} = V_{\mathrm{rel}}$. Then

$$\begin{aligned} V_{\rm rel} &= \frac{na\sin i}{\sqrt{1-e^2}}\Big[e\cos\omega+\cos(\upsilon+\omega)\Big] \\ &= \frac{2\pi a\sin i}{P\sqrt{1-e^2}}\Big[e\cos\omega+\cos(\upsilon+\omega)\Big]\,. \end{aligned} \tag{A.64}$$

The term outside of the main brackets has considerable importance for the radial-velocity function of the relative orbit, since it is its *semi-amplitude*

$$K = \frac{2\pi a\sin i}{P\sqrt{1-e^2}}\,. \tag{A.65}$$

Since a and P are related to the system mass $\mathcal{M}_{\rm S}$ by the general form of Kepler's third law, it is sometimes useful to replace the ratio a/P as follows:

$$K = \frac{2\pi\sin i}{\sqrt{1-e^2}}\sqrt[3]{\frac{\mathcal{M}_{\rm S}}{P}}\,, \qquad \text{and} \qquad K = \frac{2\pi\sin i}{\sqrt{1-e^2}}\sqrt{\frac{\mathcal{M}_{\rm S}}{a}}\,. \tag{A.66}$$

The total semi-amplitude is the sum of the semi-amplitudes of each component:

$$K_1 = \frac{2\pi a_1\sin i}{P\sqrt{1-e^2}} \qquad \text{and} \qquad K_2 = \frac{2\pi a_2\sin i}{P\sqrt{1-e^2}}\,, \tag{A.67}$$

as would be expected since $a = a_1 + a_2$ and the other parameters are the same for the relative and absolute orbits.

The relative radial velocity $V_{\rm rel}$ is also the difference of the respective component radial velocities $V_{\rm r\,1}$ and $V_{\rm r\,2}$, relative to the system's true barycentre

$$V_{\rm rel} = V_{\rm r\,2} - V_{\rm r\,1}\,, \tag{A.68}$$

and are given, in general, by

$$V_{\rm r(}n{\rm)} = K_n\Big[e\cos\omega_n+\cos(\upsilon+\omega_n\Big]\,, \tag{A.69}$$

for $n = 1, 2$. Therefore, $V_{\rm r\,1}$ and $V_{\rm r\,2}$ are the radial velocities of each star due solely to their respective motions in each absolute orbit.

A.13.1 Conservation of linear momentum

Assuming the total external force on the binary system is zero, the total linear momentum of the system is conserved. In particular, since the binary system's properties are invariant under translation along the radial direction, the total linear momentum in the radial direction

is conserved. By choosing a reference frame that moves with the same velocity as the binary system's barycentre, the linear momentum of the two components must sum to zero, i.e. $\mathcal{M}_1 V_{\mathrm{r}\,1} + \mathcal{M}_2 V_{\mathrm{r}\,2} = 0$ and therefore

$$\frac{\mathcal{M}_2}{\mathcal{M}_1} = q = -\frac{V_{\mathrm{r}\,1}}{V_{\mathrm{r}\,2}}\,. \tag{A.70}$$

Eq. (A.68) and Eq. (A.70) make it possible to deduce the proportions of the component and relative radial velocities as has been achieved for other orbital parameters previously:

$$V_{\mathrm{r}\,1} \;:\; V_{\mathrm{r}\,2} \;:\; V_{\mathrm{rel}} \;=\; -\mathcal{M}_2 \;:\; \mathcal{M}_1 \;:(\mathcal{M}_1 + \mathcal{M}_2) \;=\; -q \;:\; 1 \;:\; (1+q)\,. \tag{A.71}$$

Similarly

$$K_1 \;:\; K_2 \;:\; K \;=\; \mathcal{M}_2 \;:\; \mathcal{M}_1 \;:(\mathcal{M}_1 + \mathcal{M}_2) = \;q \;:\; 1 \;:\; (1+q)\,. \tag{A.72}$$

To conclude this section, Eq. (A.70) leads naturally to another expression for the mass ratio in terms of the derivatives with respect to time of the component radial velocities i.e. the instantaneous accelerations α_1 and α_2:

$$q = -\frac{\mathrm{d}V_{\mathrm{r}\,1}/\mathrm{d}t}{\mathrm{d}V_{\mathrm{r}\,2}/\mathrm{d}t} = -\frac{\alpha_1}{\alpha_2}\,. \tag{A.73}$$

The respective accelerations can readily be derived. Since

$$\alpha = \frac{\mathrm{d}V}{\mathrm{d}t} = \frac{\mathrm{d}V}{\mathrm{d}\upsilon} \times \frac{\mathrm{d}\upsilon}{\mathrm{d}t}\,,$$

we get

$$\begin{aligned} \alpha_{1,\,2} &= \pm\, M_{2,\,1} \times \left(\frac{a}{\mathcal{M}_{\mathrm{S}}}\right)\left[\frac{2\pi}{P}\left(\frac{1+e\cos\upsilon}{1-e^2}\right)\right]^2 \sin(\upsilon+\omega)\sin i \\ &= \pm\, M_{2,\,1} \times \left[\left(\frac{2\pi}{a}\right)\left(\frac{1+e\cos\upsilon}{1-e^2}\right)\right]^2 \sin(\upsilon+\omega)\sin i \end{aligned} \tag{A.74}$$

A.13.2 Radial velocities relative to the solar system's barycentre

Relative to the solar system's barycentre, the binary's barycentre is unlikely to be at rest. The difference of these two velocities, which is common to both components, is known as the *systemic velocity* γ of the binary system. The *total centre-of-mass* radial velocity V of each component is therefore

$$V_1 = \gamma + V_{\mathrm{r}\,1} = \gamma - \frac{q}{1+q}\,V_{\mathrm{rel}} = \gamma - \frac{\mathcal{M}_2}{\mathcal{M}_{\mathrm{S}}}\,V_{\mathrm{rel}}$$
$$= \gamma + K_1\Big[e\cos\omega_1 + \cos(\upsilon+\omega_1)\Big]\,; \tag{A.75a}$$

$$V_2 = \gamma + V_{\mathrm{r}\,2} = \gamma + \frac{1}{1+q}\,V_{\mathrm{rel}} = \gamma + \frac{\mathcal{M}_1}{\mathcal{M}_{\mathrm{S}}}\,V_{\mathrm{rel}}$$
$$= \gamma + K_2\Big[e\cos\omega_2 + \cos(\upsilon+\omega_2)\Big]\,; \tag{A.75b}$$

$$\text{and} \qquad \Delta V = V_2 - V_1$$
$$= V_{\mathrm{rel}} = K\Big[e\cos\omega + \cos(\upsilon+\omega)\Big]\,. \tag{A.75c}$$

It is worthwhile to note that, unlike the component velocities, ΔV is independent of the mass ratio.

By multiplying Eq. (A.75b) throughout by q and adding this expression to Eq. (A.75a) a particularly useful relationship is derived that allows measurement, in principle, of q (and γ) based on perhaps minimal orbital phase sampling of the radial-velocity curves of both components:

$$V_1 = -qV_2 + (1+q)\gamma\,. \tag{A.76}$$

This expression represents a straight line with slope $s = -q$ and y-intercept $(1+q)\gamma$. Linear regression applied to a data set with V_2 the independent variable and V_1 the dependent variable will result in values for q and for γ (e.g. see Paddock 1915; Wilson 1941; Irwin 1973). In principle, this method is applicable, so long as V_1 and V_2 are measured for at least two epochs at orbital phases that have different radial velocities for each star respectively. This equation and others related to it are theoretically correct, but simplified owing to the absence of parameters arising from the spectroscopic observations and the measurement process (e.g. convective blueshift and systematic errors). The significance of these additional parameters warrants careful consideration and will be discussed in § A.14.2. The re-arrangement of Eq. (A.76) provides our final elementary expression for q:

$$q = \frac{V_1 - \gamma}{\gamma - V_2}\,. \tag{A.77}$$

A.13.3 Radial-velocity curves

When the expression for V_{rel}, V_1 or V_2, is plotted as a function of υ, the resulting curve will always be a standard sinusoid, velocity-shifted as a result of the constant terms (γ and $e\cos\omega$) and phase-shifted because of ω. However, plotting any of these velocities with respect to time t will create a distorted sinusoid (for $e \neq 0$) as a consequence of the complex relationship of υ to t as expressed in Eq. (A.53). Such curves are known as radial-velocity curves. Various

analytical and graphical methods have been devised to determine most of the parameters of a binary system from its radial-velocity curves (see comments beginning on page 118). The orbital parameters $\mathcal{A} \in \{a,\ a_1,\ a_2\}$ and i appear only in the semi-amplitude term $\mathcal{K} \in \{K,\ K_1,\ K_2\}$ (and not in the bracketed sinusoid term) and consequently their influence is restricted to scaling $\mathcal{K}$. Analysis of a radial-velocity curve can therefore never reveal the true values of $\mathcal{A}$ or $\sin i$ individually. Instead the most that can be deduced is a value for $\mathcal{A} \sin i$.

A.14 Radial-velocity measurements

The radial velocity of a star is typically measured spectroscopically with regard to Doppler shifting of the spectral lines, as is described in § 2.1.3 on page 11. Whilst the *change* in velocity may be measured with high internal precision (e.g. Marcy et al. 1996; Bouchy et al. 2001), the *accuracy* with which the true space-motion, $V_{\rm T}$, can be determined continues to be hampered by the presence of various additional terms that contribute to the velocity zero-point (e.g. Lindegren & Dravins 2003), as will soon be described. Avoidance of many of these terms is possible using one of the various astrometric approaches (e.g. Dravins et al. 1999). Whilst the precision achievable by these methods is considerably less than the best spectroscopic results, the zero point is better defined.

A.14.1 The spectroscopic zero-point velocity

Ideally, any change to λ would be solely due to the Doppler-shift associated with the astrophysical process under investigation. Unfortunately, the measured wavelength of each spectral feature is a result of many influences upon the wavelength, λ, of each corresponding photon depending on how it is modified during its creation, its passage from the star, and its final detection and measurement.

The various contributions to the measured wavelength and the corresponding velocity include: orbital motion as a result of another star, $V_{\rm orb}$, or planet, $V_{\rm pl}$, as well as effects arising in the star's photosphere such as a global convective blueshift, $V_{\rm c}$, and other stellar surface activity or phenomena, $V_{\rm a}$, such as the rotation of unevenly-illuminated stars (e.g. as a result of starspots; Toner & Gray 1988), magnetic fields, macroturbulance and various pulsation mechanisms (Cummings 1998; Chap.2). Other terms that influence λ but are not due to the relative motion of the photon source to the detector include the gravitational redshift, $V_{\rm g}$, at the source, a smaller gravitational blueshift at the detector, and other relativistic effects, $V_{\rm GT}$, which usually will be negligible for local non-degenerate stars (Shapiro & Teukolsky 1983; Lindegren et al. 1999). Pulsating stars will have variable $V_{\rm g}$ inversely proportional to the changing radius of the star. When a velocity is measured relative to a template spectrum which does not have a zero-velocity, a difference term, $V_{\rm diff}$ will arise. Finally, systematic errors are a feature of all measurements, and there are many, which may occur when measuring a radial velocity. For instance, inclusion of blended lines, mismatch of the spectral type of the programme and tem-

plate images (Hill 1993), and the use of non-ideal spectrographic and detection systems which introduce an instrument profile to the spectral lines.

A.14.2 Application to binary stars

In the study of binary stars, we would prefer that all of the processes contributing to a velocity measurement that are *not* a result of motion of the star's centre of mass due to a single stellar companion, would be individually measurable, negligible or cancel each other so as to remove their influence. The combined contribution that the extra terms make to the measured velocity, V, can be collectively labelled with $V_{\rm X}$ (i.e. $V_{\rm X} = V_{\rm c} + V_{\rm g} + \dots$). When radial velocities are measured relative to a template spectrum, ideally, all of the terms making up $V_{\rm X}$ are constant, so that any change to the relative velocity measured for $V_{\rm orb}$ is a true measure of the changing motion of the star's centre of mass. The measured systemic velocity for a particular star, γ', will be $\gamma' = \gamma + V_{\rm X}$. In an SB2 system, it would be realistic to believe that $V_{\rm X1} \neq V_{\rm X2}$, and therefore

$$\begin{aligned} V_1 &= \gamma + V_{\rm X1} + V_{\rm orb1} = \gamma'_1 + V_{\rm orb1} \\ V_2 &= \gamma + V_{\rm X2} + V_{\rm orb2} = \gamma'_2 + V_{\rm orb2}\,, \end{aligned} \tag{A.78}$$

where $\gamma'_1 \neq \gamma'_2$, provided that the spectroscopic orbital solution and γ' of each star is derived independently of the other. The difference in the values for γ' is $\gamma'_2 - \gamma'_1 = V_{\rm X2} - V_{\rm X1}$.

The systematic error in the measured zero-point of any radial-velocity curve is not, though, limited to the $V_{\rm X}$-term, even if it is constant. Inherent in the orbital solution are the systematic errors for the orbital elements. These also shift the measured value of γ, as fixing all parameters other than γ to a variety of values for a spectroscopic solution (e.g. by differential corrections) for a given series of velocities will readily show[7].

The mass ratio

For an SB1 system, the system's mass ratio q can be estimated with the aid of a corresponding astrometric solution and parallax, but the sytematic errors in the elements will lead to an inaccurate measure of q as well (as is demonstrated by Eq. (3.9) on page 25). One of the considerable advantages of observing SB2 systems is that q can be measured independently of the orbital elements, such as by deriving the linear regression of the component velocities using Eq. (A.76).

If we consider Eq. (A.78) and the corresponding straight lines ($\rm L'_1$ and $\rm L'_2$ shown in Fig. A.4, it is evident that, given no systematic errors in the elements, the difference of the slopes of the

[7] A geometric perspective can also be used to understand the expected shift in γ to various γ'. Each value for γ' must divide the corresponding radial-velocity curve into two sections of equal area, one representing the star in approach, and the other with the star in recession (as defined by Kepler's second law). As the shape of the curve changes with the systematic errors included for all of the elements, it will be typical that the dividing line $V = \gamma'$ will move accordingly.

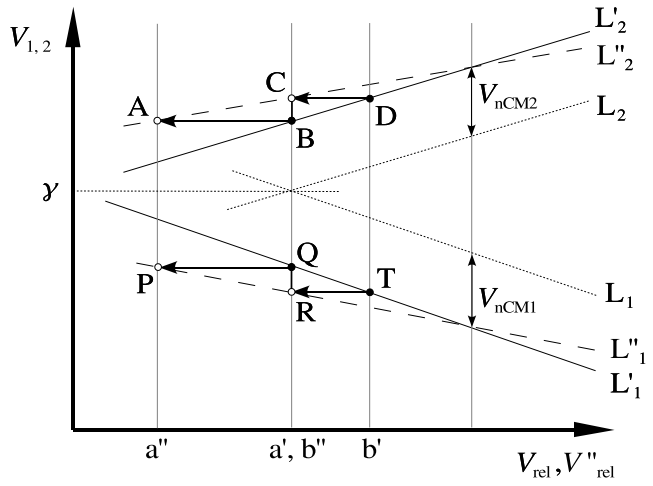

Figure A.4: The theoretical L-lines, the L′-lines shifted by the respective $V_{\rm X}$-terms, but with no systematic errors in the orbital elements (solid circles at a' and b') shifted to the L″-lines as a result of systematic errors (open circles are 'observations' at a″ and b″). The various lines correspond to a series of velocities, V_1 and V_2, and an astrometric orbital solution.

two lines, $s'_1 = s_1 = -q/(1+q)$ and $s'_2 = s_2 = 1/(1+q)$, will be $s'_2 - s'_1 = 1$, and their ratio will be $s'_1/s'_2 = -q$, regardless of the values of $V_{\rm X}$, so long as the latter are assumed to be constant.

However, when the elements are inaccurate, these lines will shift due to the variable systematic error affecting $V_{\rm rel}$, leading to $V''_{\rm rel}$ and the corresponding L″-lines. The slopes will change and typically $s''_2 - s''_1 \neq 1$, so that $q''_1 \neq q''_2$. As computer simulations and consideration of the geometry of Fig. A.4 will demonstrate, the ratio of the slopes of the shifted lines will still be $s''_1/s''_2 = -q$, since the influence of the inaccurate orbital elements is removed in this calculation: in Fig. A.4, since AB = PQ, we have $s'_1 = {\rm QR/AB}$, $s'_2 = {\rm BC/AB}$ and therefore $s''_1/s''_2 = {\rm QR/BC}$. Similarly, since CD = RT, $s_1/s_2 = {\rm QR/BC}$ also. Therefore,

$$\frac{s''_1}{s''_2} = \frac{s_1}{s_2} = -q\,. \tag{A.79}$$

We can re-arrange this pair of ratios to get

$$\frac{s''_1}{s_1} = \frac{s''_2}{s_2} = \text{constant, say } \beta, \tag{A.80}$$

where β is the factor that relates s and s''. Thus, β estimates the proximity of s'' to s and hence q'' to q. Combining these last two equations leads to an expression that allows β to be measured

for SB2 systems with an astrometric solution and known parallax:

$$\beta = s_2'' - s_1'' \,. \tag{A.81}$$

The parameter β acts as an objective estimate of the consistency of the orbital elements and the measured radial velocities. When β is applied to each calculation of $V_{\rm rel}''$, the value for $s_2'' - s_1'' \to 1$.

The systemic velocity

The y-intercept of each star's L′-line is $V = \gamma'$. When we take account of the systematic errors in the elements, the change of slope $s \to s''$ is also just as likely to shift the y-intercept as well, so that $\gamma \to \gamma'$ as a result of the $V_{\rm X}$-terms, and $\gamma' \to \gamma''$ as a result of the systematic errors in the orbital elements. The vertical line labelled (a′, b″) in Fig. A.4 corresponds to the y-axis since it is where L_1 and L_2 meet at $V = \gamma$. B and Q are on the lines $V = \gamma_2'$ and $V = \gamma_1'$ respectively, and C and R are on the lines $V = \gamma_2''$ and $V = \gamma_1''$ respectively. If we label CD = RT = ϵ, it follows that

$$\gamma_1'' = \gamma_1' + s_1\epsilon \qquad \text{and} \qquad \gamma_2'' = \gamma_2' + s_2\epsilon \,, \tag{A.82}$$

and expressions that more closely describe real radial-velocity measurements are

$$V_1 = \gamma_1'' + s_1'' \, V_{\rm rel}'' \qquad \text{and} \qquad V_2 = \gamma_2'' + s_2'' \, V_{\rm rel}'' \,. \tag{A.83}$$

The spectroscopic measurement of the zero-point velocity for each star is restricted to γ_1'' and γ_2'' respectively, and these will probably differ. The *measured common* zero-point velocity, $V_{\rm Z}$, is derived by equating the two expressions in Eq. (A.83), so that

$$\begin{aligned} V_{\rm Z} &= s_2\gamma_1'' - s_1\gamma_2'' \\ &= s_2\gamma_1' - s_1\gamma_2' \\ &= \gamma + s_2 V_{\rm X1} - s_1 V_{\rm X2} \\ &= \gamma + \frac{1}{1+q} V_{\rm X1} + \frac{q}{1+q} V_{\rm X2} \\ &= \text{constant} \,, \end{aligned} \tag{A.84}$$

regardless of any systematic errors in the orbital elements, assuming as before, the $V_{\rm X}$-terms are constant.

Based on these ideas, Eq. (A.76) can be re-expressed as follows:

$$\begin{aligned} V_1 &= -qV_2 + V_{\rm Z}(1+q) \\ &= -qV_2 + \Big[\gamma(1+q) + V_{\rm X1} + qV_{\rm X2}\Big]\,, \end{aligned} \tag{A.85}$$

which provides a better understanding of the true nature of the y-intercept of the linear equation that relates the meaured values of V_1 and V_2.

A.15 Estimating the convective blueshifts of stars

If the equality $s_2 - s_1 = 1$ is used to equate the two expressions in Eq. (A.82), we can derive

$$\begin{aligned} \Delta V_{\rm X} &= V_{\rm X2} - V_{\rm X1} \\ &= \gamma''_2 - \gamma''_1 - \epsilon\,. \end{aligned} \tag{A.86}$$

When $\Delta V_{\rm X} \neq 0$, as when the components of a binary system differ in various ways, as will be typical, we are provided the opportunity to estimate the difference between certain pairs of the contributing $V_{\rm X}$-terms, owing to the fact that some of the terms can be calculated (for example, the gravitational redshift, $V_{\rm g}$ from the mass and radius), and others may be assumed to be negligible or sufficiently similar that their difference will be zero (for example, the surface activity term as a result of other spectro-photometric observations).

One term that lends itself to such a measurement is that for the convective blueshift, $\Delta V_{\rm c}$. Since the final result is expected to be no more than a few hundred metres per second, the radial-velocity measurements must be of very high precision. If adequate orbital-phase sampling is achieved both spectroscopically and astrometrically, the necessary measurements should allow a high-precision orbital solution to be derived. The necessary assumptions that must be made are that all other difference pairs of terms are zero, and, that $\epsilon = 0$ also (or at least that these remaining terms sum to zero). For a high-precision orbital solution it seems reasonable to assume that $\beta \sim 1$ and therefore assuming $\epsilon = 0$ may be considered justified.

Ideas similar to these have been applied to the closest stellar system to us, that of α Cen AB (Pourbaix et al. 2002). Based upon assumptions as outlined above, and with the help of a high-precision spectroscopic-astrometric orbital solution and corresponding radial velocities for both components, the convective blueshift difference for these two stars has been measured to have an upper bound of about $+110\,{\rm m\,s^{-1}}$. This positive value implies that the K1V secondary star has a smaller convective blueshift than the later G-type primary star, just as is predicted theoretically (Dravins & Nordlund 1990).

The only star that has a measured convective blueshift is the Sun, $V_{\rm c} \sim -300\ {\rm m\,s^{-1}}$ (Dravins 1999). Therefore, if the difference measured is for a binary that includes a solar-type star, the

solar value can be used to estimate the convective blueshift corresponding to the non-solar companion. α Cen A is similar to the Sun, though it is slightly more massive, $\mathcal{M} \approx 1.1\,\mathcal{M}_{\odot}$ and evolved. However, the calculation gives the lower bound for the convective blueshift for α Cen B to be about $V_{\mathrm{c},\,2} \sim +110 - 300 = -190\,\mathrm{m\,s^{-1}}$. This estimate is also in excellent agreement with the theoretical value for K-dwarf stars, namely $-200\,\mathrm{m\,s^{-1}}$ (Dravins & Nordlund 1990).

The natural progession is to estimate the convective blueshift differences of as many binary systems as possible that include a solar-type component (e.g. G2V+F9V, G2V+G8V and so on), estimate the convective blueshift for each companion, and determine the distribution of this important astrophysical quantity across the H-R diagram. Confidence in this approach may be justified if consistency is found between the different systems studied. An additional test of this methodology would be to measure ΔV_{c} for binary pairs that link non-solar types, for instance, G7V and K1V. When a sufficiently large sample of measures of ΔV_{c} and V_{c} becomes available, it may be possible to use any discrepancies that arise to estimate the values of other ΔV_{X}-terms that were previously rejected from the calculations. Unfortunately, the α Cen system is not typical of most binary systems. In particular, each star can have its spectrum recorded independent of its companion so that the complexity of blended spectra is avoided. New analytical techniques aimed at blended spectra, such as TODCOR (see comments in § 6.2 on page 109), give the promise that this challenge can be met.

Appendix B

Preliminary results for θ Ant, 94 Aqr A, HD 10800 and HD 118261

θ Antliae (HD 84367 HIP 47758; $9^{\rm h}44^{\rm m}12^{\rm s}, -27°46^{\rm m}10^{\rm s}$)

θ Ant is a visual binary ($4\overset{\rm m}{.}8$ and $5\overset{\rm m}{.}7$) with a composite spectrum, possibly A7V+F2II-III (Houk 1982), A8m+G7III (Ginestet & Carquillat 2002), or both components could be giants (Heintz 1982). The 60 velocities of HD 84367 were measured with respect to a single high S/N spectrum of itself and are listed in Table C.7 Appendix C. The complex nature of spectra of this type should be remembered when considering this preliminary analysis. The spectroscopic orbital solution relied on fixing the period to the value derived for the visual orbit, $P = 18.29$ years (Mason & Hartkopf 1999). This parameter should be reasonably accurate as the astrometric solution has been assigned to grade 2 (Hartkopf & Mason 2004), hence, no major changes to the solution are expected to be required in the future. This is the first spectroscopic orbital solution estimated for this system.

94 Aquarii A (HD 219834 HIP 115126; $23^{\rm h}19^{\rm m}7^{\rm s}, -13°27^{\rm m}31^{\rm s}$)

94 Aquarii A (G5IV+G0-G2V; $5\overset{\rm m}{.}2$) is the primary star of the wide ($\rho \sim 13''$) physical pair ADS 16672. 94 Aqr B is a K2-dwarf. The radial velocity variability of 94 Aqr A was discovered by Campbell in 1922. The only spectroscopic orbital solution of it published to date was derived by Sarma (1962). The probable error of a single velocity was reported to be 1.2 $\mathrm{km\,s^{-1}}$. Resolution of the components was first achieved with interferometric observations by McAlister (1978). The first astrometric orbital solution soon followed (McAlister & Hartkopf 1982; grade 2, Hartkopf & Mason 2004).

A spectroscopic orbital solution (Table B.3, Table B.4, Fig. B.2), could not be derived from the 36 Hercules velocities (Table C.8) without fixing at least one orbital element. The element chosen for this task was the period. A mean period was derived according to the strategies outlined in § 6.9 on page 123, by comparing the time of ascending node passage of the Hercules velocities to the epoch associated with Sarma's (1962) solution. There are nine complete orbital cycles between these two epochs. The error estimated for the period is considered to be adequately determined by using the modern computation for the error in P from the historical observations: $\sigma_P \approx 17\,\mathrm{d}/9$. The mean period was found to be $\bar{P} = 2\,309.6 \pm 1.9$ days, or 6.323 ± 0.005 years, which agrees well with the astrometrically derived one.

Table B.1: Left: The spectroscopic orbital solution for θ Ant derived from HERCULES observations with the period fixed. Right: The astrometric orbital solution. No errors were reported. Ω is in the correct quadrant. T and ω_1 are in reasonable agreement.

P	=	18.29 years (fixed) $\rightarrow$	P	=	18.29 years
T	=	2002.685 ± 0.0044	T	=	1965.74
e	=	0.5283 ± 0.0026	e	=	0.466
ω_1	=	$144\overset{\circ}{.}46 \pm 0.27$	ω	=	316°
K_1	=	7.867 ± 0.058 km s^{-1}	a''	=	123 mas
$a_1 \sin i$	=	4.105 ± 0.038 AU	i	=	123°
$f_{\mathcal{M}}$	=	$2.069 \pm 0.058 \times 10^{-1}\,\mathcal{M}_\odot$	Ω	=	$174\overset{\circ}{.}5$

$\gamma_{\rm rel}$	=	$+25.203 \pm 0.077$ km s^{-1}	γ	=	$+21.925 \pm 0.080$ km s^{-1}
p''	=	8.49 ± 0.73 mas	a	$\approx$	14.5 AU
q	$\approx$	0.5	$\mathcal{M}_{\rm S}$	$\approx$	$9.1\,\mathcal{M}_\odot$

Table B.2: Additional parameters for the θ Ant system.

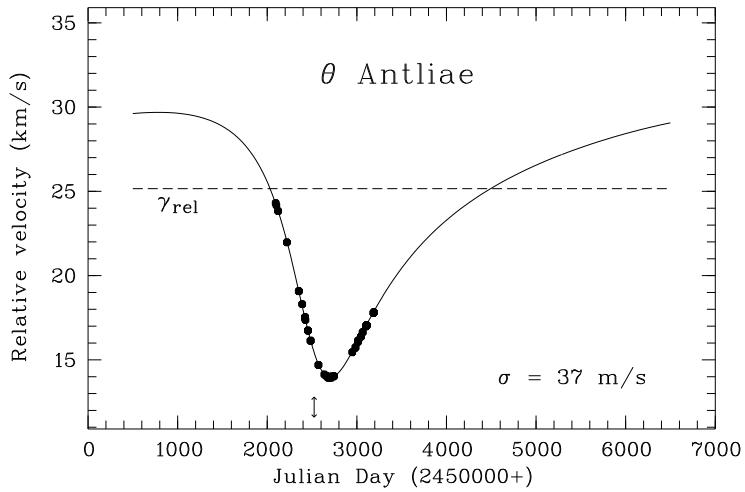

Figure B.1: The radial velocities (2001 July 3 to 2004 August 2), and curve corresponding to the spectroscopic orbital solution, for θ Ant. The '$\updownarrow$' symbol represents a time of periastron passage.

Table B.3: Left: The spectroscopic orbital solution for 94 Aqr A derived from HERCULES observations with the period fixed. The non-circularity of the orbit is confirmed. Right: The astrometric orbital solution (McAlister 1982). T and ω differ significantly for the two solutions, even if the astrometric $\omega \equiv \omega_1$.

P	=	6.323 years (fixed; see text)	P	=	6.216 ± 0.080 years
T	=	2006.531 ± 0.062	T	=	1980.840 ± 0.024
e	=	0.198 ± 0.018	e	=	0.185 ± 0.012
ω_1	=	$234\overset{\circ}{.}0 \pm 1.7$	ω	=	$209\overset{\circ}{.}3 \pm 1.9$
K_1	=	6.16 ± 0.26 km s^{-1}	a''	=	180 ± 3 mas
$a_1 \sin i$	=	1.284 ± 0.050 AU	i	=	$47\overset{\circ}{.}6 \pm 1.7$
$f_{\mathcal{M}}$	=	$5.31 \pm 0.63 \times 10^{-2}\,\mathcal{M}_\odot$	Ω	=	$170\overset{\circ}{.}3 \pm 1.9$

$\gamma_{\rm rel}$	=	$+25.16 \pm 0.10$ km s^{-1}	γ	=	$+10.12 \pm 0.17$ km s^{-1}
p''	=	48.22 ± 5.25 mas	a	=	3.73 ± 0.41 AU
q	=	0.87 ± 0.08	$\mathcal{M}_{\rm S}$	=	$1.30 \pm 0.43\,\mathcal{M}_\odot$

Table B.4: Additional parameters for the 94 Aqr A system. The uncharacteristic total mass for the system, $\mathcal{M}_{\rm S}$, predicts equally implausible masses, $\mathcal{M}_1 = 0.7 \pm 0.2\,\mathcal{M}_\odot$ and $\mathcal{M}_2 = 0.6 \pm 0.2\,\mathcal{M}_\odot$, for the G5IV+G0-G2V components.

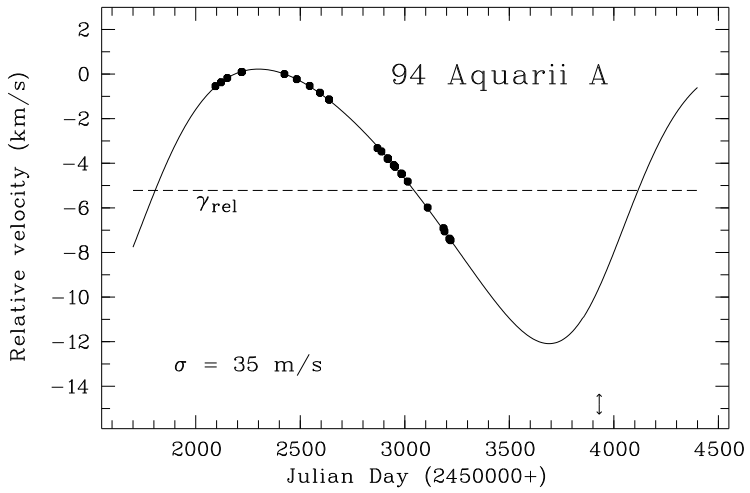

Figure B.2: The radial velocities (2001 July 3 to 2004 August 1) and curve corresponding to the spectroscopic orbital solution for 94 Aqr A. The '↕' symbol represents a time of periastron passage.

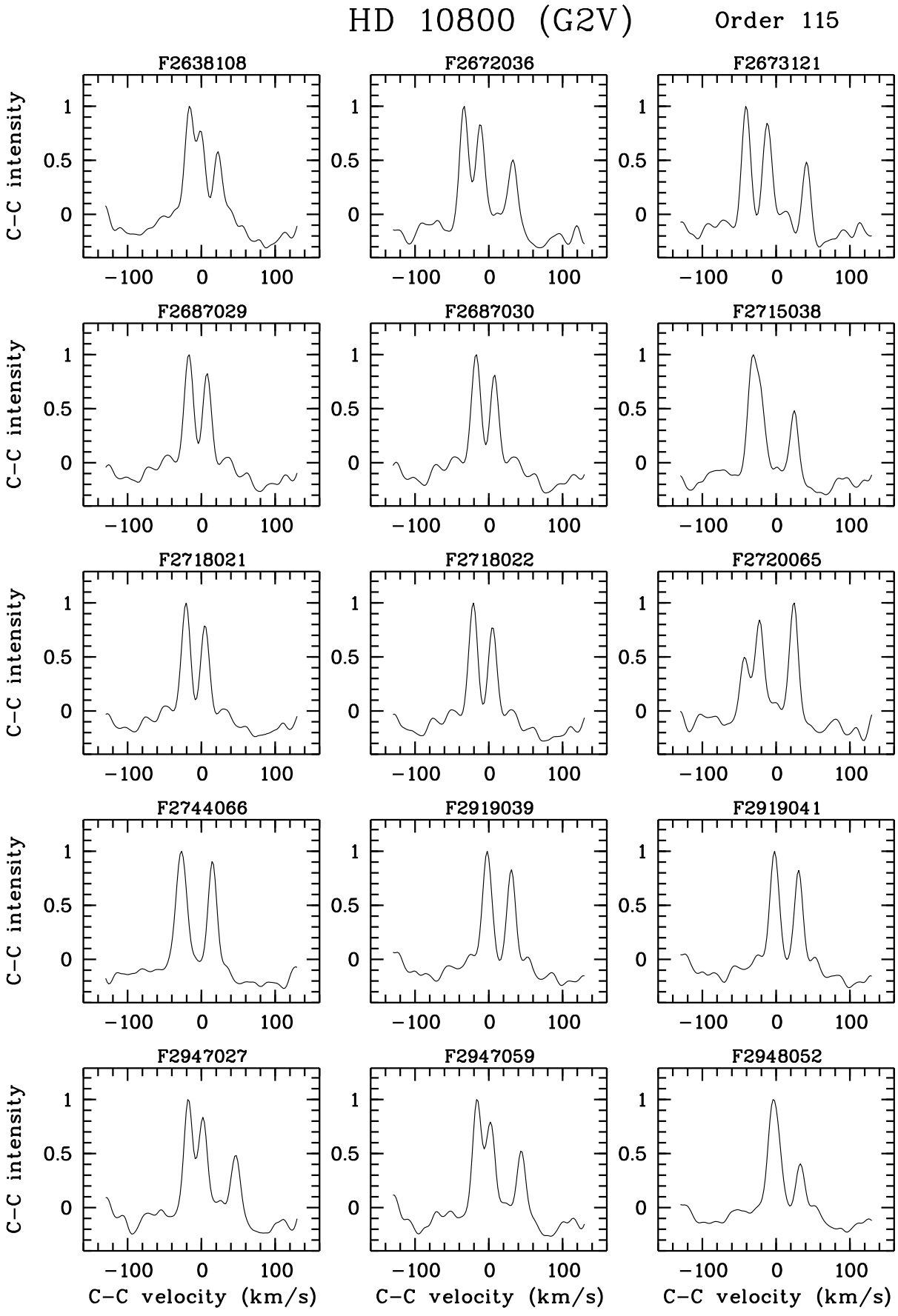

Figure B.3: Cross-correlation functions for HD 10800 (*first series*)

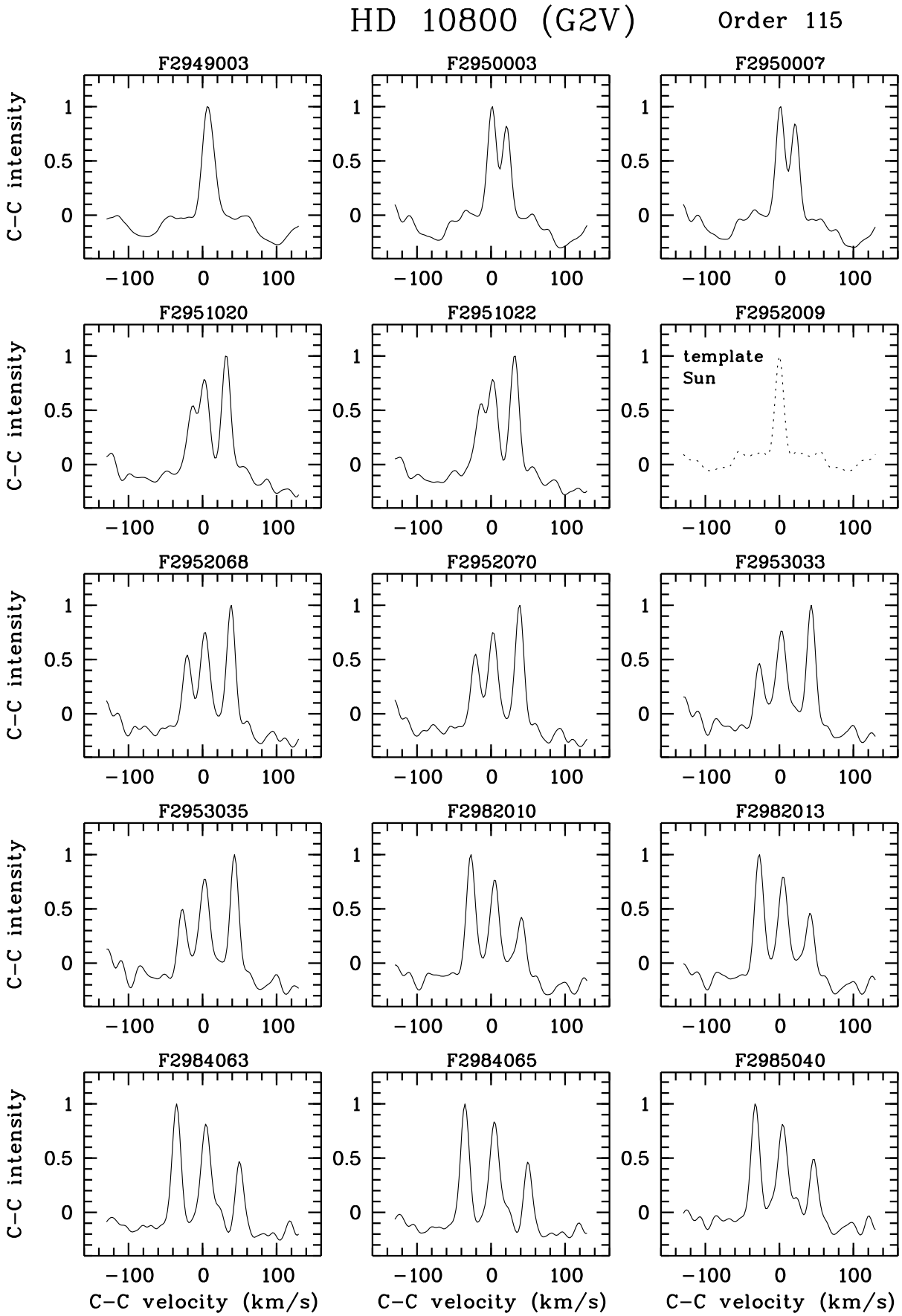

Figure B.4: Cross-correlation functions for HD 10800 (*second series*)

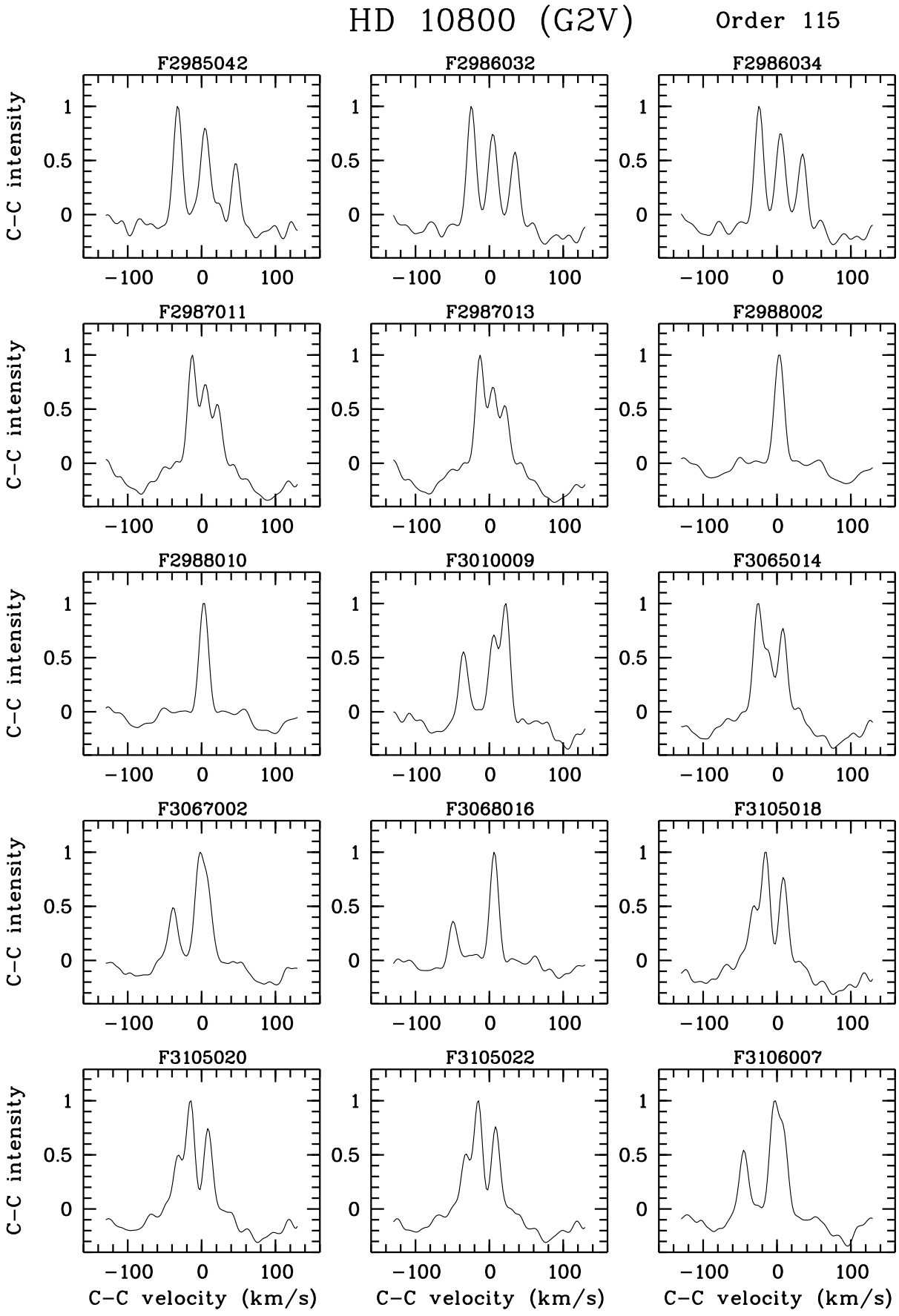

Figure B.5: Cross-correlation functions for HD 10800 (*third series*)

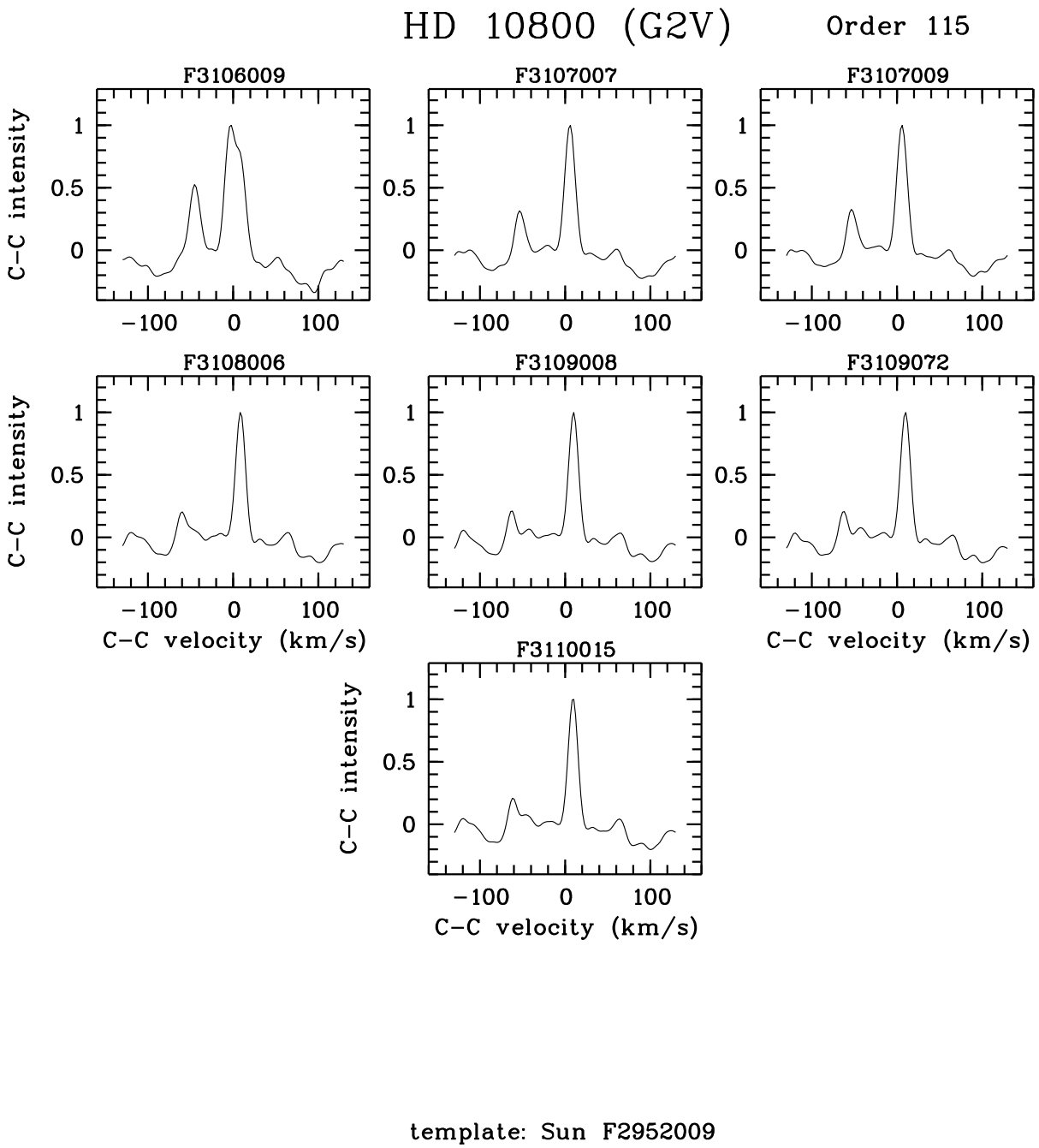

Figure B.6: Cross-correlation functions for HD 10800 (*last series*)

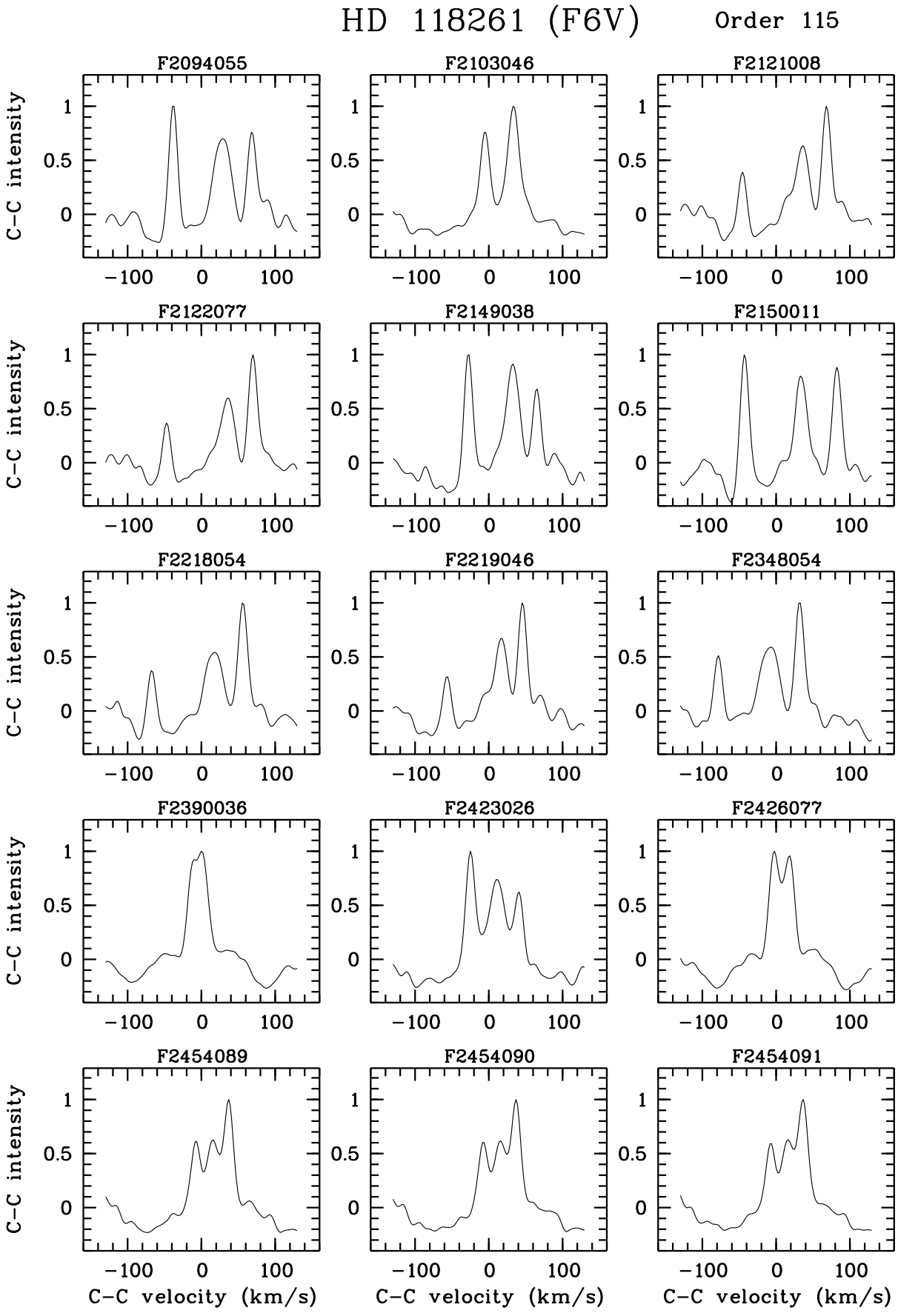

Figure B.7: Cross-correlation functions for HD 118261 (*first series*)

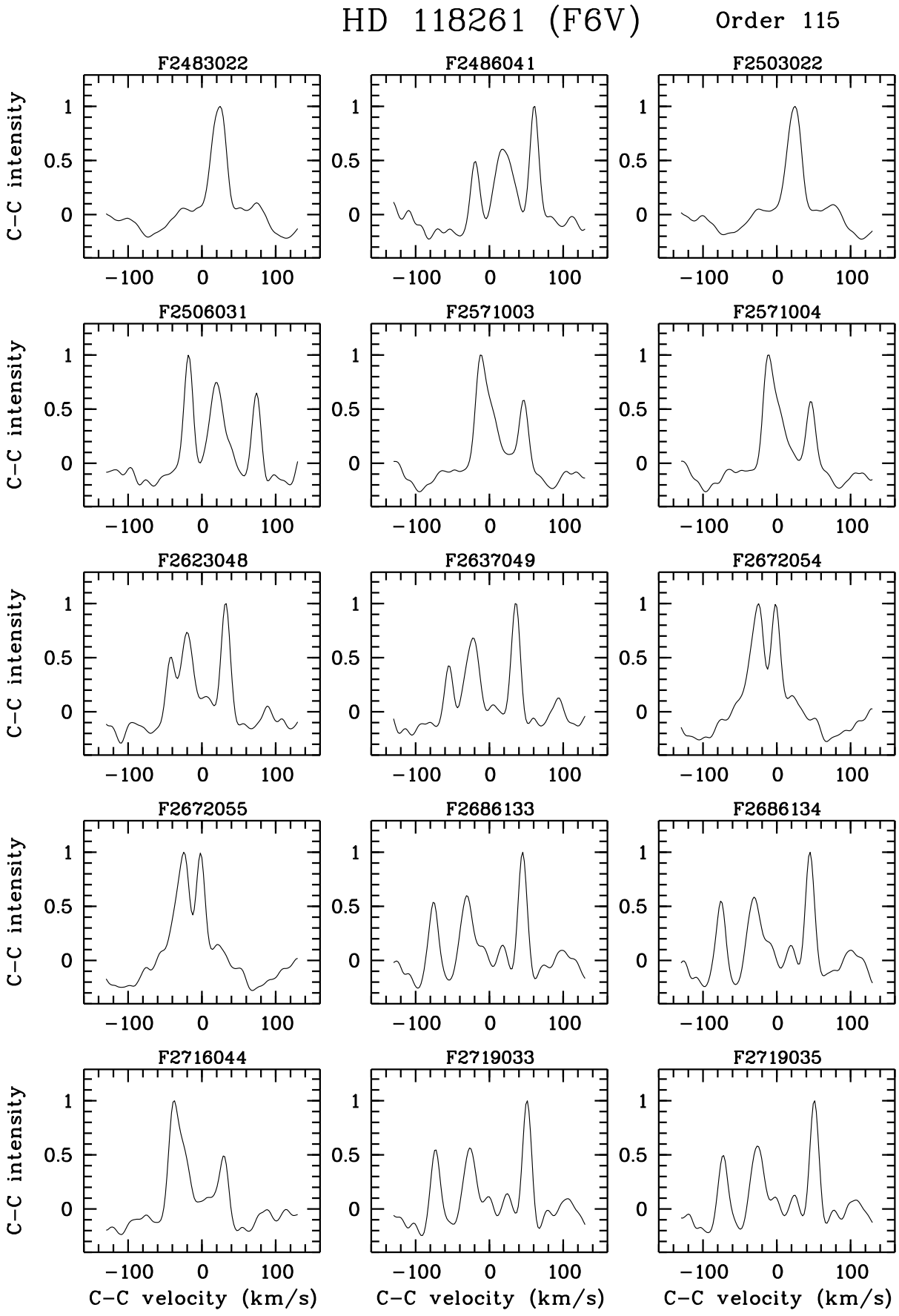

Figure B.8: Cross-correlation functions for HD 118261 (*second series*)

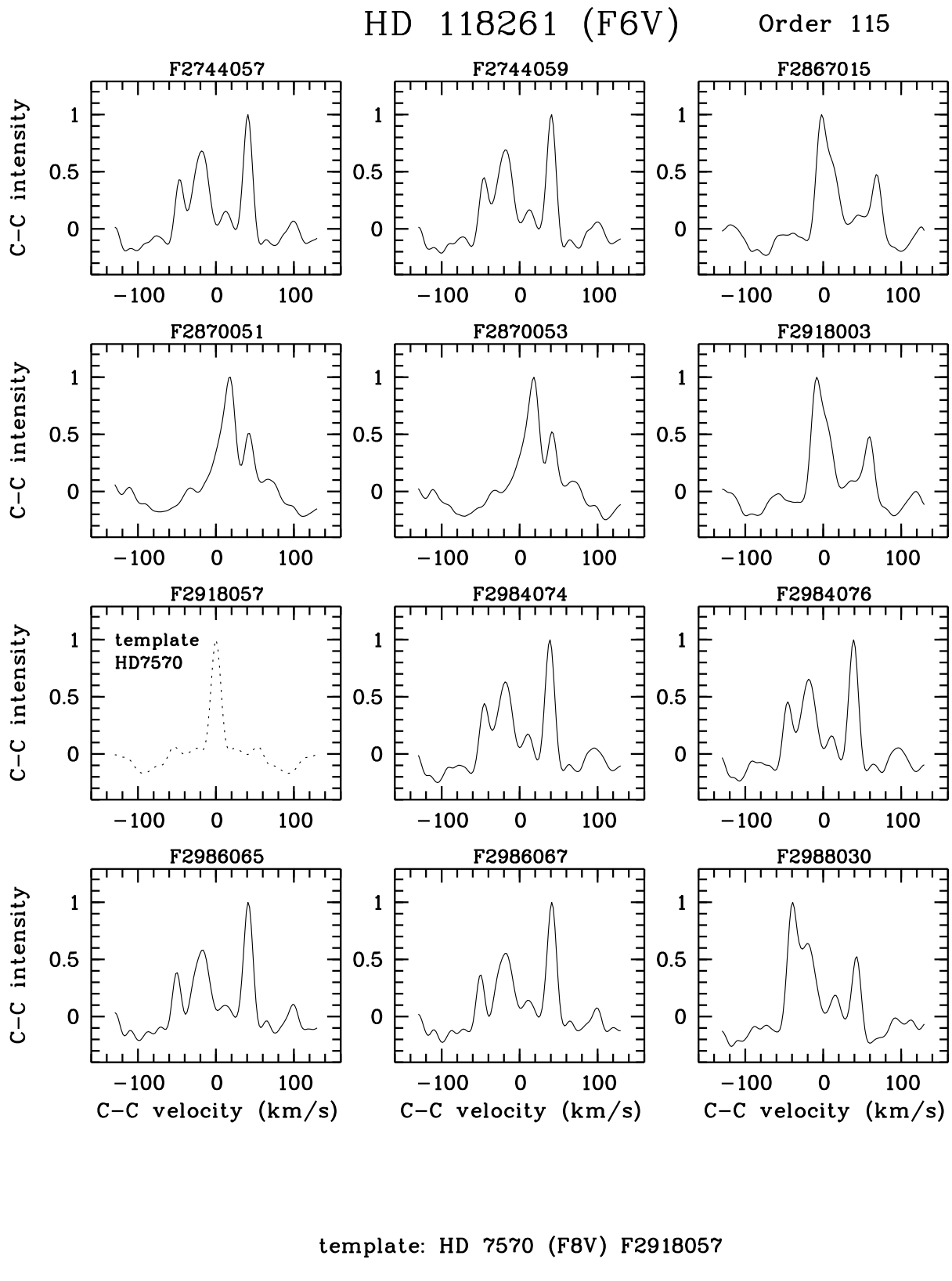

Figure B.9: Cross-correlation functions for HD 118261 (*last series*)

Appendix C

Radial velocities and orbit-fit residuals

Table C.1: Relative velocities and residuals of β Reticuli

Julian Day (245 . . .)	Radial velocity (km s^{-1})		Julian Day (245 . . .)	Radial velocity (km s^{-1})	
	relative	residual		relative	residual
2065.16447	−1.859	−0.002	2744.85462	5.241	−0.006
2094.74535	−1.558	0.038	2744.86276	5.247	−0.001
2102.21675	−1.543	−0.015	2806.04410	4.190	0.017
2151.21477	−1.041	0.023	2806.05014	4.185	0.012
2181.13573	−0.830	−0.068	2806.09937	4.187	0.015
2218.99760	−0.357	0.002	2867.19593	2.382	−0.064
2312.01308	0.745	0.006	2867.20144	2.380	−0.066
2349.98227	1.222	−0.010	2870.09485	2.371	0.015
2389.82433	1.803	0.023	2870.09761	2.374	0.018
2422.79217	2.305	0.053	2888.25297	1.779	−0.004
2425.74663	2.292	−0.003	2888.25682	1.798	0.016
2453.77932	2.744	0.034	2918.10842	0.880	0.033
2453.78182	2.729	0.019	2918.11155	0.878	0.032
2484.10614	3.155	−0.012	2918.97455	0.789	−0.031
2484.10866	3.126	−0.041	2918.97830	0.795	−0.025
2484.11145	3.107	−0.060	2918.98203	0.792	−0.027
2503.12943	3.471	0.016	2947.08906	−0.039	−0.018
2549.01606	4.132	−0.007	2947.09433	0.000	0.021
2570.11768	4.433	−0.005	2949.15276	−0.068	0.012
2570.11989	4.427	−0.011	2951.09891	−0.143	−0.008
2592.05218	4.737	0.007	2951.10242	−0.139	−0.003
2592.05427	4.752	0.022	2984.13535	−1.000	0.025
2622.91411	5.074	−0.014	2984.13947	−1.001	0.024
2622.91629	5.081	−0.007	2985.05643	−1.018	0.030
2637.05947	5.216	−0.007	2985.06355	−1.002	0.046
2670.90579	5.456	0.006	2987.93169	−1.112	0.009
2687.02467	5.494	−0.003	2987.93710	−1.111	0.009
2687.02893	5.497	−0.000	3010.03041	−1.650	−0.006
2687.03494	5.496	−0.001	3010.03292	−1.657	−0.014
2716.88510	5.487	0.030	3015.08799	−1.759	−0.003

continued on next page

Table C.1: Relative velocities and residuals of β Reticuli, *continued*

Julian Day (245 . . .)	Radial velocity (km s^{-1})		Julian Day (245 . . .)	Radial velocity (km s^{-1})	
	relative	residual		relative	residual
3015.09003	−1.751	0.005	3106.90870	−3.344	0.001
3016.11041	−1.782	−0.004	3107.94698	−3.376	−0.017
3016.11568	−1.787	−0.008	3107.94876	−3.371	−0.013
3024.90648	−1.985	−0.019	3108.80465	−3.378	−0.008
3046.02518	−2.379	0.005	3108.80689	−3.383	−0.014
3047.08656	−2.421	−0.017	3109.81084	−3.402	−0.020
3047.09139	−2.413	−0.009	3109.81245	−3.402	−0.020
3065.07514	−2.738	−0.015	3185.29753	−4.125	0.012
3065.07851	−2.714	0.009	3185.30163	−4.131	0.007
3068.92807	−2.765	0.021	3190.16811	−4.172	0.001
3068.92981	−2.781	0.006	3190.17219	−4.172	0.002
3104.81482	−3.262	0.055	3214.27584	−4.348	−0.016
3104.81696	−3.259	0.058	3214.27897	−4.352	−0.020
3105.00502	−3.352	−0.032	3217.20494	−4.341	0.008
3105.00734	−3.349	−0.029	3217.20791	−4.344	0.006
3105.92066	−3.346	−0.014	3219.24949	−4.348	0.013
3105.92314	−3.358	−0.026	3219.25129	−4.341	0.020
3106.90425	−3.344	0.001			

Table C.2: Relative velocities and residuals of ν Octantis

Julian Day (245 . . .)	Radial velocity (km s^{-1})		Julian Day (245 . . .)	Radial velocity (km s^{-1})	
	relative	residual		relative	residual
2102.11054	−2.475	−0.004	2505.80034	−11.249	0.042
2121.08905	−3.682	−0.004	2545.09414	−10.459	0.014
2180.88311	−7.812	−0.038	2569.07469	−9.892	0.043
2219.89978	−9.984	0.062	2569.07853	−9.886	0.049
2220.99555	−10.043	0.058	2592.07569	−9.352	0.043
2312.94321	−12.836	0.004	2592.07889	−9.353	0.043
2351.99649	−13.135	−0.060	2600.87444	−9.145	0.039
2351.99977	−13.132	−0.058	2600.87677	−9.152	0.032
2390.81679	−13.016	−0.073	2600.87905	−9.145	0.039
2423.86960	−12.663	−0.040	2600.93156	−9.140	0.042
2423.87425	−12.676	−0.053	2600.93390	−9.142	0.041
2423.87884	−12.670	−0.047	2622.95427	−8.630	0.011
2423.88190	−12.673	−0.050	2622.95861	−8.630	0.011
2425.20427	−12.631	−0.024	2636.96890	−8.227	0.062
2425.20673	−12.634	−0.027	2636.97216	−8.232	0.057
2425.86166	−12.646	−0.047	2658.06339	−7.743	0.004
2425.87021	−12.669	−0.070	2671.90095	−7.353	0.032
2454.21565	−12.203	0.001	2671.90803	−7.352	0.034
2454.22289	−12.200	0.004	2673.06376	−7.345	0.010
2483.05035	−11.715	0.005	2673.06671	−7.345	0.010
2483.05360	−11.706	0.014	2673.19633	−7.336	0.016
2484.16423	−11.687	0.013	2673.19960	−7.341	0.011
2484.16694	−11.663	0.037	2686.06582	−7.022	−0.011
2485.07408	−11.654	0.030	2686.06873	−7.020	−0.009
2485.07715	−11.666	0.017	2686.07152	−7.018	−0.008
2486.12048	−11.606	0.059	2686.07433	−7.015	−0.004
2487.13913	−11.649	−0.003	2716.06922	−6.201	0.002
2487.14171	−11.616	0.030	2716.07230	−6.213	−0.010
2502.96131	−11.338	0.009	2717.09393	−6.199	−0.024
2502.96416	−11.337	0.010	2717.09655	−6.186	−0.011

continued on next page

Table C.2: Relative velocities and residuals of ν Octantis, *continued*

Julian Day (245 . . .)	Radial velocity (km s^{-1})		Julian Day (245 . . .)	Radial velocity (km s^{-1})	
	relative	residual		relative	residual
2720.13728	−6.095	−0.003	2949.13038	0.024	0.005
2720.13984	−6.106	−0.014	2950.11488	0.041	0.002
2720.14251	−6.104	−0.012	2951.07987	0.109	0.050
2744.11010	−5.453	−0.021	2951.08657	0.102	0.043
2744.11305	−5.447	−0.015	2952.09750	0.098	0.019
2745.85639	−5.443	−0.059	2982.11879	0.654	0.041
2745.86040	−5.449	−0.065	2982.12588	0.656	0.043
2745.86557	−5.409	−0.025	2984.90970	0.674	0.020
2745.86805	−5.412	−0.028	2984.91433	0.671	0.017
2803.09136	−3.843	−0.060	2986.89285	0.697	0.015
2803.09628	−3.842	−0.059	2986.90124	0.746	0.064
2866.93254	−2.086	−0.077	3012.00278	0.988	0.041
2866.93739	−2.079	−0.072	3012.00738	0.986	0.039
2867.09023	−2.087	−0.084	3015.03393	1.061	0.095
2867.09721	−2.069	−0.065	3015.03998	1.062	0.095
2868.17579	−2.034	−0.060	3016.08698	0.978	0.006
2869.13783	−1.999	−0.051	3016.09794	0.989	0.016
2869.14304	−1.974	−0.025	3024.88110	1.030	0.021
2871.07237	−1.903	−0.007	3047.14552	0.991	0.017
2871.07805	−1.910	−0.014	3047.15108	0.988	0.015
2887.84602	−1.428	0.021	3065.12966	0.814	0.026
2887.85266	−1.438	0.010	3065.17450	0.801	0.013
2917.22189	−0.706	−0.003	3065.17881	0.801	0.014
2917.87346	−0.697	−0.009	3068.22410	0.753	0.012
2919.04169	−0.681	−0.021	3068.22704	0.756	0.016
2919.04630	−0.672	−0.012	3105.10975	−0.234	−0.009
2920.07516	−0.644	−0.009	3105.11588	−0.229	−0.003
2920.07903	−0.640	−0.005	3106.19441	−0.258	0.008
2946.92182	−0.005	0.022	3106.19981	−0.262	0.004
2946.93244	0.000	0.027	3107.21559	−0.336	−0.032

continued on next page

Table C.2: Relative velocities and residuals of ν Octantis, *continued*

Julian Day (245 . . .)	Radial velocity ($\mathrm{km\,s^{-1}}$)		Julian Day (245 . . .)	Radial velocity ($\mathrm{km\,s^{-1}}$)	
	relative	residual		relative	residual
3107.21832	−0.335	−0.030	3188.82020	−4.954	0.015
3108.16390	−0.374	−0.034	3188.82694	−4.949	0.021
3108.16668	−0.373	−0.033	3188.83106	−4.947	0.023
3108.17179	−0.388	−0.048	3189.80285	−5.031	0.007
3108.17415	−0.387	−0.047	3189.80820	−5.028	0.010
3109.15042	−0.411	−0.033	3189.81334	−5.027	0.012
3109.15419	−0.428	−0.049	3216.95338	−6.910	0.013
3109.15676	−0.430	−0.051	3216.95861	−6.913	0.010
3109.16064	−0.429	−0.050	3216.96403	−6.918	0.006
3109.16299	−0.425	−0.046	3216.96932	−6.913	0.012
3110.20178	−0.460	−0.040	3216.97375	−6.928	−0.003
3110.20692	−0.463	−0.043	3216.97825	−6.927	−0.002
3185.06351	−4.676	0.033	3216.98278	−6.925	0.000
3185.07323	−4.683	0.026	3216.98728	−6.927	−0.001
3187.29910	−4.859	0.005	3217.85000	−6.985	−0.001
3187.30166	−4.851	0.012	3217.85224	−6.985	−0.001
3188.08043	−4.912	0.006	3217.85650	−6.983	0.002
3188.81405	−4.954	0.016	3217.85875	−6.984	0.001

Table C.3: Relative velocities and residuals of HD 159656

Julian Day (245 . . .)	Radial velocity (km s^{-1})		Julian Day (245 . . .)	Radial velocity (km s^{-1})	
	relative	residual		relative	residual
3047.19162	2.687	0.028	3108.11820	4.220	−0.007
3048.17204	5.812	0.004	3108.13055	4.263	−0.008
3065.19492	−11.280	0.007	3108.14440	4.310	−0.010
3065.21114	−11.139	0.030	3108.18924	4.454	−0.020
3067.12874	1.477	0.015	3108.20232	4.493	−0.025
3067.15460	1.600	0.005	3109.03574	6.093	−0.032
3068.13294	5.381	0.017	3109.04878	6.094	−0.035
3068.14881	5.417	0.015	3109.06223	6.111	−0.022
3068.20700	5.559	0.026	3109.07564	6.110	−0.026
3105.13975	−14.268	−0.004	3109.08819	6.122	−0.015
3106.04275	−7.770	0.008	3109.10118	6.125	−0.014
3106.06331	−7.619	0.011	3109.11375	6.120	−0.019
3106.10894	−7.307	−0.004	3109.12754	6.117	−0.022
3106.12653	−7.191	−0.013	3109.17842	6.138	0.007
3106.15492	−6.997	−0.022	3109.19052	6.134	0.006
3106.16917	−6.886	−0.012	3109.20495	6.130	0.007
3107.01439	−1.229	0.009	3109.96347	4.468	0.009
3107.03489	−1.111	0.002	3109.98133	4.403	0.018
3107.09681	−0.753	−0.011	3110.00171	4.325	0.027
3107.11168	−0.668	−0.014	3110.08397	3.908	−0.015
3107.12879	−0.556	−0.004	3110.10538	3.812	−0.009
3107.15193	−0.424	−0.007	3110.12249	3.719	−0.017
3107.16928	−0.327	−0.012	3110.13947	3.634	−0.017
3107.18853	−0.215	−0.011	3110.22931	3.080	−0.093
3108.00912	3.815	−0.004	3184.80996	−20.255	0.028
3108.02858	3.872	−0.022	3184.98738	−19.540	−0.009
3108.04479	3.966	0.010	3185.02105	−19.373	−0.001
3108.07861	4.075	−0.007	3185.81658	−14.603	0.006
3108.09254	4.115	−0.019	3185.83502	−14.472	0.010
3108.10620	4.179	−0.005	3185.85034	−14.378	−0.001

continued on next page

Table C.3: Relative velocities and residuals of HD 159656, *continued*

Julian Day (245 . . .)	Radial velocity (km s^{-1})		Julian Day (245 . . .)	Radial velocity (km s^{-1})	
	relative	residual		relative	residual
3185.86449	−14.264	0.015	3189.93946	6.116	−0.004
3185.87934	−14.162	0.014	3189.95199	6.110	−0.004
3186.10701	−12.607	−0.037	3189.98632	6.101	0.005
3186.12142	−12.517	−0.050	3189.99953	6.097	0.010
3186.13983	−12.313	0.023	3190.01333	6.087	0.009
3186.15953	−12.199	−0.005	3212.79237	−11.742	0.009
3186.89424	−6.899	−0.011	3212.81441	−11.959	0.021
3186.91003	−6.778	−0.002	3212.91646	−13.025	−0.001
3186.92531	−6.673	−0.006	3212.94625	−13.317	0.007
3186.94140	−6.561	−0.009	3212.98932	−13.743	0.007
3187.11086	−5.378	−0.012	3213.01361	−13.993	−0.004
3187.12471	−5.285	−0.015	3213.04105	−14.259	−0.003
3187.13865	−5.183	−0.009	3213.05873	−14.422	0.004
3187.92492	−0.170	−0.021	3213.79273	−19.952	−0.001
3187.93598	−0.095	−0.009	3213.80904	−20.042	−0.010
3187.95202	0.000	−0.007	3213.82277	−20.120	−0.021
3187.96921	0.113	0.009	3213.83624	−20.173	−0.010
3187.98039	0.187	0.019	3213.84936	−20.229	−0.006
3187.99403	0.264	0.019	3213.86173	−20.281	−0.001
3188.87214	4.337	0.014	3213.87466	−20.339	−0.002
3188.89040	4.402	0.016	3213.88806	−20.399	−0.004
3188.90470	4.445	0.010	3214.02811	−20.914	0.004
3188.91816	4.492	0.011	3214.04110	−20.955	0.004
3188.93764	4.562	0.015	3214.05687	−21.007	−0.000
3188.95166	4.606	0.014	3218.93762	3.543	0.008
3189.06233	4.947	0.011	3218.95089	3.610	0.020
3189.86040	6.150	0.011	3218.96327	3.657	0.018
3189.87414	6.153	0.015	3218.97600	3.717	0.027
3189.88933	6.156	0.020	3218.99446	3.780	0.017
3189.90496	6.142	0.010	3219.00841	3.807	−0.011
3189.92594	6.121	−0.004			

Table C.4: Relative velocities and residuals of HD 206804

Julian Day (245 . . .)	Primary velocity ($\mathrm{km\,s^{-1}}$)		Secondary velocity ($\mathrm{km\,s^{-1}}$)	
	relative	residual	relative	residual
2068.20215	42.234	−0.011	23.499	0.015
2094.16113	43.899	0.002	21.835	−0.029
2095.12012	43.949	0.006	21.756	0.002
2098.11353	44.103	0.025	21.641	−0.023
2102.08301	44.241	0.007	21.456	0.001
2121.04663	44.567	0.003	21.115	0.000
2122.06006	44.553	−0.008	21.095	0.022
2149.02393	43.791	−0.031	21.894	−0.011
2150.88965	43.738	0.005	21.958	0.016
2180.99976	41.980	−0.006	23.763	0.019
2218.01147	39.804	0.015	26.076	−0.021
2219.93237	39.679	−0.006	26.153	0.009
2312.91033			32.760	
2426.11614			32.958	
2485.02203			32.891	
2720.19020			32.721	
2868.12080			32.751	
3187.07570			32.647	
3219.98775			32.785	

Table C.5: Barycentric radial velocities of HD 217166

.

Julian Day (245 . . .)	Barycentric velocity ($km\,s^{-1}$)	
	Primary	Secondary
2149.08838	-28.583	-13.692
2180.95508	-28.608	-13.693
2217.95996	-28.571	-13.692
2219.99561	-28.556	-13.700
2425.25049	-28.262	-14.086
2426.27295	-28.256	-14.080
2454.27490	-28.139	-14.201
2483.14917	-28.014	-14.297
2484.12354	-28.038	-14.297
2485.11328	-28.003	-14.356
2486.17065	-28.023	-14.345
2503.08130	-27.928	-14.378
2569.89648	-27.590	-14.818
2570.88330	-27.554	-14.808
2867.13250	-21.507	
2868.06816	-21.404	
2918.99650	-21.248	

Table C.6: Relative velocities and residuals of HD 181958

Julian Day (245 . . .)	Primary velocity ($\mathrm{km\,s^{-1}}$)		Secondary velocity ($\mathrm{km\,s^{-1}}$)	
	relative	residual	relative	residual
2007.0225	34.561		34.561	
2096.0054	45.513	0.024	23.370	−0.015
2096.1221	45.440	−0.061	23.303	0.037
2096.9741	45.546	−0.043	23.223	0.025
2097.9204	45.706	0.020	23.135	0.011
2099.9705	45.901	0.007	23.011	−0.079
2100.2930	45.909	−0.017	22.894	0.000
2100.9280	46.016	0.026	22.887	−0.057
2101.7864	46.104	0.028	22.793	−0.054
2102.1860	46.141	0.025	22.706	−0.011
2102.8206	46.188	0.009	22.660	−0.031
2103.1011	46.175	−0.032	22.616	−0.017
2120.0979	47.850	0.054	20.880	0.042
2121.0083	47.914	0.040	20.752	0.085
2121.9167	47.970	0.018	20.651	0.104
2143.9766	49.603	0.032	19.121	−0.063
2151.1609	49.961	−0.011	18.682	−0.048
2180.8660	50.722	−0.146	17.666	0.021
2215.9087	50.397	0.042	18.187	0.039
2423.8494	34.652		34.652	
2425.8916	34.637		34.637	
2482.8699	34.725		34.725	
2485.9883	34.698		34.698	
2502.8201	34.768		34.768	
2715.0269	25.827	−0.053	44.008	0.005
2744.2114	25.487	−0.033	44.353	0.037
2744.2239	25.559	0.039	44.398	−0.006
2745.9858	25.463	−0.039	44.398	0.013
2867.0417	25.237	−0.003	44.602	0.081
2870.9966	25.239	−0.029	44.640	0.017
2888.1101	25.470	0.051	44.507	−0.008
2917.9268	25.873	0.061	44.162	−0.074
2919.9810	25.838	−0.007	44.104	−0.052

Table C.7: Relative velocities and residuals of θ Antliae

Julian Day (245 . . .)	Radial velocity (km s^{-1})		Julian Day (245 . . .)	Radial velocity (km s^{-1})	
	relative	residual		relative	residual
2093.8083	24.305	0.017	3011.1365	16.072	−0.014
2101.8572	24.171	0.008	3015.0586	16.160	0.035
2121.7939	23.833	−0.010	3016.0554	16.169	0.033
2219.1348	21.992	−0.064	3047.1677	16.401	−0.049
2351.9377	19.096	−0.013	3047.1750	16.409	−0.041
2352.1052	19.102	−0.003	3065.1155	16.654	0.023
2390.0066	18.327	0.108	3065.1211	16.666	0.035
2422.8662	17.569	0.102	3104.9863	17.008	−0.022
2422.8745	17.475	0.008	3104.9919	17.021	−0.010
2425.9744	17.396	−0.002	3106.0066	17.044	0.004
2453.9109	16.764	−0.024	3106.0144	17.050	0.010
2453.9263	16.752	−0.035	3107.0645	17.077	0.027
2483.7644	16.156	−0.023	3107.0730	17.070	0.019
2483.7683	16.158	−0.021	3110.0305	17.075	−0.005
2483.7727	16.156	−0.022	3110.0598	17.063	−0.017
2571.1831	14.715	−0.050	3185.7727	17.806	−0.010
2571.1865	14.709	−0.056	3185.7827	17.810	−0.006
2637.0190	14.144	−0.015	3185.7910	17.808	−0.008
2658.1265	14.072	0.020	3188.8376	17.847	0.001
2658.1313	14.061	0.009	3188.8440	17.844	−0.001
2672.1543	13.982	−0.021	3213.7559	18.053	−0.025
2686.2136	13.936	−0.036	3213.7656	18.052	−0.027
2716.1382	14.036	0.078	3216.7690	18.161	0.054
2717.0569	13.972	0.013	3216.7791	18.159	0.052
2717.0603	13.978	0.019	3217.7566	18.111	−0.005
2743.9719	14.049	0.042	3217.7646	18.123	0.008
2743.9792	14.043	0.037	3218.7585	18.135	0.010
2949.1804	15.469	−0.002	3218.7651	18.132	0.007
2984.0981	15.762	−0.053	3219.7578	18.127	−0.008
2985.0847	15.742	−0.082	3219.7644	18.136	0.001

Table C.8: Relative velocities and residuals of 94 Aquarii A

Julian Day (245 . . .)	Radial velocity ($\mathrm{km\,s^{-1}}$)	
	relative	residual
2094.2192	−0.543	0.027
2121.1201	−0.369	−0.005
2151.0938	−0.175	−0.002
2218.9475	0.089	−0.023
2221.0215	0.098	−0.019
2424.1777	0.000	−0.007
2483.0664	−0.229	−0.000
2545.0691	−0.528	0.026
2593.9932	−0.834	0.026
2637.9075	−1.144	0.025
2637.9133	−1.141	0.028
2869.0105	−3.322	−0.086
2888.1331	−3.468	−0.032
2917.9836	−3.790	−0.033
2917.9971	−3.789	−0.032
2918.9490	−3.803	−0.036
2920.0203	−3.784	−0.006
2946.9846	−4.089	−0.012
2948.0049	−4.085	0.003
2952.0161	−4.147	−0.014
2952.9119	−4.150	−0.006
2983.9497	−4.469	0.028
2983.9607	−4.458	0.039
2984.9426	−4.484	0.025
2985.9563	−4.486	0.034
3013.8950	−4.816	0.031
3109.2615	−5.984	0.029
3185.2615	−6.918	0.070
3185.2783	−6.919	0.069
3190.1577	−7.051	0.001
3214.1665	−7.381	−0.015
3214.1738	−7.392	−0.026
3214.1809	−7.384	−0.018
3217.1221	−7.440	−0.035
3217.1284	−7.438	−0.033
3219.0427	−7.450	−0.019

Appendix D

The $e-P$ distribution

There is a well-documented observed distribution of orbital eccentricity as a function of period which is found for many different samples of binary systems. This distribution is illustrated in Fig. D.1, using orbital data from the 'Sixth Catalog of the Orbits of Visual Binary Stars' (Hartkopf & Mason 2004), and SB1 and SB2 samples from the 'Ninth Catalogue of Spectroscopic Binary Orbits' (Pourbaix et al. 2004). Only orbital solutions of higher quality have been plotted.

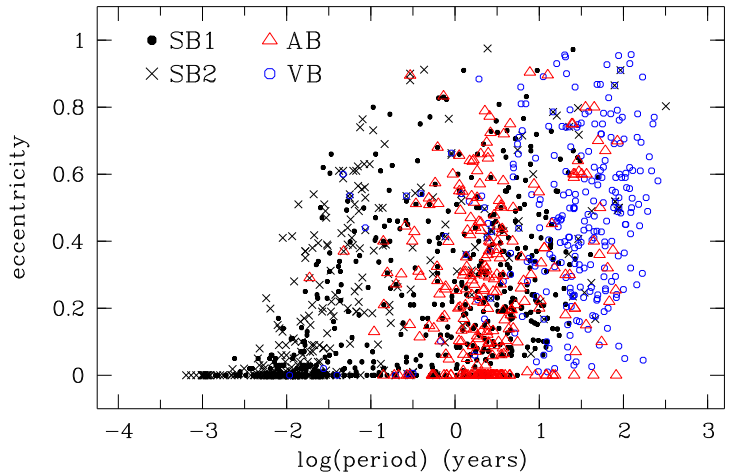

Figure D.1: Distribution of orbital eccentricity as a function of period for 258 visual binary orbits, 504 SB1 orbits and 327 SB2 orbits with 'definitive' and 'good' orbital solutions. A logarithmic scale is used for P to allow inclusion of the wide range of periods that these various systems encompass.

Inspection of this distribution will reveal several characteristics: 1. an imaginary boundary separates the $e-P$ plane into two regions, one that is populated by orbital solutions and one that isn't, 2. the boundary is gently curving, 3. the orbits with short periods tend to have low eccentricities whilst higher eccentricity orbits occur increasingly for orbits with longer periods, and, 4. there is a distinct cut-off period, $P_{\rm cut}$, below which all orbits are circular.

The general nature of this distribution is reproduced with striking similarity for many different classes of binary systems, as well as the growing list of extrasolar planets (e.g. see Marcy

et al. 2004). Binary populations displaying this distribution include: pre-main-sequence stars (Mathieu 1994), systems with A-type primary stars (Matthews & Mathieu 1992), barium and S stars (Jorissen et al. 1998; Karakas et al. 2000), normal giant stars (Boffin et al. 1993), metal poor halo binaries (Latham et al. 1992), main-sequence and evolved O-type stars (Mason et al. 1998b), late-type main-sequence stars (Koch & Hrivnak 1981, Duquennoy & Mayor 1991), and late-type stars in open clusters (Mermilliod 1997). Hilditch (2001) has assembled data for the G–K dwarfs and giants reported in the first 141 papers of Griffin's series of 'The Observatory' papers. This sample also produces the typical $e-P$ distribution.

The effects of tidal interactions are expected to have an important influence upon the observed distribution of eccentricities, in particular for the short period systems, where circularization leading to a distinctive $P_{\rm cut}$ is most strongly favoured (e.g. see Zahn 1977). Mathieu & Mazeh (1988) suggested that $P_{\rm cut}$ could be used as a means to estimate the relative ages of coeval binaries, such as are found in different clusters. Observational support for these theories includes the general trend of increasing values for $P_{\rm cut}$ as the mean ages of samples increases.

Up to the age of the Hyades, $P_{\rm cut} \sim 6$–8 days (Mayor & Mermilliod 1984, Mermilliod 1997), For older cluster systems, circularization is extended to $P_{\rm cut} \sim 12$ days (Latham et al., 1992) and for very old populations of halo binaries, $P_{\rm cut} \sim 19$ days (Latham et al. 1992; 2002). The circularization time $t_{\rm circ}$ is expected to vary depending upon whether the orbiting bodies have radiative envelopes (as do the massive O-type stars) or have convective envelopes (as do the less massive late-type stars). Whilst there is general agreement of the sensitivity of the circularization time to the period, the actual degree of that sensitivity remains a matter of debate. For stars with convective envelopes, Zahn (1977) suggested that $t_{\rm circ} \propto P^{16/3}$, whereas Tassoul (1995) proposed a different mechanism so that $t_{\rm circ} \propto P^{49/12}$. Goldman & Mazeh (1991) relaxed the dependence to the lowest degree, and argued that $t_{\rm circ} \propto P^{10/3}$, so that circularization was rarely complete in the pre-main-sequence stage of evolution, but could be achieved only if the tidal processes continued for main-sequence stars. As well as tidal interactions, other stellar processes have been implicated as having some influence on the $e-P$ distribution. For example, Karakas et al. (2000) showed that the distribution of eccentricities for their barium star sample was consistent with a model with significant wind accretion.

Thus the observed $e-P$ distribution, and in particular the general shape of the curving boundary, is ubiquitous and suggestive of some characteristic of all stellar and planetary orbital systems that may be fundamental to them all. Consequently, various attempts have been made to determine a function that describes this distribution in some way or another. For instance, in a study of late-type giants, Boffin et al. (1993) derived a linear relation between P and the mean value of e, namely, $\langle e \rangle = 0.15(\log P - 1)$. They emphasized the scarcity of low eccentricity ($e < 0.1$) binaries with longer periods ($P > 130$ d) in their sample. This latter finding has been found by others also, e.g. Duquennoy & Mayor (1991).

Pourbaix et al. (2004) point out that the boundary curve is not well understood, For the

sample of specroscopic orbits from their catalogue and reproduced in Fig. D.1, Pourbaix and co-workers report that the boundary would be best described by a curve $P(1-e)^3 = \text{constant}$. They also state that theoretical considerations, for instance, based upon the distance at periastron and dissipative tidal evolution, yield lines of the form $P^{2/3}(1-e) = \text{constant}$ (Mason et al. 1998b) and $P(1-e^2)^{3/2} = \text{constant}$ respectively, which therefore differ from the best-fit curve that they have identified.

D.1 Total orbital angular momentum and energy

Another perspective is provided by the well-known contributions of the total orbital angular momentum, J, and the total orbital binding energy, B, to the orbital eccentricity (e.g. see Lubow 1993 for a general review).

D.1.1 The relationship of e and P to J and B

The ratio J/B provides an expression in terms of only P and e:

$$R_{\rm JB} = \frac{\pi J}{B} = P\sqrt{1-e^2}\,, \tag{D.1}$$

using Eq. (A.51) on page 221 and Eq. (A.33) on page 218. Therefore J/B has the units of time.

As well as relating the orbital period and eccentricity to a single fundamental quantity $R_{\rm JB} = \pi J/B$, Eq. (D.1) is also independent of the individual masses or the mass ratio, q. Therefore it does not differentiate between the diversity of stellar, planetary or other orbiting systems, nor their stages of evolution. This equation is analogous to Kepler's third law which allows deduction of the mass sum, $M_{\rm S}$, of an orbital pair solely from the semi-major axis and period of the orbit. However, a binary system with an orbital solution of any type with any merit will include P and e, so that unlike $M_{\rm S}$, q, J, B or the mass function, $f_{\mathcal{M}}$, the ratio J/B can always be measured for these systems.

We can re-arrange Eq. (D.1) to get

$$e = \sqrt{1-\left(\frac{R_{\rm JB}}{P}\right)^2}\,. \tag{D.2}$$

For a bound orbit, $e \geq 0$. When $e = 0$, the period is the shortest it can be for the given $R_{\rm JB}$, that is, there is no excessive orbital energy in relation to the orbital angular momentum. However, if $e > 0$, then $P > P_{\rm min}$ and

$$P_{\rm min} = R_{\rm JB} = \frac{\pi J}{B} = P\sqrt{1-e^2}\,, \tag{D.3}$$

is the shortest period that the orbital system with given J/B can ever achieve. A shorter period could only occur for that system if there is an appropriate reduction of J/B for the system. For

orbits with the same J/B, increasing values of P ($> P_{\rm min}$) will require the orbital eccentricity to increase accordingly.

The curves representing Eq. (D.2), for several values of J/B, are illustrated in Fig. D.2. Masses moving in closed orbits having identical J/B will fall uniquely along a given curve. Therefore, if various lines corresponding to Eq. (D.2) are overlaid on Fig. D.1, they will identify the systems that have the same value for J/B, regardless of the types of orbiting masses involved, e.g. stars and/or planets. Systems that have long periods, which therefore are unlikely to have had time to circularize significantly, can only have a low eccentricity ($e < 0.1$) if the orbital energy is a minimum relative to the angular momentum, which is equivalent to saying that the period is very close to the shortest possible for the system's J/B. Any other longer period can only correspond to a larger eccentricity.

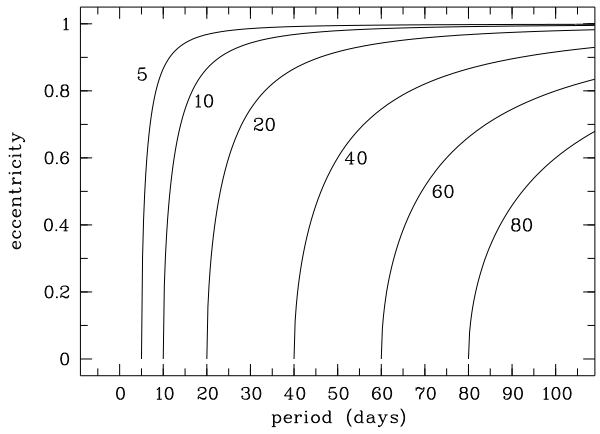

Figure D.2: Computed curves defined by Eq. (D.2) for given values of $R_{\rm JB} = \pi J/B$.

Inspection of the various examples of $R_{\rm JB}$-curves in Fig. D.2 indicates that one of the curves will mimic the $e-P$ boundary curve, although it will be displaced to the right. We shall label the best-fitting curve $R_{\rm circ}$. This curve can be shifted to coincide with $P = P_{\rm cut}$ by modifying Eq. (D.2), based on empirically determined values for $R_{\rm circ}$ and $P_{\rm cut}$. Consequently, the observed $e-P$ distribution can be reproduced by the following:

$$\left.\begin{array}{ll} \text{for} & R_{\rm JB} < R_{\rm circ}\,, \quad e = 0 \\ \text{for} & R_{\rm JB} \geq R_{\rm circ}\,, \quad e = \sqrt{1 - \left(\dfrac{R_{\rm JB}}{P + R_{\rm circ} - P_{\rm cut}}\right)^2}\,. \end{array}\right\} \qquad \text{(D.4)}$$

When the spectroscopic data included in Fig. D.1 is plotted instead as an $e-P$ distribution (but only for $P < 110$ days so as to emphasise the shape of this distribution's sloping boundary) we can see how well the selected curve $R_{\rm circ}$ offset by $P_{\rm cut}$ reproduces the observed boundary

shape (Fig. D.3).

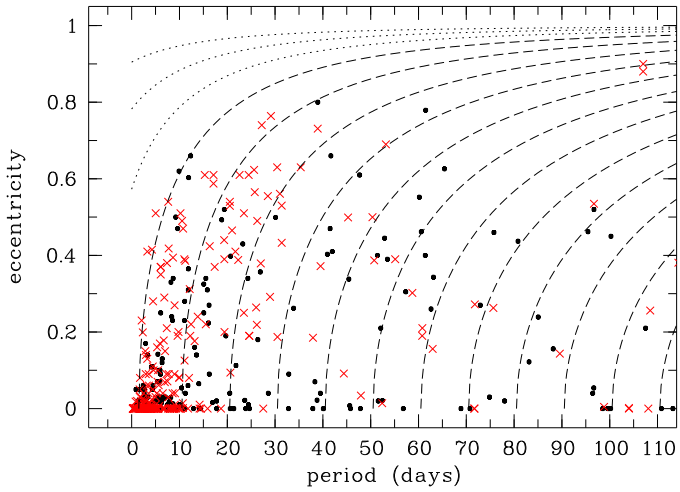

Figure D.3: Observed distribution of e vs. P and a series of possible values for $R_{\rm JB} = \pi J/B$ as defined by Eq. (D.4), with $R_{\rm circ} = 32$ d and $P_{\rm cut} = 1.5$ d. For $R_{\rm JB} < R_{\rm circ}$ the curves are plotted with '.....', whereas for $R_{\rm JB} \geq R_{\rm circ}$, the curves are plotted with '- - -'. The dashed curves represent values of $R_{\rm JB} = P_{e=0} + R_{\rm circ} - P_{\rm cut}$. The symbolism used is the same as for Fig. D.1.

The same can be done just as successfully for any other sample of orbital solutions, by the appropriate choice of $R_{\rm circ}$ and $P_{\rm cut}$. Naturally, orbital systems that have $R_{\rm JB} < R_{\rm circ}$ will, in the majority of observed cases, have circular orbits, whereas whenever $R_{\rm JB} \geq R_{\rm circ}$, systems can have $e \geq 0$. The increasing density of $R_{\rm JB}$-curves with increasing $P > P_{\rm cut}$ may help to explain the correlation of increasing $\langle e \rangle$ with increasing P, as has been demonstrated, for instance, by Duquennoy & Mayor (1991) and Boffin et al. (1993). However, when considering the possibility of any correlation of this kind, of some relevance may be the demonstration, in Fig. 4.17 on page 56, that the shorter- and longer-period samples of SB orbits form two distinct groups rather than a continuous distribution in the $e-P$ diagram (i.e., the mostly earlier+unevolved and the later+evolved systems respectively; Heintz 1969).

Appendix E

The HERCULES Thorium - Argon Atlas

E.1 Introduction

The following Atlas provides a catalogue of thorium and argon (Th–Ar) emission line data, in vacuum and air, together with the associated vacuum spectra for the échelle spectrograph HERCULES (Hearnshaw et al. 2002), and similar instruments.

Th–Ar lamps continue to be used for high-precision wavelength calibration purposes (e.g. Hearnshaw et al. 2002, Queloz et al. 2001). There are many documents and databases that present a wealth of wavelength and related data with regards thorium and argon spectra. However, there appears to be a lack of single publications with a format that provide, for instance, both air and vacuum wavelengths, the majority of both Th and Ar lines, these lines identified on the same plotted spectra, and so on. In an attempt to address this situation, a set of four Atlases have been compiled, each being defined by the four presently available HERCULES CCD regions. The tabulated data and plotted spectra are presented order-by-order. The combined coverage of the four Atlases documents the majority of Th–Ar lines occupying the wavelength range $\lambda\lambda_{\rm vac}$ 3608–7283 Å.

Electronic versions of the individual Atlases may also be found at:
`http://www.phys.canterbury.ac.nz/research/astronomy/` then follow the links to HERCULES and the Th-Ar Atlases.

The following describes the source material and layout of each Atlas. Some statistics of the data tabulated in the Atlases are presented in Table E.1 on page 270.

E.2 Sources of catalogue data

The primary source is De Cuyper & Hensberge (1998) (henceforth D&H98). Their work is based on the Th–Ar lines published by Minnhagen (1973), Norlén (1973), and Palmer & Englemann (1983). The last reference provides only thorium line data (THI, THII, and TH when the thorium ion resposible was uncertain) and is the principal contributor to D&H98. The first 2 references provide only argon line data (ARI and ARII). D&H98 tabulate all wavelengths to 8 significant figures together with the relative intensities (logarithmic scale) of each line. Their study analysed each Th–Ar line with regard to its wavelength stability (which may be variable e.g., as a result of blending) at each of 5 resolving powers (R = 25000, 33000, 43000, 50000 and 100000). The Th–Ar lamp employed was a S & J Juniper hollow cathode lamp, the same type

employed in HERCULES. The D&H98 study operated their lamp at the 'normal' current of ≈ 10 mA, and at a higher (unknown) lamp current. This 'bright' lamp current resulted in argon line (log) intensities 1.36× greater than for the 'normal' lamp current. The HERCULES lamp typically operates at 7–8 mA. D&H98 list the resulting 'blend' wavelength of each line for each resolving power and each of the 2 lamp currents (as well as other data not directly related to the format of these Atlases).

As it was obvious that many, sometimes prominent, lines imaged by HERCULES were not included in D&H98, additional sources of lines were sought. No improvement to the thorium line list in terms of scope and precision could be found. A significantly larger secondary source of argon lines was obtained from the Vienna Atomic Line Database (VALD - Piskunov et al. 1995, Ryabchikova et al. 1998, Kupka et al. 1999). VALD's reference for the additional argon lines (ArI, ArII, ArIII and ArIV) is Kurucz (1993). The wavelengths of these lines were precise to 7 significant figures. Relative line intensities or blended resolving-power-dependent wavelengths were not included in the VALD data.

The subset of lines extracted from these 2 sources for the wavelength range $\lambda\lambda_{\rm vac} \approx 3527$–7639 Å (as found in the present version of the Hercules Reduction Software Package - HRSP 1.4) includes 7003 Th–Ar lines from D&H98 and 2448 argon lines from VALD. All wavelengths provided by D&H98 and VALD are in air.

Clearly, some of the argon lines would be duplicated when the data from the 2 sources were combined. It was decided to eliminate the lower precision 'copy' of a line if the wavelengths of two identical emitting species were within 0.001 Å of each other. Whether or not this choice eliminates slightly too many or too few line duplicates seems insignificant in terms of the likely application of these Atlases, since at least one identification of the argon line in question (the more precise) will always remain. This decision resulted in the elimination of 645 argon lines sourced from the VALD list, so that the final list includes 8806 Th–Ar lines. A HERCULES master file has been constructed from this. Each Atlas is derived from this master file.

E.3 The Atlases

Each Atlas documents the orders *expected to be complete* for all Th–Ar images taken using the particular CCD region. This point deserves some explanation. Owing to run-to-run CCD position variations and the use by HERCULES of three fibres for resolving power flexibility (fibre 1: 100μm R 41000, fibre 2: 50μm R 82000, and fibre 3: 100μm with 50μm slit R 70000) it is impossible long-term for exactly the same region of the wavelength space to be imaged. For instance, inspection of numerous Th–Ar spectra taken over several months using CCD region 2 has shown that the first and last orders of this region are frequently imaged to a variable degree. Also, the endpoints of the wavelength space imaged for any other order may vary by about 1 Å. It is expected that similar variations arise for the three other CCD regions also. The Atlases address these variations as follows: 1. The first and last often incomplete orders of each region are NOT included, since a suitable line table should include only lines (orders) that will always be available for the dispersion solution, and 2. The Th–Ar lines catalogued extend 2 Å beyond both endpoints of each plotted order.

These decisions and the overlap of the four CCD regions results in almost continuous coverage in the wavelength range $\lambda\lambda_{\rm vac} \approx$ 3608–7283 Å, with the omission of only a few angströms in which 14 spectral lines are found in the master file. This situation has been rectified by extending the wavelength range of one involved order so that these additional lines are included (order 126 in the region 4 Atlas). Consequently there are 8149 individual lines identified within the four Atlases.

Each order of each CCD region is presented as a catalogue of wavelength and associated data together with the respective entire plotted spectrum for that order on the facing page, as will be described shortly. Frequently, the number of tabulated lines exceeds the page limit ($\approx$ 58 spectral lines) so that the order table extends over 2 or more pages. The entire plotted spectrum is repeated accordingly on each facing page.

E.3.1 The catalogue

Each left page begins with the order number followed by the page number and total number of pages of data for that order. The orders are arranged in increasing value beginning with the lowest for the Atlas region. This is followed by 11 columns of data for each tabulated Th–Ar line:

1	‡	indicates the line is also present in a neighbouring order in this Atlas[a]
2	$\lambda_{\rm air}$ (Å)	Air wavelength[b]
3	$\lambda_{\rm vac}^{-1}$ (cm^{-1})	Wavenumber in vacuum[b]
4	$\lambda_{\rm vac}$ (Å)	Vacuum wavelength[b]
5	Emit.	Emitting species[c]
6	$S_{\rm nm}^{43}$	Stability label at R 43000, 'normal' TH:AR relative intensity[d]
7	$S_{\rm br}^{43}$	Stability label at R 43000, AR relatively 'bright' as compared to TH[d]
8	$I_{\rm rel}^{\rm br}$	Relative intensity (log scale, for 'bright' lamp current)[e]
9	$\lambda_{\rm vac,\ br}^{43000}$ (Å)	Blended 'bright' lamp wavelength, in vacuum at R 43000[f]
10	$\lambda_{\rm vac,\ br}^{50000}$ (Å)	Blended 'bright' lamp wavelength, in vacuum at R 50000[f]
11	$\lambda_{\rm vac,\ br}^{100000}$ (Å)	Blended 'bright' lamp wavelength, in vacuum at R 100000[f]

Additional comments:

[a] Only region 4 has a significant number of lines duplicated in neighbouring orders (513 lines). Region 1 has only one line duplicated, and regions 2 and 3 have none.

[b] Air wavelength given to precision of the original source, the vacuum wavelength similarly. The wavenumber has an extra figure of significance that should be treated with caution.

[c] Emitting species labels have full-capitals for D&H98 lines, and roman for VALD lines. This assists in identifying the source etc. of a line on the plotted spectra.

[d–f] VALD lines do not provide data for columns 6–11 and each entry here is a '−'.

[d] Stability labels indicate the proximity of blend wavelengths to their laboratory values. As D&H98's data show, the blend wavelength frequently depends upon the resolving power used. When a line's blended wavelength is sufficiently uncertain, D&H98 give no value and a '⋆' identifies this. Stability labels are listed for both lamp currents. The R 43000 resolving power-dependent wavelengths were chosen for comparison with the laboratory value as this R is the lowest one relevant to HERCULES users. Lines stable at this resolving power are invariably stable at higher R as well, whereas the converse is often not the case. The labels are defined as follows:

$D = \parallel \lambda_{\rm vac} - \lambda_{\rm vac,\ nm/br}^{43000} \parallel$ (Å)	$S_{\rm nm}^{43}$	$S_{\rm br}^{43}$
$D = 0$	N	B
$0 < D < 0.001$	n	b
$0.001 \leq D < 0.002$	o	c
$0.002 \leq D < 0.003$	r	e
$D \geq 0.003$	s	s
$\lambda_{\rm vac,\ nm/br}^{43000} = \star$	⋆	⋆

The most suitable lines are those that are relatively stable regardless of the lamp current/temperature, since the latter may change during the course of an observation program (i.e. lines labelled NB, Nb, nB, or nb). Table E.1 includes some statistics of the stability labels for the most stable lines.

[e] The 'bright' lamp relative intensities are tabulated as they are typically more representative of those found on the HERCULES plotted spectra. The relative intensities of all emitting species are a general guide only as each line's strength is temperature dependent. Comparison of various lines will easily reveal specific discrepancies. To determine the 'normal' $I_{\rm rel}^{\rm nm}$ ARI and ARII values, reduce $I_{\rm rel}^{\rm br}$ by subtracting 1.36.

[f] The 'blended' wavelengths may not be blended at all if the line is sufficiently isolated. The resolving-power dependent wavelengths most relevant to HERCULES users have been included in each Atlas, i.e. with regards available R and 'bright' relative line intensities.

Ideally, lines useful for calibration purposes should be obtainable on all calibration spectra. As a guide, the lower and upper useful wavelength limit was chosen to be 0.5 Å inside the end of each plotted order and is delimited in the catalogue with a double horizontal line.

E.3.2 The plotted spectra

The plotted spectra for each Atlas were extracted from a single HERCULES Th–Ar image for that CCD region using HRSP. It was decided to use spectra obtained with the mid-resolving power fibre 3 (R 70000). Whilst the stability labels were determined with respect to R 43000, the greater resolving power of fibre 3 allows significantly better visualisation of spectral features. For each of the four CCD regions the Th–Ar image was exposed for two minutes, five times longer than recommended at that time by the HERCULES reference Th–Ar image (region 2, fibre 1: 16 s $\times$ 1.5 = 24 s). This makes many faint spectral features easier to see without saturating too many brighter lines.

Atlas / CCD region	1	2	3	4
orders included	78–123	80–125	79–124	126–157
$\lambda_{\rm vac}^{\rm max}$ (Å)	7282.4599	7135.9750	7244.3513	4537.2517
$\lambda_{\rm vac}^{\rm min}$ (Å)	4590.9569	4537.2517	4582.4570	3608.7620
Tabulated emitting species	number of lines			
THI	1535	1556	1483	1161
THII	480	488	493	664
TH	446	487	459	821
ARI+ArI	220+140	198+127	196+132	38+10
ARII+ArII	163+822	171+803	169+775	204+363
ArIII	58	56	51	59
ArIV	9	11	9	6
D&H98	2844	2900	2800	2888
VALD	1029	997	967	438
total	3873	3897	3767	3326
Plotted stability labels				
N	439	418	413	153
n	141	138	128	133
o	58	50	45	67
r	27	29	29	31
N-r / non-zero $\lambda_{\rm vac,nm}^{43000}$	665/721	635/684	615/664	384/413
B	438	421	415	188
b	165	166	149	154
c	63	57	56	66
e	34	41	38	31
B-e / non-zero $\lambda_{\rm vac,br}^{43000}$	700/761	685/736	658/712	439/463
NB	414	396	389	150
Nb	10	10	10	1
nB	15	17	20	28
nb	102	102	82	93
NB+Nb+nB+nb	541	525	501	272

Table E.1: A summary of information presented in the four Atlases. The numbers of lines of each emitting species are individual emission lines sourced from D&H98 and VALD (i.e. not including duplicates plotted). The numbers of lines with the given stability labels apply to all those lines so labelled on *each plotted spectrum*, therefore including any duplicates across orders for a given Atlas. (See § E.3.1 for most symbol definitions.)

Each order is plotted in vacuum, separated into four equal sections with an overlap of 0.5 Å between sections. Each plot extends to an intensity of 295×10^3 ADU as this is approximately the saturation value of an extracted line.

The species labels are printed below each feature. To avoid some of the overlapping of emitting species labels, a vertical offset has been applied to the following line when it is closer than the resolution computed for the line wavelength at $R = 41000$ (this varies from 0.09–0.18 Å). The label following these two lines will return to the original label position. If this line is closer than the resolution a small '$\circ$' is printed slightly above the label.

The $S^{43}_{\rm nm}$ and $S^{43}_{\rm br}$ stability labels of only the more stable lines are identified (i.e. N, B, n, b, c, r, e, o) on the plots. These are above the species label; offset to the left for $S^{43}_{\rm nm}$ and offset to the right for $S^{43}_{\rm br}$. Only lines within 0.5 Å of the end of each order have their stability labels on the plotted spectra.

The number of lines tabulated and identified for the given order is indicated towards the top of each plot page.

The reddest and bluest orders are relatively faint for two different reasons. The reddest orders (imaged in regions 1-3) are strongly filtered by the inclusion of a blue-green (BG39) filter in the Th–Ar lamp light path. This is to eliminate gross contamination by high luminosity argon lines found here. The bluest orders (imaged in region 4) are relatively faint because of the reduced sensitivity of the CCD at these wavelengths.

The following pages provide copies of the the tabulated data and spectral maps from the 'Atlas of Thorium and Argon Spectra. HERCULES CCD region 2. Orders 80–125' for one of the HERCULES échelle order $n = 105$.

Order 105

(page 1/2)

$\lambda_{\rm air}$ (Å)	$\lambda_{\rm vac}^{-1}$ (cm^{-1})	$\lambda_{\rm vac}$ (Å)	Emit.	$S_{\rm nm}^{43}$	$S_{\rm br}^{43}$	$I_{\rm rel}^{\rm br}$	$\lambda_{\rm vac,\ br}^{43000}$ (Å)	$\lambda_{\rm vac,\ br}^{50000}$ (Å)	$\lambda_{\rm vac,\ br}^{100000}$ (Å)
5397.5160	18521.8912	5399.0167	ARII	n	B	2.41	5399.0167	5399.0167	5399.0167
5397.522	18521.871	5399.023	ArII	–	–	–	–	–	–
5397.8845	18520.6268	5399.3853	THI	⋆	⋆	-0.19	⋆	⋆	5399.3853
5398.2047	18519.5282	5399.7056	THI	⋆	⋆	0.51	⋆	⋆	5399.7056
5398.5096	18518.4823	5400.0106	THI	⋆	⋆	-0.34	⋆	⋆	⋆
5398.7015	18517.8241	5400.2025	THI	⋆	⋆	1.03	⋆	⋆	⋆
5398.9219	18517.0682	5400.4230	THI	⋆	⋆	1.20	⋆	⋆	⋆
5399.0496	18516.6302	5400.5507	ARI	⋆	⋆	0.92	⋆	⋆	⋆
5399.1745	18516.2019	5400.6756	TH	⋆	⋆	1.23	⋆	⋆	⋆
5399.6218	18514.6682	5401.1230	THI	⋆	⋆	0.55	⋆	⋆	5401.1230
5399.783	18514.115	5401.284	ArII	–	–	–	–	–	–
5400.1455	18512.8724	5401.6469	THI	n	b	0.63	5401.6464	5401.6468	5401.6469
5400.623	18511.236	5402.125	ArII	–	–	–	–	–	–
5400.7760	18510.7113	5402.2776	THI	n	b	-0.43	5402.2771	5402.2776	5402.2776
5401.230	18509.155	5402.732	ArII	–	–	–	–	–	–
5401.5354	18508.1089	5403.0371	THI	N	B	-0.24	5403.0371	5403.0371	5403.0371
5401.790	18507.237	5403.292	ArII	–	–	–	–	–	–
5402.195	18505.849	5403.697	ArII	–	–	–	–	–	–
5402.2768	18505.5690	5403.7787	THI	⋆	⋆	-0.35	⋆	⋆	⋆
5402.6048	18504.4455	5404.1068	ARII	o	b	2.26	5404.1067	5404.1068	5404.1068
5403.1993	18502.4094	5404.7015	THI	n	⋆	0.88	⋆	5404.7012	5404.7015
5404.217	18498.925	5405.719	ArII	–	–	–	–	–	–
5405.2097	18495.5278	5406.7124	THII	n	b	-0.30	5406.7122	5406.7124	5406.7124
5405.7869	18493.5530	5407.2898	THI	n	b	-0.31	5407.2895	5407.2898	5407.2898
5406.7553	18490.2406	5408.2584	THI	⋆	⋆	0.34	⋆	⋆	5408.2584
5407.3439	18488.2280	5408.8472	ARII	⋆	⋆	2.41	⋆	5408.8508	5408.8472
5407.5627	18487.4799	5409.0661	THI	⋆	⋆	0.24	⋆	⋆	⋆
5407.6535	18487.1694	5409.1569	THI	⋆	⋆	1.75	⋆	⋆	5409.1558
5408.7485	18483.4268	5410.2522	THI	⋆	⋆	-0.06	⋆	⋆	⋆
5408.8642	18483.0314	5410.3679	TH	⋆	⋆	-0.28	⋆	⋆	⋆
5409.421	18481.129	5410.925	ArII	–	–	–	–	–	–
5410.4730	18477.5356	5411.9771	ARI	⋆	⋆	1.51	⋆	⋆	5411.9771
5410.475	18477.529	5411.979	ArI	–	–	–	–	–	–
5410.7687	18476.5258	5412.2729	THI	o	⋆	1.59	⋆	⋆	5412.2729
5411.669	18473.452	5413.173	ArII	–	–	–	–	–	–
5412.2212	18471.5672	5413.7258	TH	⋆	⋆	0.27	⋆	⋆	⋆
5412.4463	18470.7990	5413.9510	ARII	⋆	⋆	1.35	⋆	5413.9473	5413.9510
5412.6707	18470.0332	5414.1754	THI	⋆	⋆	-0.42	⋆	⋆	⋆
5413.3798	18467.6139	5414.8847	ARI	⋆	b	0.81	5414.8852	5414.8848	5414.8847
5413.8064	18466.1586	5415.3114	TH	⋆	⋆	-0.10	⋆	⋆	⋆
5413.9184	18465.7766	5415.4235	THI	⋆	⋆	-0.11	⋆	⋆	⋆
5414.0652	18465.2759	5415.5703	TH	⋆	⋆	-0.37	⋆	⋆	⋆
5414.5246	18463.7092	5416.0298	TH	o	c	-0.03	5416.0281	5416.0294	5416.0298
5415.4329	18460.6124	5416.9384	THII	⋆	⋆	0.89	⋆	⋆	⋆
5415.5226	18460.3067	5417.0281	THI	⋆	⋆	1.17	⋆	⋆	⋆
5415.5717	18460.1393	5417.0772	TH	⋆	⋆	-0.02	⋆	⋆	⋆
5415.880	18459.088	5417.386	ArII	–	–	–	–	–	–
5416.744	18456.144	5418.250	ArII	–	–	–	–	–	–
5417.2560	18454.3998	5418.7620	ARI	⋆	⋆	0.81	⋆	⋆	⋆
5417.2929	18454.2741	5418.7989	TH	⋆	⋆	-0.32	⋆	⋆	⋆
5417.4858	18453.6170	5418.9918	THI	n	s	1.97	5418.9865	5418.9880	5418.9918
5417.8079	18452.5199	5419.3140	THI	⋆	⋆	-0.01	⋆	⋆	5419.3139
5418.2225	18451.1079	5419.7287	THI	⋆	⋆	-0.29	⋆	⋆	5419.7287
5419.1285	18448.0232	5420.6350	THI	N	B	0.53	5420.6350	5420.6350	5420.6350
5421.2086	18440.9448	5422.7157	THII	⋆	⋆	-0.15	⋆	⋆	⋆

cont'd ...

Order 105 (R 70000)

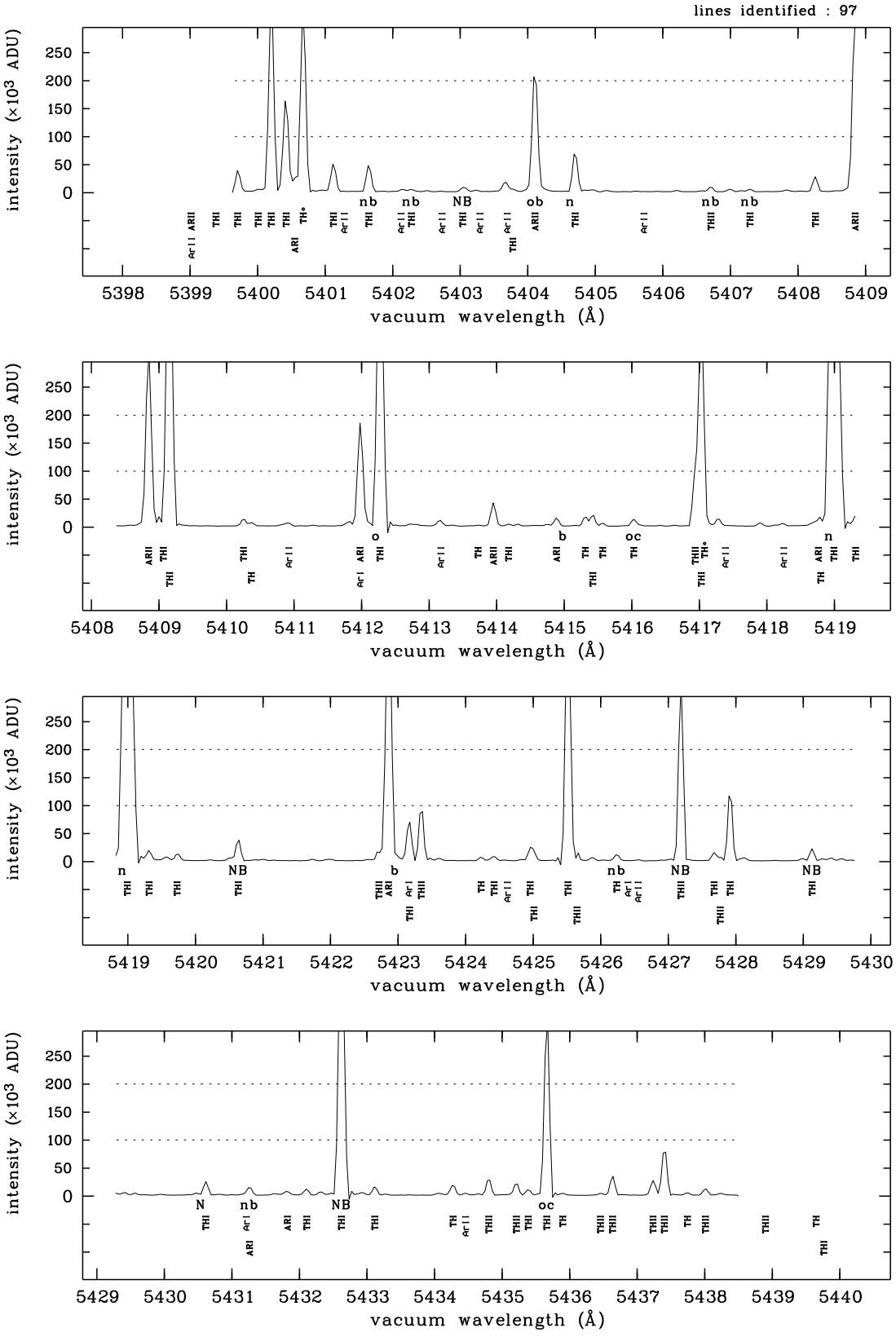

Order 105

(page 2/2)

$\lambda_{\rm air}$ (Å)	$\lambda_{\rm vac}^{-1}$ (cm^{-1})	$\lambda_{\rm vac}$ (Å)	Emit.	$S_{\rm nm}^{43}$	$S_{\rm br}^{43}$	$I_{\rm rel}^{\rm br}$	$\lambda_{\rm vac,\ br}^{43000}$ (Å)	$\lambda_{\rm vac,\ br}^{50000}$ (Å)	$\lambda_{\rm vac,\ br}^{100000}$ (Å)
5421.3517	18440.4580	5422.8588	ARI	⋆	b	2.11	5422.8590	5422.8587	5422.8587
5421.653	18439.433	5423.160	ArI	–	–	–	–	–	–
5421.6628	18439.3999	5423.1700	THI	⋆	⋆	0.38	⋆	⋆	⋆
5421.8359	18438.8113	5423.3431	THII	⋆	⋆	0.56	⋆	⋆	⋆
5422.7230	18435.7950	5424.2304	TH	⋆	⋆	-0.34	⋆	⋆	⋆
5422.9151	18435.1420	5424.4226	THI	⋆	⋆	-0.38	⋆	⋆	⋆
5423.110	18434.479	5424.617	ArII	–	–	–	–	–	–
5423.4469	18433.3344	5424.9545	THI	⋆	⋆	0.00	⋆	⋆	⋆
5423.5035	18433.1421	5425.0111	THI	⋆	⋆	0.03	⋆	⋆	⋆
5424.0079	18431.4280	5425.5156	THI	s	s	1.45	5425.5188	5425.5185	5425.5162
5424.1397	18430.9801	5425.6474	THII	⋆	⋆	0.01	⋆	⋆	⋆
5424.7296	18428.9758	5426.2375	TH	n	b	0.04	5426.2372	5426.2375	5426.2375
5424.896	18428.411	5426.404	ArI	–	–	–	–	–	–
5425.045	18427.904	5426.553	ArII	–	–	–	–	–	–
5425.6783	18425.7534	5427.1865	THII	N	B	1.35	5427.1865	5427.1865	5427.1865
5426.1705	18424.0820	5427.6788	THI	⋆	⋆	-0.05	⋆	⋆	⋆
5426.2616	18423.7727	5427.7700	THII	⋆	⋆	-0.40	⋆	⋆	⋆
5426.4075	18423.2773	5427.9159	THI	⋆	⋆	0.57	⋆	⋆	5427.9145
5427.6207	18419.1593	5429.1294	THI	N	B	0.06	5429.1294	5429.1294	5429.1294
5429.1048	18414.1243	5430.6139	THI	N	⋆	0.31	⋆	5430.6139	5430.6139
5429.704	18412.092	5431.213	ArI	–	–	–	–	–	–
5429.7510	18411.9328	5431.2603	ARI	n	b	0.92	5431.2601	5431.2603	5431.2603
5430.3130	18410.0273	5431.8225	ARI	⋆	s	0.81	5431.8262	5431.8248	5431.8225
5430.5977	18409.0621	5432.1073	THI	⋆	⋆	-0.22	⋆	⋆	5432.1071
5431.1120	18407.3189	5432.6217	THI	N	B	1.48	5432.6217	5432.6217	5432.6217
5431.6053	18405.6471	5433.1151	THI	⋆	⋆	-0.04	⋆	⋆	5433.1151
5432.7650	18401.7183	5434.2751	TH	⋆	⋆	-0.04	⋆	⋆	5434.2751
5432.950	18401.092	5434.460	ArII	–	–	–	–	–	–
5433.2919	18399.9338	5434.8022	THII	⋆	⋆	0.20	⋆	⋆	5434.8022
5433.7005	18398.5502	5435.2109	THII	⋆	⋆	0.29	⋆	⋆	⋆
5433.8767	18397.9536	5435.3871	THI	⋆	⋆	-0.11	⋆	⋆	⋆
5434.1514	18397.0236	5435.6619	THI	o	c	1.19	5435.6601	5435.6612	5435.6619
5434.3871	18396.2257	5435.8976	TH	⋆	⋆	-0.48	⋆	⋆	⋆
5434.9460	18394.3341	5436.4567	THII	⋆	⋆	-0.47	⋆	⋆	⋆
5435.1229	18393.7354	5436.6336	THII	⋆	⋆	0.54	⋆	⋆	5436.6332
5435.7236	18391.7027	5437.2345	THII	⋆	⋆	0.25	⋆	⋆	⋆
5435.8925	18391.1313	5437.4034	THII	⋆	⋆	0.97	⋆	⋆	5437.4023
5436.2319	18389.9831	5437.7429	TH	⋆	⋆	-0.25	⋆	⋆	5437.7428
5436.4980	18389.0829	5438.0091	THII	⋆	⋆	-0.09	⋆	⋆	5438.0091
5437.3877	18386.0740	5438.8990	THII	N	B	0.84	5438.8990	5438.8990	5438.8990
5438.1374	18383.5393	5439.6489	TH	⋆	⋆	0.49	⋆	⋆	⋆
5438.2515	18383.1536	5439.7631	THI	⋆	⋆	-0.36	⋆	⋆	⋆

Order 105 (R 70000)

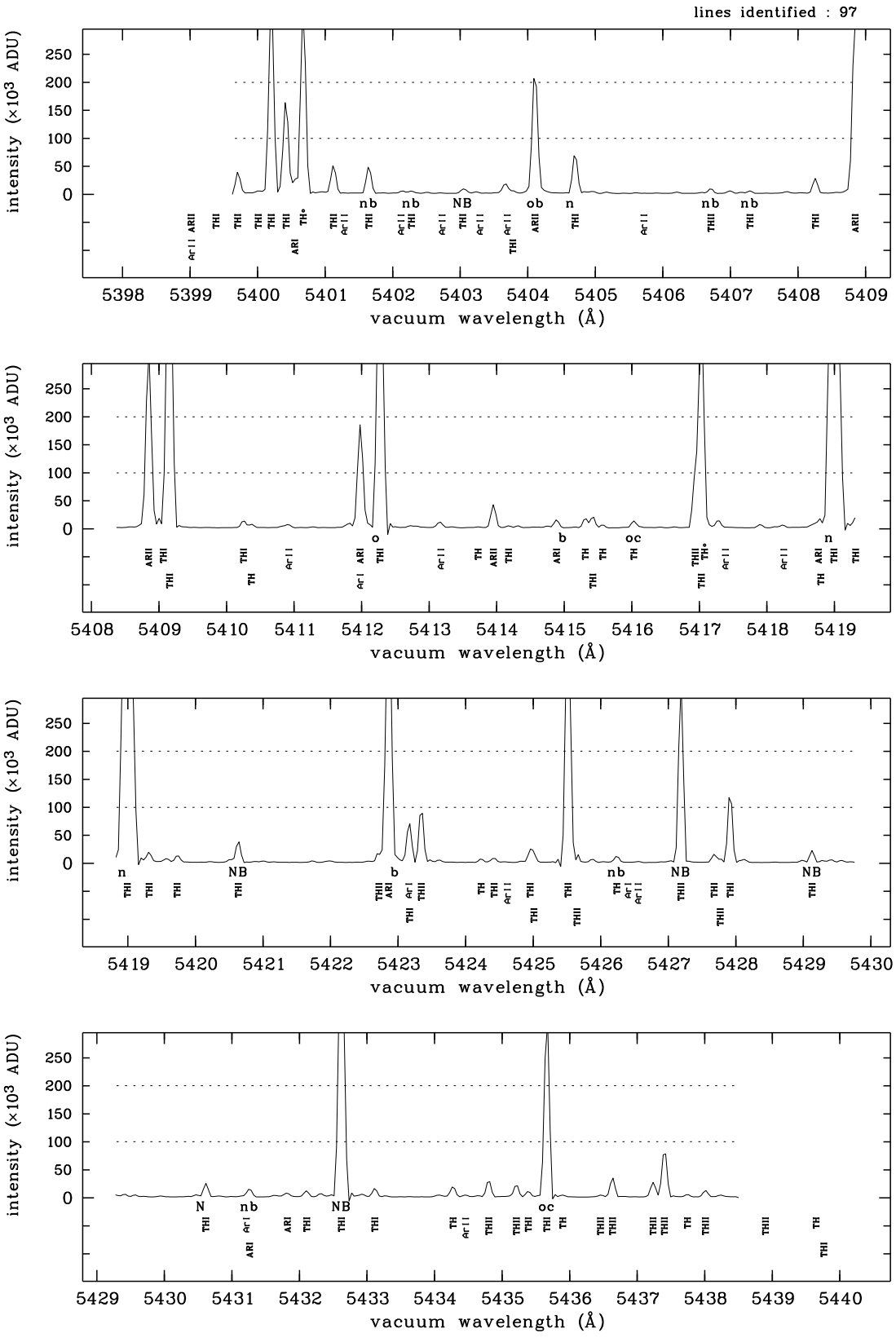

Acknowledgements

There are many individuals and organisations that have provided assistance, in one way or another, during my PhD studies.

First, my thanks go to my supervisors, Prof. John Hearnshaw and Dr Jovan Skuljan, whose advice, guidance and suggestions helped me achieve this challenging goal, after many years occupied doing something rather different. One of the memorable aspects of the many meetings with them over the past four years, was that I beleive I always went away having learnt something of interest or value to my understanding of astronomy and its many facets. I also had the benefit of the support and suggestions of a mentor, Ass. Prof. Peter Cottrell, whom I also thank.

I would next like to acknowledge the always-friendly staff at the Mt John University Observatory who helped in so many ways: Alan, Pam, Maryrose, Nigel and Steve. The contributions made by other technical staff involved with the HERCULES project based at Canterbury, Graeme, Geoff and Ross, were also appreciated.

During the course of this research I have been so very fortunate to receive the financial support of the following Scholarships: Bright Future Top Achiever Doctoral Scholarship, D. W. Moore Scholarship, and a Freemasons Postgraduate Scholarship. My considerable thanks go to the various people who make these awards possible, which of course includes the helpful University of Canterbury Scholarships Office staff, Jacky Creelman, Toni Hodge and Jane Bolton.

The efforts and kindnesses of other people I would like to acknowledge include the Physical Sciences Library staff, in particular the interloans librarian, Angela Davies, who helped me obtain several items that required her patience and skills. Thanks also to the staff of the Physics and Astronomy Department, the efforts of my many other teachers over the years, and the light (and occasionally not so light) relief provided by my fellow students and colleagues including Stuart, Ljiljana, William, Orlon, Jenny, Sarah, Mike, John, Liz, Katja, Malcolm, and Duncan.

Almost finally, I would like to thank my family (including Joan's) for their support and curiousity, and my other friends, for not forgetting I was still around somewhere (though usually in front of a computer).

Last, and absolutely not least, I would like to say thank you, thank you, thank you, to Joan for her endless love and support throughout the past four, sometimes difficult, years.

References

Abt H. A., 1979, 'The frequency of binaries on the main sequence', *AJ*, **184**, 1591–1597

Abt H. A., Sanwal N. B., Levy S. G., 1980, 'Visual multiples. V. Radial velocities of 160 systems', *ApJS*, **43**, 549–575

Adelman S. J., 2001, 'Research Note. Hipparcos photometry: The least variable stars', *A&A*, **367**, 297–298

Aitken R. G., 1935, 'The binary stars. 2nd ed.', McGraw-Hill, New York

Alden H. L., 1939, 'The orbit of ν Octantis', *AJ*, **48**, 81–84

Allen C. W., 1991, 'Astrophysical quantities', 3rd edition, The Athlone Press, London

Allende Prieto C., Lambert D. L., 1999, 'Fundamental parameters of nearby stars from the comparison with evolutionary calculations: masses, radii and effective temperatures', *A&A*, **352**, 555–562

Andersen J., 1991, 'Accurate masses and radii of normal stars', *A&AR*, **3**, 91–126

Andersen J., 1993, 'Stellar masses and radii as constraints on stellar models', Proceedings of the IAU Colloquium No. 137: 'Inside the stars', ASP Conference Series, Vol. 40, Weiss W. W., Baglin A. (eds.), Univ. of Vienna, Austria, pp. 347–360

Andersen J., 1997, 'Precise stellar mass and mass-luminosity data', Proceedings of the IAU Symposium No. 189: 'Fundamental stellar properties: The interaction between observation and theory', Bedding T. R., Booth A. J., Davis J. (eds.), Kluwer Academic Publishers, Dordrecht, The Netherlands, pp. 99–108

Andersen J., Clausen J. V., Helt B. E., Johansen K. T., Nordström B., García M., Giménez A., Stepinski T. F., Vaz L. P. R., 1993, 'Accurate masses and radii as test data for stellar models: Status and progress on the Copenhagen project', Proceedings of the IAU Colloquium No. 137: 'Inside the stars', ASP Conference Series, Vol. 40, Weiss W. W., Baglin A. (eds.), Astronomical Society of the Pacific, pp. 361–363

Bahcall J. N., Soneira R. M., 1980, 'The universe at faint magnitudes. I. Models for the galaxy and the predicted star counts', *ApJS*, **44**, 73–110

Baize P., 1950, 'Second catalogue d'orbites d'étoiles doubles visuelles', *J. des Observateurs*, **33**, 1–31

Baize P., 1966, 'Catalogue de 240 couples visuels d'étoiles naines rouges', *J. des Observateurs*, **49**, 1–42

Baliunas S. L., Donahue R. A., Soon W. H., Horne J. H., and 23 co-authors, 1995, 'Chromospheric variations in main-sequence stars', *ApJ*, **438**, 269–287

Balona L. A., 1984, 'Calibration of effective temperature, bolometric correction and mass for early-type stars using Strömgren photometric indices', *MNRAS*, **211**, 973–979

Balona L. A., 1994, 'Effective temperature, bolometric correction and mass calibration for O-F stars', *MNRAS*, **268**, 119–127

Baraffe I., Chabrier G., Allard F., Hauschildt P. H., 1998, 'Evolutionary models for solar metallicity low-mass stars: mass-magnitude relationships and color-magnitude diagrams', *A&A*, **337**, 403–412

Barbier-Brossat M., Figon P., 2000, 'Catalogue general de vitesses radiales moyennes pour les etoiles galactiques. Mean Radial Velocities Catalog of Galactic Stars', *A&AS*, **142**, 217–223

Barker D. S., Evans D. S., Laing J. D., 1967, 'Orbital elements of nine spectroscopic binaries', *Royal Obs. Bull. Series E,*, **130**, 355–362

Batten A. H., 1969, 'Sixth Catalogue of the Orbital Elements of Spectoscopic Binary Systems', Publ. Dom. Astrophys. Obs., Vic. Canada

Batten A. H., 1973, 'Binary and multiple systems of stars', Pergamon Press, Oxford

Batten A. H., Fletcher J. M., 1990, 'Some preliminary statistical results from the eighth catalogue of the orbital elements of spectroscopic binary systems', *Bull. Astr. Soc. India*, **18**, 285–294

Batten A. H., Fletcher J. M., MacCarthy D. G., 1989, 'Eighth Catalogue of the Orbital Elements of Spectoscopic Binary Systems', Publ. Dom. Astrophys. Obs., Vic. Canada

Beasley A. J., Stewart R. T., Carter B. D., 1992, 'Non-thermal radio emission from post-main-sequence stars', *MNRAS*, **254**, 1–6

Beavers W. I., Eitter J. J., 1986, 'E. W. Fick Observatory stellar radial-velocity measurements. I. 1976-1984', *ApJS*, **62**, 147–228

Beckers J. M., 1993, 'Adaptive optics for astronomy - Principles, performance, and applications', *ARA&A*, **31**, 13–62

Bensby T., Feltzing S., Lundstöm I., 2003, 'Elemental abundance trends in the Galactic thin and thick disks as traced by nearby F and G dwarf stars', *A&A*, **410**, 527–551

Bergeron P., Leggett S. K., Ruiz M. T., 2001, 'Photometric and spectroscopic analysis of cool white dwarfs with trigonometric parallaxes', *ApJS*, **133**, 413–449

Bertelli G., Bressan A., Chiosi C., Fagotto F., Nasi E., 1994, 'Theoretical isochrones from models with new radiative opacities', *A&AS*, **106**, 275–302

Bessell M. S., 1990, 'BVRI photometry of the Gliese catalogue stars', *A&AS*, **83**, 357–378

Bessell M. S., Wood P., 1984, 'A note on bolometric corrections for late-type stars and long-period variables', *PASP*, **96**, 247–249

Beuzit J.-L., Ségransan D., Forveille T., Udry S., Delfosse X., Mayor M., Perrier C., Hainaut M.-C, Roddier C., Roddier F., Martin E. L., 2004, 'New neighbours. III. 21 new companions to nearby dwarfs, discovered with adaptive optics', *A&A*, **425**, 997–1008

Bevington P. R., 1969, 'Data reduction and error analysis for the physical sciences', McGraw-Hill, New York

Binnendijk L., 1960, 'Properties of double stars', Univ. of Pennsylvania Press, Philadelphia

Boffin H. M. J., Cerf N., Paulus G., 1993, 'Statistical analysis of a sample of spectroscopic binaries containing late-type giants', *A&A*, **271**, 125–138

Böhm-Vitense E., 1992, 'Introduction to stellar astrophysics. Vol. 3: Stellar structure and evolution', Cambridge Uni. Press, New York

Bonneau D., Blazit A., Foy R., Labeyrie A., 1980, 'Speckle interferometric measurements of binary stars', *A&AS*, **42**, 185–188

Bouchy F., Pepe F., Queloz D., 2001, 'Fundamental photon noise limit to radial-velocity measurement', *A&A*, **374**, 733–739

Branch D., 1976, 'On the multiplicity of solar-type stars', *ApJ*, **210**, 392–394

Brault W. J., White R. O., 1971, 'The analysis and restoration of astronomical data via the Fast Fourier transform', *A&A*, **13**, 169–189

Buscombe W., Morris P. M., 1958, 'Radial velocities of fundamental southern stars', *MNRAS*, **118**, 609–617

Butler R. P., 1993, 'Cepheid velocity curves from the lines of different excitation and ionization. I. Observations', *ApJ*, **415**, 323–334

Cannon A., Pickering E. C., 1918, 'Henry Draper catalogue', Harvard Annals, London

Cannon R. D., 1970, 'Red giants in old clusters', *MNRAS*, **150**, 111–135

Cayrel de Strobel G., Soubiran C., Ralite N., 2001, 'Catalogue of [Fe/H] determinations for FGK stars: 2001 edition', *A&A*, **373**, 159–163

Cester B., 1962, 'Elementi della doppia visuale ADS 16417', *Mem. S.A.It.*, **33**, 331

Charles P. A., Seward F. D., 1995, 'Exploring the X-ray universe', Cambridge Uni. Press, Cambridge

Christie W. H., 1936, 'The provisional elements of 16 spectroscopic binaries', *ApJ*, **83**, 433–438

Christy J. W., Walker R. L., 1969, 'MK classification of 142 visual binaries', *PASP*, **81**, 643–649

Claret A., Cunha K., 1997, 'Circularization and synchronization times in Main-Sequence of detached eclipsing binaries II. Using the formalisms by Zahn', *A&A*, **318**, 187–197

Colacevich A., 1935, 'Provisional elements of the spectroscopic binary ν Octantis', *PASP*, **47**, 87–88

Colacevich A., 1937, 'Gli elementi orbitali di ν Octantis', *Rend. Della R. Acad. Nazionale dei Lincei*, **26**, 7–13

Colwell P., 1993, 'Solving Kepler's equation over three centuries', Willmann-Bell, Inc., Richmond, Virginia

Costa J. M., da Silva L., Nascimento J. D. Jr., de Medeiros J. R., 2002, 'The tidal effects on the lithium abundance of binary systems with giant component', *A&A*, **382**, 1016–1020

Cousins A. W. J., 1987, 'Secondary standards for the Stromgren uvby system', *South Afr. Astron. Obs. Circ.*, **11**, 93–120

Cousins A. W. J., 1990, 'Secondary standards for H-beta photometry in the Southern Hemisphere (2nd series)', *South Afr. Astron. Obs. Circ.*, **14**, 55–62

Cousins A. W. J., Stoy R. H., 1962, 'Standard magnitudes in the E regions', *Royal Green. Obs. Bull.*, **49**, 3-

Couteau P., 1981, 'Observing visual double stars', MIT Press, Cambridge, pp. 151–153

Cox A. N., 1980, 'The masses of cepheids', *ARA&A*, **18**, 15–43

Crawford R. T., 1937, 'The orbit of OΣ 536', *PASP*, **49**, 37

Cummings I. N., 1998, 'High precision radial-velocity measurements of late-type evolved stars', PhD thesis, Uni. of Canterbury

Cummings I. N., Hearnshaw J. B., Kilmartin P. M., Gilmore A. C., 1999, 'High precision radial-velocity measurements of late-type evolved stars', Proceedings of the IAU Colloquium No. 170: 'Precise stellar radial velocities', ASP Conference Series, Vol. 185, Hearnshaw J. B., Scarfe C. D. (eds.), Astronomical Society of the Pacific, pp. 204–210

Danner R., Unwin S. (eds.)., 1999, 'SIM: Space Interferometry Mission', Jet Propulsion Laboratory, California

Davis J., 1999, 'Combining high angular-resolution interferometry and spectroscopy in studies of stars and stellar systems', Proceedings of the IAU Colloquium No. 170: 'Precise stellar radial velocities', ASP Conference Series, Vol. 185, Hearnshaw J. B., Scarfe C. D. (eds.), Astronomical Society of the Pacific, pp. 390–400

De Buizer J. M., van der Bliek N. S. (eds.)., 2003, 'ASP Conference Series 'Galactic star formation across the mass stellar spectrum, Vol. 287", Astronomical Society of the Pacific, San Francisco

De Cuyper J.-P, Hensberge H., 1998, 'Wavelength calibration at moderately high resolution', *A&AS*, **128**, 409–416

de Jager C., Nieuwenhuijzen H., van der Hucht K. A., 1988, 'Mass loss rates in the Hertzsprung-Russell diagram', *A&AS*, **72**, 259–289

Delfosse X., Forveille T., Mayor M., Burnet M., Perrier C., 1999, 'GJ 2069A, a new M dwarf eclipsing binary', *A&A*, **341**, L63–L66

Delfosse X., Forveille T., Ségransan D., Beuzit J.-L., Udry S., Perrier C., Mayor M., 2000, 'Accurate masses of very low mass stars. IV. Improved mass-luminosity relations', *A&A*, **364**, 217–224

Dommanget J., Lampens P., 1993, 'A development of double star astronomy after Hipparcos', *Ap&SS*, **200**, 221–238

Donahue R. A., 1993, 'Surface differential rotation in a sample of cool dwarf stars', PhD thesis, New Mexico State Uni.

Dravins D., 1999, 'Stellar surface convection, line asymmetries, and wavelength shifts', Proceedings of the IAU Colloquium No. 170: 'Precise stellar radial velocities', ASP Conference Series, Vol. 185, Hearnshaw J. B., Scarfe C. D. (eds.), Astronomical Society of the Pacific, pp. 268–276

Dravins D., Nordlund Å., 1990, 'Stellar granulation. V. Synthetic spectral lines in disk-integrated starlight', *A&A*, **228**, 203–217

Dravins D., Lindegren L., Madsen S., 1999, 'Astrometric radial velocities I. Non-spectroscopic methods for measuring stellar radial velocity', *A&A*, **348**, 1040–1051

Drilling J. S., Landolt A. U., 2000, 'Normal stars', in Allen's Astrophysical Quantities. 4$^{\text{th}}$ ed., Cox A. N. (ed.), Springer-Verlag, New York, pp. 381–396

Duquennoy A., Mayor M., 1991, 'Multiplicity among solar-type stars in the solar neighbourhood. II. Distribution of the orbital elements in an unbiased sample', *A&A*, **248**, 485–524

Duquennoy A., Mayor M., (eds.)., 1992, 'Binaries as tracers of stellar formation', Cambridge Uni. Press, Cambridge

Eddington A. S., 1926, 'The internal constitution of the stars', Cambridge Uni. Press, Cambridge

Edvardsson B., Andersen J., Gustafsson B., Lambert D. L., Nissen P. E., Tompkin J., 1993, 'The chemical evolution of the Galactic disk – Part One – Analysis and results', *A&A*, **275**, 101–152

Edwards T. W., 1976, 'MK classification for visual binary components', *AJ*, **81**, 245–249

Eggenberger A., Halbwachs J.-L, Udry S., Mayor M., 2004, 'Statistical properties of an unbiased sample of F7–K binaries: towards the long-period systems', *RevMexAA*, **21**, 28–32

Eggen O. J., 1955, 'Magnitudes and colors for 833 Northern and Southern stars', *AJ*, **60**, 65–92

Eggen O. J., 1967, 'Masses of visual binary stars', *ARA&A*, **5**, 105–138

Eggen O. J., 1969, 'Stellar groups in the old disk population', *PASP*, **81**, 553–593

Eggen O. J., 1971, 'The ζ Herculis, σ Puppis, ϵ Indi, and η Cephei groups of old disk population stars', *PASP*, **83**, 251–270

Eggen O. J., 1993, 'Evolved GK stars near the Sun. I. The old disk population', *AJ*, **106**, 80–132

Eggen O. J., 1998, 'Kinematics and metallicity of stars in the solar region', *AJ*, **115**, 2397–2434

Eggleton P. P., 1983, 'Approximations to the radii of Roche lobes', *ApJ*, **268**, 368–369

Eggleton P. P., Tout C. A., 1989, 'The evolution of moderately close and moderately wide binaries', *Space Sci. Rev.*, **50**, 165–177

ESA, 1992, 'The Hipparcos Input Catalogue, Vol. 6, Annex 1', ESA SP–1136, p. 383

ESA, 1997, 'The Hipparcos Catalogue', ESA Publications SP-1200, The Netherlands

Evans D. S., 1961, 'Observations of twenty-four single-lined variables', *Royal Obs. Bull. Series E,*, **44**, 351–363

Evans D. S., Menzies A., Stoy R. H., 1957, 'Fundamental data for southern stars (first list)', *MNRAS*, **117**, 534–561

Forbes M. C., Dodd R. J., Sullivan D. J., 1997, 'The southern Vilnius photometric system. IV. The E region standard stars', *Baltic Astron.*, **6**, 371–376

Forveille T., Beuzit J.-L., Delfosse X., Ségransan D., Beck F., Mayor M., Perrier C., Tokovinin A. A., Udry S., 1999, 'Accurate masses of very low mass stars. I. Gl 570BC', *A&A*, **351**, 619–626

Fracassini M., Pasinetti L. E., Borella M., Pasinetti A. L., 1985, 'MKJ and MSS classification of solar-type stars within 100 parsecs of the sun: preliminary results', Proceedings of 'Calibration of fundamental stellar quantities', Hayes D. S. (ed.), IAU Symp., pp. 407–410

Fracassini M., Pasinetti-Fracassini L. E., Pasinetti A. L., 1988, 'Fermi paradox and alternative strategies for SETI programs: the anthropic principle and the search for close solar analogs', *Ap&SS*, **146**, 321–331

Fuhrmeister B., Schmitt J. H. M. M., 2003, 'A systematic study of X-ray variability in the ROSAT All-Sky Survey', *A&A*, **247**, 247–260

Ghosh H., De Poy D. L., Gal-Yam A., Gaudi B. S., Gould A., Han C., and 57 co-authors, 2004, 'Potential direct single-star mass measurement', *ApJ*, **615**, 450–459

Giannuzzi M. A., 1987, 'Visual binary systems in the solar neighbourhood: The mass-ratio distribution', *Ap&SS*, **135**, 245–252

Gil-Hutton R., Benavidez P., 2003, 'Southern stars that can be used as unpolarized standards', *MNRAS*, **345**, 97–99

Ginestet N., Carquillat J. M., 2002, 'Spectral classification of the hot components of a large sample of stars with composite spectra, and implication for the absolute magnitudes of the cool supergiant components', *ApJS*, **143**, 513–537

Girardi L., Salaris M., 2001, 'Population effects on the red clump absolute magnitude, and distance determinations to nearby galaxies', *MNRAS*, **323**, 109–129

Girardi L., Bressan A., Bertelli G., Chiosi C., 2000, 'Evolutionary tracks and isochrones for low- and intermediate-mass stars: From 0.15 to 7 $M_{\odot}$, and from $Z = 0.0004$ to 0.03', *A&AS*, **141**, 371–383

Gliese W., Jahreiss H., 1988, 'The Third Catalogue of Nearby Stars with special emphasis on wide binaries', *Ap&SS*, **142**, 49–56

Gliese W., Jahreiss H., 1991, 'Preliminary version of the third catalogue of nearby stars', Astron. Rechen-Institut, Heidelberg

Goldberg D., Mazeh T., Latham D. W., Stefanik R. P., Carney B. W., Laird J. B., 2002, 'A survey of proper-motion stars. XV. Orbital solutions for 34 double-lined spectroscopic binaries', *AJ*, **124**, 1132–1143

Goldman I., Mazeh T., 1991, 'On the orbital circularization of close binaries', *ApJ*, **376**, 260–265

Goldstein H., Poole C., Safko J., 2002, 'Classical mechanics', Addison-Wesley, San Francisco

Gray D. F., 1967, 'Photometric determination of stellar radii', *ApJ*, **149**, 317–343

Gray D. F., 1968, 'A list of photometric stellar radii', *AJ*, **73**, 769–771

Gray D. F., 1997, 'Absence of a planetary signature in the spectra of the star 51 Pegasi', *Nature*, **385**, 795–796

Gray R. O., Corbally C. J., Garrison R. F., McFadden M. T., Robinson P. E., 2003, 'Contributions to the Nearby Stars (NSTARS) Project: Spectroscopy of stars earlier than M0 within 40 parsecs: The northern sample', *AJ*, **126**, 2048–2059

Griffin R. E. M., Griffin R. F., 2004, 'Composite spectra. Paper 13: 93 Leonis, a chromospherically-active binary', *MNRAS*, **350**, 685–706

Griffin R. E. M., David M., Verschueren W., 2000, 'Accuracy of radial-velocity measurements for early-type stars. II. Investigations of spectrum mismatch from high-resolution observations', *A&AS*, **147**, 299–321

Griffin R. F., 1992, 'Spectroscopic studies of binary and multiple star systems', Proceedings of the IAU Colloquium No. 135: 'Complementary approaches to double and multiple star research', ASP Conference Series, Vol. 32, McAlister H. A., Hartkopf W. I. (eds.), Astronomical Society of the Pacific, San Francisco, pp. 98–109

Gullberg D., Lindegren L., 2002, 'Determination of accurate radial-velocity measures', *A&A*, **390**, 383–395

Gulliver A. F., Hill G., 1990, 'A test of selected comparison-line fitting techniques', *PASP*, **102**, 1200–1207

Halbwachs J.-L, 1981, 'List of estimated angular separations of spectroscopic binaries', *A&AS*, **44**, 47–53

Halbwachs J.-L, 1983, 'Binaries among the bright stars: estimation of the bias and study of the main-sequence stars', *A&A*, **128**, 399–404

Halbwachs J.-L, 1986, 'Binaries among bright stars: systems with evolved primary components and their relation to the properties of main-sequence binaries', *A&A*, **168**, 161–168

Halbwachs J.-L, Mayor M., Udry S., Arenou F., 2003, 'Multiplicity among solar-type stars. III. Statistical properties of the F7–K binaries with periods up to 10 years', *A&A*, **397**, 159–175

Hardrop J., 1982, 'The sun among the stars. V. A second search for solar spectral analogs. The Hyades' distance', *A&A*, **105**, 120–132

Harries T. J., Hilditch R. W., Howarth I. D., 2003, 'Ten eclipsing binaries in the Small Magellanic Cloud: fundamental parameters and Cloud distance', *MNRAS*, **339**, 157–172

Hartkopf W. I., Mason B. D., 2004, 'Sixth Catalog of Orbits of Visual Binary Stars', U.S. Naval Obs., `http://ad.usno.navy.mil/wds/orb6.html`

Hartkopf W. I., Mason B. D., Worley C. E., 2001, 'Fifth Catalog of Orbits of Visual Binary Stars', U.S. Naval Obs., `http://www.ad.usno.navy.mil/wds/orb5/hmw5.html`

Harwit M., 1998, 'Astrophysical concepts. 3rd ed.', Springer-Verlag, New York, p. 599

Hearnshaw J. B., 1986, 'The analysis of starlight', Cambridge Uni. Press, Cambridge

Hearnshaw J. B., Barnes S. I., Kershaw G. M., Frost N., Graham G., Ritchie R., Nankvell G. R., 2002, 'The HERCULES échelle spectrograph at Mt John', *Expt. Astron.*, **13**, 59–76

Heck A., 1977, '*uvbyβ* photometry of equatorial and southern bright stars', *A&AS*, **27**, 47–53

Heintz W. D., 1969, 'A statistical study of binary stars', *J. Royal Astron. Soc. Can.*, **63**, 275–298

Heintz W. D., 1981, 'Radial velocities of binary and proper-motion stars', *ApJS*, **46**, 247–253

Heintz W. D., 1982, 'Orbits of 16 visual binaries', *A&AS*, **47**, 569–573

Heintz W. D., 1992, 'Stars: masses, luminosities, and radii', in The Astronomy and Astrophysics Encyclopaedia, Maran S. P. (ed.), Cambridge Uni. Press, Cambridge, p. 760

Henry T. J., 2004, 'The mass-luminosity relation from end to end', Proceedings of ASP Conference Series, 'Spectroscopically and Spatially Resolving the Components of the Close Binary Stars, Vol. 318', Hilditch R. W., Hensberge H., Pavlovski K. (eds.), Astronomical Society of the Pacific, pp. 159–165

Henry T. J., McCarthy D. W., 1993, 'The mass-luminosity relation for stars of mass 1.0 to 0.8 $\mathcal{M}_\odot$', *AJ*, **106**, 773–789

Henry T. J., Soderblom D. R., Donahue R. A., Baliunas S. L., 1996, 'A survey of Ca II H and K chromospheric emission in southern solar-type stars', *AJ*, **111**, 439–465

Hilditch R. W., 2001, 'An introduction to close binary stars', Cambridge Uni. Press, Cambridge

Hill G., 1993, 'The measurement of radial velocities using cross-correlation techniques as applied to binary stars', Proceedings of ASP Conference Series 'New frontiers in binary star research, Vol. 38', Leung K.-C, Nha I.-S (eds.), Astronomical Society of the Pacific, San Francisco, pp. 127–153

Hill G., Fisher W. A., Holmgren D., 1990, 'Studies of late-type binaries. IV. The physical parameters of ER Vulpeculae', *A&A*, **238**, 145–159

Hogeveen S. J., 1990, 'The mass-ratio distribution of visual binary stars', *Ap&SS*, **173**, 315–342

Hogeveen S. J., 1992, 'Statistical properties of spectroscopic binary stars — as derived from the 'Eighth Catalogue of the Orbital Elements of Spectroscopic Binary Stars", *Ap&SS*, **193**, 29–46

Houk N., 1978, 'Michigan catalogue of two dimentional spectral types for the HD stars. (Vol.2: −52 to −40 degrees)', Univ. of Michigan, Ann Arbor

Houk N., 1982, 'Michigan catalogue of two dimentional spectral types for the HD stars. (Vol.3: −40 to −26 degrees)', Univ. of Michigan, Ann Arbor

Houk N., Cowley A. P., 1975, 'Michigan catalogue of two dimentional spectral types for the HD stars. (Vol.1, $-90^\circ < \delta < -53^\circ$)', Univ. of Michigan, Ann Arbor

Humphreys R. M., 1992, 'R136a and the possibility of supermassive stars', in The Astronomy and Astrophysics Encyclopaedia, Maran S. P. (ed.), Cambridge Uni. Press, Cambridge, p. 743

Hünsch M., Schmitt J. H. M. M., Schröder K.-P, Reimers D., 1996, 'ROSAT X-ray observations of a complete, volume-limited sample of late-type giants', *A&A*, **310**, 801–812

Hünsch M., Schmitt J. H. M. M., Sterzik M. F., Voges W., 1999, 'The ROSAT all-sky survey catalogue of the nearby stars', *A&AS*, **135**, 319–338

Hut P., 1981, 'Tidal evolution in close binary systems', *A&A*, **99**, 126–140

Ibukiyama A., Arimoto N., 2002, '*HIPPARCOS* age-metallicity relation of the solar neighbourhood disc stars', *A&A*, **394**, 927–941

Irwin J. B., 1973, 'The least-squares determination of mass ratios of spectroscopic binaries', *ApJ*, **179**, 241–247

Isobe T., Feigelson E. D., Akritas M. G., Babu G. J., 1990a, 'Linear regression in astronomy. I.', *ApJ*, **364**, 104–113

Isobe T., Norimoto Y., Noguchi M., Ohtsubo J., Baba N., Miura N., Yanaka H., Tanaka T., 1990b, 'Speckle observations of visual and spectroscopic binaries. II.', *Publ. Natl. Astron. Obs. Japan*, **4**, 381–392

Johnson H. M., Wright C. D., 1983, 'Predicted infrared brightness of stars within 25 parsecs of the sun', *ApJS*, **53**, 643–711

Jones D. H. P., 1969, 'Spectroscopic observations of two eclipsing binaries', *Mon. Not. Astron. Soc. South Afr.*, **28**, 5–16

Jones H. S., 1928, 'The orbits of four long-period spectroscopic binaries', *MNRAS*, **88**, 644–659

Jorissen A., Van Eck S., Udry S., 1998, 'Insights into the formation of barium and Tc-poor stars from an extended sample of orbital elemenets', *A&A*, **332**, 877–903

Kallrath J., Milone E. F., 1999, 'Eclipsing binary stars: modelling and analysis', Springer-Verlag, New York

Karakas A. I., Tout C. A., Lattanzio J. C., 2000, 'The eccentricities of the barium stars', *MNRAS*, **316**, 689–698

Keenan P. C., Barnbaum C., 1999, 'Revision and calibration of MK luminosity classes for cool giants by *Hipparcos* parallaxes', *ApJ*, **518**, 859–865

Keenan P. C., McNeil R. C., 1989, 'The Perkins catalogue of revised MK types for the cooler stars', *ApJS*, **71**, 245–266

Kharchenko N. V., 2001, 'All-sky compiled catalogue of 2.5 million stars (2nd ed.)', *Kinematika Fiz. Nebesn. Tel*, **17**, 409

Kilkenny D., Laing J. D., 1992, 'Secondary *uvby* standards in the Harvard E-regions', *MNRAS*, **255**, 308–318

Kippenhahn R., Weigert A., 1994, 'Stellar structure and evolution. 1st ed.', Springer-Verlag, Berlin

Koch R. H., Hrivnak B. J., 1981, 'On Zahn's theory of tidal friction for cool, main-sequence close binaries', *AJ*, **86**, 438–441

Kopal Z., 1955, 'The classification of close binary systems', *Annales d'Astrophysique*, **18**, 379–430

Kopal Z., 1959, 'Close binary systems', Chapman & Hall, London

Kuiper G. P., 1935, 'Problems of double-star astronomy. I.', *PASP*, **47**, 15–42

Kupka F., Piskunov N. E., Ryabchikova T. A., Stempels H. C., Weiss W. W., 1999, 'VALD-2, `http://www.astro.univie.ac.at/~vald/`', *A&AS*, **138**, 119–133

Kurucz R. L., 1993, 'CDROM 18', SAO

Kwok S., Volk K., Bidelman W. P., 1997, 'Classification and identification of IRAS sources with low-resolution spectra', *ApJS*, **112**, 557–584

Lampens P., Kovalevsky J., Frœschlé M., Ruymaekers G., 1997, 'On the mass-luminosity relation', Proceedings of the ESA Symposium 'Hipparcos - Venice '97', Battrick B. (ed.), ESA Publications SP-402, Venice, Italy, pp. 421–424

Larson A. M., Yang S. L. S., Walker G. A. H., 1999, 'The puzzling K and early-M giants: A summary of precise radial-velocity results for 15 stars', Proceedings of the IAU Colloquium No. 170: 'Precise stellar radial velocities', ASP Conference Series, Vol. 185, Hearnshaw J. B., Scarfe C. D. (eds.), Astronomical Society of the Pacific, pp. 193–203

Latham D. W., Mazeh T., Stefanik R. P., Davis R. J., Carney B. W., Krymolowski Y., Laird J. B., Torres G., Morse J. A., 1992, 'A survey of proper motion stars. XI. Orbits for the second 40 spectroscopic binaries', *AJ*, **104**, 774–795

Latham D. W., Stefanik R. P., Torres G., Davis R. J., Mazeh T., Carney B. W., Laird J. B., Morse J. A., 2002, 'A survey of proper-motion stars. XVI. Orbital solutions for 171 single-lined spectroscopic binaries', *AJ*, **124**, 1144–1161

Lèbre L., de Laverny P., de Medeiros J. R., Charbonnel C., da Silva L., 1999, 'Lithium and rotation on the subgiant branch. I. Observations and spectral analysis', *A&A*, **345**, 936–942

Lehmann-Filhés R., 1894, 'Über die Bestimmung einer Doppelsternbahn aus spectroskopichen Messungen der im Visionsradius liegenden Geschwindigkeitscomponente', *Astr. Nach.*, **136**, 18–30

Lejeune T., Schaerer D., 2001, 'Database of Geneva stellar evolution tracks and isochrones for $(UBV)_J(RI)_C$ JHKLL'M, HST-WFPC2, Geneva and Washington photometric systems', *A&A*, **366**, 538–546

Liebert J., 1980, 'White dwarf stars', *ARA&A*, **18**, 363–398

Lindegren L., Dravins D., 2003, 'The fundamental definition of "radial velocity"', *A&A*, **401**, 1185–1201

Lindegren L., Dravins D., Madsen S., 1999, 'What is stellar 'radial velocity", Proceedings of the IAU Colloquium No. 170: 'Precise stellar radial velocities', ASP Conference Series, Vol. 185, Hearnshaw J. B., Scarfe C. D. (eds.), Astronomical Society of the Pacific, pp. 73–76

Livio M., 1993, 'Blue stragglers: The failure of Occam's razor?', Proceedings of ASP Conference Series 'Blue Stragglers, Vol. 53', Saffer R. E. (ed.), Astronomical Society of the Pacific, pp. 3–13

Lubow H., 1993, 'Some issues in the theory of mass transfer', Proceedings of Astrophysics and Space Science Library, Vol. 177: 'The Realm of Interacting Binary Stars', Sahade J., McCluskey, Jr G. E., Kondo Y. (eds.), Kluwer Academic Publishers, pp. 25–38

Lucy L. B., Ricco E., 1979, 'The significance of binaries with nearly equal components', *AJ*, **84**, 401–412

Lucy L. B., Sweeney M. A., 1971, 'Spectroscopic binaries with circular orbits', *AJ*, **76**, 544–556

Lunt J., 1919, 'The radial velocities of 185 stars observed at the Cape', *ApJ*, **50**, 161–173

Luyten W. J., 1936, 'A rediscussion of the orbits of seventy-seven spectroscopic binaries', *ApJ*, **84**, 85–103

Luyten W. J., 1955, 'A catalogue of 1849 stars with proper motions exceeding 0.5 arsconds Annually', The Lund Press, Minneapolis

Maceroni C., Montalbán J., 2004, 'The shortest period M dwarf eclipsing system BW3 V38. II. Determination of absolute elements', *A&A*, **426**, 577–584

Maeder A., Meynet G., 2000, 'The Evolution of Rotating Stars', *ARA&A*, **38**, 143–190

Maeder A., Peytremann E., 1970, 'Stellar rotation: Uniformly rotating stars with hydrogen-line-blanketed model atmospheres. Comparison with observations of A-type stars', *A&A*, **7**, 120–132

Makarov V. V., 2003, 'The 100 brighest X-ray stars within 50 parsecs of the Sun', *AJ*, **126**, 1996–2008

Malaroda S., Levato H., Galliani S., 2003, 'Bibliographic catalogue of stellar radial velocities', `http://www.casleo.gov.ar`

Marcy G. W., Butler R. P., Williams E., McCarthy C., Dosanjh P., 1996, 'Attaining Doppler Precision of 3 $\mathrm{m\,s^{-1}}$', *PASP*, **108**, 500–509

Marcy G. W., Butler R. P., Vogt S. S., Fischer D. A., McCarthy C., and 9 co-authors, 2004, 'The California and Carnegie Planet Search', `http://exoplanets.org`

Marsakov V. A., Shevelev Y. G., 1995, 'Ages, metallicities, Galactic orbits of F stars', *Bull. Inf. CDS (Strasbourg)*, **47**, 13

Martin C., Mignard F., 1997, 'Masses of astrometric binaries', Proceedings of the ESA Symposium 'Hipparcos - Venice '97', Battrick B. (ed.), ESA Publications SP-402, Venice, Italy, pp. 417–420

Martin C., Mignard F., 1998, 'Mass determination of astrometric binaries with Hipparcos. II. Selection of candidates and results', *A&A*, **330**, 585–599

Martin C., Mignard F., Frœschlé M., 1997, 'Mass determination of astrometric binaries with Hipparcos. I. Theory and simulation', *A&AS*, **122**, 571–580

Martin C., Mignard F., Hartkopf W. I., McAlister H. A., 1998, 'Mass determination of astrometric binaries with Hipparcos. III. New results for 28 systems', *A&AS*, **133**, 149–162

Mason B. D., Hartkopf W. I., 1999, 'Commission 26 (Double Stars), Inf. Circ. 138', IAU, `http://www.usc.es/astro/circulares/c138.htm`

Mason B. D., Wycoff G. L., 2004, 'Second photometric magnitude difference catalog', U.S. Naval Obs., `http://ad.usno.navy.mil/wds/dm2.html`

Mason B. D., Henry T. J., Hartkopf W. I., ten Brummelaar T., Soderblom D. R., 1998a, 'A multiplicity survey of chromospherically active and inactive stars', *AJ*, **116**, 2975–2983

Mason B. D., Gies D. R., Hartkopf W. I., Bagnuolo W. G., ten Brummelaar T., McAlister H. A., 1998b, 'ICCD speckle observations of binary stars. XIX. An astrometric/spectroscopic survey of O stars', *AJ*, **115**, 821–847

Mathieu R. D., 1994, 'Pre-main-sequence binary stars', *ARA&A*, **32**, 465–530

Mathieu R. D., Mazeh T., 1988, 'The circularized binaries in open clusters – A new clock for age determination', *ApJ*, **326**, 256–264

Matthews L. D., Mathieu R. D., 1992, 'Orbital circularization in binaries with A-type primary stars', Proceedings of the IAU Colloquium No. 135: 'Complementary approaches to double and multiple star research', ASP Conference Series, Vol. 32, McAlister H. A., Hartkopf W. I. (eds.), Astronomical Society of the Pacific, pp. 244–248

Mayor M., Mermilliod J.-C, 1984, 'Orbit circularization time in binary star systems', Proceedings of the IAU Symposium No. 105: 'Observational tests of the stellar evolution theory', Maeder A., Renzini A. (eds.), IAU, pp. 411–414

Mayor M., Udry S., Naef D., Pepe F., Queloz D., Santos N. C., Burnet M., 2004, 'The CORALIE survey for southern extra-solar planets. XII. Orbital solutions for 16 extra-solar planets discovered with CORALIE', *A&A*, **415**, 391–402

Mazeh T., 1990, 'Eccentric orbits in samples of circularized binary systems: The fingerprint of a third star', *AJ*, **99**, 675–677

Mazeh T., Goldberg D., 1992, 'On the study of the mass ratio of spectroscopic binaries', *ApJ*, **394**, 592–598

Mazeh T., Shaham J., 1976, 'Precession of the nodes in some triple systems', *ApJ*, **205**, L147–L150

Mazeh T., Prato L., Simon M., Goldberg E., Norman D., Zucker S., 2002, 'Infrared detection of low-mass sedondaries in spectroscopic binaries', *ApJ*, **564**, 1007–1014

McAlister H. A., 1976, 'Spectroscopic binaries as a source for astrometric and speckle interferometric studies', *PASP*, **88**, 317–322

McAlister H. A., 1978, 'Speckle interferometric measurements of binary stars. II.', *ApJ*, **225**, 932–938

McAlister H. A., 1985, 'High angular resolution measurements of stellar properties', *ARA&A*, **23**, 59–87

McAlister H. A., Hartkopf W. I., 1982, 'Speckle interferometry of the spectoscopic binary 94 Aqr A', *PASP*, **94**, 832–834

McAlister H. A., Hartkopf W. I., Gaston B. J., Hendry E. M., 1984, 'Speckle interferometric measurements of binary stars. IX.', *ApJS*, **54**, 251–257

McGregor P. J., 1994, 'The MSSSO near-infrared photometric system', *PASP*, **106**, 508–514

McWilliam A., 1990, 'High-resolution spectroscopic survey of 671 GK giants. 1. Stellar atmosphere parameters and abundances', *ApJS*, **74**, 1075–1128

Menzies J. W., Cousins A. W. J., Banfield R. M., Laing J. D., 1989, 'UBV $(RI)_c$ standard stars in the E- and F-regions and in the Magellanic Clouds - a revised catalogue', *South Afr. Astron. Obs. Circ.*, **13**, 1–13

Mermilliod J.-C, 1987, 'UBV photoelectric photometry catalogue (1986): I. The original data', *A&AS*, **71**, 413–417

Mermilliod J.-C, 1997, 'Radial velocities and binarity in open clusters', *Mem. S.A.It.*, **68**, 853–864

Meynet G., Maeder A., 2000, 'Stellar evolution with rotation. V. Changes in the outputs of massive star models', *A&A*, **361**, 101–120

Mignard F., 1997, 'Astrometric properties of the Hipparcos Catalogue', Proceedings of the ESA Symposium 'Hipparcos - Venice '97', Battrick B. (ed.), ESA Publications SP-402, Venice, Italy, pp. 5–10

Minnhagen L., 1973, 'Spectrum and the energy levels of neutral argon (Ar I)', *J. Opt. Soc. Am.*, **63**, 1185–1198

Monet D. G., 1979, 'A method for solving binary star orbits using the Fourier transform', *ApJ*, **234**, 275–288

Morbey C., 1975, 'A synthesis of the solutions of spectroscopic and visual binary orbits', *PASP*, **87**, 689–693

Morgan B. L., Beckmann G. K., Scaddan R. J., 1980, 'Observations of binary stars by speckle interferometry. II.', *MNRAS*, **192**, 143–151

Murdoch K., 1992, 'A high-precision radial-velocity search for substellar companions to southern solar-type stars', PhD thesis, Uni. of Canterbury

Murdoch K., Hearnshaw J. B., 1991, 'The precision of radial-velocity determinations of solar-type stars by cross-correlation', *Ap&SS*, **186**, 137–149

Neckel H., 1986, 'The "bright stars" with UBV-colors close to those of the Sun', *A&A*, **169**, 194–200

Nidever D., Marcy G. W., Butler R. P., Fischer D. A., Vogt S. S., 2002, 'Radial Velocities for 889 Late-Type Stars', *Ap&SS*, **141**, 503–522

Nordström B., 1989, 'On "the" spectral type-mass relation for main-sequence stars', *ApJ*, **341**, 934–938

Nordström B., Mayor M., Andersen J., Holmberg J., Pont F., Jørgensen B. R., Olsen E. H., Udry S., Mowlavi N., 2004, 'The Geneva-Copenhagen survey of the Solar neighbourhood. Ages, metallicities, and kinematic properties of ∼14 000 F and G dwarfs', *A&A*, **418**, 989–1019

Norlén G., 1973, 'Wavelengths and energy levels of Ar I and Ar II based on new interferometric measurements in the region 3400–9800 Å', *Physica Scripta*, **8**, 249–268

Noyes R. W., Hartmann L. W., Baliunas S. L., Duncan D. K., Vaughan A. H., 1984, 'Rotation, convection, and magnetic activity in lower main-sequence stars', *ApJ*, **279**, 763–777

Olsen E. H., 1994, 'Strömgren photometry of F- and G-type stars brighter than $V = 9.6$. I. *uvby* photometry', *A&AS*, **106**, 257–266

Paczyński B., Stanek K. Z., 1998, 'Galactocentric distance with the OGLE and *HIPPARCOS* red clump stars', *ApJ*, **494**, L219–L222

Paddock G. F., 1913, 'The derivation of the radial-velocity equation', *PASP*, **25**, 208–211

Paddock G. F., 1915, 'Spectroscopic orbit formulae for single and double spectra and small eccentricity', *Lick Obs. Bull.*, **274**, 153–179

Palmer B. A., Englemann R., Jr., 1983, 'Atlas of the thorium spectrum', Sinoradzky, H. (ed.), Los Alamos National Laboratory, LA-9615

Pasinetti-Fracassini L. E., Pastori L., Covino S., Pozzi A., 2001, 'Catalogue of Apparent Diameters and Absolute Radii of Stars (CADARS) 3rd ed. Comments and statistics', *A&A*, **367**, 521–524

Petrie R. M., 1962, 'The determination of orbital elements of spectroscopic binaries', in Stars and Stellar Systems. Vol. II, Astronomical Techniques, Hiltner W. A. (ed.), Univ. of Chicago Press, Chicago, pp. 560–583

Piskunov N. E., Kupka F., Ryabchikova T. A., Weiss W. W., Jeffery C. S., 1995, 'VALD-1', *A&AS*, **112**, 525–535

Popova E. I., Tutukov A. V., Yungelson L. R., 1982, 'Study of physical properties of spectroscopic binary stars', *Ap&SS*, **88**, 55–80

Popper D. M., 1967, 'Determination of masses of eclipsing binary stars', *ARA&A*, **5**, 85–104

Popper D. M., 1974, 'radial-velocity measurements and spectrographic orbits', *AJ*, **79**, 1307–1313

Popper D. M., 1980, 'Stellar masses', *ARA&A*, **18**, 115–164

Popper D. M., 1993, 'Some applications of cross-correlation to double-lined spectra', Proceedings of ASP Conference Series 'New frontiers in binary star research, Vol. 38', Leung K.-C, Nha I.-S (eds.), Astronomical Society of the Pacific, San Francisco, pp. 275–279

Pourbaix D., 1998, 'Simultaneous least-squares adjustment of visual and spectroscopic observations of binary stars', *A&AS*, **131**, 377–382

Pourbaix D., 2000, 'Resolved double-lined spectroscopic binaries: A neglected source of hypothesis-free parallaxes and stellar masses', *A&AS*, **145**, 215–222

Pourbaix D., Boffin H. M. J., 2003, 'Reprocessing the Hipparcos Intermediate Astrometric Data of spectroscopic binaries', *A&A*, **398**, 1163–1177

Pourbaix D., Nidever D., McCarthy C., Butler R. P., Tinney C. G., Marcy G. W., Jones H. R. A., Penny A. J., Carter B. D., Bouchy F., Pepe F., Hearnshaw J. B., Skuljan J., Ramm D. J., Kent D., 2002, 'Constraining the difference in convective blueshift between the components of α Centauri with precise radial velocities', *A&A*, **386**, 280–285

Pourbaix D., Tokovinin A. A., Batten A. H., Fekel F. C., Hartkopf W. I., Levato H., Morrell N. I., Torres G., Udry S., 2004, 'S_{B^9}: The ninth catalogue of spectroscopic binary orbits', *A&A*, **424**, 727–732

Press W. H., Teukolsky S. A., Vetterling W. T., Flannery B. P., 1994, 'Numerical recipes in C: the art of scientific computing', Cambridge Uni. Press, New York

Queloz D., Mayor M., 2001, 'From CORALIE to HARPS: the way towards 1 $\mathrm{m\,s^{-1}}$ precision Doppler measurements', *Messenger*, **105**, 1–7

Queloz D., Casse M., Mayor M., 1999, 'The fibre-fed spectrograph, a tool to detect planets', Proceedings of the IAU Colloquium No. 170: 'Precise stellar radial velocities', ASP Conference Series, Vol. 185, Hearnshaw J. B., Scarfe C. D. (eds.), Astronomical Society of the Pacific, San Francisco, pp. 13–21

Ramm D. J., 2003, 'Atlas of thorium and argon spectra (3608–7283 Å)', Uni. of Canterbury, http://www.phys.canterbury.ac.nz/research/astronomy/

Ramm D. J., Skuljan J., Hearnshaw J. B., 2004, 'The orbit of a new double-lined spectroscopic binary: HD 181958', *Observatory*, **124**, 167–173

Ramm D. J., Hearnshaw J. B., Skuljan J., 2005, 'Spectroscopic mass ratios for two visual binaries: HD 206804 and HD 217166', *Observatory*, **125**, 30–43

Ribas I., Jordi C., Giménez A., 1997, 'Biparametric calibrations of stellar mass, radius and surface gravity using *uvby*-H_β photometry', *A&A*, **327**, 207–214

Richichi A., Percheron I., 2002, 'CHARM: A Catalog of High Angular Resolution Measurements', *A&A*, **386**, 492–503

Rocha-Pinto H. J., Maciel W. J., 1998, 'Metallicity effects on the chromospheric activity-age relation for late-type dwarfs', *MNRAS*, **298**, 332–346

Rossiter R. A., 1977, 'Orbites nouvelles', *Circ. Inf. IAU Comm. 26,*, **72**

Russell H. N., 1902, 'An improved method of calculating the orbit of a spectroscopic binary', *ApJ*, **15**, 252–260

Ruymaekers G., Cuypers J., Boffin H. M. J., 2000, 'Statistical properties of visual binaries', Proceedings of the IAU Symposium No. 200: 'The Formation of Binary Stars', Reipurth B., Zinnecker H. (eds.), Astronomical Society of the Pacific, San Francisco, pp. 172–174

Ryabchikova T. A., Piskunov N. E., Stempels H. C., Kupka F., Weiss W. W., 1998, 'VALD-2', *Physica Scripta*, 162–173

Sahade J., 1962, 'Composite and combination spectra', in Stars and Stellar Systems. Vol. VI, Astronomical Techniques, Greenstein J. L. (ed.), Univ. of Chicago Press, Chicago, pp. 466–508

Sahade J., McCluskey, Jr G. E., Kondo Y. (eds.)., 1993, 'The realm of interacting binary stars', Kluwer Academic Publishers, Dordrecht, The Netherlands

Sarma M. B. K., 1962, 'The orbit of the spectroscopic binary 94 Aquarii', *ApJ*, **135**, 301–303

Savedoff M. P., 1951, 'On $e\cos\omega$ for eclipsing binaries', *AJ*, **56**, 1–9

Scalo J. M., 1986, 'The initial mass function', Gordon and Breach, New York

Scalo J. M., Dominy J. F., Pumphrey W. A., 1978, 'Masses of red giants. I. Mean initial mass from visual binary data', *ApJ*, **221**, 616–626

Scardia M., Prieur J.-L, Aristidi E., Koechlin L., 2000, 'Speckle observations of double stars with PISCO at Pic du midi: measurements in 1998', *ApJS*, **131**, 561–569

Schönberner D., Harmenec P., 1995, 'On the brightnesses and masses of early-type stars', *A&A*, **294**, 509–514

Ségransan D., Delfosse X., Forveille T., Beuzit J.-L., Udry S., Perrier C., Mayor M., 2000, 'Accurate masses of very low mass stars. III. 16 New or improved masses', *A&A*, **364**, 665–673

Shapiro S. L., Teukolsky S. A., 1983, 'Black holes, white dwarfs and neutron stars: the physics of compact objects', J.Wiley & Sons, New York

Simkin S. M., 1974, 'Measurements of velocity dispersions and doppler shifts from digitized optical spectra', *ApJ*, **31**, 129–136

Singh M., 1984, 'The determination of a spectroscopic binary orbit', *Ap&SS*, **100**, 13–30

Skuljan J., 1999, 'A study of moving groups of stars in our Galaxy', PhD thesis, Uni. of Canterbury

Skuljan J., 2003, 'A detailed analysis of the short- and lomg-term precision of stellar radial velocities obtained using HERCULES', Proceedings of ASP Conference Proceedings, '8$^{\rm th}$ Asian-Pacific Regional Meeting', Vol. 289, Ikeuchi S., Hearnshaw J. B., Tomoyuki H. (eds.), Astronomical Society of the Pacific, San Francisco, pp. 17–20

Skuljan J., 2004, 'HRSP: a dedicated échelle reduction software package for HERCULES', Proceedings of the IAU Colloquium No. 193: 'Variable stars in the Local Group', ASP Conference Series, Vol. 310, Kurtz D. W., Pollard K. R. (eds.), Astronomical Society of the Pacific, pp. 575–578

Skuljan J., Hearnshaw J. B., Cottrell P. L., 2000, 'High-precision radial-velocity measurements of some southern stars', *PASP*, **112**, 966–976

Skuljan J., Ramm D. J., Hearnshaw J. B., 2004, 'Accurate orbital elements for the bright southern spectroscopic binary ζ Trianguli Australis — an interesting case of a near-circular orbit', *MNRAS*, **352**, 975–983

Slee O. B., Stewart R. T., Bunton J. D., Beasley A. J., Carter B. D., Nelson G. J., 1989, 'A microwave survey of southern red giants', *MNRAS*, **239**, 913–922

Smith R. C., 1983, 'An empirical stellar mass-luminosity relationship', *Observatory*, **103**, 29–31

Smith R. C., 1995, 'Observational astrophysics', Cambridge Uni. Press, Cambridge

Soderblom D. R., Duncan D. K., Douglas K., Johnson D. R. H., 1991, 'The chromospheric emission-age relation for stars of the lower main sequence and its implications for the star formation rate', *ApJ*, **375**, 722–739

Söderhjelm S., 1999, 'Visual binary orbits and masses post Hipparcos', *A&A*, **341**, 121–140

Sowell J. R., Wilson J. W., 1993, 'All-sky Strömgren photometry of Speckle binary stars', *PASP*, **105**, 36–43

Staniucha M., 1979, 'Statistical analysis of the seventh catalogue of spectroscopic binaries', *Acta. Astron.*, **29**, 587–608

Starikova G. A., 1979, 'Absolute magnitudes and masses for three types of variable stars', *Sov. Astron. Lett.*, **5**, 188–192

Stefanik R. P., Latham D. W., Torres G., 1999, 'Radial-velocity standard stars', Proceedings of the IAU Colloquium No. 170: 'Precise stellar radial velocities', ASP Conference Series, Vol. 185, Hearnshaw J. B., Scarfe C. D. (eds.), Astronomical Society of the Pacific, pp. 354–366

Sterne T. E., 1941a, 'Notes on binary stars. IV. A source of spurious eccentricity in spectroscopic binaries', *Proc. Natl. Acad. Sci.*, **27**, 168–175

Sterne T. E., 1941b, 'Notes on binary stars. V. The determination by least-squares of the elements of spectroscopic binaries', *Proc. Natl. Acad. Sci.*, **27**, 175–181

Strassmeier K. G., Fekel F. C., Bopp B. W., Dempsey R. C., Henry G. W., 1990, 'Chromospheric Ca II H and K and H_α emission in single and binary stars of spectral types F6–M2', *ApJS*, **72**, 191–230

Tassoul J-L., 1995, 'On orbital cicularization in late-type close binaries', *ApJ*, **444**, 338–341

ten Brummelear T., Mason B. D., McAlister H. A., Roberts L. C. Jr., Turner N. H., Hartkopf W. I., Bagnuolo W. G., 2000, 'Binary star differential photometry using the adaptive optics system at Mount Wilson observatory', *AJ*, **119**, 2403–2414

Tinbergen J., 1979, 'A list of zero-polarization standards', *A&AS*, **35**, 325–326

Tinbergen J., 1982, 'Interstellar polarization in the immediate solar neighbourhood', *A&A*, **105**, 53–64

Tinsley B. M., Gunn J. E., 1976, 'Luminosity functions and the evolution of low-mass population I giants', *ApJ*, **206**, 525–535

Tokovinin A. A., 1982, 'Interferometer observations of double stars. I.', *Sov. Astron. Lett.*, **8**, 22–24

Tokovinin A. A., Smekhov M. G., 2002, 'Statistics of spectroscopic sub-systems in visual multiple stars', *A&A*, **382**, 118–123

Toner C. G., Gray D. F., 1988, 'The stapatch on the G8 dwarf ξ Bootis A', *ApJ*, **334**, 1008–1020

Tonry J., Davis M., 1979, 'A survey of galaxy redshifts. I. Data reduction techniques', *AJ*, **84**, 1511–1525

Trimble V., 1974, 'On the distribution of binary system mass ratios', *AJ*, **79**, 967–973

Trimble V., 1984, 'The angular momentum-vs-mass relation for spectroscopic binaries', *Ap&SS*, **104**, 133–143

Trimble V., 1990, 'The distribution of binary system mass ratios – A less biased sample', *MNRAS*, 79–87

Twarog B. A., 1980, 'The chemical evolution of the solar neighborhood. I. A bias-free reduction technique and data sample', *ApJS*, **44**, 1–29

Udalski A., Soszynski I., Szymanski M., Kubiak M., Pietrzynski G., Wozniak P., Zebrun K., 1998, 'The optical gravitational lensing experiment. Eclipsing binary stars in the Small Magellanic Cloud', *Acta. Astron.*, **48**, 563–651

Udry S., Mayor M., Queloz D., 1999, 'Towards a new set of high-precision radial-velocity standard stars', Proceedings of the IAU Colloquium No. 170: 'Precise stellar radial velocities', ASP Conference Series, Vol. 185, Hearnshaw J. B., Scarfe C. D. (eds.), pp. 367–377

van Altena W. F., Lee J. T., Hoffleit E. D., 1995, 'The General Catalogue of Trigonometric Stellar Parallaxes, $4^{\rm th}$ ed.', Yale Univ. Obs.

Vanbeveren D., De Loore C., Van Rensbergen W., 1998, 'Massive stars', *A&AR*, **9**, 63–152

van Biesbroeck G., 1936, 'Measurements of Double Stars', *Publ. Yerkes Obs.*, **8**, 47–95

van de Kamp P., 1962, 'Astrometry with long-focus telescopes', in Stars and Stellar Systems. Vol. II, Astronomical Techniques, Hiltner W. A. (ed.), Univ. of Chicago Press, Chicago, pp. 487–536

van de Kamp P., 1967, 'Principles of astrometry : with special emphasis on long-focus photographic astrometry', W. H. Freeman, San Francisco

van den Bos W. H., 1934, 'Provisional orbit of OΣ536 = BDS 12090 = ADS 16417', *Union Obs. Circ.*, **92**, 102–104

van den Bos W. H., 1950, 'The orbit of Φ 283', *Union Obs. Circ.*, **109**, 370

van den Bos W. H., 1962, 'Orbit determination of visual binaries', in Stars and Stellar Systems. Vol. II, Astronomical Techniques, Hiltner W. A. (ed.), Univ. of Chicago Press, Chicago, pp. 537–559

van der Hucht K. A., Hidayat B., 2001, 'Wolf-Rayet Binaries', Proceedings of the IAU Symposium No. 200: 'The Formation of Binary Stars', Weiss W. W., Baglin A. (eds.), Astronomical Society of the Pacific, pp. 79–83

Vogt S. S., Allen S. L., Bibelow B. C., Bresee L., and 23 co-authors, 1994, 'HIRES: the high-resolution échelle spectrometer on the Keck 10-m telescope', Proceedings of 'SPIE Instrumentation in Astronomy VIII', Vol. 2198, Crawford D. L., Craine E. R. (eds.), Proc. Soc. Photo-Opt. Instr. Eng., pp. 362–375

Walker R. L., 1978, 'A catalogue of visual binaries with one or more variable components', U. S. Naval Obs. Flagstaff, Ariz.

Warner B., 1969, 'CaII K emission in southern late-type stars', *MNRAS*, **144**, 333–350

Wichmann R., Schmitt J. H. M. M., Hubrig S., 2003, 'New spectroscopic binaries among nearby stars', *A&A*, **400**, 293–296

Wilson O. C., 1941, 'On the determination of mass ratios of spectroscopic binaries', *ApJ*, **93**, 29–32

Wilson O. C., 1963, 'A probable correlation between chromospheric activity and age in main-sequence stars', *ApJ*, **138**, 832–848

Wilson O. C., Bappu M. K. V., 1957, 'Emission in late-type stars: Dependence of line width on luminosity and related topics', *ApJ*, **125**, 661–683

Wilson R. E., 1979, 'Eccentric orbit generalization and simultaneous solution of binary star light and velocity curves', *ApJ*, **234**, 1054–1066

Wood F. B., 1950, 'On the change of period of eclipsing variables stars', *ApJ*, **112**, 196–206

Woolley R., Epps E. A., Penston M. J., Pocock S. B., 1970, 'Catalogue of stars within twenty-five parsecs of the Sun', Royal Obs. Annals, No.5, Herstmonceux

Worley C. E., 1989, 'Publ. USNO', 25, pt 3

Wozniak P., Stanek K. Z., 1996, 'Variations of the selective extinction across the Galactic bulge: implications for the Galactic bar', *ApJ*, **464**, 233–237

Wright J. T., Marcy G. W., Butler R. P., Vogt S. S., 2004, 'Chromospheric Ca II emission in nearby F, G, K, and M stars', *ApJS*, **152**, 261–295

Zahn J.-P, 1977, 'Tidal friction in close binary stars', *A&A*, **57**, 383–394

Zahn J.-P, Bouchet L., 1989, 'Tidal evolution of close binary stars. II - Orbital circularization of late-type binaries', *A&A*, **223**, 112–118

Zucker S., 2003, 'Cross-correlation and maximum-likelihood analysis: a new approach to combining cross-correlation functions', *MNRAS*, **342**, 1291–1298

Zucker S., Mazeh T., 1994, 'Study of spectroscopic binaries with TODCOR. I. A new two-dimensional correlation algorithm to derive the radial velocities of the two components', *ApJ*, **420**, 806–810

Zucker S., Torres G., Mazeh T., 1995, 'Study of spectroscopic binaries with TODCOR: III. Application to triple-lined systems', *ApJ*, **452**, 863–869

Zucker S., Mazeh T., Santos N. C., Udry S., Mayor M., 2003, 'Multi-order TODCOR: Apllication to observations taken with the CORALIE échelle spectrograph. I. The system HD 41004', *A&A*, **404**, 775–781

It is gratefully acknowledged that this research has benefited from the use of the databases provided by SIMBAD and the VizieR catalogue access tool (both operated at CDS, Strasbourg, France), the NASA ADS, and the 'Washington Double Star Catalog' maintained at the U. S. Naval Observatory.